Author:
Day, Matthew

Title:
Microfabricated Optics for Quantum Control of Trapped Ions

Microfabricated optics for quantum control of trapped ions

By

MATTHEW L. DAY

Department of Physics
UNIVERSITY OF BRISTOL

A dissertation submitted to the University of Bristol in accordance with the requirements of the degree of DOCTOR OF PHILOSOPHY in the Faculty of Science.

SEPTEMBER 2018

Abstract

Trapped ions have been established as a useful resource for a number of quantum protocols. In all applications, from precision timing to quantum information processing, it is beneficial to increase the number of trapped ions in one system. Microfabricated ion microtrap arrays have provided a route to scaling the number of trapped ions, however a corresponding scalable optical interface for coupling to the electronic and motional states of the ions has not yet been realised. One identified technique to scaling the optics is to use microfabrication techniques. Microfabricated optics have been previously coupled to trapped ions, either for imaging or laser beam addressing, however no complete architecture has been realised, with the state of the art being the addressing of a single ion trap segment with a single beam of red wavelength. In this thesis, we propose and develop a novel micro-optical assembly for laser beam addressing and ion fluorescence collection of multiple ion microtrap segments. The assembly is composed of fibre, laser-written waveguide and diffractive microlens arrays for delivering laser beams from blue to near-IR wavelengths with the correct k-vectors to drive electronic and motional transitions in $^{88}Sr^{+}$ ions, as well as collecting the resulting blue wavelength fluorescence. The realisation of the optical assembly required the development of laser-written waveguides for guiding blue wavelengths, as well as efficient on and off-axis diffractive microlenses. The developed optical components allowed the fabrication of a demonstrator optical assembly for delivering three blue wavelength beams and two near-IR wavelength beams to two spatially separated points in space corresponding to the centres of two microtrap segments. The fabricated assembly has high transmission, accurate beam pointing and low crosstalk which supports the future viability of the platform.

Dedication and acknowledgements

This thesis would not have been written if it weren't for the help and support of numerous people. My deepest gratitude goes to my thesis supervisors, Graham Marshall and Alastair Sinclair, who have provided a fundamental backbone to the project and owe a great deal to its success. Graham, your tireless and exhaustive well of knowledge has allowed me to achieve things I otherwise could not have; thank you in particular for teaching me to accept that things happened in the past. Alastair, you have shown me what true scientific rigour looks like and taught me to dig deeper and go further than initially thought possible; your sage advice and life lessons were always welcome. You have both been invaluable mentors, and I am a better scientist for it.

To the other academics who have supported me: Mark Thompson, thank you for having the vision to initiate the project; and thank you Ruth Oulton for taking over and providing pastoral care when things got tough. Kaushal Choonee, you provided substantial momentum to the project and were indispensably helpful. I could not have achieved the results I did in the cleanroom without the help and advice of Andrew Murray, who patiently explained many cleanroom processes and techniques, and was always on hand when things went wrong, so thank you. To Sebastian Knauer, for being so much more than a colleague. To the team at Macquarie University, thank you for being such kind and welcoming hosts. In particular, thank you Zachary Chaboyer for the training and long days in the lab, and thank you to Simon Gross for your enthusiastic help and input into the project - as well as making sure I had a proper Australian pub experience.

I would especially like to thank my cohort of the Quantum Engineering Centre for Doctoral Training, for the camaraderie, for the company, and for the fresh perspectives - I'm sure I'll use one of you in the future for a job connection. In particular, thank you Sam Morley-Short and Sam Pallister for the cheese and beer making sessions, which weren't as much a break from science as one would hope. To Euan Allen, for the tea breaks and office company. And to those without which the CDT would not be the same: Andrea Watkins and Lin Burden, thank you for being reliable, getting me to Australia and always helping. Thank you to Peter Turner for steering the ship, and Chris Erven thank you for the advice and helping hands, I will treasure my *Most Canadian* award for always.

Of course, this research could not have been conducted if I could not afford to live or purchase vital research equipment. Thank you to my primary sponsor, the *Defence, Science and Techology Labs* for funding and belief in the project. Other funding sources include the *Engineering and Physical Sciences Research Council* which have supported both the *Quantum Engineering Centre for Doctoral Training* and *Quantum Integrated Photonic Circuits*, which were invaluable to my education and device fabrication respectively.

And, most importantly, to my eternal cheerleader and wife, Brigitta, for the unfaltering support when I needed it and giving me the space and encouragement to flourish. Throughout this time you were a companion, a sounding-board, a proofreader, an inspiration, a best friend, and so much more. Thank you.

Author's declaration

I declare that the work in this dissertation was carried out in accordance with the requirements of the University's Regulations and Code of Practice for Research Degree Programmes and that it has not been submitted for any other academic award. Except where indicated by specific reference in the text, the work is the candidate's own work. Work done in collaboration with, or with the assistance of, others, is indicated as such. Any views expressed in the dissertation are those of the author.

SIGNED: ..... DATE: .....

Contents

List of initialisms

BIM Boundary integral method

CCD Charge-coupled device

DC Direct current

DML Diffractive microlens

EBL Electron beam lithography

FEM Finite-element method

FFT Fast Fourier transform

FIB Focused ion beam

GSA Gerchberg-Saxton algorithm

HDR High-dynamic range

HDRBP High-dynamic range beam profile

HPO High power oscillator

IR Infrared

LMA Large mode area

LW Laser-written

LCC Leadless chip carrier

MFD Mode-field diameter

MMF Multi-mode fibre

NA Numerical aperture

NPL National Physical Laboratory

PECVD Plasma-enhanced chemical vapour deposition

PL Photoluminescence

PMMA Poly(methyl)-methacrylate

PML Perfectly matched layer

PMT Photomultiplier tube

RCWA Rigorously coupled wave analysis

RF Radio frequency

RIE Reactive ion etching

SDT Scalar diffraction theory

SMC Single-to-multi core

SMF Single-mode fibre

TDIC Transmission differential interference contrast

UV Ultraviolet

VGA V-groove array

List of Figures

List of Tables

1

Introduction

Atomic ions held in radio-frequency (RF) traps are a well understood and mature quantum system. Coherent quantum state preparation, control and measurement of trapped ions can be performed for applications in quantum information processing, ultra-precise spectroscopy and quantum-enhanced metrology. The general scheme common to most trapped ion systems is to use a metastable electronic state of the ion as a two-level system with a long coherence time. When the metastable state is an electric quadrapole transition, arbitrary superpositions between these energy levels can be driven using a resonant laser; often called the *qubit* or *clock* laser. Metastable states that do not use the electronic fine structure, such as Zeeman sublevels or hyperfine levels must either be directly driven with microwave radiation, or through Raman transitions with two slightly detuned lasers. A projective measurement of the two-level system can be performed by driving a strongly-allowed electronic transition that is state dependent. Detecting the presence or absence of fluorescence provides a high fidelity state determination. An additional quantum resource is the motional state of the ion, which is quantised due to the harmonic trapping potential. The motional states can be used either for cooling the ion, or as a bus for generating entangled states of multiple ions. Due to the relatively weak coupling of the ion to the motional states, entangling operations typically occur on the 10–100 μs timescale. Recently, entangling gates on timescales of <1 μs have been proposed [1] and demonstrated [2, 3] using ultra-fast laser pulses, which makes trapped ions a competitive platform for universal quantum computation. The promise of using trapped ion crystals for quantum Hamiltonian simlations has recently been demonstrated with a chain of 53 qubits [4]; the limiting factor to qubit scaling and Hamiltonian complexity being the linear ion chain stability and individual ion addressing capability respectively.

The low noise and precise control of isolated trapped ions makes them excellent candidates for quantum-enhanced sensing, either as a frequency reference or for the measurement of very small peturbative fields and forces on the ions. It has been well established that quantum-enhanced metrology approaching the Heisenberg limit, where measurement precision scales as $1/N$ (with N being

the number of ions), is possible with trapped ions [5, 6]. As the precision increases with the number of entangled ions, it is desirable to design a scalable system where large entangled states can be generated. Microfabricated ion traps containing multiple, reconfigurable trapping zones provide one technological advance for achieving a scalable ion trap system. However, current trapped ion systems typically use bulk optical set-ups such that it is difficult to increase the number of quantum controlled ions, particularly if they are trapped in separate segments as the optics either have to be duplicated or realigned. The duplication of the optics is costly, requiring the purchase of a set of new optics, and the realignment of an existing optical set up is time-consuming and limits quantum operations that can be performed. Bulk optical set-ups can also undergo alignment drift, where the position of the laser radiation moves over time, changing the interaction strength with the ion. To overcome these limitations it is desirable to both fix the alignment to increase stability and decrease user involvement, and to dramatically decrease the cost of adding additional addressing beams and fluorescence detection optics to increase the number of simultaneously controlled trapped ions. We refer to the aim of minimising the cost of adding additional optical elements as *optical scalability*. Increasing optical scalability while employing a similarly scalable ion trap would allow for individually addressable trap segments, which would increase trapped ion system complexity and capability not just for sensing, but also for computation and simulation.

To provide context and motivation for the contents of the thesis, the quantum system of trapped ions will first be outlined before discussing the current operational set up at the National Physical Laboratory (NPL). The applications of trapped ions and limitations to more advanced protocols will be introduced in further detail, followed by an overview of previous attempts at increasing stability and scalability using integrated and microfabricated optics.

1.1 Theory of trapped ions

Experimental schemes for controlling trapped ions depend on the ion species used, as well as the internal energy levels controlled for implementing desired protocols [7]. This thesis will concentrate on single-ionised strontium-88 ($^{88}Sr^{+}$) where quantum protocols are performed by manipulation of the fine structure of the outermost electron. A metastable quadrapole transition is used as the qubit state and is a common scheme in alkaline-earth metal ions of calcium, strontium, and barium [8–10]. A second form of qubit implementation is the use of hyperfine transitions, driven either indirectly by Raman beams or directly by microwave sources [11]. Hyperfine transitions require non-zero nuclear spin and careful selection of ion species isotopes. The isotope of strontium considered in this thesis has zero nuclear spin and therefore no hyperfine transitions are available. The third dominant qubit implementation is in Zeeman sublevels [12]. Quantum protocols performed in the system under consideration here do use specific Zeeman sublevels split by an external magnetic field, however

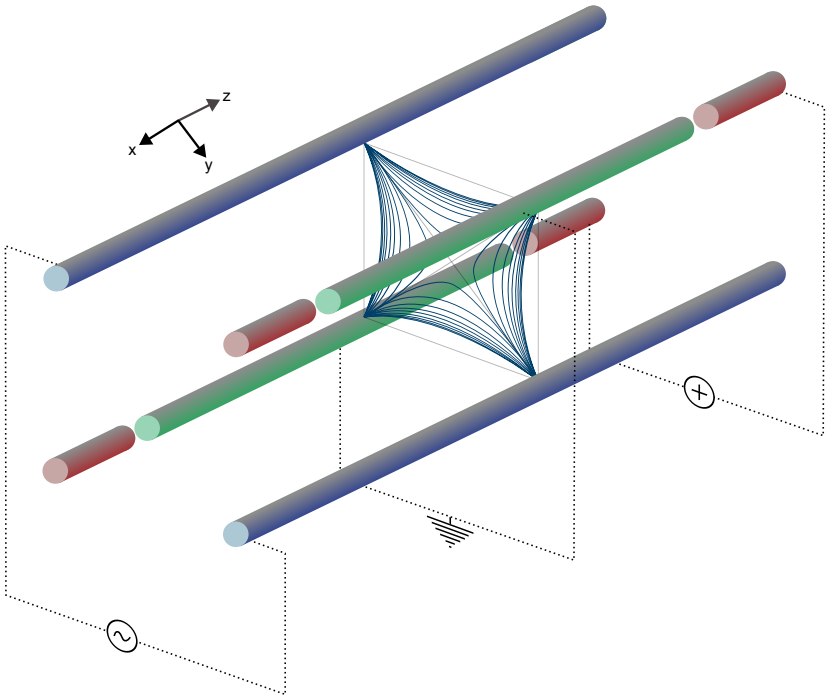

Figure 1.1: Schematic of a linear Paul trap demonstrating the pseudopotential (blue lines) generated by 4 rods, 2 with in-phase RF frequency (blue) and 2 set to ground (green). DC end caps for z-axis confinement are shown in red.

they do not use the Zeeman sublevels within the same electronic energy level as a qubit. The fine structure and Zeeman sublevels are discussed further in Section 1.1.4. We begin with an outline of radio-frequency traps for confining of ionised atoms.

1.1.1 Radio-frequency traps

The confinement of charged particles to a single point in space is restricted to dynamic electric potentials due to Gauss' law for electrostatic fields which states that no 3-dimensional potential minima can be generated in free-space. To trap charged particles, one can use the time-varying electric potential [13]

$$\phi(x, y, z, t) = \frac{1}{2}\alpha(x^2 - y^2)(U_{RF}\cos(\Omega_{RF}t) + U_{DC}) + \frac{1}{2}\beta z^2 U_z \,, \tag{1.1}$$

where Ω_{RF} is the drive frequency of the time-varying potential U_{RF}, and static potential voltages are given by U_{DC} and U_z in the $x(y)$ and z direction respectively. The potential in Equation 1.1 represents a linear Paul trap, and sets up a rotating quadrapole potential in the x–y plane with static z-axis confinement. The trapping potential is typically generated using 4 rods at corners of a rectangle, with the potential minimum located at the centre of the rectangle as shown in Figure 1.1. The time-averaged potential, the pseudopotential, seen by the ion is given by

$$\bar{\phi}(x, y, z) = \frac{(Qe)^2}{4m\Omega_{RF}^2}|\nabla\phi(x, y, z)|^2 \tag{1.2}$$

which has a minimum at $x = y = 0$, where Q and m are the charge and mass of the ion respectively. The full, classical equations of motion of the ion in the time-varying potential can be solved for and in the pseudopotential approximation the motion of the ion becomes a superposition of *secular motion* and *micromotion*. The secular motion is the fundamental oscillation of the ion in the pseudopotential, with frequency along each trap axis given by

$$\omega_x = \frac{1}{2\pi}\sqrt{\frac{1}{m}\frac{d^2\phi(x,0,0)}{dx^2}}\,, \tag{1.3}$$

$$\omega_y = \frac{1}{2\pi}\sqrt{\frac{1}{m}\frac{d^2\phi(0,y,0)}{dx^2}}\,. \tag{1.4}$$

Micromotion occurs at the drive frequency of the RF field, Ω_{RF} and is due to the ion oscillating around the potential minimum through secular motion. Any perturbation of the ion away from the RF field saddle point increases the amplitude of the micromotion and is therefore undesirable, leading to anomalous heating of the ion.

1.1.2 Quantum motional states

As well as classical motion, the ion's motion is quantised by the harmonic potential of the ion trap. To illustrate this we consider the static confinement along the z-axis; the time-dependent quantum mechanical motion along the x and y direction follows a similar treatment but with higher-order corrections from the frequency of the RF drive [13]. The centre-of-mass quantum mechanical motion along the z-axis is given by the static Hamiltonian [14]

$$H_{ho} = \frac{p^2}{2m} + \frac{1}{2}m\left(\frac{\omega_z}{2\pi}\right)z^2 = h\omega_z\left(a^\dagger a + \frac{1}{2}\right) \tag{1.5}$$

where ω_z is the secular frequency along the z-axis. The operators a and $a^\dagger$ are the creation and annihilation operators for quanta of vibration and the eigenstates of H_{ho} are correspondingly the number states $|n\rangle$ for $n \in \mathbb{Z}^+$. The energy levels of the Hamiltonian are then $E_n = h\omega_z(n + 1/2)$ which define an equally spaced ladder of energy states that the ion can occupy. All ions in the same harmonic potential see the same Hamiltonian, sharing the same motional states and can therefore be used to interact multiple ions together even if they are not spatially close to one another. These large-scale interactions can be used as multi-qubit gates for entangling all ions trapped in the same potential [15]. The implementation time of the so-called *Mølmer-Sørensen* gate depends directly on the secular frequency of the ions' motion and therefore high secular frequencies are desired for fast multi-qubit gate operations.

1.1.3 Photoionisation of neutral strontium

The loading of $^{88}Sr^+$ into the trapping potential is performed by photoionising an atomic vapour of neutral strontium [16]. An oven is used to thermally evaporate Sr atoms, and is located such that

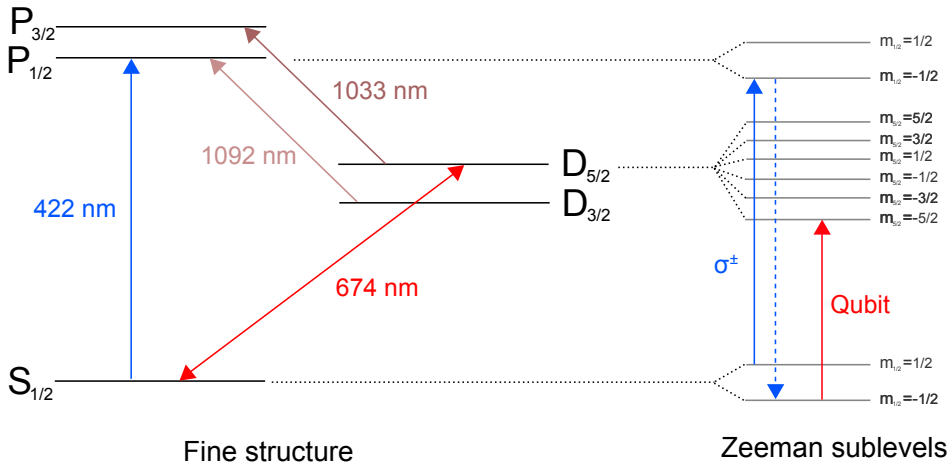

Figure 1.2: The fine structure and Zeeman sublevels of $^{88}Sr^{+}$ indicating employed transitions in quantum protocols. Included is the circularly polarised optical pumping transition for qubit preparation using Zeeman sublevels, and the 674 nm qubit transition currently employed at NPL.

the vapour passes through the ion trap aperture. Two-photon ionisation is performed using two laser sources at wavelengths of 461 nm and 405 nm. The 461 nm first excites an electron in the outer shell of the Sr atom to an intermediate state, and the 405 nm radiation excites the electron above the ionisation threshold. The atom is left ionised with a single valance electron, and the now charged atom experiences the trapping potential and is confined near the potential minimum. Calibration of the photoionisation rate for the used beam powers and geometry allows for the highly-controlled loading of single ions. To load multiple ions, the photoionisation procedure is repeated until the desired number of ions are trapped.

1.1.4 Electronic structure

The presence of a single electron in the outer shell of singly-ionised alkaline-earth metals allows for coherent manipulation and storage of quantum information. For illustration, the simplified and full energy level diagram of $^{88}Sr^{+}$ is given in Figure 1.2. At the simplest level, the dipole forbidden $S_{1/2} \rightarrow D_{5/2}$ transition can be treated as an effective two-level system. Due to the state only being quadrapole allowed, it has a long lifetime (396 ms) and narrow linewidth (0.4 Hz) facilitating its use either as a qubit or a ultra-precise frequency standard. The transition is therefore referred to as the *qubit* or *clock* transition. In the qubit scheme, the $S_{1/2}$ level is the $|0\rangle$ state and $D_{5/2}$ level is the $|1\rangle$ state. Coherent superpositions of the two states can be prepared by Rabi oscillations with a laser at the resonant frequency of the transition. The dipole allowed transition $S_{1/2} \rightarrow P_{1/2}$ then provides a qubit measurement process whereby when laser radiation resonant at this transition's wavelength is incident on the ion, the ion will only interact with the beam if it is in the $|0\rangle$ state. As the $S_{1/2} \rightarrow P_{1/2}$ transition has a linewidth of 20.22 MHz, then 8×10^{6} photons are emitted by the ion per second at saturation [17]. The collection and measurement of this fluorescence provides a state deterministic

signal that allows for high fidelity measurement of the qubit state. After excitation to the $P_{1/2}$ state there is a finite branching ratio to the metastable state $D_{3/2}$. A laser resonant with the $D_{3/2} \rightarrow P_{1/2}$ transition can be used to repump the electron back to the bright state where it quickly decays to the ground state. Likewise, if the electronic state is measured to be $D_{5/2}$, then a clearout laser connects the transition $D_{5/2} \rightarrow P_{3/2}$ where decay to the ground state can quickly occur. The use of the clearout laser is useful for resetting of the quantum state after measurement without waiting for the metastable state to naturally decay. The wavelengths of all these transitions for $^{88}Sr^{+}$ are given in Figure 1.2, spanning from blue (422 nm) to near-infrared (1092 nm). The fine structure can be further split using a magnetic field, defining a quantisation axis and making the Zeeman sublevels non-degenerate. In practice, qubit operations are performed on specific sublevels of the $S_{1/2}$ and $D_{5/2}$ levels which requires ground-state preparation into the $m_{1/2} = -\frac{1}{2}$ Zeeman sublevel. The process, called *optical pumping*, uses circularly polarised light to decrease $m_{1/2}$ by 1 through conservation of angular momentum via the $P_{1/2}$ Zeeman sublevel.

1.1.5 Laser-cooling of trapped ions

One important operation in trapped ions is the cooling of the ion to its motional ground state using laser radiation, and it serves as a useful example of a light-matter interaction. Our intention is to demonstrate that when coupling lasers to ions there are specific requirements to successfully drive the desired transitions. The essential aim in laser cooling is to reduce the energy eigenvalue of the quantum motional state of the ion by sequentially reducing the number state. Put succinctly, this can be performed by illuminating the ion with a laser along the axis of motion to be cooled and red-detuning the frequency of the laser from an electronic transition such that the ion only absorbs laser light when moving towards the laser source due to the Doppler effect. Remission of the absorbed photon with a different k-vector thereby reduces the momentum of the ion, and continuous application of the laser source can cause the ion to lose the majority of its energy.

More formally, one can consider a laser field $\vec{E}(z,t) = E_0\vec{\epsilon}cos(\omega_r t - k_z z)$ where $\vec{\epsilon}$ is the polarisation, E_0 is the amplitude and $k_z = |\vec{k}|\cos\theta$ is the projection of the laser wavevector on the z-axis [14]. For an ion at the position z at time t with a dipole moment, $\vec{d}$ and resonant frequency ω_0, between the ground, $|g\rangle$ and excited $|e\rangle$ states the Hamiltonian driven by the laser field is given by

$$H = H_{ho} - \hbar(\omega_o - \omega_r)\,|e\rangle\langle e| + \left(\hbar\frac{\Omega}{2}\right)\left[|e\rangle\langle g|\, e^{ik_z z} + |g\rangle\langle e|\, e^{-ik_z z}\right] \tag{1.6}$$

where $\Omega = \vec{d}\cdot\vec{\epsilon}E_0/\hbar$ is the Rabi frequency. The operators $e^{\pm ik_z z}$ describe the emission or absorption of a photon, which for the motional states is between the number states $|n\rangle$ and $|n'\rangle$. It is important to recognise that the operators in the Hamiltonian are proportional to the projection of the laser polarisation onto the dipole moment of the transition through the Rabi frequency. The laser polarisation

therefore plays a role in the strength of the coupling of the ion to the laser source and must be carefully chosen, ideally along the dipole axis. The k-vector of the laser plays a similar role; if the laser is perpendicular to the z-axis then $k_z = 0$ and $e^{ik_z z} = 1$, and no number state change occurs.

The motional energy states of the ion have energy $E_n = h\omega_z(n + 1/2)$ and therefore augment the spectrum of the transition with sidebands of frequency $\omega = \omega_0 \pm m\omega_z$, $m \in \mathbb{Z}^+$. By tuning the laser frequency to $\omega_L = \omega_0 - \omega_z$ the transition $|n\rangle \rightarrow |n-1\rangle$ is preferentially driven over $|n\rangle \rightarrow |n+1\rangle$ and the ion is driven down the energy ladder. In the *Doppler cooling* regime, the linewidth of the transition (~20 MHz for $^{88}Sr^+$) is broader than the trap frequency (~$2\pi \times 2$ MHz) such that laser source partially drives the $|n\rangle \rightarrow |n+1\rangle$ transition which limits the ultimate lowest value of n that can be achieved. In the *resolved-sideband cooling* regime, a narrower transition (such as $S_{1/2} \rightarrow D_{5/2}$) can be used such that only $|n\rangle \rightarrow |n-1\rangle$ is driven at the expense of the spontaneous emission rate. To increase the emission rate the transition linewidth can be artificially broadened by using the repumper transition [14].

The extension to cooling of all 3-dimensions is relatively straightforward, however it is clear that when a laser source is orientated for optimal cooling of one axis, it is perpendicular to the other two axes and no cooling occurs. By orientating the laser source such that it is non-parallel with any trap axis then simultaneous cooling of all quantum motional states can be achieved. The above techniques can also be considered for reducing the micromotion of the ion, which carries its own motional spectrum. Micromotion of the ion in each of the trap axis can be measured using the fluoresence modulation technique, which requires three non-coplanar beams for dominantly coupling to each of the axes of motion [18, 19]. Excess micromotion leads to second-order Doppler shifts on the atomic transitions and therefore if it is not minimised then the application of the trapped ions as an ultra-precise frequency standard is compromised. As the same beams for Doppler cooling are used for micromotion monitoring and minimisation, in practice three cooling beams are included in the optical setup.

1.2 Current set-up at the National Physical Laboratory

The ion trapping experimental apparatus at NPL has undergone many iterations of trap design and control systems. The most recent era is the design [20], fabrication [21] and demonstration [22] of a microfabricated, segmented Paul trap. In the following we briefly introduce this current era of trap design, with more detail found in references [9, 23].

1.2.1 The microtrap

The ion traps currently used at NPL are linear Paul microtrap chips that are fabricated at wafer-scale in a silicon substrate using standard microelectricalmechanical-system (MEMS) processes. The trap

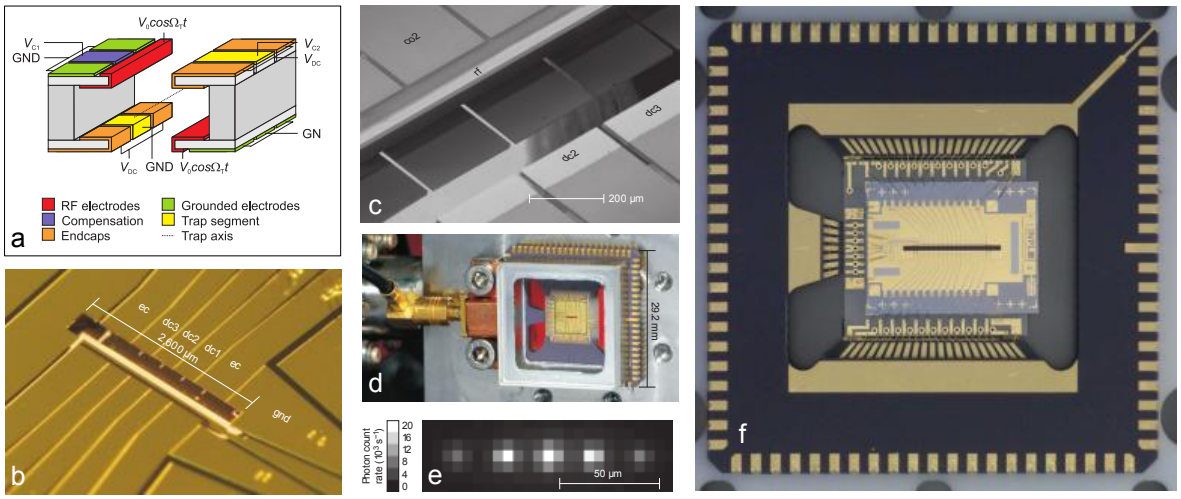

Figure 1.3: The NPL microtrap (a) Design of a unit cell of the segmented microtrap showing 3 segments, with the two outer segements providing the confining, static z-axis potential, reprinted under creative commons from [20]; (b) An optical image of a fabricated, monolithic microtrap with gold-coated electrodes and 3 operational segments, with two endcaps to provide z-axis confinement, reprinted with permission from [22]; (c) An SEM image of the same microtrap shown in (b), reprinted with permission from [22]; (d) The microtrap mounted in a leadless chip carrier for vacuum feedthrough with a large window for optical access, reprinted with permission from [22]; (e) A string of 5 ions trapped in one segment, reprinted with permission from [22]; (f) The latest trap iteration with 11 segments, reprinted with permission from [24] Copyright 2017 IEEE.

design is shown in Figure 1.3(a), with multiple segments of DC electrodes sharing a common RF electrode. The DC segment voltages can be independently tuned to allow for reconfigurable confinement regions such that ions can be deterministically held in a particular segment or shuttled to other sections of the microtrap. Further DC electrodes are located behind the RF rail to allow for fine tuning of the pseudopotential for micromotion minimisation. The first fabricated trap design is shown in Figure 1.3(b-d) with three operational segments and dedicated end cap electrodes for z-axis confinement. The electronic access to the microtrap when housed inside a vacuum chamber is provided by a leadless chip carrier (LCC), which the microtrap is wire-bonded to through an intermediate substrate. For high optical access a large, 4 mm thick glass window is indium sealed to a metal spacer that itself is indium sealed to the LCC; we refer to the side of the microtrap facing this optical window (shown in Figure 1.3(d)) as the *back* side. Optical access is also available on the *front* side of the microtrap through a larger vacuum window on the opposite side of the vacuum chamber. Figure 1.3(e) shows a fluorescence image of five ions trapped in the same microtrap segment, and up to 14 ions were confined in the same segment with this microtrap.

As the fabrication process is not affected by increasing the number of segments, more complex trap designs are readily fabricated. The latest, fabricated, trap design is shown in Figure 1.3(e) mounted on an LCC. The design has 11 segments, of which seven are designated for operation, one is designated for loading of ions through photoionisation and three are used for transferring the loaded ions to the operation segment. The microtrap is currently in operation, however its full potential is yet to be

realised due to limitations on the current optical setup that is composed of bulk optics which are not readily able to address multiple segments.

1.2.2 The optics

The large size of the vacuum windows on both microtrap sides allows for flexible optical addressing of the ions in the microtrap [9]. The required wavelengths for $^{88}Sr^{+}$ photoionisation and control are delivered using polarisation maintaining fibre, collimators and lenses to focus light onto the addressed microtrap segment. Due to the number of laser beams required, these addressing optics surround the optical access windows of the vacuum chamber. Fluorescence collection is performed from both sides of the microtrap using high numerical aperture lenses which each covers 0.25π sr of the ions' emission. On one side the fluorescence is imaged onto a electron-multiplying CCD camera, and on the other it is collected into a photomultiplier tube (PMT) for counting of the individual photons; filters are used to reject the 674–1092 nm wavelengths to reduce background counts. Currently, the number of optics is limited to addressing only one operational and one loading segment which is a severe restriction on the operation of the 11 segment microtrap. Ions are first loaded, with successful loading first confirmed by fluorescence detection with the PMT, and then shuttled to an operation segment where fluorescence detection is performed with the CCD. More advanced protocols cannot be implemented unless all addressing and collection optics are duplicated for other segments. The limited space available around the microtrap means it is not possible to address all seven operational segments with the current optical configuration.

1.3 Applications of trapped ions

The trapping and control of a deterministic number of individual ions at well known positions in space allows for the implementation of numerous and useful operations. The available applications of trapped ions depend on the fact that each atom responds identically to the same control operation in the absence of external noise that may perturb the atomic energy levels. Here we introduce three applications of trapped ion systems in decreasing order of maturity: atomic clocks, quantum-enhanced sensing and quantum information processing.

1.3.1 Atomic clocks

The current definition of the second is based on a microwave frequency transition in caesium. A microwave source is locked to the caesium transition and the frequency of the microwave source is used to provide a clock signal by directly counting the number of microwave cycles. The laser-cooled caesium atoms are typically launched upwards and then interogated at the peak of their ballistic

trajectory, which limits the interrogation time of the atoms. Recent developments have used individual ions held in ion traps to increase interrogation times and reduce noise sources by cooling the ions to their motional ground state. Both microwave and optical transitions have been used as novel frequency standards [25–28] where the counting of optical frequencies is enabled by the technique of optical frequency combs [29]. The benefits of using trapped ions has allowed for demonstrations of atomic clocks based on optical frequency transitions at uncertainty levels of $\sim 10^{-18}$ [30, 31]. A compact ion-trapping apparatus has demonstrated operation at a systematic uncertainty of $\sim 10^{-17}$ [32], indicating that near-term portable optical atomic clocks are possible. The prospect of portable atomic clocks based on trapped ions with these uncertainties is of application to space and precision navigation [33]. The smallest frequency uncertainty measurements have been performed with single ions, however schemes exist for improving these uncertainties by entangling multiple ions [5]. Optical atomic clocks therefore provide a motivation for both decreasing the size of the ion trap control apparatus (including the optics) and increasing the number of addressed trapped ions in one system to improve on systematic uncertainties.

1.3.2 Sensing

The sensitivity of classical sensors are limited by a fundamental noise floor called the *shot-noise limit*. Certain quantum states can be prepared that have enhanced sensitivity to measure quantities of interest such that the shot-noise limit can be surpassed. The sensitivity of trapped ions to external noise sources, which limit atomic clock operation, make them useful as classical sensors of anything that perturbs the frequency of their electronic and motional transitions. Trapped ions have been used to measure electric fields [34], magnetic fields [35], forces [36], and relativistic effects such as time dilation and gravitational redshift [37]. The additional promise of being able to prepare quantum states for enhanced sensing [38] offers a compelling application for trapped ions outside the laboratory, particularly for precision gravitational mapping which could allow for resource exploration from orbit. One method of quantum-enhanced sensing is to use the entanglement of many trapped ions [5, 6] and therefore the creation of large-entangled states of trapped ions is of use for sensing applications.

1.3.3 Quantum information processing

The field of quantum computation has developed rapidly in the past few years, with many technological developments towards physical devices that promise to outperform classical devices for certain problem classes. Analogue simulation is a specialised form of quantum computation where a Hamiltonian of interest can be prepared, the ground state physically realised and the eigenvalue of the ground state measured [39]. Linear chains of trapped ions provide a natural platform for simulating Hamiltonians of Ising or Heisenberg form, offering a large and complex parameter space for realising

Hamiltonians of interest [40], including for studying condensed matter systems [39]. To realise the full suite of available Hamiltonians it is crucial to be able to tune arbitrary couplings between ions which requires single-ion addressing. The difficulty of this task is exemplified in the state of the art simulation with a 53 qubit ion chain where no ions were individually addressed [4].

While analogue quantum simulators are restricted by the range of naturally accesible Hamiltonians in the physical implementation used, digital quantum computers provide a route to simulating arbitrary Hamiltonians through the application of single and pair-wise unitary operations on qubits. Digital quantum computers could be used for simulations, as well as a wide range of other proposed algorithms [41] for applications including quantum machine learning [42, 43], database searching [44] and finite-element methods [45]. Many physical platforms are being pursued to realise the grand goal of universal quantum computation [46–48], including trapped ions where the state of the art is 20 fully controlled and individually addressed qubits in a single ion trap [49]. It is predicted that useful quantum computers will require many thousands of qubits [50] and therefore a technological exercise for scaling all system components to large numbers is required.

1.4 Limits to large-scale trapped ion systems

In all applications outlined in the previous section, increasing the number of trapped ions is beneficial. As a frequency standard, the more ions addressed simultaneously, the higher the signal to noise ratio. If entanglement of all ions is performed then a Heisenberg limited measurement of the clock transition could potentially be achieved, decreasing the measurement uncertainty by a factor of $1/N$. For digital and analogue computation, a linear increase in system size exponentially increases computational resources. However, there are currently limiting factors on the maximum system size and capabilities of trapped ion experiments. In the following we outline these limitations to motivate the core subject of the thesis.

Trapping and ion chain lifetime If the depth of the ion trapping potential is less than the average energy of free particles in the vacuum chamber then there is a small but finite chance of trapped ions being ejected from the trap due to collisions with these free particles. This is a common problem for surface traps, where the electrode layout of linear Paul traps is planarised for ease of fabrication at the cost of the trap depth. As the number of trapped ions in the system is increased, the probability of at least one being ejected from the trap during a protocol increases exponentially. For ion chains, the issue is not limited to surface traps. It has been demonstrated that for individual ion lifetimes of 1 hour, ion chains of 53 ions held in a linear Paul trap have a lifetime of approximately 5 minutes [4].

Number of ions in single potential Due to the ability to easily entangle all ions in the same harmonic trapping potential, it is desirable to trap as many ions as possible in the same potential. To achieve this, the trapping potential is distorted to flatten the minimum such that linearly spaced ion chains can be confined. However, there are limits to this technique whereby the lowest-energy motional mode of the ion chain will transition to a zig-zag configuration. As ions are no longer located on the trap axis, they undergo excess micromotion. The largest demonstrated linear ion chain for coherent quantum operations contained 53 ions. To maintain linearity of the ion chain the secular frequency of the trap must decrease for each additional ion [51]. Therefore, there is a compromise between the number of trapped ions in one potential and multi-qubit gate times.

Individual addressability The majority of trapped ion experiments either address all trapped ions simultaneously, shuttle ions in-and-out of an interaction zone, or focus a repostionable beam on individual ions in a chain. Quantum simulation provides the strongest motivation to singly address multiple ions simultaneously. To access the full Hilbert space of N trapped spins, the individual (2^N) couplings between all spins must be tunable. This places the requirement of individual addressing of every spin. For digital computation, a similar motivation of arbitrary single and two-qubit gates for individual ions places the same requirement. Frequency standards and quantum-enhanced sensing provide less of a motivation however it cannot be ruled out that more advanced protocols could not be accessed with individual addressing of ions.

Proposed solutions The solution to increasing trapping and the lifetime of single trapped ions and ion chains is by reducing the energy of the free particles in the vacuum chamber, which is achieved by cooling the ion trap to cryogenic temperatures. Recent proposals for large scale ion trap experiments have all proposed planar ion traps in cryogenic environments [52–54]. However, we note that linear ion traps with deep confinement and stiff trapping potentials do not suffer from the same issues. In using stiff traps (with high secular frequencies), the number of ions that can be stored in a single potential is limited. The solution is to use a segmented trap where multiple trapping potentials can be created in the same device. Ions in separate regions can interact either by shuttling ions to interaction zones [55], or the fluorescence of the ions can be used to entangle remotely located ions [56]. Complex devices capable of realising multiple trapping regions and shuttling operations have been widely demonstrated, typically utilising microfabrication techniques. We refer to these devices as *ion microtrap arrays*. For complex systems with many trapping regions there is a requirement for multiple optically addressable regions to reduce the number and length of shuttling operations. Therefore, there is a motivation for a scalable technique to address and image multiple trapping regions. This technique does not currently exist.

Individual addressing of multiple ions has been previously achieved using either MEMS mirrors [57] or a multi-channel AOM [58]. The common element to both schemes is to reimage a bulk optical system onto the linear ion chain in order to achieve the required beam diameters and capability for focusing onto each ion separately. The MEMS mirror approach requires all single qubit gates to be performed sequentially and therefore adds significant overhead to quantum algorithm implementations. It can be envisioned that additional MEMS mirrors could be added at the expense of complexity of the apparatus. Multi-channel AOMs offer a more scalable approach, with up to 32 channels available in commercial systems at wavelengths suitable for trapped ion addressing. As the channels are arranged in a linear array, they are appropriate for implementations of addressing chains of ions. However, multi-channel AOMs are a fundamentally bulk-optical solution to the optics scaling challenge and will suffer from alignment drift as well as occupy significant real-estate around the vacuum chamber. The even pitch of the AOM channels are also inflexible, typically optimised for a single wavelength and suffer from significant crosstalk between channels. To reduce the footprint, and increase stability of optical addressing it is required to reduce the optic sizes to be on the order of the size of a single segment in an ion microtrap array. As the optical addressing requires the delivery of many beams of different wavelengths it is necessary for the optic designs to be tunable for different wavelength and function. As microtrap segments widths are on the order of ~100 μm it is natural to consider microfabricated optics. Proposals for segment addressing using microfabricated optics include diffractive micromirrors patterned in a surface trap for deflecting and focusing light delivered from planar waveguides [59], and planar waveguides integrated directly into a trap surface and delivered to ions using grating couplers [60]. These proposals are suitable for realising recent architectures for fault tolerant quantum computation where many modules are required with only segment and global addressing [61]. Such schemes will require an optical module to accompany each ion trap module such that they can be separately controlled. If the microfabricated optical module can be either integrated into the microtrap directly, or affixed to the microtrap assembly then stability could be improved over bulk optical solutions while dramatically reducing the optics footprint. The suitability of microfabricated optics for individual ion addressing would depend on the ability of reducing the size of the optics to the spacing between ions – on the order of 5 to 10 *upmu*m - which would require significant progress in the field of microfabricated optics for reducing their size to only several wavelengths across.

1.5 Previous reports of microfabricated optics for trapped ion applications

While there is no complete solution to the scalable, optical addressing and imaging of ion microtraps there are many examples of microfabricated optics coupled to trapped ions (see Figure 1.4). Fibre optics have been integrated into ion traps for both collection of the ion fluoresence [62], and addressing of an optical qubit transition [63]. In both cases, the line of sight to the ion was through an aperture in

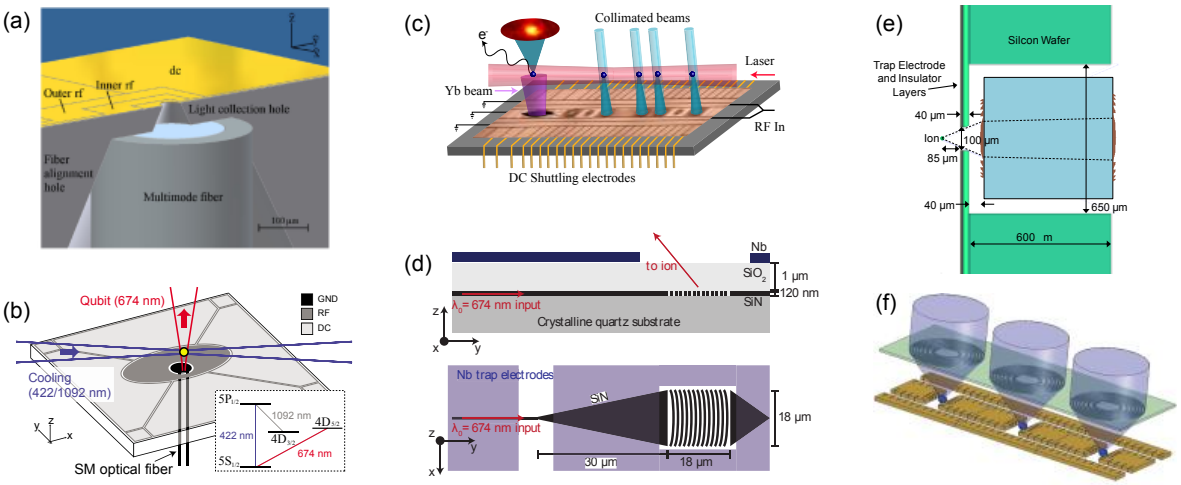

Figure 1.4: Examples of previously reported integrated and microfabricated optics for coupling to trapped ions, (a) A multimode fibre integrated into a surface microtrap for fluorescence collection, reprinted with permission from [62] Copyright 2010 American Physical Society; (b) A single-mode fibre integrated into a surface microtrap for driving the qubit transition of $^{88}Sr^{+}$, reprinted with permission from [63]; (c) Diffractive micro-mirrors patterned into a surface microtrap for fluoresence collection enhancement, reprinted under creative commons from [64]; (d) Silicon nitride waveguides embedded below a surface microtrap for addressing the qubit transition in $^{88}Sr^{+}$ using a focusing grating coupler, reprinted with permission from [60]; (e) The collection of ion fluorescence from a surface microtrap using two diffractive optics coupled into a fibre optic, reprinted with permission from [65]; (f) The concept of a microfabricated diffractive optic array for collecting trapped ion fluoresence, reprinted with permission from [66] Copyright 2011 American Physical Society.

a surface trap, and no focusing optic was used between the ion and the fibre. While the integration of fibres into the microtrap was a challenge in itself, it does not offer a scalable, manufacturable platform for interfacing with many multiple ion qubits.

Diffractive and reflective micro-mirrors defined in surface microtraps have been used to collect ion fluorescence, increasing the effective solid angle imaged by an external, bulk optic lens [64, 67, 68]. Micro-mirrors have been proposed as a solution to address trapped ions [59], however this is yet to be demonstrated. While micro-mirrors offer a significant advantage in increasing the solid angle for coupling to trapped ions using microfabrication techniques, they do not provide a complete solution without development of a scalable way to address each micro-mirror individually and therefore do not offer a solution to the optics scaling challenge.

Single microfabricated Fresnel lenses have been used for imaging of individual ions [66, 69] by bringing the lenses close to the ion trap and projecting the output of the lens into a bulk imaging system - effectively increasing the numerical aperture of the imaging system. Multiple Fresnel lenses have also been integrated close to a microtrap in an array configuration for fluoresence collection of multiple trap segments into fibre optics [65, 70]. The demonstration of multiple microfabricated optics close to a microtrap was a significant advance, however the hand-assembly of the individual components of the assembly poses a challenge to the scalability of the scheme, as well as the absence of the addressing beams.

The most advanced demonstration of microfabricated optics coupled to trapped ions is the use of silicon nitride planar waveguide integrated into a surface trap. The 674 nm qubit light from the waveguide was coupled to a single trapped ion using a focusing grating coupler [60] and coherent manipulations of the qubit transition in $^{88}Sr^{+}$ were demonstrated. The combination of the optical layer beneath the electrode layer offers an attractive, scalable interface for trapped ions and while no collection optics were included it may be feasible to directly integrate detectors into the surface trap at the expense of cryogenic operation [71].

1.6 Summary and author contribution

Trapped ions held in radio-frequency traps are a useful and rich quantum system that is well supported by a wealth of technological advancements. The use of scalable, microfabricated ion traps is now a routine practice in many laboratories, however the optical addressing has not followed in step. Previous reports of individual addressing of ions are limited to bulk optical solutions which limit them to small-scale laboratory demonstrations. Our aim is to engineer a compact, stable optical assembly with design flexibility in its functionality. Such an assembly is best realised by microfabricated optics and would be suitable for portable frequency standards and sensors as well as optical modules for fault-tolerant quantum computation schemes. There have been many previous reports at initial progress towards scalable optical addressing using microfabricated optics but no complete solution has emerged. The microtrap developed at NPL has many advantages, including its strong confinement and high optical access when compared to surface traps, however the geometry poses its own set of challenges when considering the interfacing of ions in the microtrap with microfabricated optics. This thesis explores these challenges and develops a microfabricated optical assembly for interfacing with multiple trapping segments in a microfabricated, linear Paul trap. We begin in Chapter 2 with the requirements of such a system before designing a potential solution. The rest of the thesis will be introduced at the end of Chapter 2 once a clear path forward is identified.

A note on coordinate systems There are two different coordinate systems used throughout the thesis, however we use the same (x, y, z) notation for both. The first coordinate system is with respect to the trap axes as introduced in Section 1.1.1 which allows for clear descriptions of the ion motion and laser k-vectors. The second coordinate system is used for optical design, fabrication and testing and is the dominant convention used; it will be introduced in Chapter 4 and whenever we refer to the trap axis coordinate system it will be made clear.

Author contributions The majority of the design, fabrication and testing performed throughout the thesis is the work of the author, however there were other important contributors. Graham Marshall

(GM), Kaushal Choonee (KC), Alastair Sinclair (AS), Mark Thompson (MT) and Guido Wilpers (GW) contributed to the concept considerations outlined in Chapter 2. KC constructed and verified the numerical model of the NPL microtrap used and extended by the author in Chapter 3. Zachary Chaboyer (ZC) trained and assisted the author in waveguide fabrication in Chapter 4, while Simon Gross (SG) fabricated an initial development sample and provided ideas on mode expansion. GM was also instrumental in his advice on important tests and considerations with laser-written waveguides. KC assisted in the development and testing of diffraction theory models in Chapter 5 and was closely involved in the fabrication of surface-relief diffractive optics by focused ion beam milling which was performed by David Cox (DC) in Chapter 6. In Chapter 7, SG fabricated the final waveguide chips used, GM assisted in the aligning and bonding of the fibre array and waveguide chip, as well as its bonding to a support structure, AS assisted in the testing of the full assembly during a research visit to NPL.

2

Optical assembly design

This chapter details the design process of an optical assembly composed of microfabricated optics for interfacing with trapped ions. The use of microfabrication techniques allows for the realisation of compact arrays of large numbers of optical elements which we have previously identified as a solution to the optics-scaling challenge. The trapped ion system imposes constraints on the microfabricated optics that can be used and therefore we consider the system requirements for $^{88}Sr^{+}$ ions presently used at NPL to aid the design process. The requirements that constrain the micro-optical system design include the wavelengths of operation, collection of ion fluorescence, vacuum compatibility and influence of the micro-optics on the electric fields of the ion trap. As well as the optical system requirements, an additional constraint is that we opt to maintain the current technique for routing the RF and DC control lines inside the vacuum chamber, which is a ceramic leadless chip carrier (LCC). Future iterations could redesign the electronic feedthrough solution if it would improve the optical assembly capabilities, however using the LCC is sufficient for our proof-of-principle ambitions. Further, we aim for the optical assembly to interface with fibre-optics already used in the laboratory such that integration into previous experimental operations is as seamless as possible. After considering the system requirements we will find two potential technologies for realising an optical interface for trapped ions: planar waveguides with grating couplers, and laser-written waveguides with diffractive microlenses. The choice between these two platforms can be performed by careful consideration of the ease of satisfying the system requirements. The choice of platform will be discussed and then an optical assembly concept outlined based on the chosen technology. The thesis will then detail the development of the micro-optical assembly for a proof-of-principle demonstration.

2.1 System requirements

There are a number of requirements for designing a novel optical assembly for interfacing with the ion microtrap array at NPL. Firstly, there are several functions the system must achieve, such as the

addressing of multiple microtrap segments and collection of ion fluorescence. Secondly, there are things the system must not do, such as perturb the ion's behaviour or cause a degradation in other system component performance, such as the quality of the vacuum. In this section we outline both the functional requirements and the restrictions on the system, starting with the required wavelengths for operations.

2.1.1 Addressing beams

The electronic and motional transitions of the $^{88}Sr^{+}$ ions are driven using lasers, with the wavelength of the laser set by the addressed transition frequency. The k-vectors and polarisations of the addressing laser beams are determined by the corresponding atom-light interaction they are used to drive. The required laser wavelengths, with their associated k-vector and polarisation requirements for creating and interacting with trapped $^{88}Sr^{+}$, were previously outlined in Section 1.1.4 and are summarised in Table 2.1. The operational wavelengths range from near-ultraviolet for photoionisation, to near-infrared for dark state repumping. As we aim to make the system interface readily with fibre optics in the lab, the designed platform must have an efficient and intrinsic way to couple to single-mode fibre over this full wavelength range. Optimising the coupling to single-mode fibre decreases both power losses and scattering of excess light within the optical assembly. Instead of prescribing the k-vectors to be identical to the ones used in the bulk-optical NPL experimental apparatus we instead relax the requirements to the k-vectors that will correctly drive the corresponding transition. For example, the magnetic field for Zeeman splitting the fine structure is currently at 45° to the trap $z-$axis and thereby fixes the probe and optical pumping beams' direction. By allowing for a flexibility in the magnetic field direction, the final design is not unnecessarily restricted. Similarly, the current beams are focused at the ion position with a set beam waist. We do not aim to recreate this beam waist, instead imposing the condition that the beam must not clip the trap electrodes and there must be enough laser power concentrated at the ion. As well as this, the beams must have minimal crosstalk with unaddressed ions; by introducing the capability to address individual ions, or electrode segments, it should be ensured that only those ions are addressed. Minimal crosstalk rates requires low scattering of beams entering, within and exiting the optical assembly. The optical assembly must therefore be capable of both preparing addressing beams of the correct k-vector and focus them onto the ion trap segments with beam waist diameters of <340 μm. These focusing optics must either be polarisation insensitive, or be able to prepare required polarisations states before interacting with the trapped ions. There are a variety of different polarisation states required; from circular, to linear, to unpolarised. Some beams do not have a critical requirement on the exact polarisation state, however the presence of beams with specific polarisation enforces that the designed system must be able to accommodate them.

In summary, the micro-optical assembly must be able to guide, steer and focus light over the

wavelength range 405 nm – 1092 nm in the same system. The microfabricated optics must either be polarisation versatile, such that defined polarisation states can propagate to the ion, or be able to readily manipulate polarisation states before interaction.

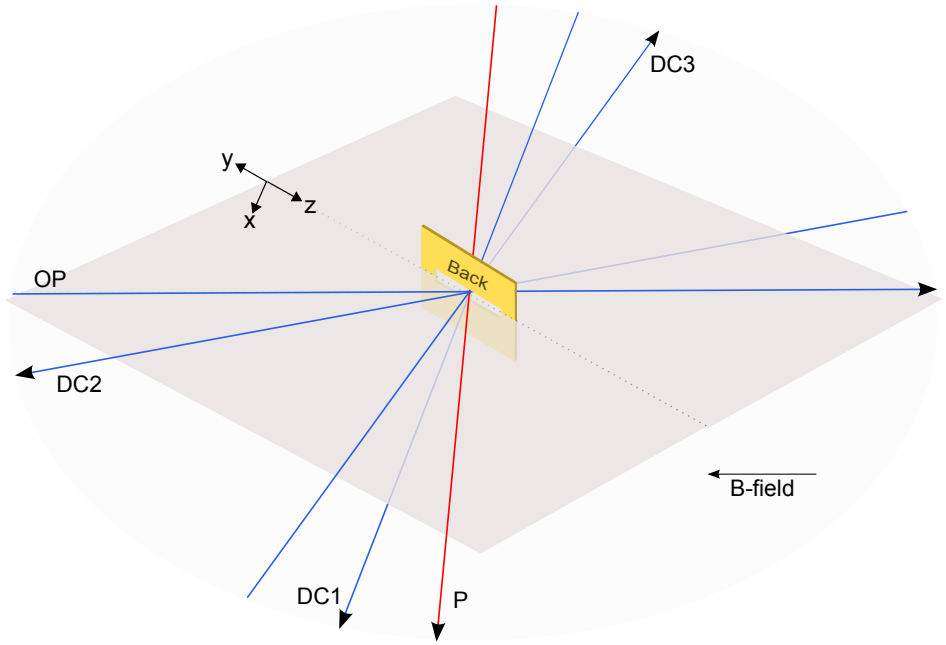

Figure 2.1: Current orientation of some of the most critical laser beams for Sr^+ control. Shown is the microtrap with the back side being the one facing away from the atomic oven. The horizontal plane is shown in dark grey to highlight beams that are propagating in and out of the plane. Beam labels are correspond to (OP) Optical pump, (DC1/2/3) Doppler cooling 1/2/3, (P) Probe.

2.1.2 Fluorescence collection

Ion state measurement is performed using fluorescence detection, as previously outlined in Section 1.1.4. A laser resonant with a strongly allowed transition (e.g. $S_{1/2} \rightarrow P_{1/2}$) is incident on the trapped ion such that if the ion is in the ground state it strongly fluoresces. If the ion is not in the ground state, it will appear dark. To reduce the amount of time for state determination the amount of scattered excitation laser light must be minimised otherwise background photons of the same wavelength as the ion fluorescence will lead to false detection events. Further, the more photons per second that can be collected, the faster it can be discerned whether the ion is fluorescing, as determined by a statistically significant number of photons above background. Measurement is an intrinsic part of any quantum protocol, and so there is a desire to reduce measurement times and increase state determination fidelity. These two measurement requirements, low background intensity and high collection efficiency set requirements on the optical assembly. The 422 nm Doppler cooling beams which are used to drive the measurement transition in $^{88}Sr^+$ ions must have low background intensities away from the ion so that light doesn't scatter from the electrodes into the collection optics. To provide sufficient collection efficiencies, the collection optic must have a high enough numerical

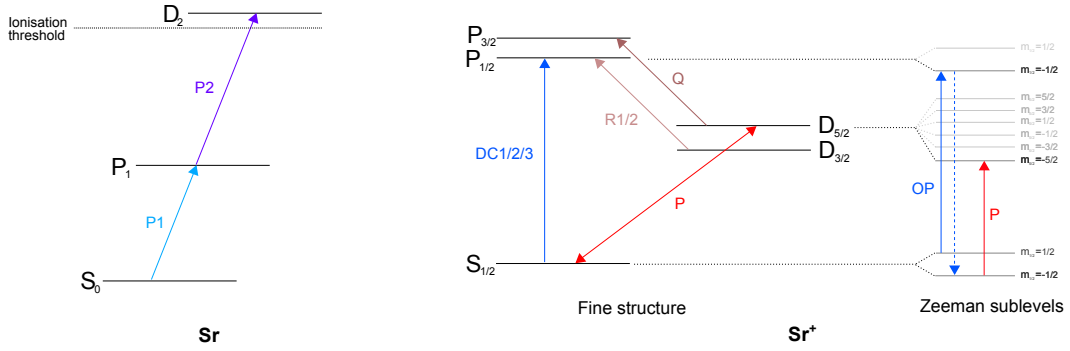

Name	λ (nm)	Description	Orientation	Polarisation
Photoionisation 1 (P1)	461	Resonantly excite neutral Sr atoms from their ground state.	Orthogonal to atom loading vector	Non-critical
Photoionisation 2 (P2)	405	Resonantly excite Sr atoms already excited by P1 to remove an electron.	Orthogonal to atom loading vector	Non-critical
Doppler Cooling 1/2/3 (DC1/2/3)	422	Doppler cool the trapped ion. Used for state detection. One beam is sufficient but 3 beams are required for full micromotion minimisation	Oblique to principal trap axes, with each of the 3 beams roughly orthogonal to each other.	Non-critical but affects operation
Optical pumper (OP)	422	State preparation for sideband cooling	Aligned with magnetic field direction	Circular
Repumper 1/2 (R1/2)	1092	Return the ion back into the cooling cycle after decay into the metastable state. 1 beam is sufficient but 2 can be used.	1 beam: Non-critical, 2 beams: 45° from each other.	1 beam: time-varying, 2 beams: Linear, orthogonal to each other. [72]
Probe/clock/qubit (C)	674	Side-band cooling, spectroscopy and qubit manipulation	Approximately orthogonal to magnetic field direction	Linear
Quencher/clearout (Q)	1033	Couples metastable state to ground state to allow for resolved-sideband cooling	No specific orientation requirement.	Unpolarised

Table 2.1: Laser requirements for creation and control of trapped strontium ions. The corresponding energy levels are diagramatically shown above.

aperture to collect the ion fluorescence which is, on average, directed into all 4π steradians. The solid angle coverage of the collection optic determines its maximum collection efficiency. For a collection lens of diameter D and distance L from the trapped ion, then the collection efficiency, in percent, is given by

$$\eta_c = 100 \times \frac{1}{2}\left(1 - \frac{D}{\sqrt{D^2 + L^2}}\right) . \tag{2.1}$$

The linewidth of the $S_{1/2} \rightarrow P_{1/2}$ transition in $^{88}Sr^+$used for fluorescence collection is 20.22 MHz. Therefore for a collection lens with collection efficiency of 1% (0.01π sr) then ~$8{\times}10^4$ photons/second will be collected, comparable to the current measured count rates when detector efficiencies of 20% are taken into account [9]. Using Equation 2.1 we can determine that for a lens placed 400 μm from the ion, a 1% collection efficiency corresponds to a diameter of 162 μm. The further the optic is from the ion, the larger it must be, imposing constraints on both the addressing optic size and positions. To maximise functionality it is required that a collection optic is placed on every microtrap segment, which limits the optic diameter to the electrode pitch of 350 μm. It is possible instead to use shuttling of ions to a dedicated collection segment, however this would increase state determination time significantly. We set the 1% collection efficiency considered above as a soft requirement, with any designs considering collection efficiencies below this threshold to be supported by statistical analysis of corresponding state determination rates as required by the protocol to be implemented.

2.1.3 Vacuum conditions

The NPL microtrap is housed in an ultra-high vacuum (UHV) chamber with a target pressure of ~10^{-11} Torr. As previously discussed, such low pressures are required to maintain ion coherence and, in extreme cases, to prevent loss of the ion from the microtrap due to collisions with free atoms or molecules still present in the chamber. The vacuum pressure places requirements on the optical assembly as it must both interface with the current vacuum chamber, as well as be composed of vacuum compatible materials. The current NPL system is optically addressed through large vacuum windows, and it is likely that any optical assembly would have to either replace or significantly modify this interface. The optical assembly will have to route many laser beams into the vacuum chamber to bring them close enough to the microtrap for addressing with microfabricated optics. An option is to bring the large number of required fibre optics inside the vacuum chamber, however there is currently a lack of commercial fibre-optic feed-throughs for bringing many fibres inside vacuum chambers $<10^{-10}$ Torr. Therefore a technique for bringing large numbers (~8 per electrode segment) of beams inside the vacuum chamber must be developed, either by designing a novel vacuum feed-through, or through another means. The UHV pressures also place requirements on materials placed in the vacuum chamber. Specifically they must be able to be thoroughly cleaned, survive vacuum bake-out temperatures (130–240°C [73]) and have minimal levels of out-gassing when under vacuum. We rule

out the use of any organic materials (e.g. polymers) inside the vacuum chamber, as they cannot be easily cleaned with solvents, flow at modest temperatures (~100°C) and typically out-gas.

2.1.4 Electric field perturbations

The fragile internal and motional states of the trapped ion rely on a well defined and consistent electric field environment, with the trapping potential the ion experiences being as close to harmonic as possible. If an optical assembly is to be brought in close proximity to the microtrap, such as to satisfy the 1% collection efficiency requirement, then it must not disturb the trapping potential in a way that negatively affects ion operation. Static DC fields which could be generated by charge accumulation on dielectric materials will displace the ion from the potential minimum and cause excess micromotion of the ion. If the optical assembly is brought so close as to distort the RF trapping field then distortions to the pseudopotential could occur which may sacrifice the harmonicity of the trap and displace the ion from the potential minimum. We therefore place the requirement that the optical assembly must negligibly impact ion trap operation, with the acceptance that there may be some cost in terms of the purity of the quantum state manipulations that can be performed in the interest of achieving larger quantum states and optical functionality. For the 3D microtrap considered here, where the ion is strongly confined, there is a larger latitude for compromise of the trapping potential due to its increased trap depth (~1 eV) over surface microtraps (~0.1 eV).

2.1.5 Summary

The outlined requirements for interfacing of microfabricated optic with $^{88}Sr^{+}$ ions cover many considerations of trapped ion operation. The optical assembly must deliver light to multiple trapping segments with wavelengths from 405–1092 nm and of versatile polarisation and k-vectors. Ion fluorescence must be collected at λ = 422 nm with a collection efficiency that allows fast state determination, which we set to be 1%. The micro-optics must not disturb either the vacuum or the electric field environment of the trapped ion system and therefore must be composed of non-organic materials and must not accumulate charges. Having identified the key requirements of the optical assembly we now identify candidate platforms and discuss their advantages and disadvantages for satisfying the system requirements.

2.2 Considered platforms

The introduced system requirements led to the identification of two candidate microfabricated optic platforms. The micro-optical technology must consist of regions that can guide light, as well as optical elements that can steer and focus light into free space. Two micro-optical platforms with these capa-

bilities are: planar waveguides with grating couplers; and laser-written waveguides with diffractive optics. The micro-optics could be placed in a number of different ways with respect to the microtrap, as shown in Figure 2.2, with the considered locations being:

1. Outside the microtrap but fixed to the microtrap electrodes, with direct-line-of-sight to the ion through an aperture in the trap electrode.

2. Outside the microtrap in a self-contained, separate optical system. This is currently how the ions are addressed and imaged, albeit from some distance away from the microtrap and using bulk optics.

3. Inside the microtrap, with light guided through the SiO_2 electrode layer. The direct light of sight is provided by an aperture in the trap electrode.

4. The same as (3) but with direct line of sight provided by a structure on the outer face of the electrode that redirects light out of the electrode onto the ion.

These potential placements can further aid platform selection along with the system requirements. We now discuss the two identified candidate technologies in the context of the discussed constraints imposed by the trapped ion system.

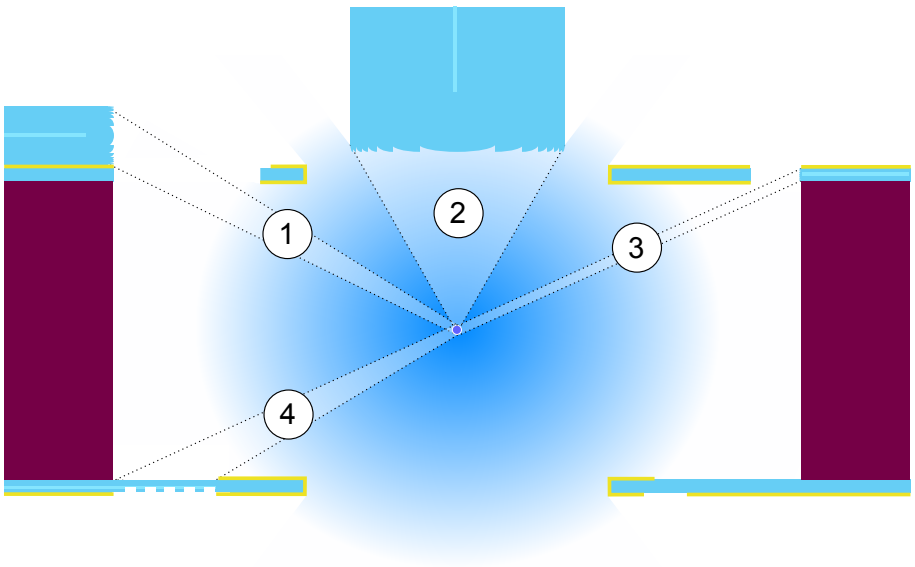

Figure 2.2: Potential placements of optics for the coupling of light to and from a trapped ion. (1) Through an aperture in the microtrap electrode, from a seperate optical system (e.g. a lensed fibre) (2) Optics completely seperate from the microtrap, coupling to the trapped ion through the existing trap aperture (3) Light guided through the glass electrode layer and then coupled to the ion through an aperture in the trap electrode (4) Light guided through the glass electrode layer, deflected to the ion using a structure on the surface of the trap electrode.

2.2.1 Planar waveguides and grating couplers

Planar waveguides are light-guiding structures fabricated lithographically in thin films. Silicon photonics is the most established planar waveguide platform and has a range of applications using telecommunication band radiation, from quantum information processing [47, 74, 75] , through communication and computing networks [76–79] to classical analogue computation [80]. The techniques developed for CMOS device fabrication can be translated to silicon planar waveguides and large numbers of optical components can be fabricated in parallel, using UV photolithography and reactive ion etching, to create advanced waveguide circuits. However, silicon is not suitable for our application as it is opaque at wavelengths <1100 nm due to its relatively small bandgap. Silicon nitride is another mature planar waveguide platform, and is transparent for wavelengths $\gtrsim$400 nm that can be fabricated in a CMOS-compatible way [81, 82]. The transparency of silicon nitride at blue wavelengths makes it a candidate material for our application, however in practice fabricating silicon nitride waveguides for guiding blue light with low loss proves to be difficult [83]. Other waveguide material platforms that are less established, but have optical transparencies at blue wavelengths are aluminium nitride [84, 85], aluminium oxide [83, 86], aluminium gallium nitride [87], titanium dioxide [88] and Ti:$LiNbO_3$ [89, 90], with the majority being high-κ (refractive index$\gtrsim$2) materials to increase mode-confinement. The high mode confinement allows for smaller bend radii and more compact waveguide circuits such that more waveguides can be fabricated in the same area, waveguide can be shorter, and more functionality can be included in each waveguide such as beam-splitters or switches. There are a number of high-κ materials with large bandgaps that have been recently identified, such as BeS, that may allow for high quality planar waveguides for blue and UV wavelength transmission [91]. However, the development of a waveguide platform on a novel material would be challenging, time-consuming and would delay the realisation of a final device. A consideration for planar waveguides is that fabricating planar waveguides that support single-mode radiation at blue and near-IR wavelengths in the same thin film is challenging. When fabricating planar waveguides, the fixed thickness of the film determines the height of the final waveguide, and it is the waveguide width that is used to control the propagating waveguide mode. Preliminary studies of mode guidance of silicon nitride waveguides, simulated in *Lumerical MODE*, found that single-moded guidance of 405 nm and 1092 nm radiation could not be acheieved in the same thin film. For all waveguide widths, if the film is thin enough to support blue single-modes then near-IR wavelengths are not guided and if the film is thick enough for near-IR guidance then only blue multi-modes are supported. The solution is to develop a multi-layer waveguide stack, where the waveguides for blue light are in a separate layer to the near-IR waveguides [92, 93], however this adds fabrication steps not typically supported by a foundry and, at the time of considering which platform to pursue, could not be performed in-house.

As well as guiding light close to the microtrap, we require a micro-optic platform that can couple the guided light to trapped ions in free space. Light is typically coupled in and out of planar waveguides using diffractive structures referred to as *grating couplers*. Grating couplers are typically used to couple fibre modes into waveguides with reasonable efficiency. As planar waveguide mode sizes are typically much smaller than fibre mode sizes, the grating coupler is connected to the waveguide using an adiabatic taper region. If grating couplers are spaced evenly at a pitch matching a commercial fibre array (either 127 or 250 μm), then large numbers of waveguides can be coupled into simultaneously. Grating couplers are typically limited in efficiency both due to the preference to fabricate binary structures, limiting diffraction efficiencies, and the fact that light is being deflected up to 90° from the waveguide plane. Fibre edge-coupling is possible, however mode-converters are required to match the fibre mode to the much smaller waveguide mode field diameters [94, 95]. Once in the waveguides, our application has the relatively unique requirement of extracting the light from the waveguides and focusing it some distance above the waveguide chip, at the trapped ion position. Previous work on focusing grating couplers has been performed for optimising coupling into fibres [96, 97], and optical pick-ups for data storage [98–100]. However, the most advanced work to date is for trapped ion applications, which was reported after our platform selection was finalised [60]. In the work of Mehta et al. [60] coupling efficiencies from the waveguide to the ion position are low, with 5–9 dB losses, however trapped ion control is performed and shows viability of the platform. Grating couplers approaching 100% efficiencies would be challenging to fabricate, and any light not diffracted into the desired order causing excess light scatter into potentially undesirable locations of the ion trap. The use of grating couplers for addressing trapped ions does not extend well to fluoresence collection. Grating couplers typically have a small numerical aperture and along with their low efficiencies could not easily satisfy the 1% collection efficiency requirements. To overcome this, single-photon detectors could be integrated into the waveguide chip to directly measure fluorescence without any guiding regions [71]. However, the detectors demonstrated by Slichter et al. required cryogenic temperatures due to their reliance on superconducting materials. As the current NPL system does not use cryogenics it is desired that such a solution is avoided.

The capability for planar waveguides to guide and focus laser radiation makes them a potential candidate for trapped ion addressing. However, planar waveguides typically only support single polarisation states due to their rectangular geometry. As we require multiple orientations of linear polarisation, this requires polarisation manipulation at the output grating couplers, further complicating their design. In the case of circularly polarised light, advanced grating coupler design would be required, perhaps employing two overlapping waveguides of opposite linear polarisation incident at 90° on the same grating coupler [101]. The lack of polarisation versatility in planar waveguides is a major drawback in their application to trapped ion addressing.

The advantage of planar waveguides would be the possibility of directly integrating them into the microtrap structure. This has been demonstrated with silicon nitride waveguides in a planar ion trap [60]. However, in contrast to 2D surface traps, the 3D nature of the NPL microtrap complicates the integration. It is possible that planar waveguides could be integrated into the electrode structure, on top of the SiO_2 layer. Grating couplers could then be patterned on top of the waveguide layer to direct the light down through the SiO_2 layer onto the ion (see (4) in Figure 2.2) [102]. However, the k-vectors of the beams will be approximately co-linear with the trap axes and therefore cannot satisfy the k-vector requirements for Doppler cooling. The microtrap has been designed for the addressing beams to be incident through the trap aperture, and therefore the current k-vectors cannot be realised for beams incident from the trap electrodes. For this scheme, the microtrap would have to be redesigned taking into account the optic requirements; it is not immediately clear what form this redesign would take.

2.2.2 Laser-written waveguides and diffractive optics

Laser written (LW) waveguides are light guiding regions of dielectric material where the refractive index relative to the host material has been increased using focused femtosecond laser pulses. To fabricate LW waveguides, a femtosecond laser is focused into a dielectric using a high numerical aperture microscope objective. The intensity of laser light at the focus causes non-linear electron excitation mechanisms to occur only very close to this focus. The excitation of one or more electrons above the material bandgap causes permanent structural modifications, altering the local refractive index. The focused beam can then be translated in 3 dimensions through the dielectric, creating pathways of refractive index modifications. If this refractive index change is positive, then the modified region can act as a light guiding region in the same principle as a fibre optic. Waveguides can be fabricated at speeds on the order of 1 cm/s, allowing for multiple waveguide circuits of 3D geometry to be quickly fabricated in bulk dielectrics. A common host material for LW waveguides are glasses which are transparent from blue to near-IR wavelengths. Therefore LW waveguides are a suitable candidate for the guiding of the operational wavelengths of $^{88}Sr^{+}$ ions.

Unlike planar waveguides fibre optics are typically directly coupled to LW waveguides without any intermediate optical elements. As the refractive index contrast of LW waveguides is comparable to that of fibres, the process development task is to design LW waveguides with high mode overlap with the interfacing fibre optic. High mode overlaps of close to 100% are possible and allow for very high coupling efficiencies when compared to planar waveguides. The high coupling efficiencies decreases both scattered, uncoupled light and the power requirements of the system, which is an important consideration when attempting to scale to many waveguides. As with planar waveguides, LW waveguides can be fabricated with a spacing of a fibre array standard pitch, and many waveguides

can be directly coupled to simultaneously. The drawback of the low refractive index contrast, which allows for high mode overlap with fibre, is that bend radii are limited to approximately 20 mm [103] to minise bend losses. However, the advantage is low propagation losses of ~0.5 db/cm [104] for straight waveguides. In contrast to planar waveguides, LW waveguides are approximately circular and they exhibit negligible polarisation sensitivity [105], allowing for arbitrary polarisation states to propagate with minimal polarisation distortion.

To produce the correct k-vectors for interacting with the trapped ion, the LW waveguide outputs must be deflected and focused. Attempting to angle the waveguides inside the material itself would add fabrication complexities, and the beams would still need focusing onto the ion, therefore we propose using the same optical element to deflect and focus the light. We do not consider refractive lenses as they are bulky (~100 μm height) and lack design flexibility to deflect light off axis, which could result in severe aberrations. Diffractive optics allow for advanced optic design by implementing spatially dependent phase shifts on incident beams. As the phase shift can be implemented in a material of optical depth of 2π, they can be very thin (~1 μm), allowing for the optics to be brought close to the microtrap. Transmissive diffractive optics have theoretical efficiences of 100% for on-axis lenses [106], and can have large numerical aperture [107], making them ideal for collecting ion fluorescence. Diffraction efficiencies of off-axis diffractive optics are reduced [108] but can be improved with advanced design methods [109]. Diffractive optics for polarisation manipulation are also possible through the recently developed field of dielectric metasurfaces, where both phase and polarisation of incident light can be manipulated simultaneously [110].

2.3 The proposed assembly

Considering the two technologies proposed in the previous section, we note several advantages of using LW waveguides over planar waveguides. The first advantage is the opportunity for greater system power efficiencies. The direct coupling of the waveguides to fibre optics with near-unity efficiency both reduces power requirements, increasing the number of waveguides that can be driven from a single laser source, and background light scatter. The use of transmissive diffractive optics with high diffraction efficiencies has the same advantage. The second advantage is polarisation purity and control. The capability of the waveguides to support all polarisation states, and maintain them over short waveguide lengths is an important consideration when interacting with the quantum states of ions. The further potential for polarisation manipulation with metasurfaces allows for advanced beam manipulation, and with it, advanced protocols. The third advantage is the potential for integration of waveguides for supporting single-modes of different wavelengths in the same substrate, and in the same fabrication step. This greatly reduces fabrication complexity and allows for rapid prototyping of advanced waveguide circuits. Considering these numerous advantages for trapped ion addressing

Figure 2.3: A selection of schematics and illustrations of the proposed concept, (a) A 2D schematic outlining the concept of a fibre array coupled to a laser written waveguide array which remaps the beam positions to correctly interface with a diffractive microlens array. The lens array deflects and focuses the light onto the ion in the centre of the microtrap (blue cross). Wavelengths from blue, through red, to near-IR are included in the same assembly. The end facets are shown demonstrating how the beams change positions, to interface with an example lens array layout. Both addressing beams and collection optics are included in the same assembly, with the collection optic centred over the ion position. The black dashed lines indicate connecting faces that are bonded when assembled. (b) An exploded 3D render of the 2D schematic, a glass support block with an aperture for the waveguide chip to slot through is included both for stability and to reinforce the focusing chip substrate. (c) A 3D render looking through the microtrap at the optical assembly. Two trapping regions are being addressed simultaneously demonstrating the scalability of the concept. (d) The assembled optical system with all components bonded together. Here, the assembly is mounted on the LCC chip carrier such that the optical assembly becomes the vacuum window.

and fluorescence collection of LW waveguides, we choose to develop an optical assembly based on LW waveguides and diffractive optics.

The proposed assembly for optical interfacing with ions confined in a microtrap is as follows, and is illustrated in Figure 2.3. The fibre optics for delivering the required wavelengths to each microtrap segment are selected. If the segment also requires ion fluorescence collection then a fibre for carrying this light to a detector is also included. The fibres are populated into a fibre array, which can be commercially purchased to specification. A laser-written waveguide chip is used to remap the fibre beam positions to the positions of a diffractive microlens array. The microlens array is fabricated on a separate substrate such that the light emerging from the waveguides freely propagates and expands to fill the lenses. The microlenses focus the light onto the relevant microtrap segments, with the relative position of the microlens to the microtrap segment chosen such that the k-vector of the beam is as required. The microlens array is placed a distance from the microtrap such that a high-NA collection optic has a reasonable diameter (<200 μm) and does not infringe on surrounding addressing optics. Fluorescence from the ion is coupled back into a LW waveguide, into the fibre optic in the fibre array and then detected. The optical assembly therefore serves as the complete solution for optical addressing of trapped ions in microtrap arrays. The capability to write suitable waveguides at ~1/second allows for a semi-scalable technique for repositioning beams from the purchased fibre array. It is therefore desirable to find a technique for fabricating diffractive microlens arrays with similar manufacturability.

There is a potential for the optical assembly to avoid the issue of routing multiple fibre optics inside the vacuum chamber. If the microlens array were written on the inside of the vacuum chamber window then the waveguide chip, and fibre array, would sit outside the vacuum chamber. The challenge then becomes defining the position of the vacuum chamber window with respect to the microtrap to within a few microns, however it would allow for many beams to be routed inside the vacuum chamber, with the correct k-vectors for ion control, without the need for vacuum feedthroughs. The current vacuum chamber window is 4 mm thick, and as the output beams from single-moded waveguides expand rapidly, the microlens array chip must be made thinner than this to accommodate for reasonable optic diameters. Therefore, a support block is required to be bonded to the back of the focusing chip, with an aperture cut-out for the waveguide chip, to support the thinner focusing chip from bending, or even cracking, under the vacuum pressures.

2.4 Discussion and thesis outline

While the proposed optical assembly offers multiple advantages over using planar waveguides, there remain open questions and challenges before it can be realised. These challenges span all areas of the assembly, from the interaction of the microlens plane with the RF trapping field, to the demonstra-

tion of LW waveguides and diffractive optics at blue wavelengths. The investigation of the required research avenues forms the rest of the chapters of the thesis, the contents of which we will now introduce and motivate.

The first open question to resolve, before any optics can be designed, is to determine how close the assembly can be brought to the microtrap. As the microlens array will be fabricated in a dielectric material, the effect of its proximity to the RF trapping field and charge-sensitive trapped ion must be studied. The current distance of the ion to the vacuum window is ~8 mm, demonstrating no adverse affects. However, for high collection efficiency of the ion fluorescence the assembly must sit <1 mm from the microtrap centre. We opt to study these effects numerically, and the results of this investigation (as well as prior studies) will be presented in Chapter 3.

While LW waveguides are commonly fabricated in materials transparent to blue wavelengths, there are no previous reports of buried, 3D LW waveguides in glass that support single-modes at blue wavelengths. Surface-skimming waveguides in glass have been demonstrated, as well as buried waveguides in polymer, but it is an open question as to the potential for fabricating low-loss, high coupling efficiency, 3D laser written waveguides in glass. The secondary issue of the rapid expansion of the waveguide output has also not been solved in the literature. In planar waveguides, adiabatic expansion tapers can expand single-modes to many multiples of their original size [111–114]. If an adiabatic mode-expansion taper could be developed in LW waveguides it would allow for smaller microlens diameters and a greater density of addressing beams, as well as a thicker vacuum window. The results of the development of waveguides for supporting blue wavelengths, as well as the development of mode-expansion tapers is addressed in Chapter 4.

Diffractive optics are typically fabricated as surface-reliefs in a dielectric material. Often, the surface-reliefs are quantised into a number of levels (sometimes only 2), which restricts their diffraction efficiency. We aim to develop high efficiency diffractive optics in a vacuum compatible material. For on-axis lenses this seeks to maximise the collection efficiency of ion fluorescence. For off-axis lenses, this is to minimise the propagation of light into undesired diffraction orders. The theory and design of surface-relief, diffractive microlenses is detailed in Chapter 5 where we also numerically explore the potential of dielectric metasurfaces for advanced phase and polarisation control. In Chapter 6 we fabricate diffractive microlenses using a variety of techniques including focusing ion beam milling, electron beam lithography and reactive ion etching.

The developmental work of micro-optics in chapters 3-6 allows the realisation of a demonstrator assembly at operational wavelengths to be fabricated and tested in Chapter 7. The proposed optical assembly promises high efficiencies, however in reality, attaining these efficiencies may be difficult. We evaluate the performance of a fully assembled proof of concept and discuss the merits and drawbacks of the approach in practice.

Finally, there are a number of considerations that would eventually need to be addressed before the demonstrator optical assembly could be interfaced with trapped ions. Primarily, the mounting of the optical assembly to the vacuum chamber to within optical alignment tolerances is the next technological step. This issue, as well as any other challenges or extensions that present themselves along the way will be discussed in Chapter 8 where we consider the viability of the presented optical assembly and its potential for trapped ion control going forward.

3

Numerical studies of dielectrics in proximity to ion traps

The optical assembly concept introduced in Chapter 2 involves locating a microlens array in close proximity to the ion microtrap. The microlens array substrate will be composed of a dielectric material, such as glass, so as to be transparent to the required laser wavelengths while also being vacuum compatible. The presence of a dielectric, and therefore electrically insulating, substrate close to the trapping field could cause two unwanted, and potentially ruinous, effects. The first effect is charge accumulation on the dielectric surface that would generate DC electric fields and, if the substrate was close enough, would distort the pseudopotential of the microtrap and create an excess electric field at the ion position. Stray charges on microtrap electrodes have been determined to be a limiting factor for trapped ion coherence [34, 115], and therefore additional sources of accumulated charges are undesirable to optimal ion trap operations. The second potentially negative effect is the action of dielectrics to minimise their internal electric field. The electric fields generated by the RF electrodes in a linear Paul trap extend outside the trapping region. If the dielectric substrate is located within the extended electric field of the microtrap it will distort it as the electric field will not be able to propagate inside the dielectric substrate in the same way as the vacuum. These two effects would cause the ion to be displaced from the RF null, causing excess micromotion which leads to anomalous heating of the quantum motional states as well as second-order Doppler shifts on the atomic transitions. As these resulting degradations of the trapped ion state are disastrous for many quantum information protocols we explore the limits of bringing dielectric close to ion traps. These limits will then inform micro-optical design so as not to degrade ion trap operation at the expense of a more compact and scalable form factor.

The effect of bringing dielectrics close to ion traps has been previously studied both numerically [116] and experimentally [63, 117, 118]. As well as deliberate investigations, various dielectric optics

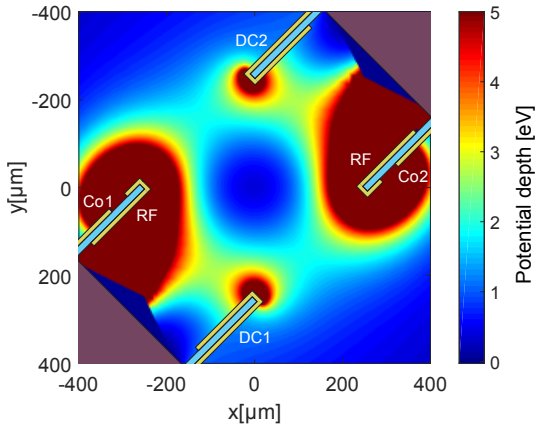

Figure 3.1: The pseudopotential of the unperturbed microtrap demonstrating a minimum at the trap centre due to the application of RF and DC electric fields. The microtrap electrodes have been overlaid on top for reference where Co1 and Co2 are the first and second DC compensation electrodes respectively. Changing the relative bias between DC1 and DC2 allows for a third compensation degree of freedom. The simulation axes are aligned with the principal axes of the trap.

have been brought close to ion traps, including optical fibres [62, 63, 118], glass microlenses [65, 66, 69], and Si_3N_4 grating couplers [60]. Kim et al. found that for a glass fibre optic with no discharge mechanism, positive charge accumulation due to the photoelectric effect was measured using the ion as an electric field probe [63], even for red wavelength incident radiation. For glass microlenses used to collect trapped ion fluoresence, a conductive coating was used by Clark et al. [70] to shield most of the dielectric surface, and normal operation of the trap was demonstrated using DC voltages to compensate for perturbations to the trapping field. While these results confirm that dielectric materials have perturbative effects on the microtrap potential, they are not readily generalisable to our particular microtrap geometry and proposed optical system. In this chapter we aim to find the acceptable limits of operation for a fused silica substrate placed close to the NPL microtrap using finite-element method (FEM) simulations. Microtrap parameters of secular frequency, displacement of the pseudopotential minimum, and the anharmonicity of the trapping potential, are investigated as a functions of the distance of the glass substrate from the microtrap centre. We investigate a range of scenarios, including techniques to mitigate the dielectric influence on the trapping field, such as conductive coatings for charge dissipation and use of DC compensation electrodes for pseudopotential correction.

3.1 Model and methods

The model for the numerical study must be computationally efficient while also being faithful to the physical implementation of the NPL microtrap. To decrease computation time we simulate the 2D radial cross-section of the microtrap, allowing for larger parameter scans and the investigation of a variety of different scenarios. The FEM simulation was implemented in COMSOL as a time-

averaged, electrostatic field of the NPL microtrap geometry. The RF electrodes have a 16.5 MHz, 150 V RF electric field applied to them, while the other two electrodes are grounded for the majority of simulations, but can have a DC bias applied for pseuodopotential compensation. The projection of the end-cap voltage used for z-axis confinement into the x–y plane is 1 V. The pseudopotential is the time averaged sum of the DC and RF potentials, which for an unperturbed microtrap has a minimum at the trap centre (shown in Figure 3.1), with principal trap axes being those that connect RF (x-axis) and DC (y-axis) electrodes. The pseudopotential is approximately harmonic, with the degree of anharmonicity being measured by fitting a higher order polynomial

$$\Phi(x) = \Phi(0) + \sum_{n=2}^{6} c_{x,n} x^n \tag{3.1}$$

to the pseudopotential and the anharmonicity parameters are defined as the ratios

$$A_{x,n} = c_{x,n}/c_{x,2} \tag{3.2}$$

with equivalent equations for the y-axis. The definitions of the anharmonicity parameters can include a length scale, however we use the ratio of the coefficients for ease of interpretation. The ideal trap would have zero-valued anharmonicity parameters, and so deviations of these parameters from zero signals non-ideal trapping conditions. Anharmonicity parameters with even values of n were found to be zero, and were not affected by any perturbations to the trapping; therefore we only quote odd n valued anharmonicity parameters in the results.

The secular frequency of the trapping potential was calculated along the x and y principal axes using Equation 1.3 and 1.4 respectively, where we used the mass of $^{88}Sr^{+}$. For the unperturbed trapping potential we found simulated secular frequencies at the pseudopoential minimum of $\omega_x = 2\pi \times 2.03$ MHz and $\omega_y = 2\pi \times 2.19$ MHz, we normalise all calculated secular frequencies to these values in the results. The trap efficiency can be calculated by

$$\eta_{x,y} = \frac{\sqrt{2} m \omega_{x,y} \Omega_{\mathrm{rf}} \ell_{\mathrm{eff}}^2}{e V_{\mathrm{rf}}} \tag{3.3}$$

where $\ell_{\mathrm{eff}} = 240$ μm for the NPL microtrap [119]. The simulated trap efficiencies of the microtrap are then 0.65 and 0.71 for the x and y principal axes respectively. The measured radial trap efficiency is 0.72 ± 0.03 [22], in agreement with the y–axis result. For the instances when the pseudopotential is perturbed, any increase or decrease in the secular frequency corresponds directly to a proportional change in the trap efficiency.

If the pseudopotential minimum does not correspond to the trap centre, excess micromotion of the ion occurs. Due to fabrication imperfections and the existence of stray charge on the trap surface the pseudopotential can be perturbed from the trap centre. The microtrap has four DC electrodes that can be used for pseudopotential compensation. Dedicated compensation electrodes are located

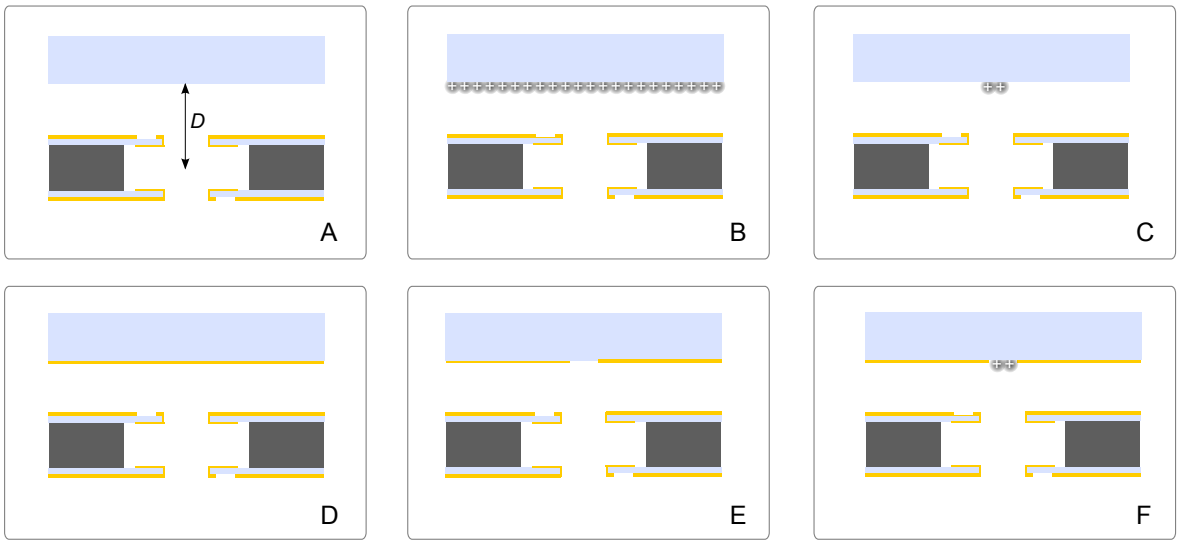

Figure 3.2: Diagrams of the considered scenarios. The microtrap is shown a distance D from: (a) Uncoated, uncharged glass, (b-c) fully and partially charged glass, (d) uniformally conductively coated glass, (e-f) conductively coated glass with exposed aperture for an optic, without and with charge respectively.

behind each RF electrode on the outside face of the microtrap. These electrodes are referred to as Co1 and Co2 for the top left and bottom right electrodes respectively. DC1 and DC2 are the bottom left and top right electrodes of the microtrap. In the operational microtrap, DC1 and DC2 are either grounded or used as end cap voltages for neighbouring segment confinement. For later investigations of pseudopotential correction, we will consider a relative absolute bias between the DC1 and DC2 electrodes as an effective third compensation electrode which we refer to as Co3.

3.1.1 Considered scenarios

After confirmation that the FEM model of the unperturbed microtrap matched experimental observation, we investigated perturbations to the pseudopotential for a variety of scenarios in order to isolate different contributions to modifications of trapping parameters. The different scenarios are summarised in Figure 3.2. In all instances the value of D, the distance of the glass surface to the ion position, was varied and the trap parameters calculated at each position. The trap parameters used are the anharmonicity coefficients, pseudopotential minimum displacement, and the secular frequency at the minimum. The threshold position value, D_T, where the trap parameters are perturbed from their baseline value can then be determined. For the displacement of the trap centre, D_T is the value of D for when the pseudopotential minimum is displaced by the resolution of the simulation mesh of ~210 nm. For the secular frequency, we use the value of D when $\omega_{x,y}$ changes by 0.1% from its baseline value, corresponding to shifts on the order of ~kHz. Johnson et al. [120] have previously demonstrated active stabilisation of an ion trap with secular frequency fluctuations of ~kHz to the 10 Hz level and we therefore assume the frequency shifts up to our chosen threshold are manage-

able with demonstrated control systems. The threshold for anharmonicity is determined as when the third-order anharmonicity coefficient changes by an order of magnitude over their unperturbed values of 3×10^{-5} and 4.5×10^{-6} for $A_{x,3}$ and $A_{y,3}$ respectively. In the instance that the pseudopotential minimum is displaced, the principal trap axes are taken through the found minimum but no analysis of the rotation of the principal trap axes is performed.

The first scenario (A) was used to isolate the effect of distortions to the pseudopotential due to the action of the dielectric to minimise its internal electric field. The effect was isolated by using a bare, uncharged glass substrate. The effect of charging of this substrate on the trap parameters was then explored in scenarios B and C for homogeneous and patch charging respectively on the glass surface. We expect homogeneous charging to be a worst case scenario which can place an upper bound on multiple, local patch charges. The magnitude of the charge accumulation used will be discussed in Section 3.1.2. When simulating a single patch charge we used a 100 μm length on the glass surface corresponding to a typical considered lens diameter. An aperture diameter of 100 μm is chosen due to being a sensible microlens size, with a numerical aperture (NA) of 0.4 at a distance of 400 μm, comparable to the currently used numerical aperture in the bulk optical setup. For addressing optics, 100 μm diameters are required to be able to place all the required optics for complete ion control.

Scenarios D-F all investigate the use of a 100 nm thick gold, grounded conductive layer on the dielectric surface to mitigate charge accumulation. Scenario D was used to isolate the effect of just the conductive film placed close to the microtrap, with no apertures for optics included in the gold layer. Scenario E includes a single, centred aperture which explored the combined effect of the conductive layer and exposed dielectric. Finally, scenario F considered the additional effect of charge accumulation on the dielectric surface despite the inclusion of a charge dissipation layer. We expect scenario C or E to be the most physically realistic depending on whether the conductive layer is included, however the worst case scenarios of B and F allow upper bounds to be placed on the threshold values, D_T. For scenario F we also consider the fixed position D = 400 μm and investigate pseudopotential perturbations for varying aperture positions on the dielectric surface. The flexibility to place micro-optics off-centre is a requirement to deliver beams to the ion with the correct k-vectors. We also investigate the capabilities for pseudopoential correction using the DC compensation electrodes on the microtrap, to compensate for the found perturbations from the presence of the dielectric.

3.1.2 Charging considerations

For the scenarios where a charge density is present on the surface (B, C, F) the magnitude of the charge must be chosen. To calculate the expected charge density, two charging mechanisms are considered: (a) light-induced charging from UV and blue radiation due to the photoelectric effect, leading to positive charge accumulation on the dielectric surface due to electron depletion, (b) electron transfer from

Scenario	Charge density ($\mu C/m^2$)	D_T (μm)			
		$A_{x,3}$	$A_{y,3}$	Displacement	$\omega_{x,y}$
A	0	< 665	< 974	< 1086	< 407
B	+1	< 1680	< 2600	< 2600	< 873
C	+1	< 345	< 1591	< 1775	< 534
D	0	< 665	< 1086	< 1211	< 629
E	0	< 534	< 665	< 974	< 629
F	+1	< 564	< 826	< 1028	< 741

Table 3.1: The values of D_T, where the trap parameters are perturbed from their baseline values for the six considered scenarios.

trap electrodes to the dielectric surface. The effects of dielectric charging have been experimentally measured using trapped ion probes [117]. It was found that case (b) was not observed at the sensitivity of the experiment and so we only concentrate on light-induced charging, noting that any electron transfer would act to neutralize positive charge accumulation. Harlander et al. [117] measured that 0.4×10^{-10} electrons per photon are ejected from the surface of glass under illumination with 397 nm radiation. Considering 20 μW of 397 nm radiation, a power an order of magnitude higher than typically experimentally used, the number of incident photons per second is 2×10^{15}. Assuming the photons are incident on a 100 μm × 100 μm square area (i.e. a microlens) then the resulting charge density after 1 second of illumination is 26 nC/m^2. Charge saturation occurs on the timescale of 38 seconds, suggesting a very low dissipation rate of surface charge and maximum charge buildup would saturate at ~1 $\mu C/m^2$. Harlander et al. found that no charge accumulation occurs for 422 nm radiation above the measurement sensitivty of 0.64 $nC/m^2/s$, the lowest operational laser wavelength for strontium ions. The wavelength of 405 nm is used for photoionisation, however this occurs away from the operation segments, and distortions to the trapping potential in the loading segment are less critical. We therefore use charge densities of 1 $\mu C/m^2$, corresponding to a worst-case scenario. The effect of multiple patches can be upper bounded by the homogeneously charged case. The charge density of 1 $\mu C/m^2$ is consistent with that used by Podoliak et al. [116] and enables direct comparison. For operation of $^{88}Sr^+$, where the lowest operational wavelength is 422 nm, we expect charging effects to be orders of magnitude less as the derived charge density is for powers an order of magnitude more than operationally used, and the charge induced at 422 nm is at least an order of magnitude less than induced by 397 nm light. As the considered charging effect is induced by laser radiation, we do not expect significant charging to occur for collection lenses. Therefore for all scenarios with charging, we assume addressing optics are present.

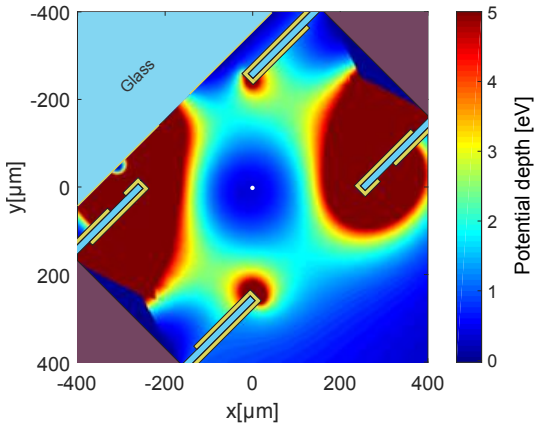

Figure 3.3: The pseudopotential of a perturbed microtrap in scenario F with D = 250 μm, illustrating the 15 μm displacement of the pseudopotential minimum due to the presence of the dielectric near the microtrap. Distortion of the trapping potential to the presence of the dielectric is clearly illustrated. The yellow line on the glass surface indicates the location of the thin conducting film. The white circle denotes the centre of the microtrap. Potential units are in eV.

3.2 Results

In all the simulated scenarios, the microtrap pseudopotential parameters were found to be perturbed from their baseline values for a small enough value of D. It was found that below the perturbation threshold, the trap parameters either increased or decreased in an exponential trend for reducing values of D as demonstrated in Figure 3.4 for scenario B. The threshold values of D for which the trap parameters were found to be perturbed from their baseline values are summarized in Table 3.1 for all considered scenarios. The perturbation threshold is different for the each of the considered trap parameters, with the displacement of the pseudopotential minimum occurring at the furthest away from the microtrap centre, followed by distortions to the harmonicity of the pseudopotential in the y-axis. The secular frequency, and therefore the trap efficiency, is modified at the closest distances to the microtrap indicating that it is the least sensitive parameter to pseudopotential distortions due to its dependence on the second derivative of the pseudopotential at the minimum.

The effect of the dielectric to minimize its internal field is isolated for scenario A, for which no charging is included. We found that the pseudopotential minimum is displaced when the glass substrate is brought closer than ~1.1 mm to the trap centre. As expected, the additional static electric field generated by charging of the substrate perturbs the pseudopotential at a significantly greater distance away from the microtrap: homogeneous charging the substrate restricts the ion-glass distance to be greater than 2.6 mm, while a single patch charge allows for closer ion-to-glass distances of >1.8 mm. The coating of the dielectric in a conductive film to mitigate the charging perturbations (scenario D) actually increases the value of D_T for the pseudopotential minimum displacement compared to scenario A by ~0.2 mm. However, this offers a significant improvement over the charged scenarios where no charge dissipation is present. The presence of an aperture in the conductive coat-

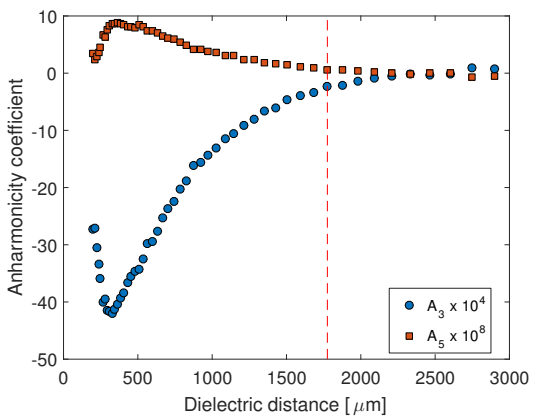

(a) Anharmonicity parameters of the principal x-axis.

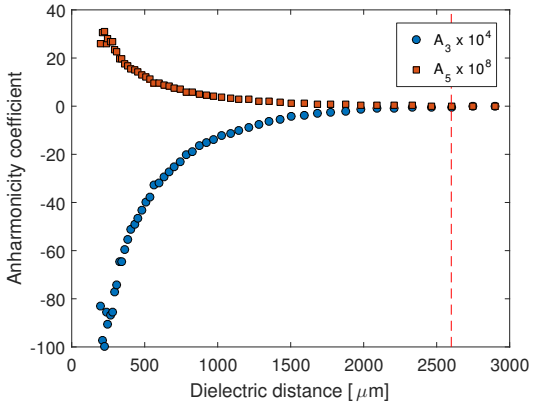

(b) Anharmonicity parameters of the principal y-axis.

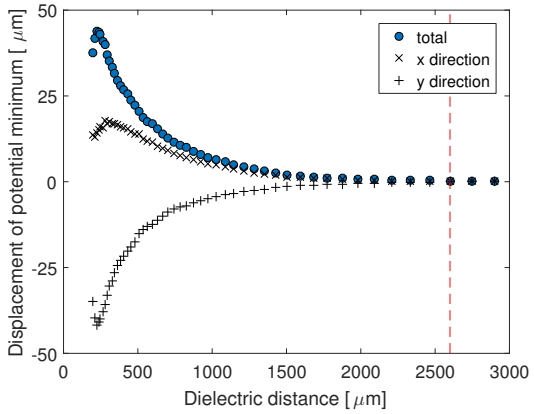

(c) Displacement of the pseudopotential minimum.

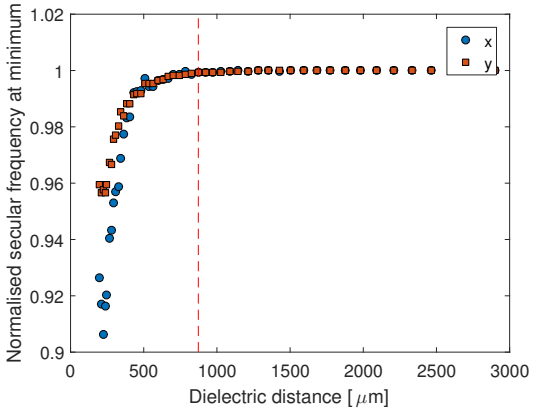

(d) Secular frequency at the pseudopotential minimum.

Figure 3.4: Trap parameters for a charged, uncoated dielectric substrate (scenario B) over a range of D values. An exponential trend in D is shown after a threshold value, D_T at which the trap parameters become perturbed from their baseline value, shown as red dashed line.

ing (scenario E) allows for closer ion-glass distances than when there is no aperture, even when the aperture is charged (scenario F). The effect of local charging in the aperture is greatly decreased over the case where no conductive coating was used (scenario C). The distortion of the pseudopotential for scenario F, with D = 250 µm, is shown in Figure 3.3 illustrating displacement of the pseudopotential minimum, clearly due to distortion of the RF field.

3.2.1 DC compensation

Having found significant perturbations to the pseudopotential for glass-to-ion distances of interest for an operational micro-optical assembly we now consider the capability of the compensation electrodes to correct for the perturbations of the trap parameters. We performed simulations with a fixed substrate distance from the trap centre of D = 400 µm for scenario F. It was found that voltage applied to compensation electrode 1 (Co1) had little effect on the pseudopotential, most likely due to the proximity to the grounded conductive layer on the dielectric. We therefore used a combination of Co2

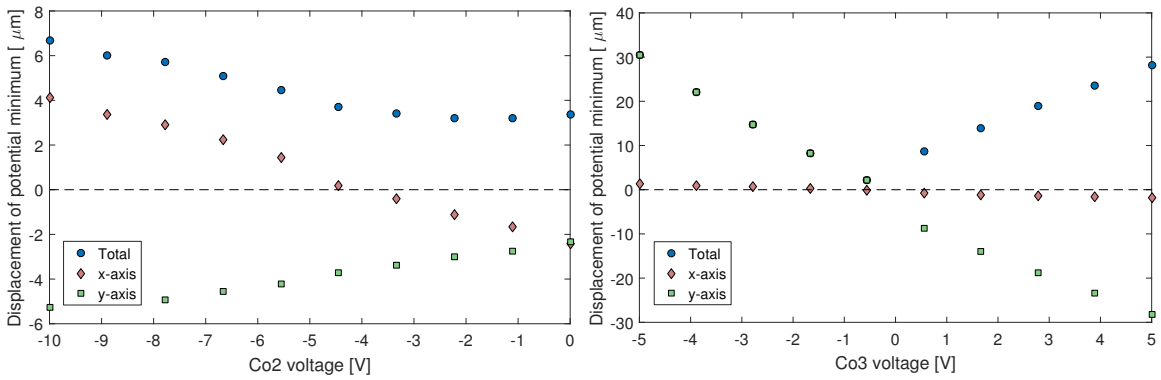

(a) Displacement of the pseudopotential minimum by varying the bias on compensation electrode 2, keeping compensation electrode 3 grounded.

(b) Displacement of the pseudopotential minimum by varying the bias on compensation electrode 3, keeping compensation electrode 2 at −3.4 V.

Figure 3.5: Displacement correction with compensation electrodes (a) 2 and (b) 3, where the voltage of compensation electrode 2 is set to −3.4 V when varying compensation electrode 3. The pseudopotential minimum crosses the origin point for applied voltages of −3.4 V and −0.6 V, with the exact values to be determined experimentally.

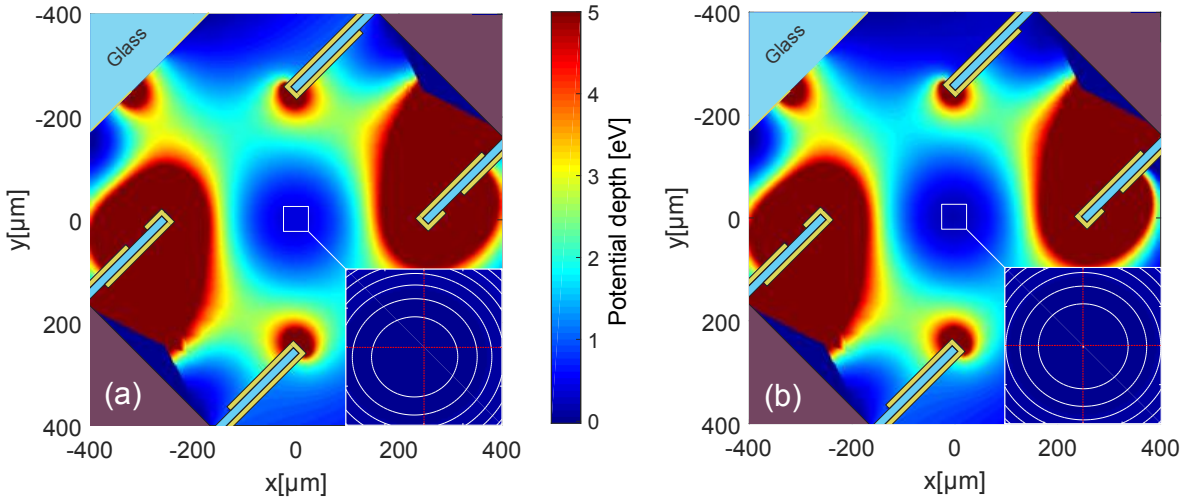

Figure 3.6: The pseudopotential of a perturbed microtrap in scenario F with D = 400 μm, (a) without and (b) with DC voltages of −3.4 and −0.6V applied to compensation electrodes Co2 and Co3 respectively . The inset shows contours of the potential at the trap centre (red dashed lines).

and Co3 which provides compensation vectors along both trap axes.

It was found that −3.7 V was required to be applied to compensation electrode 2 (Co2) to move the pseudopotential minimum 2.4 μm along the y-axis to the $x = 0$ μm line, as shown in Figure 3.5. When applying voltage to Co3, we find cross-talk with y-axis movement. Accounting for the cross-talk, it was found that the voltages required to bring the pseudopotential minimum to the trap centre were −3.4 V and −0.6 V for Co2 and Co3 respectively. The pseudopotential of an uncorrected and corrected microtrap with the calculated compensation voltages is shown in Figure 3.6. Once compensated, the secular frequency at the origin is within 2% of its unperturbed value, indicating favorable trap efficiencies. After compensation, the third-order x-axis anharmonicity coefficient, $A_{x,3}$ is less than twice its baseline value, however $A_{y,3}$ is increased $\sim 10^2$ over the unperturbed case. We attribute the excess anhamonicity to the correction of the displacement of the pseudopotential minimum not fully correcting the shape of the pseudopotential. Higher anharmonicity coefficients add higher order terms to the equations of motion and therefore there is some sacrifice to the ability to faithfully control the ion's motional state [121]. Assessing the magnitude of the effect of the residual anharmonicity is beyond the scope of this work, however we note that $A_{y,3} \sim 10^{-4} \ll 1$ and the harmonic term is dominant.

We have shown that the pseudopotential displacement can be corrected for $D = 400$ μm with modest compensation voltages. However, because the displacement of the pseudopotential minimum exponentially increases with decreasing D then the ultimate limit of how close a dielectric can be brought to the microtrap centre is determined by the maximum voltage that can be applied to the compensation electrodes. For the microtrap under consideration, this is approximately ±100 V and so there is further scope for bringing the glass substrate closer to the microtrap centre, however one would expect further degradation of the $A_{y,3}$ which cannot be fully corrected. As well as using the compensation electrodes, we also considered directly biasing segments defined in the conductive coating on the glass substrate for pseudopotential correction. It was found that higher voltages were required for displacement correction over the compensation electrodes on the microtrap due to the increased distance away from the trap centre and shielding of the ion position from the trap electrodes. Due to the compensation electrodes on the microtrap being sufficient for pseudopotential correction and the added complication of defining DC electrodes on the glass surface we do not explore this further, however it is noted that this option is available for advanced future implementations.

3.2.2 Aperture position

To realise the required k-vectors for trapped ion addressing, some of the addressing optics must be off-axis from the centre of the microtrap. We therefore investigated the effect of the aperture position on the microtrap parameters in scenario F with $D = 400$ μm. The summary of the investigation is shown

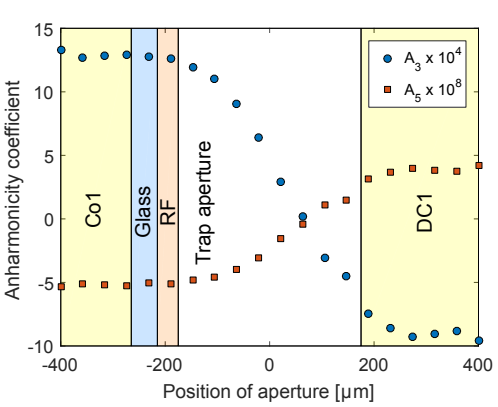

(a) Anharmonicity parameters of the principal x-axis.

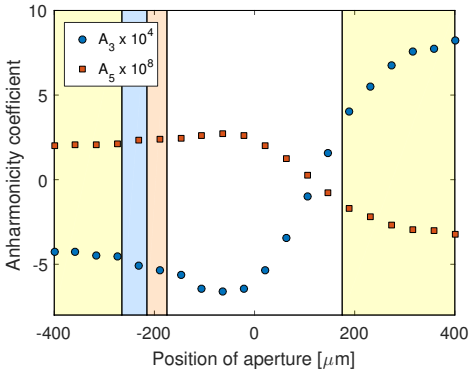

(b) Anharmonicity parameters of the principal y-axis.

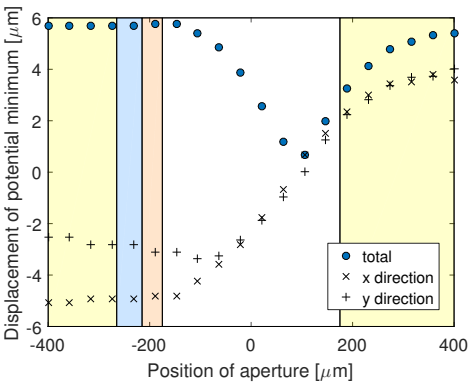

(c) Displacement of the pseudopotential minimum.

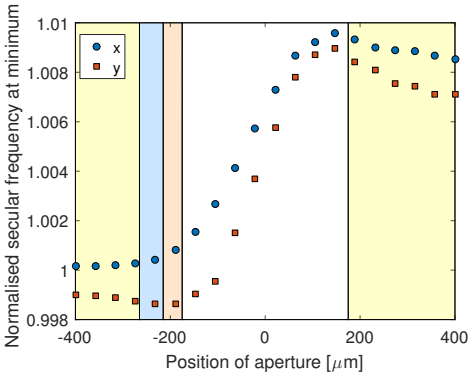

(d) Secular frequency at the pseudopotential minimum.

Figure 3.7: Trap parameters for Scenario F, an charged aperture in a grounded conductive coating on a dielectric substrate placed at D = 400 μm, as the lateral aperture position is varied. The data points are overlaid on a plan view of the microtrap, indicating the element of the microtrap that the aperture centre is positioned over. The light yellow is the position of DC electrodes, blue is the glass opening in trap electrode, orange is the RF electrode.

in Figure 3.7. We found that as the aperture was moved along the glass surface, there was a large variation in all the trap parameters. While the secular frequency perturbation is minimised when the exposed aperture is over the RF electrode, we find that at the same position both the anharmonicity coefficients and the pseudopotential minimum displacement are increased over the instance when the aperture is over the trap centre. The placement of the aperture over the DC electrode increases the perturbations in all trap parameters. As the aperture position has a large effect on the trap parameters it is recommended that simulations are performed when determining optic layouts. In some instances flexibility in the optic position may not be possible due to k-vector requirements on some beams with respect to the principal trap axes. In this instance, pseudopotential minimum perturbations must be corrected using the compensation electrodes.

3.3 Discussion and conclusion

We explored a variety of different scenarios for bringing a glass substrate close to a linear, Paul microtrap using numerical simulations. Homogeneous charging of the glass caused dramatic perturbations of the trap parameters and a discharge mechanism must be employed so as to bring the dielectric within 2.6 mm of the microtrap centre. We therefore recommend a conductive coating, which was shown to dramatically reduce trap perturbation thresholds to ion-glass distances of ~1 mm for open, charged apertures. We expect light-induced charging of open apertures to be minimal at wavelengths of 422 nm and the overall charge of the aperture is expected to be dominated by the discharge rate of the conductive layer. Use of ion species requiring UV wavelength control will have light-induced charging effects that may limit the ion-dielectric spacing that can be used. However, it remains that the dominant degradation of the pseudopotential is due to distortion of the RF potential by the presence of the dielectric.

We found that pseudopotential minimum displacements caused by proximal dielectrics could be corrected by the compensation electrodes already present on the microtrap. The ultimate limit of ion-dielectric spacing will be determined by the maximum DC bias that can be applied to these electrodes. As the pseudopotential minimum displacement grows exponentially with decreasing dielectric distance, there will be a limit to how close the dielectric can be brought to the trap centre. It was found that a conductively coated dielectric, with a single, charged aperture placed 400 μm from the trap centre could be compensated for by biases on two separate electrodes of −3.4 and −0.6V. When displacements are corrected for, the secular frequencies at the pseudopotential minimum (and therefore, trap efficiencies) differ < 2% from their unperturbed values. We find elevated trap anharmonicity in the y-axis even after pseudopotential correction, however the harmonic term is still dominant by 4 orders of magnitude.

In all simulations we considered static charge densities. For collection optics it has been experimentally shown that an assumption of static charges is valid, even for D = 165 μm [70]. For addressing optics, charging will be time-dependent up until saturation [117]. Due to the use of pulse sequences used to address trapped ions, the surface charge density induced by short wavelength addressing beams could be time-varying, depending on the time-scales of the laser pulses and the charge accumulation dissipation. It may be possible for the pseudopotential minimum shifts induced by these time-varying surface charge densities to be dynamically compensated for by characterizing ion positions shifts as a function of addressing laser pulse length. However the required additional calibration adds further experimental complications that must be weighed up against the benefit of placing microfabricated optics in proximity to the microtrap.

While we have considered a glass, which has a modest dielectric constant (ϵ_r = 4.2), we briefly

considered trap perturbations for higher dielectric constants. Replacing SiO_2 with TiO_2 (ϵ_r = 100) we find an increase in D_T of approximately 100 μm in all parameters for an uncharged, bare substrate. The increase in D_T is due to the greater capacity of the material to null its internal electric field, further distorting the pseudopotential. Therefore permittivity is a consideration in selection of micro-optic materials however this must be balanced against any optical advantages a material with a higher dielectric constant, and therefore refractive index, might have.

We conclude that dielectric-trap distances of ~1 mm are possible with a simple mechanism of a thin, grounded conductive film for removing charge accumulations on dielectric surfaces. Closer distances would require experimental study of conductive coating discharge rates, light-induced charging dynamics and harmonicity degradation effects on ion motion which would be best explored in proximity to an operational microtrap. While we have not drawn any firm conclusions about a particular optical assembly design, we have constructed a model and method of extracting important microtrap parameters for providing guidance on optical layouts and their proximity to the microtrap for future design procedures.

4

Laser-written waveguides

The use of ultrafast pulsed lasers to modify dielectric materials, especially glasses, is a rapidly maturing fabrication technique with many applications, including integrated optical waveguiding [103, 122], quantum photonics [123, 124], microfluidics [125, 126], micromachining [127], active photonic devices [128] and deterministic creation of quantum emitters [129]. One of the most advanced application areas is of writing light-guiding structures directly inside glass, which we refer to as laser-written (LW) waveguides. In the technique femtosecond laser pulses are tightly focused in glass such that nonlinear excitation of electrons across the band-gap leads to material modifications and permanent changes at the laser focus. By translating the laser focus extended and continuous material modifications can be written. Fine-tuning of the laser parameters can be used to tailor the material modification such that a refractive index contrast with the surrounding material is created which can then guide light, in exactly the same principle as for fibre optic guidance.

Our goal in this chapter is to develop LW waveguides suitable for guiding and collecting the necessary wavelengths for $^{88}Sr^{+}$ close to the ion trap. As one of the most important wavelengths for $^{88}Sr^{+}$ is 422 nm, the main challenge is the sparsity of literature on LW waveguides for supporting a single, Gaussian mode at blue wavelengths. At the start of this work we were aware of only two prior demonstrations of such waveguides, with the first being the writing of *surface-skimming* waveguides suitable for guiding 405 nm light [130] and the second was waveguides in *polymer*, shown to support a 397 nm wavelength single-mode [131]. Therefore, the robust and flexible writing of waveguide circuits for supporting blue wavelength single-modes buried in glass remained an open challenge. We identified several potential issues before commencing a study of waveguides for blue wavelengths with the primary concern being the capability of fabricating waveguide diameters small enough for single-moded guidance of blue light. LW waveguides for guiding a single mode of red and near-IR wavelengths have been routinely demonstrated in the literature [132–135] however the reduction in waveguide size could lead to several complications, especially if we are required to operate near the

modification threshold of the material. If the desired diameters are attainable it was also a requirement that they can be reliably and repeatably fabricated such that they could be incorperated into a manufacturing process with large numbers of waveguides. A secondary concern, after the determination that small enough waveguides could be written, was whether their mode field diameters could be tuned for high mode overlap with single-mode fibre (SMF). Any discrepancy in the mode overlap between the waveguide and the input fibre will lead to losses, and specifically to the free propagation of laser radiation towards the trapped ions. It is therefore critical that we have full process control for tuning this mode overlap as close as possible to unity. Another factor that could cause undesired losses is Rayleigh scattering due to any inhomogeneities in the waveguide structure. As Rayleigh scattering scales as λ^{-4} it is of great influence at blue wavelengths, where it is often a severe issue in planar waveguides due to sidewall scattering [84]. There is no guarantee that LW waveguides will be smooth on the required length scales for efficient guiding of blue light, which could lead to unworkable losses and a ruling out of LW waveguides for trapped ion applications. A final concern is that color-centre formation is known to occur during the laser-writing process which could lead to absorption of blue wavelengths and remission into longer wavelengths, leading to interactions of undesired wavelengths with the trapped ion. We seek to at least partially address all of these identified concerns throughout the chapter. As well as blue wavelengths, $^{88}Sr^{+}$ control also requires wavelengths from 674 nm to 1092 nm. Due to these wavelengths being typical for previously reported applications our study of waveguides for these wavelengths is limited to practical demonstrations. In the interest of demonstrating a waveguide chip with waveguides designed for single-mode guidance of wavelengths from blue to near-IR in the same substrate we briefly developed waveguides for near-IR wavelengths.

A second open challenge was in the capabilities of expanding the mode field diameter of the supported waveguide mode. The mode exiting from a singe-mode fibre optic expands rapidly due to its small mode size. As our proposed concept includes a ~1 mm distance between the end of the waveguide and the focusing optic plane, the faster the expansion, the larger the lenses have to be. The smaller the lenses can be, the more lenses can be placed in the same area and therefore the more addressing beams we can use. We therefore wish to expand the waveguide mode size from its optimal fibre coupling MFD to a larger MFD that expands more slowly after exiting the waveguide. The concept of mode expansion tapers is well established in planar waveguides [111–114], however we know of no such precedent existing for LW waveguides where the only pre-existing mode tapers are for single-mode to multi-mode conversion [136]. As we require maintaining the guidance of a fundamental Gaussian mode after expansion these tapers are not suitable for our application.

In this chapter we will first introduce the theory of LW waveguides, before moving onto our practical investigations into the open challenges listed above. We first fabricate and test single-mode waveguides supporting blue light, before fine-tuning the fabrication parameters for optimal overlap

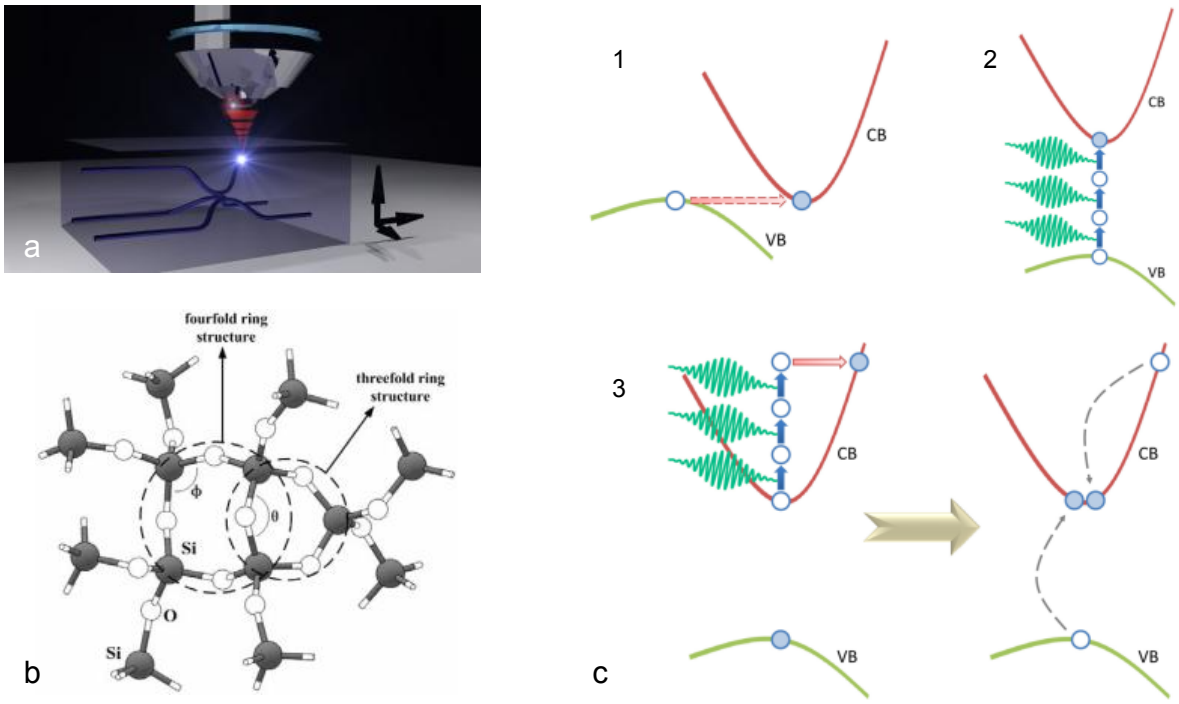

Figure 4.1: (a) Formation of light-guiding circuits in transparent dielectrics using focused femtosecond laser radiation, reprinted with persmission from [124] (b) Bond structure of pure fused silica showing the characteristic 3 and 4 ring structures, reprinted with persmission from [148]; (c) Nonlinear excitation mechanisms of electrons across the dielectric bandgap by ultrafast laser pulses, (1) bandgap distortion, (2) multi-photon ionisation, (3) avalanche ionisation, reprinted with persmission from [137] Copyright 2008 IEEE.

with blue single-mode fibre. The loss and spectral response of single-mode waveguides for blue light is then explored. The development of waveguides for the single-moded guidance of near-IR light are briefly outlined before we explore a variety of mode-expansion techniques in LW waveguides to advance the capabilities of the LW waveguide platform for trapped ion addressing.

4.1 Theory

The mechanisms that induce refractive index changes in glass exposed to tightly focused femtosecond laser beams long remained elusive. The wide range of laser conditions (pulse energy, repetition rate) and materials (fused silica, multi-component glasses, actively doped dielectrics, polymers) creates a large parameter space to be understood [137]. The fabrication of material modifications in glasses is the most well understood portion of the parameter space, and is the one we will concentrate on. The practical use of these refractive index changes in glass was first recognised by Davis et al. [122]. By translating the focused femtosecond laser through a glass sample, continuous paths of refractive index modifications can be written as illustrated in Figure 4.1. Tuning the size and refractive index profile of these regions allows for the supporting of modes of laser radiation. Laser-written waveguides have since been demonstrated in a wide range of materials [138–147].

Glasses, being transparent at visible wavelengths, have low linear absorption at the typical wavelengths of Ti:Sapphire femtosecond lasers (~800 nm). This is due to the photons at this wavelength not possessing sufficient energy to excite electrons in the valence band of the glass to the conduction band. The tight focusing of femtosecond radiation within the material allows for non-linear absorption of photons such that electrons can be promoted to the conduction band. Due to the non-linearity of the effects, the absorption falls away rapidly from the focus centre leading to localised absorption of the radiation. These non-linear effects include band-gap distortion, multi-photon ionisation, and avalanche ionisation [137] as illustrated in Figure 4.1(c). The sudden excitation of electrons to the conduction band creates a hot gas of electrons in the cold glass lattice, and equilibrium must be restored through electron energy being deposited into the lattice through phonon coupling inducing modifications to the lattice. The modification can take the form of color-center formation, bond-angle changes, and bond-shortening [149], which can be either caused by bond breaking or by electron reorganisation. Color-centre formation increases the molar refractivity of the glass, increasing the effective local refractive index with respect to its host. Bond-angle is decreased by the formation of smaller ring structures in the glass (illustrated in Figure 4.1(b)), reducing the internal bond angle of the rings. Both bond-angle decreases and bond-shortening lead to a densification of the glass and an increase in the effective local refractive index. It has been found that when the repetition rate of the laser is low (~kHz), and the time between pulse is longer than the thermal relaxation time of the glass (~10 μs), then the dominant refractive index change in fused silica [150] and BK7 glass [149] is color-centre formation due to bond-breaking. When the repetition rate of the laser is such that electrons are excited to the conduction band faster than they can deposit energy back to the lattice (~MHz), then the dominant modification is bond-shortening leading to densification of the glass [149]. This latter regime, with repetition rates of ~MHz is referred to the cumulative heating regime [151–153]. In this regime, the lattice remains at an elevated temperature for longer, allowing for more complete reorganisations of its structure, erasing color-centre formation. The modification is no longer limited to the focal volume, with thermal diffusion linearly growing the modification region diameter with incident power, which is controlled either by dwell time, or pulse energy [153]. The *cumulative heating threshold* is the femtosecond laser fluence where waveguide diameter growth transitions from non-linear to the linear behaviour characteristic of the cumulative heating regime, determined by the energy dissipation rate in the host material. The resulting modifications are also more permanent then modifications fabricated below the cumulative heating threshold, both because the dominant refractive index modification cannot be photobleached, in contrast to color-centres, and because the temperature of the glass at the modification region is raised above the annealing point of the glass. The rapid, local densification of the glass places stress on the surrounding lattice, leading to complex refractive index changes around the modification region. As these stress regions have not

been raised above the annealing temperature of the glass, a thermal annealing routine can simplify the refractive index profile of the modification.

4.1.1 Refractive index profile models

As one of our main tasks is to tune the mode-field diameter (MFD) of single-mode waveguides for maximal mode overlap with fibre, we require a predictive model of mode-field diameter with waveguide diameter. Mode-guiding structures, such as waveguides and fibre optics, can be parameterised by the V-number [154]

$$V = \frac{2\pi}{\lambda_0} a \sqrt{(n + \Delta n)^2 - n^2} \tag{4.1}$$

where λ_0 is the vacuum wavelength, a is the core radius and $\Delta n = n' - n$ is the refractive index contrast between the core (n') and the cladding (n) respectively. The optimal guidance region occurs for $1.3<V<2.405$, where for $V<2.405$ the waveguide supports only the fundamental mode and in this regime V represents the proportion of mode power within the waveguide volume. The weakly-guiding regime occurs for $V < 1.3$ when most of the power is located outside of the waveguide and the propagating light is susceptible to bend-losses and leaking of radiation from the guiding region.

For step-index profiles, typical in fibre optics, where the refractive index is defined as

$$n_{SI}(r) = \begin{cases} n' & \text{if } r \leq a \\ n & \text{if } r > a \end{cases}$$

the beam radius, w, of a mode propagating in the waveguide is given by the empirical Marcuse formula [155]

$$w = a\left(0.65 + \frac{1.619}{V^{3/2}} + \frac{2.879}{V^6}\right) \tag{4.2}$$

valid for $V>1$. However, in the cumulative heating regime, the resulting heat accumulation from the femotosecond laser radiation has been shown to be accurately modelled by a Gaussian heat distribution [153]. We therefore model waveguides in the cumulative heating regime with a Gaussian refractive index profile, given by

$$n_G(r) = n + \Delta n \exp\left(-\frac{2r^2}{a^2}\right), \tag{4.3}$$

with beam radius of the resulting waveguide now taking the analytic form [154]

$$w = \frac{a}{2\sqrt{V - 1}} \tag{4.4}$$

also valid for $V>1$. In the Gaussian refractive index model waveguides support only the fundamental mode for $V<2.592$, which is an increase over the step-index model [154]. We experimentally confirmed the Gaussian refractive index model for LW waveguides, and found that step-index and other possible refractive index profiles (such as a power-law [156]) did not suitably predict waveguide MFD with diameter.

4.2 Procedures and techniques

Multiple procedures and techniques are common to all LW waveguide investigations presented throughout the chapter, including sample fabrication, processing, analysis and optical testing. In the following we outline these techniques before moving onto the results of our investigations.

4.2.1 Laser-writing

The laser source used for writing, located at Macquarie University, was a high repetition rate Ti:Sapphire oscillator (*Femtolasers FEMTOSOURCE XL500*, 800 nm, 5.1 MHz, <50 fs), henceforth referred to as the HPO (high power oscillator). A computerised half-waveplate and polarisation beam splitter allowed for fine control of the beam pulse energy. The beam path was sent through a Pockel cell and polariser set up to allow for fast variation of the beam power. The beam could be deflected into an autocorrelator to check for pulsed operation; the number of autocorrelation fringes, and therefore laser pulse length, was kept approximately constant from run to run to maintain repeatability. When used for writing the beam was deflected to a housing containing a mechanical switch, beam profiler and mirrors to direct the beam vertically down onto a vacuum chuck mounted on a set of precision airbearing 3-axis stages (*Aerotech*). A microscope objective was mounted in this vertical beam path to provide a focus. In all samples fabricated the objective was a Zeiss N-Achroplan 100×/1.25 NA oil-immersion lens. Such a high NA was required to provide sufficient power at the focus such that the cumulative heating threshold could be reached with modest pulse energy. The sample was placed on the vacuum chuck and aligned such that it was flat with respect to the focus plane of the objective, with immersion oil between the objective and the sample. The stages, mechanical shutter, computerised half-waveplate and Pockels cell were all controlled using g-code such that complex waveguide circuits could be fabricated in three dimensions using scripts. The speed at which the focus is translated through the sample is referred to as the feedrate, and together with the pulse energy determines the fluence of the beam through the glass. Typical parameter ranges of the feedrate are 250–2000 mm/min, and of the pulse energy 20–500 nJ for the multi-components glasses used. The Pockels cell was used either for reducing the effective repetition rate of the laser, or for switching faster than the mechanical shutter (useful for inscribing text, damage marks, Bragg gratings etc.).

The inherent sensitivity of a femtosecond laser with a 5.1 MHz repetition rate to environmental variations, causing a change in properties such as the spectrum and pulse duration, meant a calibration procedure was required before each fabrication run. The calibration procedure aimed to determine a pulse energy to waveguide diameter relationship for each of the feedrates used in the sample design. Typically, the approximate pulse energy is known and so a range around this value is taken to find the exact value for that day's laser operation. Sets of waveguides were written in the same material as the

sample to be written, over the range of pulse energies chosen. The number of written pulse energies was set by the requirement of fitting a linear regression to the pulse energy-to-waveguide diameter relationship. As we were operating in the cumulative heating regime the waveguide diameter grows linearly with pulse energy, however below a certain pulse energy (~30 nJ in our case) the conditions for cumulative heating are not met and the relationship deviates from linearity. If we wish to fabricate waveguides near the cumulative heating threshold then it is typically necessary to use linear interpolation and a greater number of calibration points. After fabrication of the calibration sample, the waveguide diameters were measured visually using transmission differential interference microscopy (described below) and the required pulse energies to achieve a certain waveguide diameter in the design sample can be determined. Once determined these parameters are fed into the g-code and the sample can be written. Delay between writing the calibration and final sample was minimised to reduce the effect of variation of the laser parameters with time. It was found that laser parameter drift was reduced if the HPO had been running for >24 hours.

If the waveguide depths in the design vary considerably then a calibration of the waveguide diameter with depth for a fixed pulse energy must also be performed - though this is assumed to not vary with laser parameters as it is due to distortions of the focus with depth. At shallow writing depths (~50–150 μm) the immersion oil begins to absorb laser power and power at the focus is reduced. Therefore for shallow waveguides the pulse energy required to keep the same waveguide diameter is increased. For deep waveguides (~300–400 μm), the power required also increases, however a full explanation for this is not known. It is likely to be a combination of focus broadening (despite the pseudo-matched index) and power absorption by the glass. Depth calibration will be expanded on in more detail in Chapter 7, and demonstrated in Figure 7.6, where it is required for fabricating waveguide circuits.

4.2.2 Waveguide diameter analysis

Written waveguides are imaged using transmission differential interference microscopy (TDIC). As the waveguides are optically transparent (a requirement for low loss waveguides) they typically cannot be imaged using an optical microscope. TDIC microscopy is performed by spatially separating the vertical and horizontal linearly polarised components of the illumination light using a birefringent prism, transmitting through the sample and then interfering the light using another prism - converting the relative phase shift information between the two polarisations into intensity gradients. As the waveguides are perturbations of the surrounding refractive index of the host glass, they are clearly represented in TDIC images. Example images of the same waveguide before and after thermal annealing is shown in Figure 4.2(a-b) showing the simplification in the refractive index profile.

The waveguide diameters were measured manually in software by defining the two edges of the

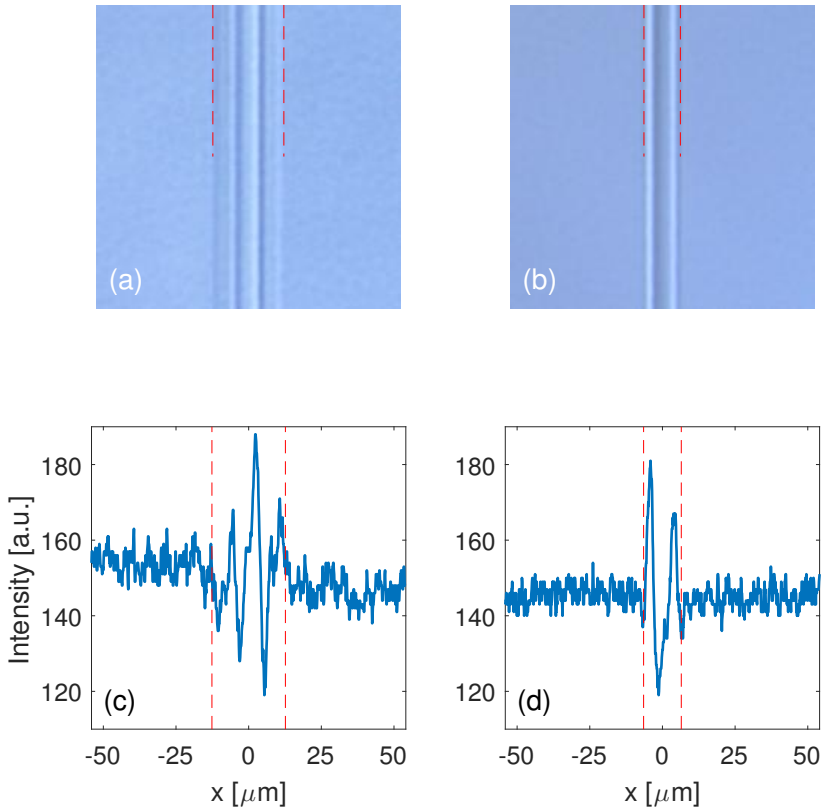

Figure 4.2: Example TDIC images of LW waveguides with red dashed lines to indicate used boundaries for diameter measurements, (a) colour image of unannealed waveguide, (b) colour image of the same waveguide but thermally annealed; (c) a 1D intensity cross-section of the unannealed waveguide in (a); (d) a 1D intensity cross-section of the annealed waveguide in (b).

waveguide. We take the point of greatest contrast at the waveguide edges as the start and end points for measurement and typical measurement variations of ±0.5 μm are common due to uncertainty in these positions - especially for thermally annealed waveguides. Waveguides with diameters <2 μm cannot be reliably measured due to resolution limits of the microscope. The used boundaries at the edges for both unannealed and annealed waveguides are shown as red dashed lines in Figure 4.2.

4.2.3 Thermal annealing

After sample fabrication in the cumulative heating regime the sample was placed in an high-temperature oven. The oven temperature was slowly increased (over 2 hours) to just above its annealing point (722°C) and was then allowed to slowly cool over 8 hours to just below its strain point (666°C) where it could then be cooled to room temperature over 2 hours [103]. The numbers used in brackets correspond to *Corning Eagle2000* display glass which we predominantly used for all waveguide development.

4.2.4 Lap and polish

As the glass edge of the sample chip distorts the focus of the fabrication beam, the waveguides are distorted near the end facets of the sample, which is typically manifested as a tapering of the waveguide diameter towards the sample face. Therefore the waveguides internal to the chip must be exposed which is performed by the grinding and optical polishing of the end facets of the waveguide sample.

First, the sample was protected by bonding cover slips of the same dimension to the top and bottom of the sample using a temporary UV adhesive (*Norland Blocking Adhesive*) - this was to protect the sample edges from chipping during the grinding and polishing. The sample was then mounted to a jig (*Logitech PP5*) using either bonding wax (*Logitech Quartz Wax*) or temporary UV adhesive (*Norland Optical Adhesive 61*) on its top or bottom face. The sample was mounted such that the end facet is flush with glass sacrificial pieces mounted on the face of the jig to prevent shear pressure on the sample. The sample face was levelled with respect to the flat jig surface by reflecting a red laser beam off one of the sacrificial glass surfaces (or, ideally, the sample itself) and comparing its reflected beam position with respect to the reflection from a flat piece of glass the jig is sat on. The beam spots were compared a distance of at least 1 m from the jig face, and the levelling screws on the jig are adjusted so that the two beams are congruent. The jig was then placed on the grinding wheel of a lapping and polishing system (*Logitech PM5*), first using a coarse lapping slurry (calcined aluminium oxide powder, either 20 μm or 25 μm particle size) to remove the majority, typically 100–500 μm, of the required glass. A fine lapping slurry (calcined aluminium oxide powder, either 3 μm or 5 μm particle size) was then used to grind ~25 μm to reduce the surface roughness caused by the coarse lap. Optical polishing of the end facets was then performed on the same machine but with the lapping wheel replaced by a polishing polyurethane foam wheel. An alkali, colloidal silica-suspension polishing slurry (*Logitech SF1*) was dripped onto the polishing cloth, as well as a pH 10 solution of NaOH to prevent the colloidal silica from coming out of suspension. The end facet was polished until visually smooth under a microscope, typically taking 2 to 3 hours. The whole process was repeated for the other end facet. The sample was unmounted from the jig either by heating (for hot wax) and an acetone bath (to remove the cover slips and cleaning), or simply an acetone bath to dissolve the temporary adhesives. The waveguide end facets were then further cleaned using lens tissue and acetone/IPA to prepare the sample for optical testing.

4.2.5 Optical testing

Waveguides were tested using a variety of methods to extract quantities such as mode-field diameter, transmission loss and excitation spectrum. In all instances the waveguide input facets were interfaced with a single, unjacketed and cleaved fibre. The input fibre was mounted on a 6-axis flexure stage

(*Thorlabs Nanomax*, or *Elliot Gold*) such that all degrees of freedom for coupling into the waveguide modes can be accessed. The waveguide chip under test was held on a vacuum chuck mounted on a 3-axis stage for coarsely aligning the waveguide chip to the fibre before fine tuning was performed with the fibre stage. Initial fibre-waveguide alignment could be performed by using either the far-field projection of the output facet on a screen, or a 10× objective to view a near-field image of the waveguide output. Waveguides present near the fibre output appeared as shadows in either projection and allowed for visual alignment of fibres to waveguides. After initial coupling we used the fact that all waveguides are fabricated at the same depth to easily translate from one waveguide to the next. Once the desired waveguide was coupled to, the required measurements could be performed, with the most common measurement being a recording of the beam profile for mode-field diameter determination.

Mode-field diameter (MFD) The output mode of the waveguide was projected onto a CCD using a microscope objective with magnification such that the beam profile had at least a width of 10 CCD pixels for robust Gaussian fitting. Blue wavelength modes were typically imaged with a 100× or 150× objective, and near-IR wavelength modes were imaged at 10× or 50×. To image the waveguide output mode the camera was translated along the optical axis such that the minimum MFD was observed, and this was further confirmed to be the output facet by imaging the sharply focused chip edge. The MFD was either read from live calculations by camera software, or the image saved and fitted with a 2D Gaussian function in MATLAB taking the form

$$I(x,y) = I_0 \exp(-(A(x-x_0)^2 - 2B(x-x_0)(y-y_0) + C(y-y_0)^2)) \,, \tag{4.5}$$

where,

$$A = \frac{\cos(\theta)^2}{2\sigma_M^2} + \frac{\sin(\theta)^2}{2\sigma_m^2} \,, \tag{4.6}$$

$$B = -\frac{\sin(2\theta)}{4\sigma_M^2} + \frac{\sin(2\theta)}{4\sigma_m^2} \,, \tag{4.7}$$

$$C = \frac{\sin(\theta)^2}{2\sigma_M^2} + \frac{\cos(\theta)^2}{2\sigma_m^2} \,, \tag{4.8}$$

where θ is the orientation of the major axis (clockwise from the y-axis), and $\sigma_M > \sigma_m$ are the major and minor $1/e^2$ beam variances such that the Gaussian mode-field diameter is $2w = 4\sigma$. The coordinate system is such that the output facet of the waveguide chip forms the x–y plane, with x and y corresponding to the horizontal and vertical direction respectively. The x–y coordinates are established by the effective pixel size of the images, given by the pixel size of the CCD and the magnification of the beam which is calibrated using a reference graticule imaged at the same wavelength as the measured mode.

For the comparison of two different modes we used the *mode overlap integral* to determine the theoretical coupling efficiency between, for example, a waveguide and a fibre mode. The mode overlap

is given by

$$O = \frac{|\iint E_1^*(x,y)E_2(x,y)dxdy|}{\iint |E_1(x,y)|^2 dxdy \iint |E_2(x,y)|^2 dxdy} \tag{4.9}$$

$$\approx \frac{\iint \sqrt{I_1(x,y)}\sqrt{I_2(x,y)}dxdy}{\iint I_1(x,y)dxdy \iint I_2(x,y)dxdy} \tag{4.10}$$

where E is the electric field and the approximation $E \approx \sqrt{I}$ is valid when the two modes have a constant phase profile, as is approximately the case at fibre-waveguide interfaces.

Spectra To record the spectra of light propagating in fibre optics and LW waveguides we used a spectrograph (*Andor Shamrock 750*) optimised for maximum fluence from the 0.22 NA input of a 1 m length of multimode fibre (MMF,*Thorlabs M42L01*) using an f = 40 mm singlet lens. Spectra were measured by coupling radiation into the MMF and filtering the pump wavelength (~405 nm) with a λ = 407 nm long-pass edge filter (*Semrock RazorEdge*), with further attenuation performed using neutral-density filters. The light input into the spectrograph was diffracted off an internal grating onto a single-photon sensitive EMCCD (*Andor Newton 970*) cooled to −70°C. The association of each camera pixel with wavelength was performed by calibrating with a mercury-argon source to ±0.1 nm resolution. Spectra were obtained by accumulating the signal over multiple frames, with each frame background corrected for residual light coupled into the spectrograph from light sources in the lab (for example, the computer monitor).

4.3 Investigation of laser-written waveguides supporting a blue wavelength single-mode

The development of LW waveguides for the guidance of single-modes at blue wavelengths is critical to the viability of the proposed concept in Chapter 2. We begin with an initial parameter scan of waveguide diameters spanning a large parameter space of the fabrication parameters as a preliminary check for blue single-moded guidance. We then further refine these parameters during a research trip to Macquarie university where the remaining fabricated devices presented in the chapter were developed.

4.3.1 Initial parameter scan

An initial parameter scan for testing LW waveguides with blue light was provided by Simon Gross at Macquarie University using the HPO. The same set of fabrication parameters were scanned over in two candidate materials, *Corning Eagle2000* and *Schott AF45*, of approximate length of 5 cm. Waveguides were fabricated for 14 different pulse energies from 20–70 nJ. Each pulse energy scan was fabricated at feedrates of 250, 500, 750, 1000, 1500, 2000 mm/min, yielding 84 waveguides per sample. Each

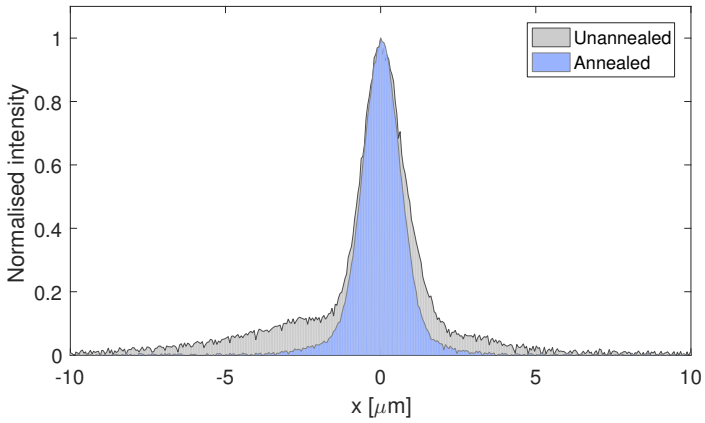

Figure 4.3: Mode profiles at λ = 404 nm of two waveguides fabricated at a feedrate of 750 mm/min in Corning Eagle2000. The unannealed waveguide is fabricated at a pulse energy of 35 nJ and the annealed waveguide is fabricated at a pulse energy of 40 nJ. The unannealed waveguide exhibits long tails in its mode profile while the annealed waveguide has a simpler mode profile. The unannealed waveguide fabricated at a pulse energy of 40 nJ was multimoded.

sample was cut in half, in the direction perpendicular to the waveguides, to yield two identical samples with waveguides of length ~2.5 cm. One sample of each material was then thermally annealed and all the samples were then ground and polished back to expose the waveguide end facets. The aim was to find single-moded guidance of blue light, the associated fabrication parameters, and whether thermal annealing improved propagation.

The samples were sent to the University of Bristol where they were initially tested at 404.3 nm using a *Toptica iBeam Smart* laser fixed at a constant output power of 100 mW to stabilise the spectrum. The laser power launched into the delivery fibre was controlled using two Glan-Taylor polarisers and a $\lambda/2$-waveplate. The power coupled into the waveguides was kept below 1 mW in case high power blue light modified the waveguides through photo-bleaching or colour-centre depletion, which we aimed to study after MFD testing.

Initial testing was performed using SM400 fibre due to its availability. MFDs were measured using a *DataRay WinCamD* beam profiler and a long working-distance 100x objective, separated by ~16 cm lens tube such that the beams were imaged at a magnification of 89.0×. Single-mode beam profiles, having MFDs with >99% overlap with SM400 ($2w$ = 2.1 μm), were found in both the annealed AF45 and Eagle2000. It was found that coupling into the non-annealed samples was both technically more difficult and had higher loss as evidenced by reduced intensities on the CCD, consistent with findings by Eaton et al. [152]. The mode profiles in the unannealed waveguides exhibited long tails, as shown in Figure 4.3, most likely due to the complex refractive index profile surrounding the guiding region. The finding of complex mode profiles for unannealed waveguides, along with the theoretically higher spectral purity of annealed waveguides led us to focus only on annealed waveguides going forward. A selection of measured beam profiles in the annealed Corning Eagle2000 sample is shown in Figure 4.4,

demonstrating the expected behaviour with waveguide diameter from weakly guided modes, through single-moded, to multi-moded waveguides with increasing pulse energy.

Currently, blue light is delivered to the trapped ions using PM405-XP fibre. Due to the added complications of using polarisation maintaining (PM) fibre, we chose to use the non-PM equivalent fibre of S405-XP which has the same MFD as PM405-XP and should make the transfer to PM fibre easier in the future. The MFD of S405-XP is larger than SM400, measured to be 2.8 μm along the major axis at λ = 404.3 nm. Measurements of the Schott AF45 confirmed from initial findings using SM400 that the waveguides had too high a refractive index contrast and the mode sizes were too small to efficiently couple to S405-XP. Corning Eagle2000 was therefore chosen as the material of choice due to its lower refractive index contrast and resulting larger mode sizes. Optimum waveguides for coupling to S405-XP were not found, however MFDs were found that were both bigger and smaller than the MFD of S405-XP and so it was concluded that we should perform a finer parameter scan around the found parameter range supporting single-moded guidance of blue light. It was identified that waveguide diameters between 4–10 μm (before annealing) exhibited blue single-moded guidance with the optimal pulse energy predicted to be ~40 nJ.

4.3.2 Fine parameter tuning

To begin the fine tuning of fabrication parameters we performed a scan of waveguides fabricated over a range of laser pulse energy around the identified 40 nJ pulse energy for blue single-mode guidance. Measurements of the waveguide diameters both confirmed the linear growth of waveguide diameter with pulse energy, and found that the cumulative heating threshold was at ~31 nJ for all tested feedrates (250–2000 mm/min). The cumulative heating threshold corresponds to waveguides with unannealed diameters of ~6 μm, as shown in Figure 4.5. The waveguides were then annealed, reducing their diameter to ~60% of their unannealed diameters. Waveguides fabricated at pulse energies <29 nJ were either not visible under TDIC, or large enough (>1 μm) to be reliably measured. The waveguide end facets were lapped and polished before testing with S405-XP fibre excited with 406 nm wavelength light.

An *Olympus MDPlan* 150× objective was used to expand the output beam profiles onto a *Pulnix TM-745* analogue camera. MFDs were calculated using *Spiricon LBA-PC* software, calibrated using a calibration graticule imaged at the excitation wavelength. Where MFDs were much larger than the fibre mode, significant coupling into the slab mode of the chip occurred and fitting of the beam profiles was sometimes not possible. The MFD of the S405-XP fibre was measured in the same way for mode overlap comparison with the measured waveguide modes. The results of these measurements for two different feedrates are shown in Figure 4.6a. The optimum waveguide parameters for coupling to S405-XP was a ~5.5 μm (annealed) diameter waveguide fabricated at a feedrate of 1000 mm/min,

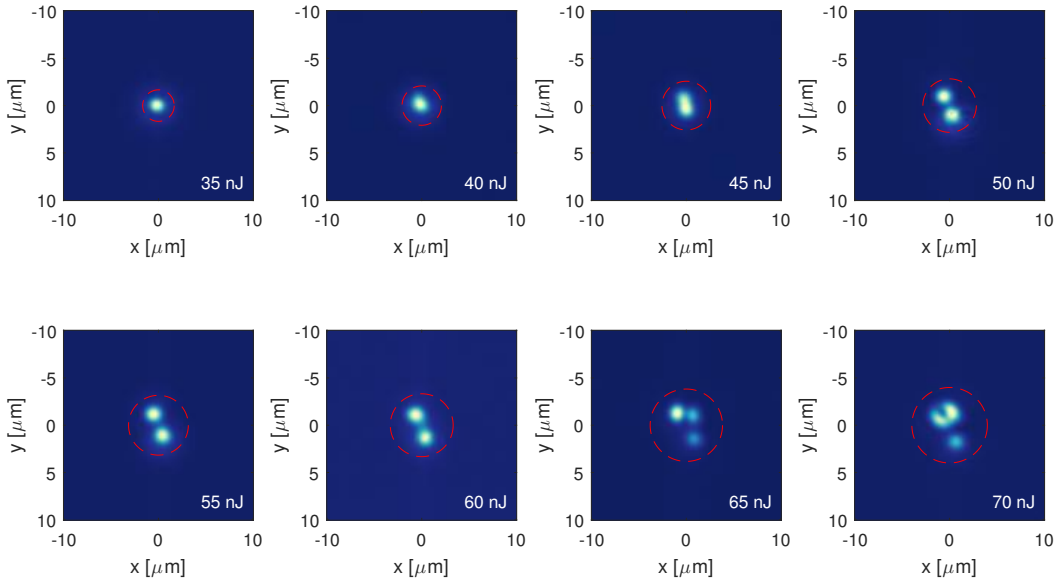

(a) 500 mm/min

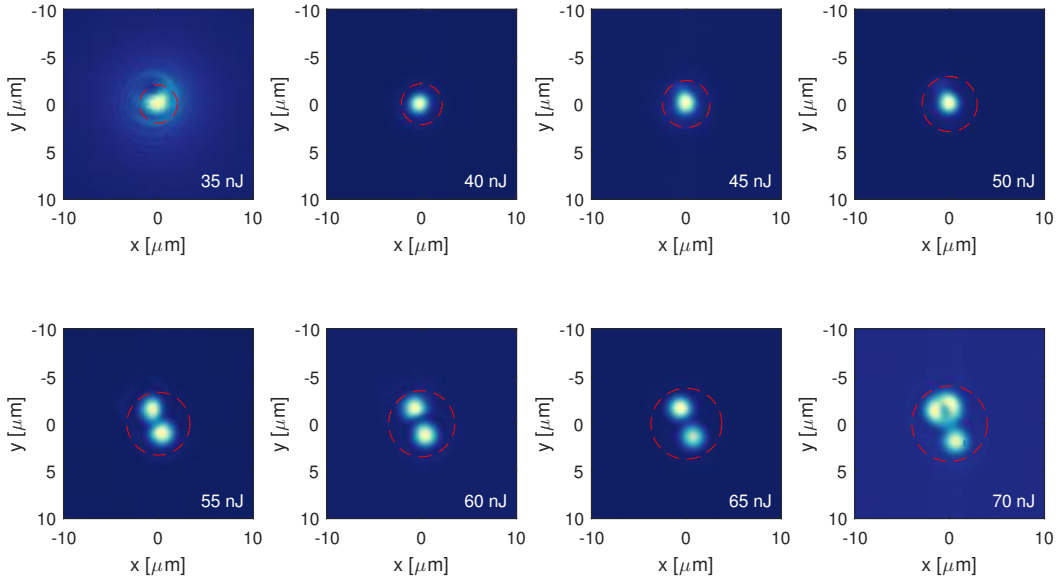

(b) 1000 mm/min

Figure 4.4: Mode profiles of annealed laser-written waveguides in Corning Eagle2000 glass excited with 404 nm wavelength light for two different feedrates. As the pulse energy (shown inset) is increased we see a transition from weakly guiding, to single-moded guidance, through to multi-moded guidance. It is evident that changing the feedrate changes the optimal pulse energy for single-moded guidance. The measured waveguide diameter is shown as red dashed lines, where the position of the mode in the waveguide core has been approximated.

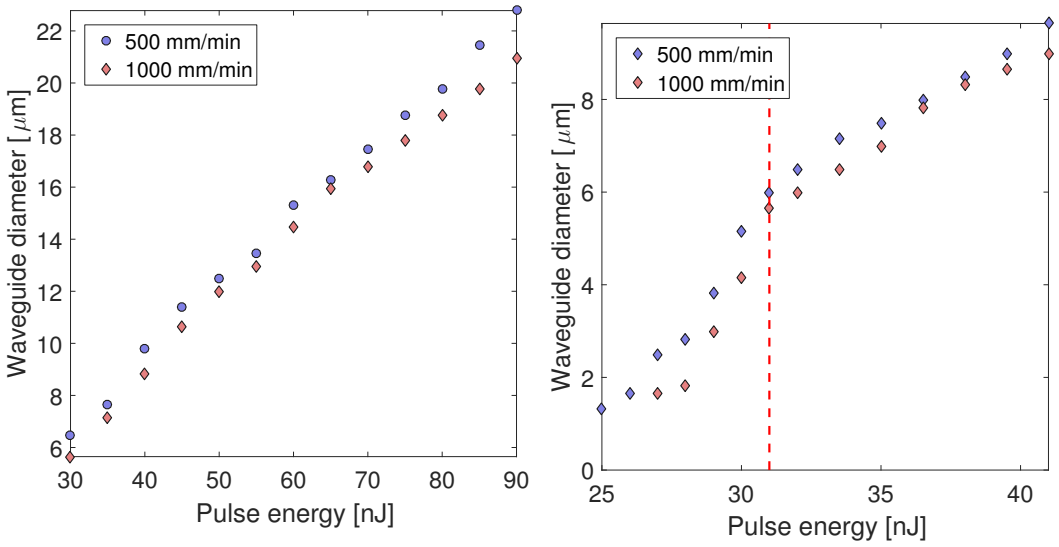

(a) Coarse scan of pulse energies for two different feedrates, demonstrating linear growth with pulse energy.

(b) Fine scan of pulse energies near the cumulative heating threshold (red dashed line).

Figure 4.5: Measured relationship between laser pulse energy and the resulting unannealed waveguide diameter for two different feedrates. For energies >31 nJ the trend is linear, as predicted by the cumulative heating growth model. For energies <31 nJ, energy fluence is not above the cumulative heating threshold and waveguide diameter dependence becomes non-linear. The red dashed line signifies the cumulative heating threshold.

having 99.9% mode overlap with the fibre mode. In practice, repeated fabrication of 5.5 μm diameter waveguides proved difficult due to variations in the HPO properties between calibration and fabrication. An example beam profile of a 5.15 μm diameter waveguide is shown in Figure 4.6b with comparison to the fibre mode, showing a 98% mode overlap. We considered mode overlaps of >90% suitable for our application and note that even with laser variations we were able to reliably fabricate waveguides with >95% mode overlap with S405-XP. With improved laser stabilisation it is expected that mode overlaps could be reliably tuned arbitrarily close to 100 % as shown by the demonstrated 99.9% mode overlap at a waveguide diameter of 5.5 μm.

For assessing the capability of the LW waveguides to guide UV wavelengths, beyond the blue wavelengths demonstrated here, one can note that the waveguide diameter of 5.5 μm corresponds to an unannealed diameter of ~9.2 μm which is comfortably above the cumulative heating threshold. There is latitude in this process to fabricate waveguides supporting a single-mode for a wavelength of ~350 nm where the optimum waveguide diameter as calculated by the Gaussian refractive index model would be ~4.5 μm, corresponding to an unannealed diameter of 7.5 μm - above the cumulative heating threshold. This is of interest to trapped Yb ions where the $S_{1/2} \rightarrow P_{1/2}$ transition has a wavelength of 369.5 nm [157], and Raman transitions are performed at wavelengths of ~355 nm. However, at these wavelengths Corning Eagle2000 has a non-negligible absorption [158] and so further studies of waveguide losses must be performed before making conclusions about its suitability.

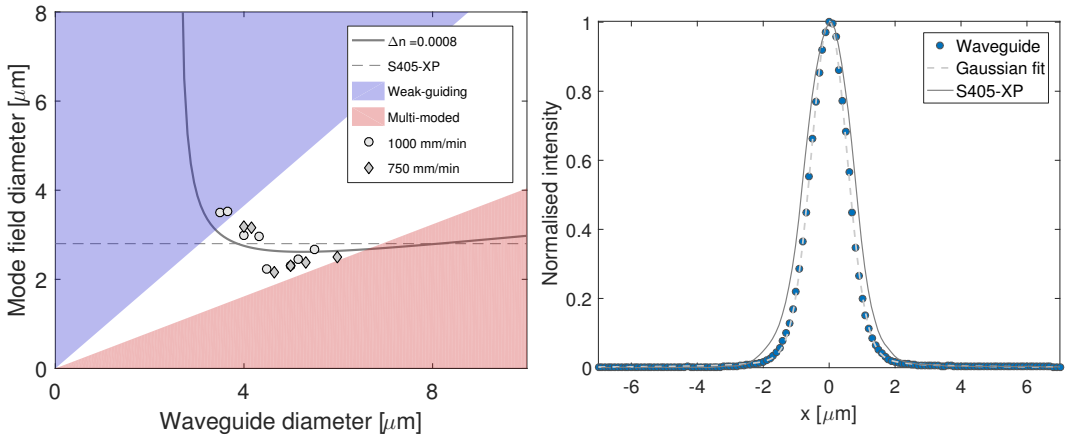

(a) **(b)**

Figure 4.6: (a) Measured mode-field diameter (MFD) of λ = 406 nm radiation with annealed waveguide diameter for feedrates of 750 mm/min and 1000 mm/min. Both the weakly guiding region (V<1.3) and the multimoded region are indicated (V>2.592) as shaded areas. The solid line is the Gaussian refractive index model with $\Delta n = 8 \times 10^{-4}$. The MFD of S405-XP is shown as a guide; (b) Measured profiles of S405-XP and a LW waveguide of diameter 5.15 μm with a mode overlap of 98%.

4.3.3 Low loss single-mode waveguides for blue wavelengths

Having optimised the fabrication parameters for the optimal coupling between S405-XP and LW waveguides we now measure the total transmission loss of the waveguides. Typical transmission loss measurements of LW waveguides involve the measurement of multiple waveguide lengths, which involves cutting and repolishing the waveguide chip several times. More detailed studies for optimising blue waveguide transmission would involve such a cut-back measurement however here we only attempt to provide an upper bound on the waveguide losses for direct comparison to state-of-the-art planar waveguides for blue wavelengths.

For a measurement of the total waveguide loss we use the set of waveguides fabricated with a feedrate of 1000 mm/min in the sample produced for fine parameter tuning and demonstrating the highest mode overlap with S405-XP. We characterise the transmitted power in the 5 waveguides in the optimal guiding regime, as indicated on Figure 4.6a(a), to find the optimal waveguide diameter for maximum transmission. Light of wavelength λ = 404 nm was delivered to each waveguide using S405-XP fibre with index matching gel on the fibre facet to reduce Fresnel losses. The transmitted radiation was collected using a multimode fibre (MMF) with a 50 μm core and index matching gel on the collection facet, the other end of which was coupled to a fibre power meter (*Thorlabs S151C*). Both the MMF and the S405-XP were mounted on 6-axis flexure stages (*Thorlabs Nanomax*) allowing for full optimisation of alignment to the waveguides. The fibres and waveguide chip were observed in plan view using a high magnification vision system displayed on a monitor, allowing for viewing of fibre positions and illuminated waveguides. Power calibration was performed by interfacing the S405-XP to the MMF both before and after the waveguide power measurements and measuring the

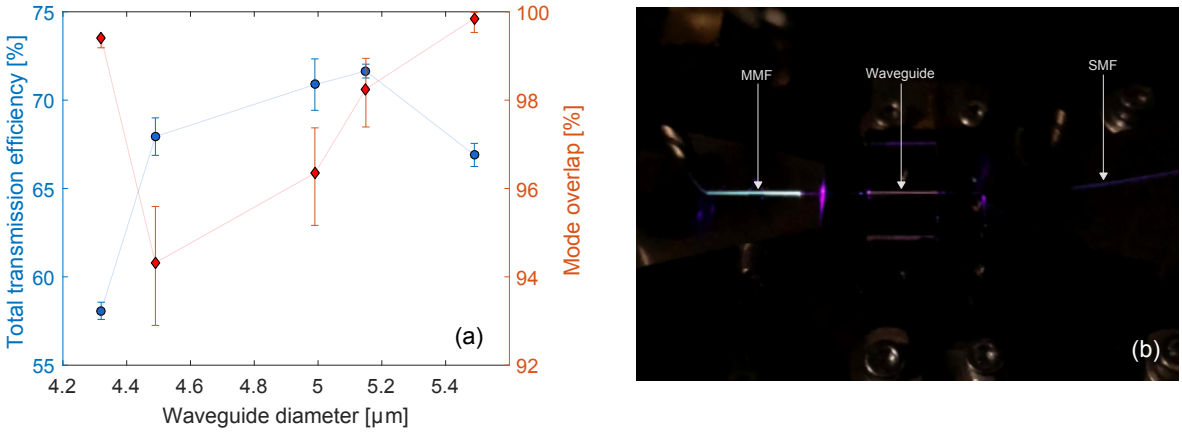

Figure 4.7: (a) Measured total transmission efficiency of 5 waveguides fabricated with a feedrate of 1000 mm/min (blue circles) and measured mode overlap of tested waveguides with S405-XP (red circles) for guidance; (b) Optical image of a waveguide illuminated with a single-mode fibre (SMF) and being collected into a multi-mode fibre (MMF). The contrast between the blue light being scattered in the SMF and MMF, and the red light being scattered in the waveguide can be clearly seen.

throughput power. We test the dependence of the power measurement with the location of the MMF fibre core by translating it both horizontally across the S405-XP core as well as along the optical axis away from the SMF, finding a 1σ power variation of 0.4% over the MMF horizontal core position with a steep reduction in power (5×10^4 in contrast) at the core edge. The equivalent error for the MMF position along the optical axis is 0.2% as long at the index matching gel of the two fibres touches; a step change in power when the index matching gel of the two fibre facets no longer touch is observed, with a contrast of ~7.

The S405-XP fibre yaw was coarsely aligned to the waveguide chip using the straight edge of the chip as a reference, with the starting pitch of flat as determined by a spirit level. Fibre to waveguide coupling was initially performed by observing the far-field image of the waveguide chip output facet on a screen. The MMF was then aligned to the waveguide output to provide feedback for coupling optimisation. All six degrees of freedom were used to optimise SMF-waveguide coupling and to assess repeatability and confidence in correct coupling each waveguide was coupled to three separate times after complete decoupling. For each optimised coupling 100 power measurements were taken, with each data point corresponding to 100 averages in software. The three separate coupling attempts were averaged and the error calculated as the standard deviation on the mean. Total transmission efficiencies, the combined coupling and propagation efficiency, were calculated as the ratio of the measured waveguide power to the SMF-MMF power. The measurement results are presented in Figure 4.7, demonstrating a dependence of total transmission efficiency with waveguide diameter. We find that the waveguide with the optimal overlap with S405-XP, with a diameter of 5.5 µm does not correspond to the maximum transmission efficiency, which occurs for a diameter of 5.15 µm. For decreasing diameter below the maximum, we find decreasing total transmission efficiency despite an

λ (nm)	**LW parameters**		**Diameter (μm)**		**MFD (μm)**		**MO (%)**	**T (dB/cm)**
	PE (nJ)	FR (mm/min)	UA	A	Major	Minor		
~405	~41	1000	9.2	5.5	2.7	2.6	99.9(0.3)	<1.97
~405	~40	1000	8.6	5.15	2.4	2.3	98.3(0.9)	<1.55

Table 4.1: A summary of two found fabrication recipes for single-mode guidance of blue wavelength radiation tested at wavelengths of 404–406 nm. List of abbreviations used in the table: PE, pulse energy; FR, feedrate; UA, unannealed; A, annealed; MFD, mode field diameter; MO, mode overlap (with single-mode fibre); T, transmission.

increase in the mode overlap for a diameter of 4.3 μm. This indicates that there exists an optimal V-number for minimising propagation losses, which does not necessarily correspond to the optimal mode overlap. Propagation losses evidentially play a much more critical role to device transmission than mode overlap, as the transmission efficiencies differ by 14% in two waveguides with mode overlap differences of <1%. The decrease in transmission for decreasing waveguide diameter indicates that there is a loss mechanism involved as the waveguide diameter approaches the weakly guiding regime, for which a full explanation would require further study. Visual observation of the waveguide when optimally coupled showed the waveguide isotropically emitting light that is predominantly red in colour. The presence of red light indicates that the dominant loss mechanism is material absorption and isotropic re-emission at longer wavelengths, referred to as photoluminescence (PL). The relative lack of blue light emitted isotropically from the waveguide indicates that scattering is not a dominant loss process. The PL is observed even when not coupled to a waveguide with the fibre emission propagating freely in the glass, indicating that the PL mechanism is a fundamental property of the material and not the laser writing process. An optical image of the waveguide chip under test is shown in Figure 4.7(b) attempting to faithfully represent the colours seen in the laboratory, with a clear chromatic distinction seen between the light propagating in the SMF/MMF and the waveguide.

To provide an upper bound on the minimum waveguide propagation losses we divide the measured transmission efficiency for the waveguide of 5.15 μm diameter by its measured mode overlap with S405-XP. We find a transmission of 72.9% corresponding to a loss of 27.1%, which provides an upper bound on the propagation loss of <1.55 dB/cm as the waveguide is 0.882 cm long. This number is comparable to the state-of-the-art planar waveguide propagation loss of 1.23 – 1.61 dB/cm in aluminium nitride for λ = 405 nm [83]. More thorough cut-back measurements would be able to improve on our quoted upper bound, eliminating any coupling inefficiencies. It is likely that the loss could be further reduced by optimising the fabrication parameters as we have only considered one feedrate value, providing a wide parameter space to explore. Ideally, a parameter set would be found that both maximised propagation transmission and mode overlap simultaneously. The two found parameter sets found for the highest mode overlap and lowest propagation loss are summarised in Table 4.1.

4.3.4 Spectral response of laser-written waveguides at blue wavelength excitation

The visual observation of red luminescence from the waveguides under excitation with blue light observed during the loss measurements implies that some spectral conversions are occuring within the glass. The laser writing process injects a large amount of energy into the glass matrix within the waveguide formation region and it is possible that the resulting material modifications occuring during this process lead to undesired changes to the spectral response of the glass [159]. For the addressing of trapped ions in particular, the spectral purity of the delivered laser wavelengths is important so as not to cause undesired coupling to other energy levels in the atomic system. Despite this, we know of no previous reports on studies of the spectral purity of laser light delivered to trapped ions via fibre optics. Numerous spectral shifts occur when light propagates in dielectric materials including Raman scattering and photoluminescence (PL). Raman scattering is the interaction of the excitation light with the vibrational and rotational energy levels of the molecules present in the material and is independent of the excitation wavelength. The Raman shift is referred to as Stokes (anti-Stokes) if the frequency shift on the re-emitted photon is negative (positive). PL is the absorption of the excitation wavelength and remission at longer wavelengths, typically due to phononic relaxation with the host lattice.

There have been numerous studies on the spectral response of glasses after modification of femtosecond lasers as a measurement for determining the structural changes induced by the laser radiation. A typical Stokes Raman spectra of pristine fused silica is shown in Figure 4.8(a) where D_1 and D_2 correspond to four and three ring structures in SiO_2 respectively. The ratio of the relative intensities of D_1 and D_2 has been used to determine that bond breaking of four ring structures to form three ring structures occurs during LW fabrication [160, 161]. The dominant contribution to PL in LW waveguides is the formation of non-bridging oxygen hole centres (NBOHC) in fused silica due to bond-breaking which can significantly increase PL intensity over pristine fused silica for high femtosecond pulse energies [162]; the PL increase is typically at red wavelengths as shown in Figure 4.8(b). Bond-breaking in multi-component glasses can lead to similar defects and more complex PL spectra which is of importance to our glass of choice, Corning Eagle2000, which we know of no detailed studies of its spectral response after thermal annealing which may heal NBOHC and other color-centres.

In an attempt to briefly study these effects for LW waveguides in Corning Eagle2000, we first measured a reference spectrum of 1 metre of S405-XP coupled into 2 metres of a 50 μm core MMF, excited with λ = 404.3 nm light. As shown in Figure 4.8(b) the Stokes Raman spectrum exhibits the typical peaks associated with glass, slightly shifted from those of fused silica which is most likely due to the presence of other material components in the fibre cladding. The PL spectrum shown in

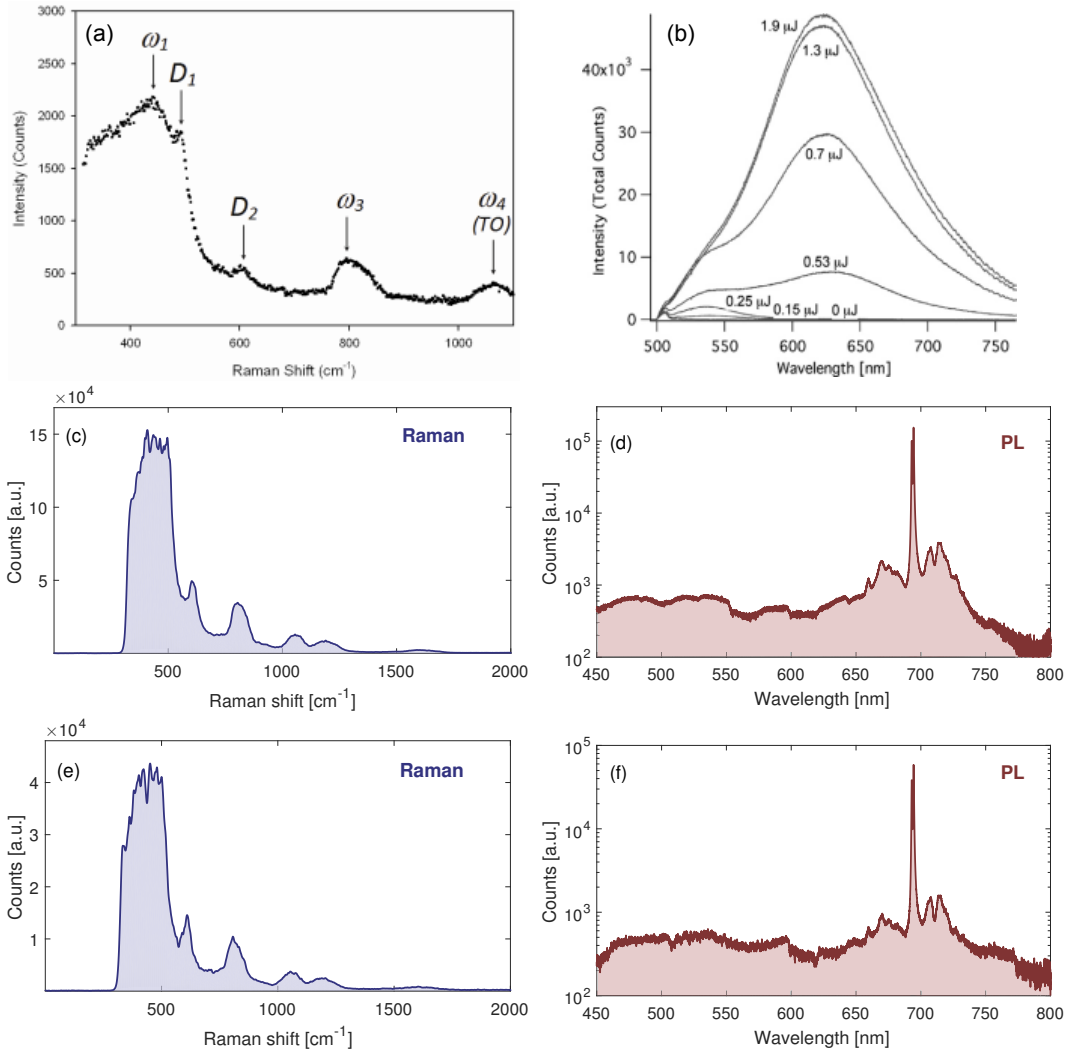

Figure 4.8: (a) Typical Raman spectrum of prinstine fused silica, image from [160]; (b) Change in PL spectrum of fused silica for increase femtosecond pule energy in the modification region, image from [162]; Spectral response of (c-d) S405-XP and MMF fibre and (c-d) S405-XP, LW waveguide and MMF fibre to λ = 404.3 nm radiation. The reduced counts when the waveguide chip is included is due to propagation and coupling loss into the waveguide.

Figure 4.8(c) shows broad emission from 450–800 nm with sharp peaks at 693 nm and 694 nm. After recording the reference spectrum, a thermally annealed, ~2.5 cm long, LW waveguide of 5.15 µm diameter, was placed between the S405-XP and MMF and the measured spectra is shown in Figure 4.8(c-d) for direct comparison with the reference spectra of the fibres. We found slight shifts in the measured wavenumber peaks of the Raman spectrum due to the addition of a different glass composition in the beam path, however no additional peaks are present. The wavelength peaks in the PL spectrum are identical to the reference case indicating no significant color-centre numbers have been created during the laser-writing process, however we cannot rule out broad, weak emission from NBOHC or other color-centres below the signal of the fibre PL. Due to the reduction in power from the waveguide coupling it is difficult to draw firm conclusions about the relative change in the PL power as

the MMF is excited with a lower pump power and therefore its spectrum contributions will be reduced. Further study would require precise calibration of the S405-XP and MMF's spectral contribution with power to allow for precise conclusions about the spectral contributions of LW waveguides in order to rule out the possibility of increased, broadband PL over visible wavelengths. However, we can conclude that we do not see significantly increased PL in LW waveguides over fibre optics, and as fibre spectral shifts is an effect not taken into account during precision quantum optics experiments with trapped ions we do not expect the addition of a short length of LW waveguide to have a detrimental effect.

4.4 Fabrication of waveguides for single-mode guidance of near-IR wavelengths

Motivated by the desire to guide a single-mode of 1033 nm and 1092 nm wavelength radiation close to the ion trap for interacting with $^{88}Sr^{+}$ we develop a fabrication recipe for single-mode guidance of λ = 976 nm. The test wavelength was chosen due to its ease of availability at Macquarie University and was deemed close enough to the target wavelengths to provide a suitable recipe. We opted to optimise the mode overlap with 1060XP single-mode fibre due to its low attenuation losses and large MFDs in comparison to the alternative of 980HP. We measured the major MFD of 1060XP to be 5.75 μm at the test wavelength, consistent with the manufacturer's quoted MFD of 5.9 ± 0.5 μm at λ = 980 nm.

During the same fabrication run as for the blue fine tuning chip we fabricated two sets of waveguides designed for near-IR guidance. One set contained waveguides written with pulse energies 49–62 nJ at a feedrate of 250 mm/min and the other set has waveguides written with pulse energies of 38–53 nJ at a feedrate of 500 mm/min. The results of MFD measurements of the resulting waveguides excited with λ = 976 nm radiation is shown in Figure 4.9(a), demonstrating consistency with the Gaussian refractive index model with a refractive index contrast of $\Delta n \approx 1.1 \times 10^{-3}$. The model predicts robust high mode overlap with 1060XP for annealed waveguide diameters of 8–12 μm, leading to the later measurement of a 10.5 μm diameter waveguide in a later sample with 99.6% mode overlap with 1060XP, as shown in Figure 4.9b. We know from loss measurements of blue waveguides that while the mode overlap is high, this does not necessarily correspond to maximum waveguide transmission. Further study would explore the optimal waveguide diameters for low loss waveguides for near-IR guidance, attempting to approach previously reported numbers of 0.32 dB/cm for λ = 1550 nm [135]. The found optimal LW waveguide fabrication recipe for high overlap of near-IR wavelengths in single-mode fibre is summarised in Table 4.2.

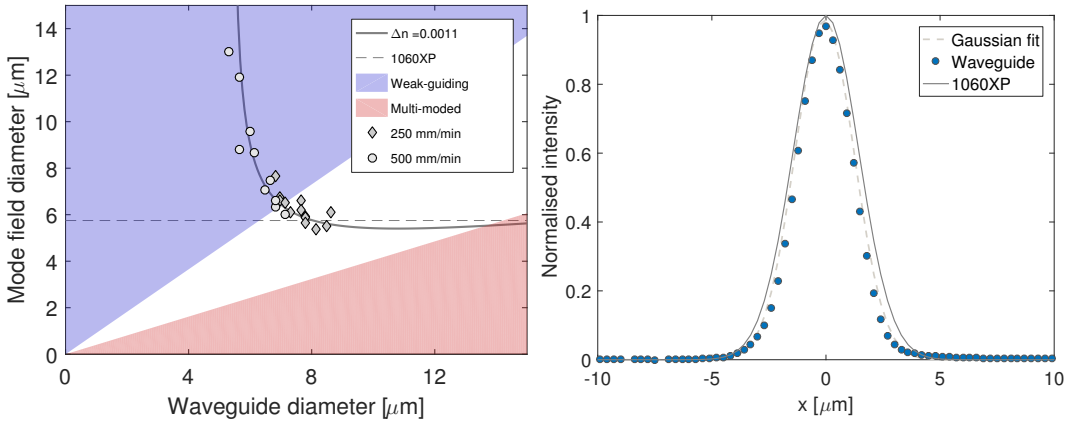

(a) **(b)**

Figure 4.9: (a) Measured mode-field diameter (MFD) of λ = 976 nm radiation with annealed waveguide diameter for feedrates of 250 mm/min and 500 mm/min. Both the weakly guiding region (V<1.3) and the multimoded region are indicated (V>2.592) as shaded areas. The solid line is the Gaussian refractive index model with $\Delta n = 1.1 \times 10^{-3}$. The MFD of 1060XP is shown as a guide; (b) Measured profiles of 1060XP fibre and a LW waveguide of diameter 10.5 μm (feedrate of 500 mm/min) with a mode overlap of 99.6%.

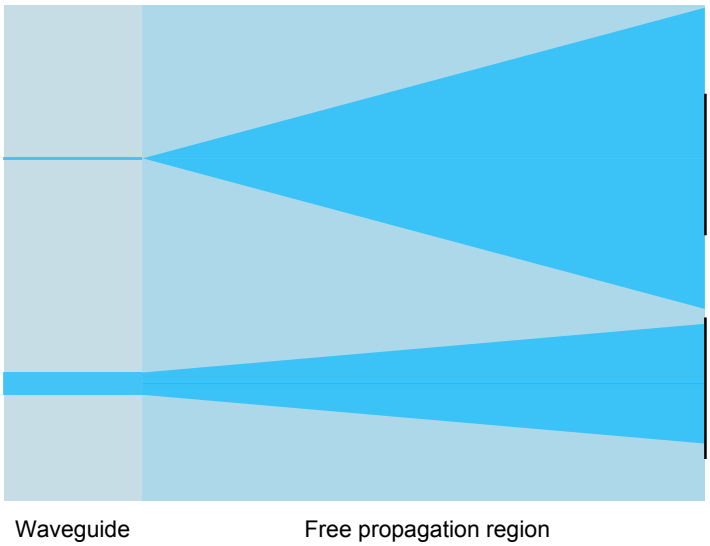

Figure 4.10: Illustration of the effect of increasing the MFD of waveguide mode on the expansion rate of the light freely propagating from the waveguide output to a lens plane. Increasing the MFD causes the beam to expand slower and therefore can enable smaller beam diameters at the lens plane which allows for the underfilling of smaller lens diameters (shown in black).

4.5 Mode expansion

In the proposed concept for coupling light to and from trapped ions using LW waveguide and diffractive optics there is a free propagation zone between the end facet of the waveguide and the microlens plane. Within this free propagation region, for addressing beams, light exiting the waveguide expands rapidly due to diffraction as the mode diameter of the waveguide is an effective pinhole. As illustrated in Figure 4.10, increasing the size of the MFD, and therefore the pinhole, reduces the expansion rate and therefore the size of the beam when it reaches the lens plane. Smaller beams at the lens plane allow for smaller lenses for fully capturing all the incident light and therefore a higher density of lenses can be used. Having developed waveguides for efficient SMF coupling to single-mode waveguides at blue and near-IR wavelengths, the aim is now to expand the modes over the length of the waveguide such that at the output they expand slower in the free propagation zone. We aim to design mode expansion tapers such that we can use diffractive optic radii of 50 μm in the microlens array, allowing for compact optical layouts. For a waveguide output to microlens distance of 1 mm we find that waveguide MFDs must approximately double from their fibre-matched MFD such that the beam radius in the lens plane is 2/3 of the desired lens radius so as to minimise scattered light. Our task in this section in then to find a technique for doubling the MFD of the fibre-matched waveguides.

4.5.1 Power tapers

When optimising waveguide diameters for coupling to single-mode fibre, we varied both the pulse energy and the feedrate of the laser-writing process to control the waveguide MFD. In Figure 4.6a it is shown that the Gaussian refractive index model provides two avenues for increase MFDs for a fixed feedrate. Reducing the waveguide diameter rapidly expands the MFD when in the weakly-guiding regime. Increasing the waveguide diameter slowly increases the MFD in the multi-moded regime. Therefore, by continuously changing the diameter of the waveguide over the sample length we can transition between two different MFDs. We begin by investigating the case where we reduce the diameter of the waveguide, which we refer to as down-tapers.

λ (nm)	**LW parameters**		**Diameter (μm)**		**MFD (μm)**		**MO (%)**
	PE (nJ)	FR (mm/min)	UA	A	Major	Minor	
976	~ 80	500	18	10.5	5.69	4.68	99.6

Table 4.2: A summary of fabrication parameters for single-mode guidance of near-IR wavelength radiation tested at a wavelength of 976 nm for high mode overlap with 1060XP fibre. List of abbreviations used in the table: PE, pulse energy; FR, feedrate; UA, unannealed; A, annealed; MFD, mode field diameter; MO, mode overlap (with single-mode fibre).

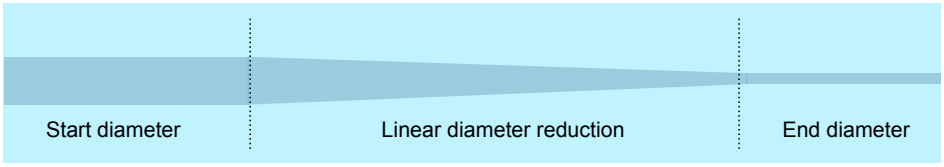

Figure 4.11: A schematic of a down-tapered waveguide where the start diameter is larger than the end diameter, with a linearly decreasing region connecting the beginning and end sections.

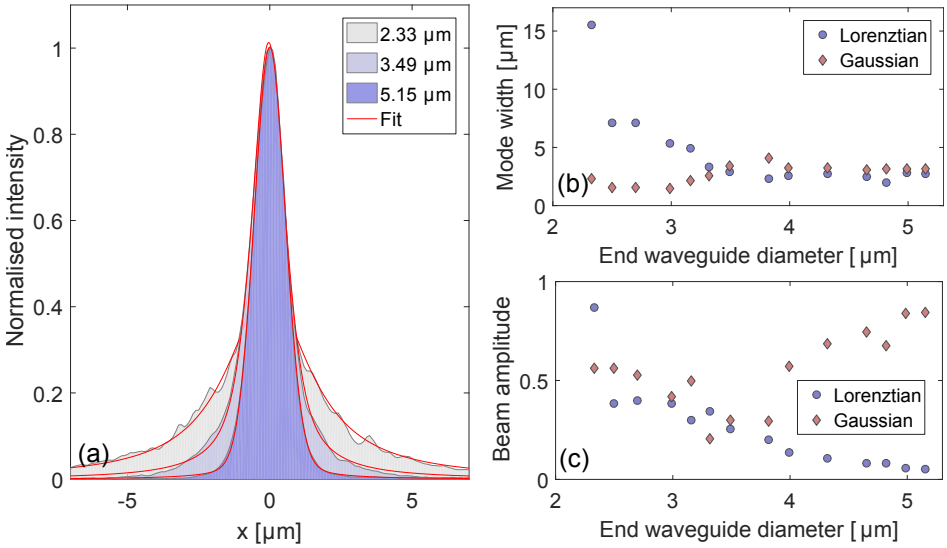

Figure 4.12: (a) Mode profile cross-sections of three waveguides at λ = 406 nm with end diameters of 5.15 µm (untapered), 3.49 µm and 2.33 µm. Lorentzian-Gaussian fits are incuded in red for each profile. (b) Mode widths of measured down-tapers where the plotted values are $4\sigma_L$ and $4\sigma_G$ for the Lorentzian and Gaussian components respectively. (b) Amplitudes, A_L and A_G of the fits to the down-tapered mode profiles.

Down-tapers

The prediction of the Gaussian refractive index model is that MFD should increase rapidly with decreasing waveguide diameter when in the weakly guiding regime. We therefore begin with tapering to smaller waveguide diameters along the length of the waveguide chip (see Figure 4.11). The drawback to the rapid MFD growth is a high sensitivity to variations in the exact pulse energy of the fabrication laser, as well as the previously measured increase in propagation loss.

To investigate down-tapers at blue wavelengths, we fabricated three sets of 20 waveguides. Within each set, the design end (unannealed) diameter of the waveguides were varied from 9.2 µm to 3 µm, where 9.2 µm was the waveguide start diameter. As these range of diameters went below the cumulative heating threshold, we calibrated the pulse energy-diameter relationship using linear interpolation. Each set had a different taper length of 4, 6 and 8 mm over which the pulse energy is linearly decreased from its start value to the design end value corresponding with the required diameter. After fabrication the sample is thermally annealed, lapped and polished.

The waveguide tapers were tested with 406 nm wavelength radiation and imaged onto a *Pulnix*

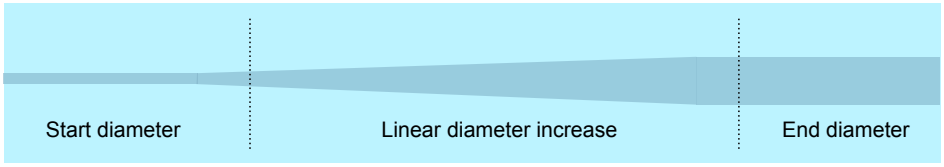

Figure 4.13: A schematic of a up-tapered waveguide where the end diameter is larger than the start diameter, with a linearly increasing region connecting the beginning and end sections.

TM-745 camera with a 150x objective. It was found that mode expansion occurs through Lorentzian broadening of the beam profile, with excess power in the profile wings increasing with decreasing waveguide diameter. For end diameters $\lesssim$2 μm, waveguide modes could not be faithfully imaged due to excess background scatter. Cross-sections of an example set of down-tapered waveguide modes is shown in Figure 4.12. We model the change in mode profile by a linear superposition of Lorentzian and Gaussian profiles

$$I(x) = A_L \frac{\sigma_L}{(x - x_0)^2 + \left(\frac{\sigma_L}{2}\right)^2} + A_G \exp\left(\frac{-2(x - x_0)^2}{\sigma_G^2}\right), \tag{4.11}$$

where σ_L and σ_G are the variances of the Lorentzian and Gaussian profiles respectively. Fitting Equation 4.11 to the beam profiles in Figure 4.12 we find that σ_L increases for decreasing waveguide diameter, whereas σ_G remains approximately constant, with consistent behaviour found for all three taper lengths investigated. The purely Lorentzian expansion of the waveguide mode profile excludes the use of down-tapers for our application as we wish to preserve Gaussian mode shapes, we therefore move onto tapers fabricated by increasing, rather than decreasing, the end diameter.

Up-tapers

The concept of increasing waveguide diameters to increase MFDs is well established in planar waveguides, routinely used to match fibre modes to smaller waveguide modes. Here, we investigate the limits of up-tapering in laser-written waveguides (see Figure 4.13). As the waveguide diameter expansion extends into the multi-moded regime of guidance, the tapers must expand slowly enough that only the fundamental mode is excited. The conditions for adiabicity are that the waveguide must not expand faster in diameter than the waveguide would expand if freely propagating in the glass from a terminated waveguide [163].

Waveguide test sets were fabricated for both 406 nm and 976 nm wavelengths, with three sets per wavelength. Each set of 7 waveguides with varying end diameter had a different taper length, with lengths taking the values 1, 2 and 8 mm. Unfortunately, during fabrication the HPO suffered an extreme change in properties between calibration and writing and waveguide diameters were ~75% of their design after annealing however conclusions can still be drawn from optical testing of the tapers. Blue waveguides had starting waveguide diameters of 4 μm and end diameters in the range

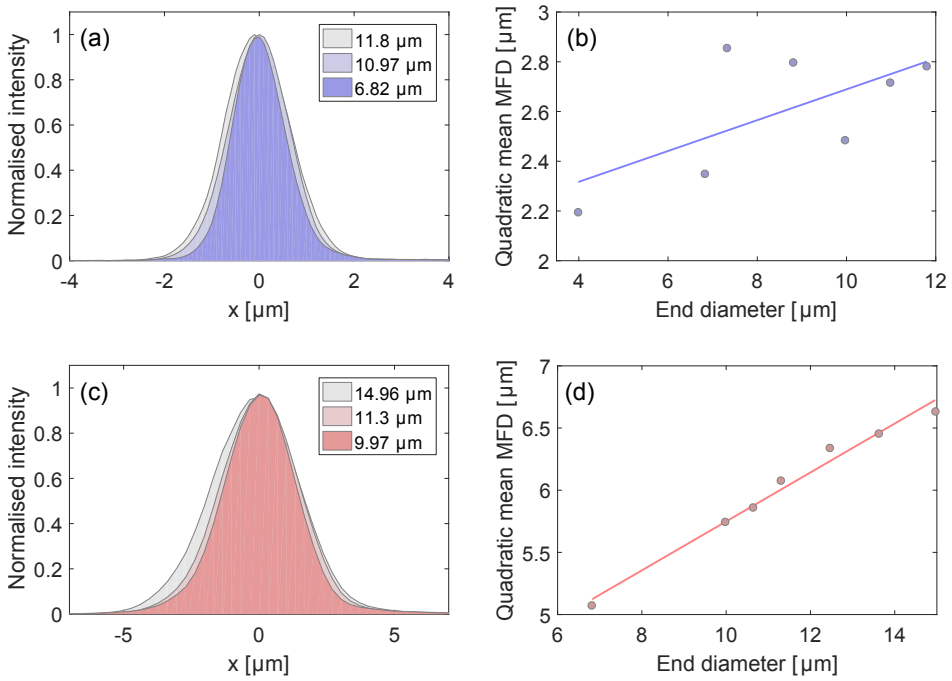

Figure 4.14: (a) Mode profile cross-sections of λ = 406 nm light in up-tapered waveguides with end diameters of 6.82 µm, 10.97µm and 11.80 µm; (b) The quadratic mean MFD as a function of end diameter for λ = 406 nm, with a linear fit; (c) Mode profile cross-sections of λ = 976 nm light in up-tapered waveguides with end diameters of 9.97 µm (untapered), 11.30µm and 14.96 µm; (d) The quadratic mean MFD as a function of end diameter for λ = 976 nm, with a linear fit.

4–11.5 µm. Near-IR waveguides had starting waveguide diameters of ~7 µm and end diameters in the range 7–15 µm. The waveguide chip was lapped and polished before testing.

Up-tapers tested at λ = 406 nm were found to have higher-order mode profiles, and were therefore non-adiabatic, at taper lengths of 1 and 2 mm, while fundamental modes were observed and measured for a taper length of 8 mm, with MFD approximately linearly increasing with end waveguide diameter. A plot of the quadratic mean MFD with end diameter is shown in Figure 4.14(b). Deviations from a linear fit are thought to be due to imperfect adiabatic transfer of the fundamental mode, leading to mixing with higher order modes and stretching the MFD. It is unclear why an 8 mm long taper is non-adiabatic as theoretically a 1 mm taper length should suffice for the MFD expansion demonstrated, and further study for this discrepancy would be required if up-tapers were to be pursued further. For a wavelength of 976 nm adiabatic mode expansion was observed in all taper lengths, with MFD increasing linearly with the end waveguide diameter with good agreement to a linear fit of the quadratic mean MFD.

Linear fits of the MFD expansion with end diameter predict 2× mode expansion would be achieved at waveguide diameters of 60 µm, corresponding to unannealed waveguide diameters of 100 µm. The limit of waveguide diameters using the HPO in Corning Eagle2000 glass is approximately 30 µm after annealing, and therefore our required 2× MFD expansion is not achievable using simple up-tapers and so we investigated the use of multi-core structures for fabricating the required waveguide diameters.

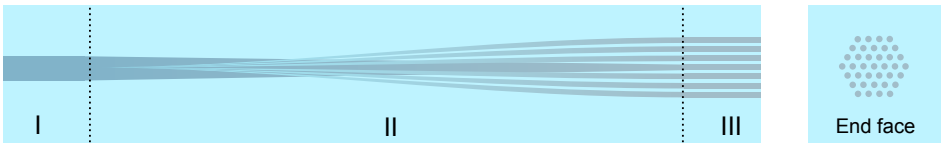

Figure 4.15: Single-to-multi core waveguide taper concept, composed of 3 regions. Region I is a single-mode waveguide optimised for coupling to SMF; region II contains multiple waveguide fabricated as cosine curves from the centre of the region I waveguide to their position in the hexagonal lattice in region 3; region 3 is a large mode area waveguide composed of individual waveguides with an effective refractive index profile that supports a fundamental Gaussian mode.

4.5.2 Single-to-multi core tapers

After demonstrating that Gaussian mode expansion was possible by adiabatically increasing the waveguide diameter, the next step is to find a technique for finding a way to fabricate large diameter, laser-written structures in glass. Hexagonal bundles of individual waveguides for guiding a large, single-modes have previously been demonstrated [164–166], with the resulting structures called large-mode area (LMA) waveguides. Other applications of such evanesecetly coupled structures investigate propagation of modes between the individual waveguides [167]. While LMA waveguides have been previously reported, we are unaware of demonstrations of the adiabatic transfer of single-mode waveguides to LMA structures. The demonstration of LMA structures for guidance of blue light has also not been shown, where tighter tolerances will be placed on fabrication due to the short wavelength of blue radiation.

We propose a single-to-multi-core (SMC) taper concept (see Figure 4.15), that adiabatically transfers between a single core waveguide NA-matched to a single mode fibre (region I), and a large-mode area (LMA) structure composed of a hexagonal array of individual *sub-waveguides* (region III). The end diameter and lattice spacing of the sub-waveguides in the hexagonal array is tailored such that the LMA structure supports a TEM_{00} mode. While the LMA structure can support multiple modes, if the transfer is performed adiabatically only the fundamental mode is excited, as with previously demonstrated up-tapers. The taper (region II) is created by fanning out waveguides from the centre of the fibre-coupled waveguide to their end position on the hexagonal array; the fibre-coupled waveguide is simultaneously tapered in diameter to match the end diameter of the outer waveguides. To prevent excess modification at the start of the taper, the start pulse energy of the taper waveguides must be optimised. As we fabricate waveguides in the cumulative heating regime, modifications must be made above the cumulative heating threshold otherwise they are erased by the annealing process. To explore the viability of LMA structures for creating uniform Gaussian beams we begin by demonstrating the LMA concept with numerical simulations. We then explore the fabrication of SMC tapers in two different fabrication regimes.

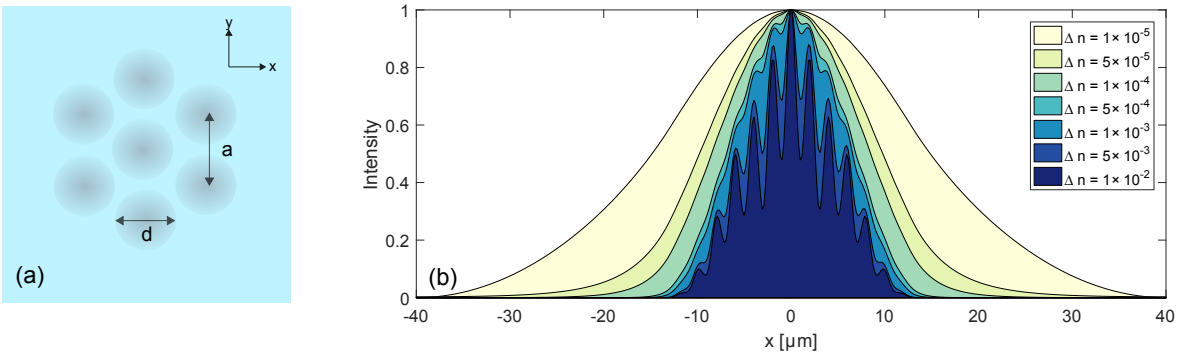

Figure 4.16: (a) The simulation geometry of an hexagonal array of individual Gaussian refractive index profile waveguides (darker colour indicates increased refractive index) of diameter d and lattice spacing a; (b) Cross-section at y=0 of supported fundamental modes in the LMA structure for a range of refractive index contrasts, Δn. A full range of behaviour can be seen from weakly guiding to individual guiding of each waveguide.

Simulation

LMA structures are simulated in *Lumerical MODE* at a wavelength of 405 nm. The LMA is composed of a hexagonal array of waveguides (see Figure 4.16(a)) with diameter d, lattice constant a and with Gaussian refractive index profiles of maximum contrast of Δn. After preparing a suitable geometry, modes are found using the *Eigenmode Solver*, and in all cases, the fundamental mode of the structure is found. Higher-order modes are found for the large structures, however as we are interested in adiabatic excitation of the fundamental mode we do not analyse them further. The fundamental modes of a 25 μm diameter hexagonal array of a=d=2 μm individual waveguides are shown in Figure 4.16(b) for varying values of Δn of the individual waveguides. It can be seen that for weak enough guidance of the sub-waveguides ($\Delta n \leqslant 5 \times 10^{-4}$), an effective large Gaussian profile is supported in the LMA waveguide. If the refractive index contrast is too high, individual guiding of the waveguides is exhibited, distorting the beam profile. However, a balance must be found, and as with for single waveguides we see an increase in Lorentzian wings in the beam profile for too weak a refractive index contrast (Δn=1×10^{-5}).

Fabrication

SMC tapers were fabricated as sets of individual waveguides, with full passes of the entire waveguide chip performed for each individual waveguide. The central waveguide was written as a normal power taper waveguide, from the start diameter to the end diameter of the sub-waveguides in the hexagonal array. Array waveguides were written as cosine bends from the taper start position to their final position on the waveguide array. We aimed to fabricate the structures from bottom to top in order to prevent distortion of the laser focus during writing by already written waveguides. The starting pulse energy of the array waveguides was optimised during the study, but we begun by investigating

waveguide starting pulse energies of 0 nJ to avoid the repeated deposition of laser energy at the same position in the glass.

Results

Ideally the number of individual waveguides in each taper would be as small as possible and therefore we initially tested SMC tapers in the strongly-guiding regime. In this regime the constituent waveguides are all up-tapers, with end diameters of the sub-waveguides greater than the diameter in region I. From simulations we do not expect this to produce simple Gaussian modes as it is in the strong refractive index contrast regime, however we seek to confirm this experimentally.

Strongly guiding waveguides We fabricated SMC tapers with seven end sub-waveguides (a central waveguides and six surrounding waveguides) in a hexagonal arrangement. Using taper lengths of 6 mm we fabricated sets of SMC tapers where between sets we varied the lattice constant of the hexagonal array and within the sets we varied the end diameter of the individual waveguides. Lattice constants take the values 10, 20 and 30 μm, while end (unannealed) diameters were varied from the region I diameter (9.2 μm for blue, 17 μm for near-IR) to 35 μm. The region I diameter was chosen to be optimal for fibre coupling blue or near-IR modes respectively. After fabrication, the maximum LMA end diameters were found to be ~68 μm after annealing. End facet views of a selection of near-IR structures are shown in Figure 4.17, showing a variation from fully separated to overlapping LMA structures as the individual waveguide diameter is increased.

Excitation of the tapers at λ=406 nm found that only the central waveguide in the hexagonal array was coupled to for all parameters, confirming that these structures do not act like LMA structures in this regime. This behaviour was replicated for 976 nm radiation at 20 μm and 30 μm lattice constants, however coupling into surrounding waveguides was observed for a lattice constant of 10 μm and small waveguide diameters (as shown in Figure 4.17). The experimental confirmation that strongly guiding sub-waveguide LMA structures do not support large Gaussian modes leads us to abandon their use for our application. We now move onto the theoretically predicted optimal case, where a large number of weakly guiding waveguides form the LMA structure.

Weakly guiding waveguides In the weakly-guiding regime the sub-waveguides are smaller, and therefore to make suitably large structures many more waveguides must be written. As each waveguide takes approximately 1 second to write, the limit on the size of structures that can be written is fabrication time, with the risk that laser parameters will drift during the waveguide writing.

We fabricated SMC tapers with a design LMA diameter of 25 μm. Three sets of SMC tapers were fabricated for blue wavelength radiation. Within each set, the lattice constant was varied from 1 to 5 μm over four structures. Between sets, the end individual waveguide diameter was varied from

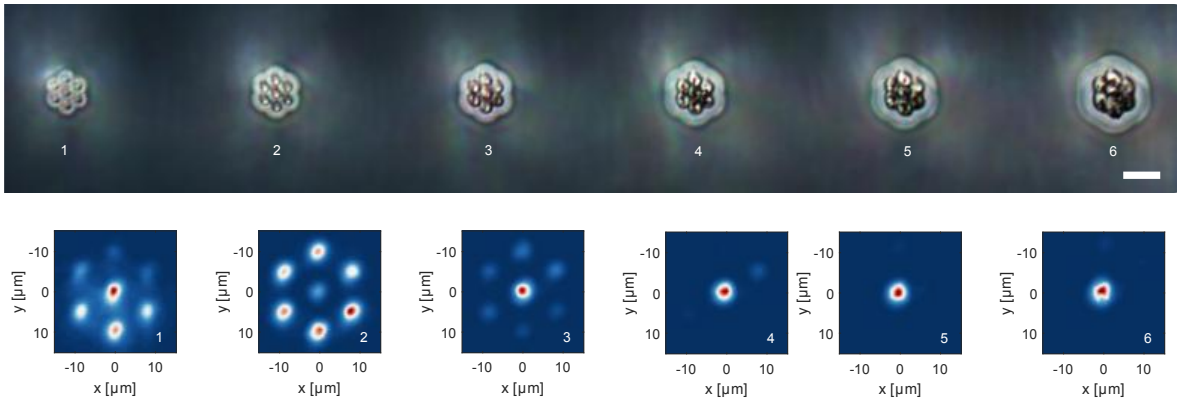

Figure 4.17: Strongly confining waveguide SMC tapers designed for λ=976 nm. (Top) A TDIC image of the unannealed end facets, the scale bar is 50 µm. The waveguide diameter is increasing with labelled number. (b) Mode profiles of the fabricated structures under excitation with λ=976 nm demonstrating a range of modes from all individual waveguides coupled to only the central waveguide coupled. Distortion of the mode is evident in structure 6 due to the overlapping of the written individual waveguides.

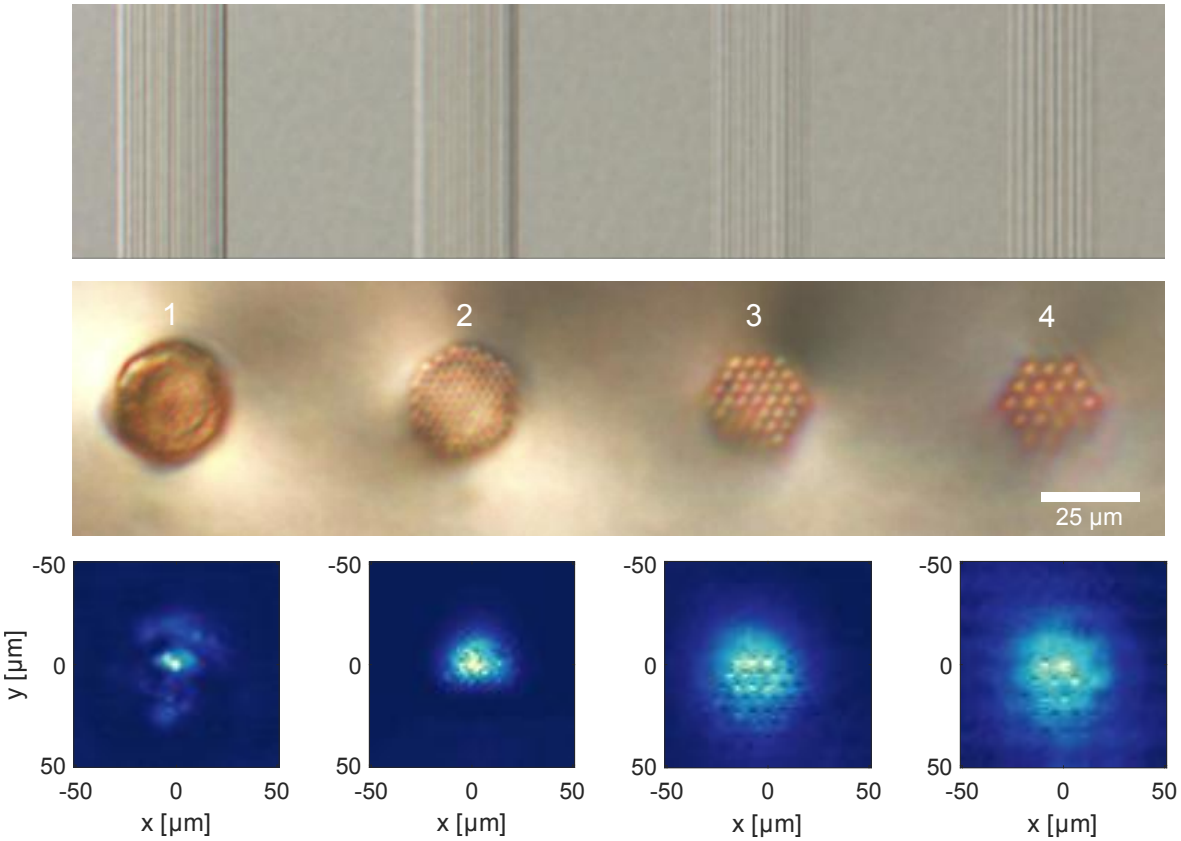

Figure 4.18: A set of weakly guiding mode-expansion tapers with lattice constants of: (1) 1.0 µm, (2) 2.3 µm, (3) 3.7 µm, (4) 5.0 µm; (Top) Plan view TDIC image of unannealed LMA structures. Strong refractive index changes can be seen on the edges of structure 2 with a fairly flat refractive index profile over its width. (Middle) End facet views of the unannealed structures, damage at the bottom of the structures is evident, along with the effect of changing the lattice spacing. (Bottom) Beam profiles for a wavelength of 406 nm demonstrating multimoded to weakly guiding behaviour. Beam profiles are centred on their maxima and not on the LMA centre.

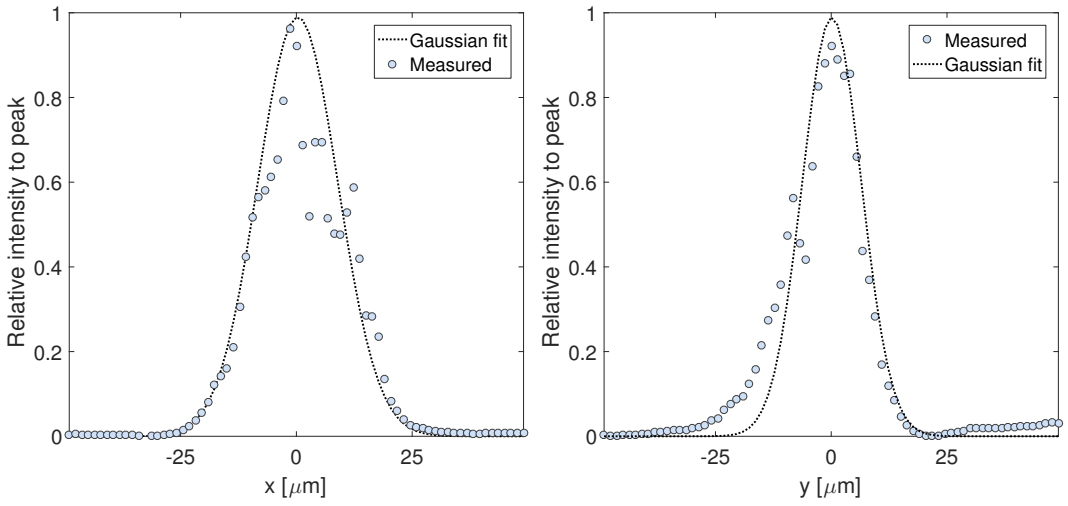

(a) **(b)**

Figure 4.19: Mode profile cross-sections of a mode-expanded single-mode of λ=406 nm radiation in the (a) x and (b) y axis. Gaussian fits are included and their widths are those used in the text.

3–6 μm. The starting pulse energy of the array waveguides was set to be 0 nJ so as not to damage the starting region of the taper by repeatedly exposing it to the HPO. As these structures were fabricated below the cumulative heating threshold, calibration is performed by interpolating a measured pulse energy-diameter relationship rather than a linear fit. End-facet images of the fabricated structures are shown in Figure 4.18. Annealed LMA diameters range from 25–30 μm depending on the individual end waveguide diameters.

To conserve time, after fabrication the waveguide chip is roughly ground back using a diamond wheel to expose input and output waveguide facets. On the input face, index matching fluid was used to increase fibre-waveguide coupling by removing scattering from the rough surface produced by the diamond wheel. On the output face, a 100 μm thick cover slip was similarly placed over the end facet, with index matching fluid between the cover slip and the waveguide chip. Waveguide modes were then imaged through the cover slip.

A full range of modes were observed, from weakly guiding to multi-moded. Set 2, with waveguide end annealed diameters of 2 μm, LMA structures and beam profiles are shown in Figure 4.18. When the lattice spacing is smaller than the sub-waveguide diameters we found complex mode profiles consistent with inhomogeneous refractive index profiles. When the lattice spacing is larger than the individual waveguides, we see a weakly guided mode superposed on individual guiding in each of the component waveguides. For the instance where the end individual waveguide diameter was ~2 μm and the lattice constant was also ~2 μm we find a fundamentally moded, approximately Gaussian beam with a major (minor) MFD of 34.5(26.7) μm with a 95 % mode overlap with an ideal Gaussian profile (shown in Figure 4.19). As the LMA has a refractive index profile that is approximately a step change, this MFD is consistent with the LMA radius of ~26 μm for a refractive index contrast of

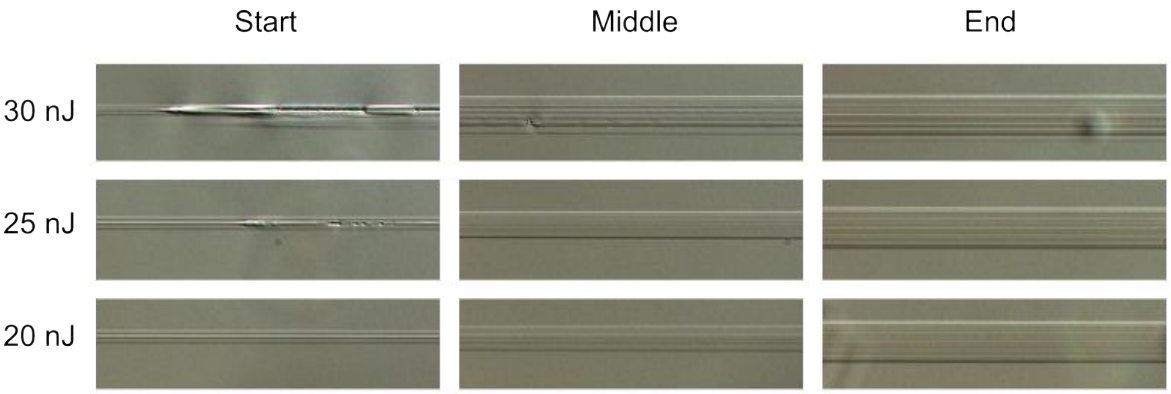

Figure 4.20: TDIC images of SMC tapers with varying starting pulse energy of the array waveguides. Above 20 nJ damage can be seen. For a pulse energy of 20 nJ no damage is present and the step-index LMA structure is present by mid-taper.

1×10^{-3}, as previously found for individual, single-mode blue waveguides. The expansion corresponds to an 12–14× increase over the fibre-coupled waveguide MFD, more than sufficient for our application. We note that there is a slight asymmetry in the mode profile, most likely due to the LMA structures being written from left to right rather than bottom to top. The incorrect writing direction is evident as distortions of the bottom of the LMA structure due to deflections of the HPO beam by already written waveguides. It is expected that mode profiles could be improved by writing from bottom to top. It is unknown whether the noise in the Gaussian profile is from inhomogeneities in the refractive index profile, or due to the fact that the end facets of the LMA waveguides were not optically polished.

Further study of SMC tapers were not able to replicate the previously demonstrated expansion of a fundamental Gaussian beam. The large number of sub-waveguides in the desired structure causes long write times, and a limited number of structures can be written in one write session. As the end individual waveguides are below the cumulative heating threshold, any variation in the HPO after calibration or over the course of a long write session can lead to large changes in the written waveguides due to the operating in a regime where the waveguide diameter changes by large amounts for small changes in HPO pulse energies. It is possible that further stabilisation of the HPO would allow for laser parameters consistent enough for reliable and repeatable fabrication of LMA structures.

During later investigations we found an optimal start energy for the array waveguides of 20 nJ. Above this value, damage was found at the taper start. Below this value, the taper begins too slowly and there is a region where there is no strong confinement of the waveguide mode. See Figure 4.20 for TDIC images of the variation in waveguide start energy and the result on the SMC taper.

Overall, the SMC taper concept shows promise. The further development of the concept requires dedicated study and is warranted. The development of LMA structures with diameters of ~6 μm would satisfy our 2× MFD expansion requirement due to the step-index nature of the waveguides, while decreasing the number of individual waveguides to seven.

4.6 Discussion and conclusion

The development of waveguides for the single-moded guidance of blue wavelengths was critical to the realisation of an optical system based on LW waveguides for coupling to $^{88}Sr^{+}$ ions. We have demonstrated single-moded guidance of ~405 nm wavelength radiation in Corning Eagle2000 glass with 98.3(0.9)% mode overlap with S405-XP fibre and <1.55 dB/cm transmission loss, as determined by an insertion loss measurement and correcting for the theoretical coupling efficiency. It was found that a waveguide with optimal mode overlap with SMF (99.9(0.3)%) had increased transmission loss over the waveguide with 98% mode overlap, and as our fabrication process was optimised using the mode overlap as the figure of merit then there is room in the parameter space to explore lower propagation losses. Despite the visual observation of red fluorescence from waveguides excited with $\lambda \approx 405$ nm light, we find no significant elevation of PL emission when referenced to 2 m of fibre optics, with further study required to quantify the amount, if any, of increase present for the short waveguide lengths.

Attempts at mode expansion of both blue and near-IR wavelengths lead to multiple approaches being explored. We found the regular, single-waveguide tapers with the diameter either decreasing or increasing to the final diameter were not sufficient for providing the required mode expansion. Down-tapering led to increased power in Lorentzian wings of the mode profile, with no measured increase in the central Gaussian portion of the mode. Up-tapering did provide some mode expansion, however for blue modes we found that even 8 mm of taper length were not sufficient for full adiabatic transfer to the multi-moded structures. Further, the expanded modes increased too slowly with increasing end diameter such that the required waveguide sizes were beyond the capabilities of the fabrication process. We therefore developed a fabrication process for the adiabatic transfer of single-mode waveguides to large-mode area structures composed of many waveguides. Simulations predicted that the mode profile in the final LMA structure could be controlled using the refractive index contrast of the individual waveguides, with a low contrast providing the smoothest Gaussian profile. We first confirmed that large, strongly confining waveguides were not suitable for fabricating such structures, demonstrating well confined individual modes in each sub-waveguide. The fabrication of LMA structures with weakly guiding constituent waveguides with diameter equal to the hexagonal lattice spacing provided the best mode profile with a 12–14× mode expansion. However, instabilities in the laser-writing process meant that this result could not be replicated due to the sub-waveguides being fabricated below the cumulative heating threshold. Further study would explore ways to make the fabrication process robust and repeatable, as well as fabricate smaller tapers with only seven individual waveguides to satisfy our 2× mode expansion requirement.

The presented results demonstrate the viability of LW waveguides for optical interfacing with

trapped $^{88}Sr^{+}$ ions, with viable low loss, high overlap waveguides for coupling to S405-XP fibre at blue wavelengths. The application to other trapped ion species is still an open question when UV wavelengths are required, however it is thought that the limiting factor will be material absorption and not the fabrication process. The extension of the LW waveguide processes developed here to a full waveguide circuit for $^{88}Sr^{+}$ control will be presented in Chapter 7 where we explore further considerations such as variable depth waveguides and the simultaneous coupling of multiple waveguides.

5

Diffractive optics: theory

Part of the work presented in this chapter appears in ***Day, Matthew, et al. "Continuous-relief diffractive microlenses for laser beam focusing." Optics express 25.22 (2017): 26987-26999.***

Diffractive optics implement spatially dependent phase shifts on beam fronts, with the change in the phase front of the propagating beam modifying its future evolution. In contrast to refractive optics, flexible and advanced beam profile transformations are possible using diffractive optics, such as beam focusing, deflection and shaping. The cost of this design flexibility is increased wavelength specificty, with diffractive optics typically performing to specification over a small wavelength bandwidth unless dispersion-free phase shifts are implemented [168, 169]. The relative flatness of diffractive optics, on the order of the wavelength of controlled light, and design flexibility make them ideal candidates for microfabricated optics for interfacing with trapped ions. Each optical transition of trapped ions have a linewidth much smaller than the bandwidth of diffractive optics and therefore a single diffractive optic can be associated with a single optical transition. As outlined in Section 2.3, on-axis diffractive optics can be used to image trapped ion fluoresence, while off-axis diffractive optics can be used to address optical transitions with the requried k-vectors. With the exception of reflective micromirrors, all microfabricated optics previously reported for trapped ion applications have utilised diffractive optics. One common diffractive optic used is the Fresnel lens as they lend themselves to ease of design [106]. However the design simplicity of Fresnel lenses limits design flexibility (for example, the lenses must focus on axis) which we can regain with a similarly simple design model, as will be introduced in the next section. In this chapter we aim to design diffractive optics that generate similar beam waists to those routinely used in trapped ion experiments, on the order of 10 to 100 μm. These beam waists correspond to ones small enough to not clip trap electrodes while also being able to be generated by lenses placed outside the vacuum chamber. There has been recent interest in deterministic interaction of light and single atoms by matching beam diameters with the scattering cross-section of the corre-

sponding atomic transition [170, 171]. By mode-matching the addressing laser beam with the atomic cross-section laser-power requirements can be greatly reduced, and in principle a single photon can be used to control the state of the ion allowing for deterministic entanglement of two remotely located atoms. The scattering cross-section of a two-level atom is given by $3\lambda_0^2/2\pi$, corresponding to an effective diameter of ~290 nm for Doppler cooling light and ~470 nm for probe light in $^{88}Sr^+$. The minimum numerical apertures required to produce such beam waists are approximately 0.7 for both wavelengths. Achieving such a high numerical aperture would require large diffractive optics placed close to the microtrap, posing both a fabrication challenge and a potential deleterious effect on the trapping potential as studied in Chapter 3. The interfacing of trapped ions with beam diameters larger than the scattering cross-section allows for simpler design models and relaxes alignment tolerances, especially for hot ions which have spatial extensions much larger than the wavelength of the addressing light. The realisation of higher numerical apertures would require novel design procedures that are beyond the design models used here, and where extensions to such optics are possible it will be noted.

The implementation of diffractive optics as surface-relief profiles in optical materials is a mature procedure. Due to the optical material having a different refractive index to the surrounding medium (typically air), variations in the material thickness implement spatially dependent phase shifts at the material interface. Diffractive optics have been demonstrated in a number of materials for a wide range of applications (see Figure 5.1), including beam shaping [172], optical pickups [108], waveguide mode converters [173] and optical lithography [107]. An important figure of merit for determining the quality of diffractive optics is the diffraction efficiency, defined as the ratio of power in the desired diffraction order to the input power. In most applications the diffraction efficiency is typically sacrificed in favour of fabrication simplicity by the quantisation of the height profile into discrete steps, with the number of levels typically ranging from 2 to 8 [174–176]. The theoretical diffraction efficiency increases with the number of discretisation levels and so a compromise is typically made between performance, cost and complexity of manufacture. As we wish to maximise the diffraction efficiency, we opt for designing continuous-relief surface profiles where it is intended that the only discretisation is in the pixel size of the fabrication process. The added complexity of continuous-relief profiles is in precisely controlling the profile shape, rather than the etch depth of a discrete number of levels. As we will see in Chapter 6, such precise profile control is possible by applying functional corrections to fabrication maps through precise calibration of fabrication parameters.

While surface-relief diffractive optics offer a significant number of advantages for trapped ion addressing there are some drawbacks, such as difficulty in controlling the polarisation of the light, which is an important consideration for tailoring atom-light interactions. A recent, and rapidly developing field, is the realisation of metasurfaces in dielectric materials which allow for more advanced opti-

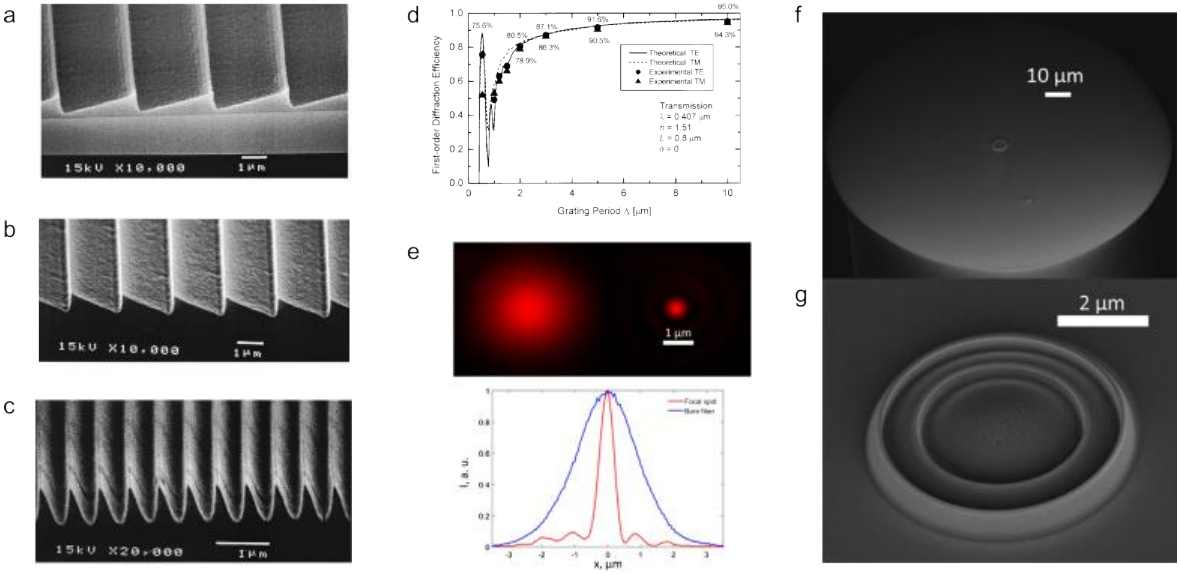

Figure 5.1: (a-c) SEM images of transmissive surface-relief gratings in polymer for deflection of λ = 407 nm light, reproduced with permission from [108] (d) Diffraction efficiency of gratings for blue light compared to theoretical values, reproduced with permission from [108] (e-g) Diffractive microlens on a fibre tip for focusing λ = 660 nm light, (e) shows mode profiles with and without the lens, reproduced with permission from [177]

cal functionality than surface-relief diffractive optics as shown in Figure 5.2(d-e). Electromagnetic metasurfaces are periodic arrays of subwavelength features, which use variations in properties of the features to control the phase shift on an incident electromagnetic wave. Historically, metasurface unit cells have been implemented using thin metal structures (see Figure 5.2(a-c)) [178–180]. The plasmonic resonances of the metal structures can be tuned by changing their dimensions, allowing for arbitrary spatial phase shifts [181]. Additionally, polarisation control is possible by changing the size of the metal structure along the polarisation axis under consideration. Rotation of the metal structures can similarly rotate the polarisation axis of the incident light. However, plasmonic metasurfaces are typically lossy as some of the incident energy is converted into plasmonic modes within the metal itself. The use of dielectric nanorods in place of metal structures can solve the loss issue, due to their transparency to the design wavelength. Tuning of the diameter of the nanorod modifies its resonance with the incident wavelength of light, along with the implemented phase shift. If a nanorod with an elliptical footprint is used, polarisation dependent phase shifts and polarisation axis rotations can be performed by independently varying the radius of the major and minor ellipse radius as well as their angle from the polarisation axis. By selectively choosing the height of the nanorod, metasurfaces can be designed with near unity efficiency for all phase shifts. The challenge is then to fabricate nanorods with sub-wavelength lattice spacing in a high refractive index material. As we will show, for blue wavelengths this provides some demanding fabrication requirements. While we do not fabricate any dielectric metasurfaces, we simulate metasurface unit cells in silicon nitride demonstrating the

potential for high transmission efficiency dielectric metasurfaces at blue wavelengths for phase and polarisation control.

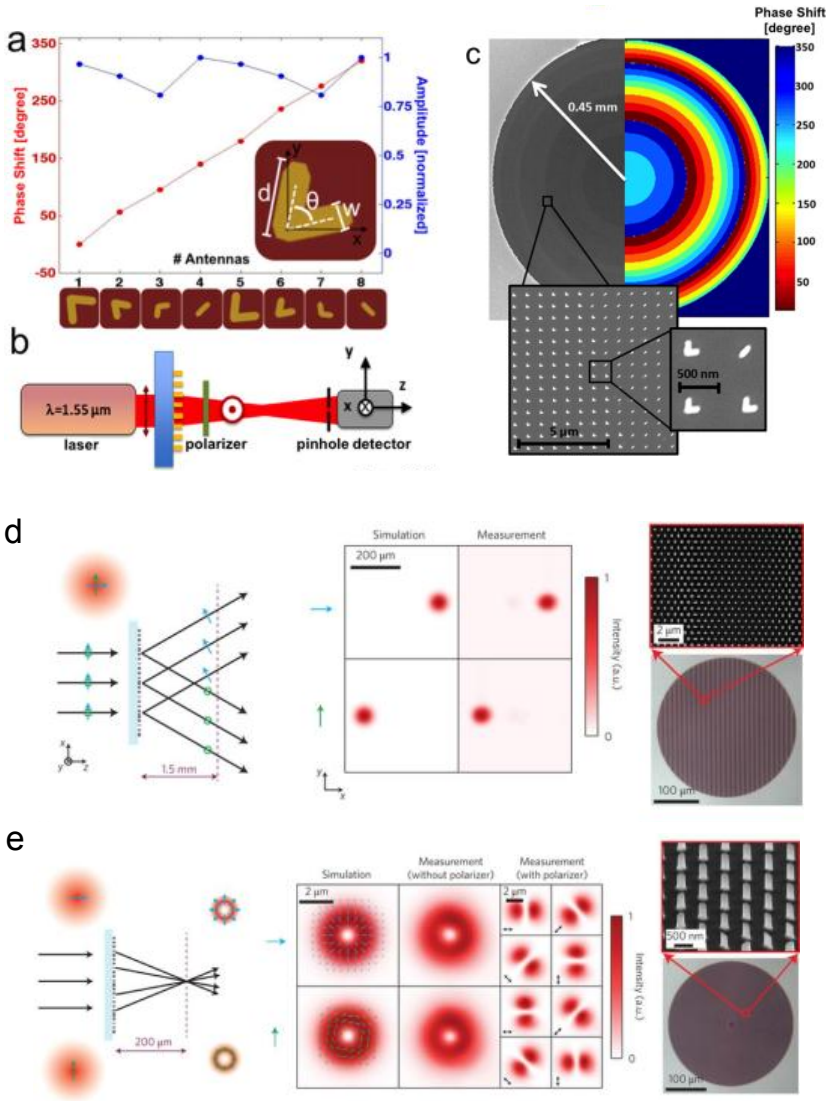

Figure 5.2: (a-c) Plasmonic metasurface for focusing of λ = 1550 nm light, reproduced with permission from [182] Copyright 2012 American Chemical Society; (d-e) Dielectric metasurface for phase and polarisation control of λ = 1550 nm light, demonstrating polarisation dependent profiles in the output beam, reproduced with permission from [110].

In summary, in this chapter we aim to find an appropriate diffractive optic model suitable for realising a micro-optical assembly for trapped ion control and imaging. We start with a general theory of diffractive optics, beginning with scalar diffraction theory and then moving onto implementing a model for the design of useful, and advanced, phase profiles. The conversion of phase profiles into surface profiles in optical materials is then explored and the vector simulations of surface-reliefs demonstrated, with the fabrication of surface-relief diffractive optics explored in Chapter 6. Finally, we present designs of dielectric metasurfaces for blue wavelengths, along with a proposed fabrication process.

5.1 Diffraction theory

The design and simulation of diffractive optics can be performed in many ways, with each technique a method to approximately solve Maxwell's equation in the presence of a phase-modulating interface. Simulation methods of physical diffractive structures often serve as design methods by iterative design of phase fronts to realise a desired optical behaviour. Numerous simulation models exist which, in order of increasing complexity and accuracy, include scalar diffraction theory (SDT) [106, 183], boundary integral methods (BIM) [184, 185], rigorous coupled wave analysis (RCWA) [186–190], and finite element methods (FEM) [191, 192]. The choice of model is determined by the required accuracy and available computing power, with full solutions to Maxwell's equation using FEM being the most resource intensive. For vectorial simulation of diffractive optic structures, RCWA offers a reduction in computing resources at the expense of design flexibility as it can only readily treat periodic grating structures. BIM (sometimes called bounday element methods) relax the periodic requirement at expense of some accuracy but can still treat multiple polarisation states of inputted electric fields [193]. SDT is the least resource intensive at the sacrifice of any polarisation information, however accuracy may be regained as it allows many design iterations and in some cases, simple analytical expressions for diffractive optic design, such as the Fresnel lens. We opt to design diffractive optics using SDT due to its ease of implementation over BIM and we choose to simulate the resulting designs using FEM in 2D. We find the accuracy of SDT to be appropriate for our application, and that the beam pointing accuracy is not compromised as the grating pitch approaches the wavelength of the light, however it is likely that diffraction efficiencies could be improved by a more rigorous design method. SDT is only applicable to low-NA diffractive optics, especially as polarisation becomes a critical consideration for tightly focused beams. For the design of high-NA diffractive optics, an iterative FEM procedure would have to be employed to take into account the full vector nature of the electromagnetic field and its interaction with the physical structure of the diffractive optic.

5.1.1 Scalar diffraction theory

Scalar diffraction theory is a well established theory to model how electric fields transform at phase-changing interfaces [106, 183]. A simplification to the investigation of how electric fields respond to spatially dependent phase shifts is performed by assuming the electric field to be scalar and therefore SDT is valid when the phase-shift imparted on the electric field is not polarisation dependent. If the phase-shift is polarisation-dependent, SDT can still be used for each polarisation component provided there is no polarisation-mixing during the phase-shift. Such polarisation mixing can happen for physical implementations such as when thick surface-reliefs are used with feature sizes approaching the wavelength of the incident light [194]. We begin by designing diffractive optics with SDT

before testing the model with vector simulations to confirm their behaviour even when these limits are approached.

The foundation of SDT is the diffraction integral, which directly finds the solution to the Helmholtz equation for the electric field in the (x', y') plane given the electric field in the (x, y) plane

$$E(x', y', z + L) = \frac{L}{i\lambda} \int \int_{-\infty}^{\infty} E(x, y, z) \frac{e^{ikr}}{r^2} dx dy \,, \tag{5.1}$$

with $k = 2\pi/\lambda$ where $\lambda = \lambda_0/n$ is the wavelength of the light in a material of refractive index n, and where

$$r = \sqrt{(x' - x)^2 + (y' - y)^2 + L^2} \,, \tag{5.2}$$

and the two planes are separated by a distance, L, as illustrated in Figure 5.3. SDT makes the approximation that $\vec{k} \cdot \vec{r} = k|\vec{r}|$, that is, the wave vector of the electric field is aligned with the direction of propagation. In general this assumption is not true as it requires the direction of the Poynting vector to align with the direction of the phase velocity. For lossless, isotropic mediums this condition holds and as the materials we are designing for (vacuum and glass) satisfy these conditions then we can safely make this approximation.

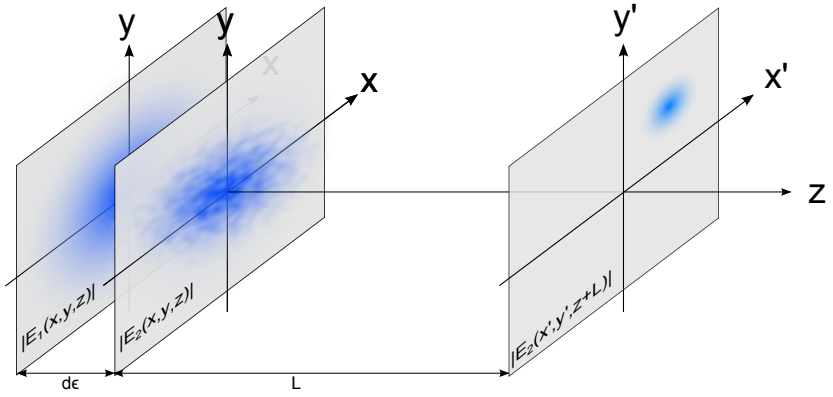

Figure 5.3: Illustration of the coordinate systems used in the diffraction integral and trasnmittance function. The diffraction integral maps from $E_2(x, y, z)$ to $E_2(x', y', z + L)$ while the transmittance function maps from $E_1(x, y, z)$ to $E_2(x, y, z)$.

We will use Equation 5.1 to find a suitable $E(x, y, z)$ for a desired $E(x', y', z + L)$, as illustrated in Figure 5.3. In our instance, we define a source electric field (e.g. from a waveguide) at $z - d$ where d is the distance of the source from the (x, y) plane. The source field is propagated to the position $z - d\epsilon$ where $d\epsilon$ is an infinitesimal distance. We then wish to linearly transform $E(x, y, z - d\epsilon)$ to an electric field such that when propagated using the diffraction integral to $z + L$ we recover the desired electric field $E(x', y', z+L)$. The linear transformation is represented by the transmittance function, $T(x, y)$ such that

$$E_T(x, y, z) = T(x, y)E(x, y, z - d\epsilon) \,, \tag{5.3}$$

where E_T is the transformed electric field. Separating the electric fields into their amplitude and phase components, $E = E_0 e^{i\Phi}$, we find the transmittance function can be expressed

$$T(x,y) = \frac{E_0(x,y,z)\exp[i\Phi(x,y,z)]}{E_{T,0}(x,y,z-d\epsilon)\exp[i\Phi(x,y,z-d\epsilon)]} \,. \tag{5.4}$$

We concede that arbitrary modulation of electric field amplitudes is difficult and therefore make the approximation $E_0(x,y,z-d\epsilon) \approx E_{T,0}(x,y,z)$ and our *phase* transmittance function becomes

$$t(x,y) = \exp[i(\Phi(x,y,z) - \Phi(x,y,z-d\epsilon))] \,, \tag{5.5}$$

$$= \exp[i\Psi(x,y)] \,, \tag{5.6}$$

where $\Psi(x,y)$ is the phase change induced by the optical element in the (x,y) plane to transform our source field to our desired field. The phase change can be calculated as

$$\Psi(x,y) = [\Phi_{\text{out}}(x,y,z) - \Phi_{\text{in}}(x,y,z-d\epsilon) + \Phi_0]_{\text{mod } 2\pi} \,, \tag{5.7}$$

where Φ_0 is a phase degree of freedom that can be used to tune physical implementations of the diffractive optic without affecting its transmittance function. Determination of Ψ requires precise definition of the incident and output electric fields, an example of which we present in Section 5.1.2. We refer to the physical realisation of a spatially varying phase transmittance function as a *diffractive optic*.

Scalar simulations of the Helmholtz equation

In order to simulate the output field of a given phase profile, we must numerically solve the Helmholtz equation. The simulations allow us to confirm designed diffractive optics perform as desired, to compare measured diffractive optics to theory, as well as being used for advanced design of diffractive optics. We use two different simulation methods depending on the application.

Direct integration Direct integration involves numerically solving Equation 5.1. First, we define our source beam, typically a Gaussian beam or point source such that the electric field propagation is analytically defined, and propagate it to the transformation plane. At the transformation plane we map the source beam onto a linear mesh of finite dimension and apply the phase transfer function. We then define a mesh in the (x',y') plane, with pixel size determined by the desired resolution. Using trapezoidal numerical integration of the diffraction integral we then populate the pixels in the image plane. This is then repeated for different values of z to build up a full 3D construction of the output electric field.

Due to computational resource requirements of the trapezoidal integration method we typically restrict simulations to the $(x',0)$, $(0,y')$ or $(0,0)$ planes to reduce simulation times. The direct integration method is typically accelerated using the Fresnel approximation, by which the integral reduces

to a Fourier transform and therefore Fast Fourier Transform (FFT) methods can be used. The Fresnel approximation is essentially that the lens focal length must be much larger than the lens radius, which for geometries we consider in this work is not necessarily valid and so we must solve the Helmholtz equation exactly. FFT methods can also be used without using the Fresnel approximation through the angular spectrum method.

Angular spectrum method The angular spectrum method is another way to numerically solve the Helmholtz equation. The propagation of the electric field is performed in the spatial frequency domain and direct integration is avoided. The equivalent equation to Equation 5.1 is [195]

$$E(x', y', z + L) = \mathcal{F}^{-1}\{H(k_x, k_y)\mathcal{F}\{E(x, y, z)\}\} \tag{5.8}$$

where $\mathcal{F}$ is the Fourier transform and H is the Helmholtz propagator

$$H(k_x, k_y) = \exp(ik_z L) = \exp(i\sqrt{k^2 - k_x^2 - k_y^2}L) \tag{5.9}$$

where a postive sign in the exponent ensures that evanescent waves ($k_x^2 + k_y^2 > k^2$) exponentially decay, with $\vec{k} = (k_x, k_y, kz)$ the wavevector in vector form. Note that backwards propagation ($L < 0$) reverses the sign of the exponent and the exponentially decaying evanescent waves become exponentially increasing such that the inverse Fourier transform becomes undefined. To solve this problem we set the Helmholtz propagator to zero when $k_x^2 + k_y^2 > k^2$, an approximation that is valid when propagating more than a few wavelengths [196].

Equation 5.8 can be numerically solved using FFT methods and therefore yields fast solutions for electric field propagations. The drawbacks are that the output mesh has to be the same as the input mesh, and the mesh array size grows exponentially with the spatial sampling. Simulations of off-axis propagation is also cumbersome as the output plane must be centred on the lens center. We typically use the angular spectrum method for implementation of iterative design methods (see Section 5.1.4) or for full 3D simulations of on-axis diffractive optics.

5.1.2 Point-to-Point Model

For rapid and easy design of diffractive optics for on and off-axis focusing of laser beams we aim to develop a simple model for the analytical determination of Equation 5.7. Consider the case of point source at (x_1, y_1, z_1), the object, emitting plane waves in all directions and collecting some of those plane waves and redirecting them to a point (x_2, y_2, z_2) , the image, a visualisation of which can be seen in Figure 5.4. Assuming a lossless, homogeneous, isotropic medium such that the wavevector is parallel to the plane wave's direction of travel the electric field of a plane wave is given by

$$E(x, y, z) = E_0 \exp(i\Phi) = E_0 \exp(\pm ikr)\,, \tag{5.10}$$

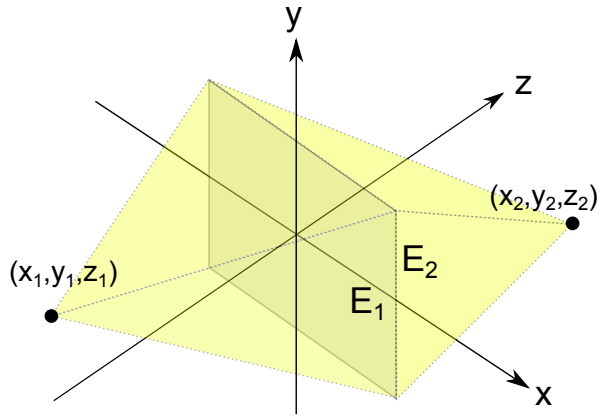

Figure 5.4: The coordinate space used for designing DMLs using scalar diffraction theory. A point source at (x_1, y_1, z_1) is mapped onto a point image at (x_2, y_2, z_2) by the DML at the $z = 0$ plane.

where

$$r = |\vec{r}| = \sqrt{(x - x_j)^2 + (y - y_j)^2 + (z_j)^2}\,, \tag{5.11}$$

with (x_j, y_j, z_j) being the coordinates of either the object ($j = 1$) or the image point ($j = 2$). We have defined $z = 0$ at the transformation plane. The sign of the exponent is determined by whether the plane waves are expanding (+) or contracting (−). The continuous phase change profile in the (x, y) plane is now given by

$$\Phi_{PS}(x, y) = \Phi_{out}(x, y, 0) - \Phi_{in}(x, y, -d\epsilon)\,, \tag{5.12}$$

$$= -\frac{2\pi n_2}{\lambda_0}\sqrt{(x - x_2)^2 + (y - y_2)^2 + (z_2)^2} - \frac{2\pi n_1}{\lambda_0}\sqrt{(x - x_1)^2 + (y - y_1)^2 + (z_1)^2}\,, \tag{5.13}$$

where n_j is the refractive index of the medium before ($j = 1$) and after ($j = 2$) the transformation plane and λ_0 is the wavelength of the propagating plane waves in a vacuum. Implementing the phase change on the incoming plane waves at the transformation plane will redirect them to the image point at (x_2, y_2, z_2). By using plane waves, which have a well defined propagation, we have avoided directly solving the diffraction integral to find the required transmittance function.

We refer to diffractive optics with phase functions of the form of equation 5.13 with $(x_j, y_j) = (0, 0)$ as on-axis diffractive microlenses (DMLs), as they recover the behaviour of the standard thin lens formula for point sources and the dimensions under consideration are on the micron scale. We refer to the case when $(x_j, y_j) \neq (0, 0)$ as off-axis DMLs due to their focusing behaviour. The advantage of using the point-to-point model over the standard Fresnel lens model is the ability to image source points off-axis - a feature we require for the realisation of the proposed optical assembly for trapped ion addressing.

5.1.3 Single parameter optimisation for finite sources

The point-to-point model is valid for sources that can be approximated as point sources; trapped ion fluorescence for example. However, in the instance that the source has finite extent, the required phase function to position its image at (x_2, y_2, z_2) will be modified. As we aim to focus and deflect Gaussian laser beams for trapped ion addressing it is important to take these modifications into account for accurate focusing. For finite sources we start with Φ_{PS} and vary the values of (x_2, y_2, z_2) such that the image of the source is placed at the desired image point. In practice this is performed using an optimisation routine by iteratively solving the diffraction integral for $E(x_D, y_D, z_D)$ where (x_D, y_D, z_D) are the starting values of (x_2, y_2, z_2), the desired image point. The figure of merit is the maximisation of the quantity $|E(x_D, y_D, z_D)|^2$, that is, the intensity at the desired image point. The three-parameter optimisation routine can be reduced to a single-parameter routine by noting that $x_D = x_2 z_D/z_2$ and $y_D = y_2 z_D/z_2$ to maintain the same optical axis after the transformation plane. The intensity at the desired image point can therefore be maximised by just varying z_D. The optimisation itself is performed using the *fminsearch* routine in MATLAB, minimising the inverse of the intensity.

The optimisation is of particular use for Gaussian beams, which we use to test fabricated DMLs. For on-axis designs, we note that Gaussian beam propagation equations can be combined with the thin lens formula to derive an expression for z_2 analytically[1]. However, the main advantage of the optimisation routine is for off-axis DMLs, where there is no geometric optics analogue for finding z_2 analytically.

5.1.4 Gerchberg-Saxton algorithm

In some instances, it may be favourable to not only faithfully image the source field, but to distort it into a new intensity profile. Such a technique is referred to as *beam shaping*. An application would be designing diffractive optics that could address multiple ions simultaneously while avoiding others. Demonstration of successful beam shaping is also a good test of fabrication capabilities.

The Gerchberg-Saxton algorithm (GSA) is an iterative method of designing a transmittance function for beam shaping [198, 199]. A seed phase profile is first generated (in our case, using Equation 5.13) and implemented on the source beam. The algorithm then proceeds in the iterative steps:

1. Propagate the electric field to the image plane.

2. Replace the amplitude of the propagated beam with the amplitude of the desired intensity profile, leaving the phase profile unmodified.

[1]The geometric derivation of the required z_2 for a particular Gaussian beam waist was outlined by an anonymous reviewer during the peer review of [197] and the analytical calculations are in good agreement with the found values from the optimisation routine

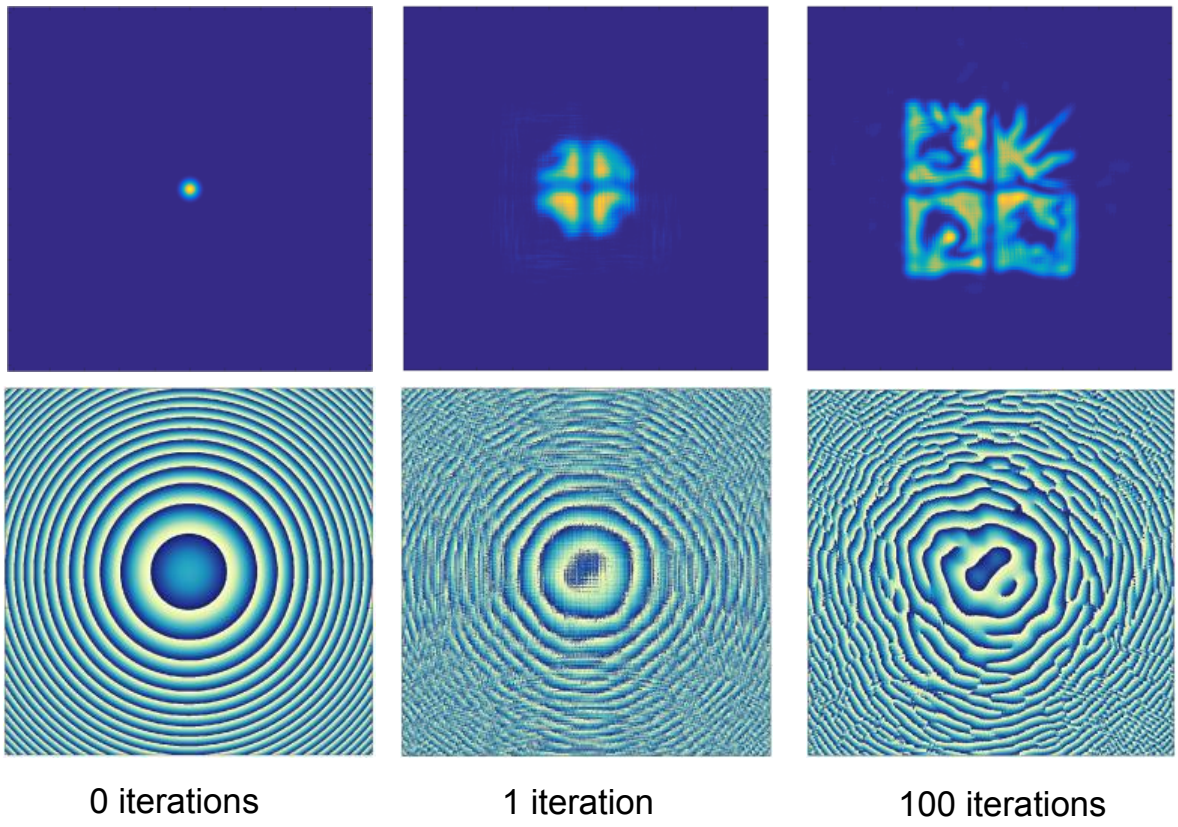

Figure 5.5: Demonstration of convergence of the Gerchberg Saxton algorithm to a design intensity profile (the University of Bristol logo). (Top) Electric field intensities in the image plane, before modification (Bottom) The required phase profile. The seed profile is a diffractive optic that focuses a Gaussian beam at 500 μm from the transformation plane. Each square is 100 μm across.

3. Backpropagate the electric field to the transformation plane

4. Replace the amplitude of the backpropagated beam with the amplitude of the source intensity profile

The steps 1–4 are iteratively performed until the propagated electric field in the image plane, after step 1, is sufficiently close to the desired intensity profile. The required phase profile to produce the desired intensity profile is found by the phase difference between the source and backpropagated electric fields, after step 3. Convergence of the GS algorithm is guarenteed, though not necessarily to the optimal solution and more advanced iterative procedures exist that find better solutions [200]. We find that the unmodified GS algorithm is suitable for our applications and so do not consider advanced modifications. Due to the required number of iterations, the angular spectrum method must be employed to reduce iterations times. An example design at 1 and 100 iterations of an optic for imaging the University of Bristol logo at $z = 500$ μm is shown in Figure 5.5 demonstrating convergence of the algorithm.

5.2 Surface-relief diffractive optics

Surface-relief diffractive optics are one way to implement the phase profiles outlined in the previous section. A material is selectively patterned to create a height profile that imparts relative phases on an incident beam front. We first detail the process of determining the required surface-relief for a given phase profile, and validate the process using vector simulations of the profiles.

5.2.1 Implementing phase profiles as surface reliefs

To implement the designed phase profiles as surface-reliefs in a material substrate, we consider the optical path difference between a beam that travelled a distance d_1 in a material of refractive index n_1 to a beam travelling d_2 through a refractive index n_2. The optical path difference, D, is given by

$$D = d_1 n_1 - d_2 n_2 \ . \tag{5.14}$$

We consider surface-reliefs in air and as such set $n_2 = 1$ and let n_1 take the value of the refractive index of the surface-relief material, n. We restrict the surface-relief to have a maximum height, h and compare optical path differences over this height, such that

$$D = h(n-1) \ . \tag{5.15}$$

An optical path difference of λ_0 is required for the maximum phase shift of 2π and therefore a phase shift at the point (x, y) is related to the optical path difference by

$$D(x,y) = \lambda_0 \frac{\Psi(x,y)}{2\pi} \ , \tag{5.16}$$

and therefore we find an expression for the height of the surface-relief at (x, y) of

$$h(x,y) = \frac{\lambda_0}{n-1} \frac{\Psi(x,y)}{2\pi} \ , \tag{5.17}$$

with $\Psi(x, y)$ determined by Equation 5.7.

The phase-to-height conversion in Equation 5.17 is only valid for incident and output beams with flat wavefronts that are perpendicular to the transformation plane. However, it can typically used for low-NA DMLs and small (<5°) off-axis diffractive optics. An example low-NA DML is shown in Figure 5.6 demonstrating the characteristic surface-relief shape of on-axis DMLS of vertical phase discontinuities and sloped annuli.

When the incident and/or the output beam is at an angle to the lens normal then the thickness of material required to induce the required phase shift becomes a more complex calculation [109]. For an input beam incident through a substrate of refractive index n_s on a surface-relief in a material of

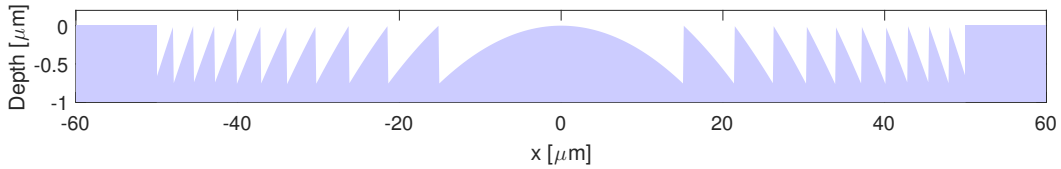

Figure 5.6: An example DML surface-relief with $z_1 = -1000$ μm, $z_2 = 500$ μm for $\lambda = 405$ nm in BK7 glass.

refractive index n_ℓ the generalised surface-relief profile expression is

$$h(x,y) = \frac{\lambda_0}{\mu}\frac{\Phi(x,y)}{2\pi} \tag{5.18}$$

$$\text{where } \mu = \sqrt{n_\ell^2 - n_s^2(1-(|z_1|/r_1)^2)} - |z_2|/r_2 \tag{5.19}$$

$$r_i = \sqrt{(x-x_i)^2 + (y-y_i)^2 + z_1^2} \tag{5.20}$$

with (x_i, y_i, z_i) being the coordinates of the object ($i = 1$) and image ($i = 2$) point respectively. Note that in the limit $|z_i| \to r_i$ then $\mu = n_\ell - 1$, and Equation 5.18 reduces to Equation 5.17. The result of the generalised expression is to reduce feature heights where an off-axis beam is incident or outputted from. As the pitch of features for large off-axis deflection is typically small, this has the beneficial effect of reducing the aspect ratio of these features and relaxing fabrication requirements.

5.2.2 Vector simulations of surface-reliefs

The simulation methods considered up until now for diffractive optics only consider phase profiles and do not take into account their physical implementation. To simulate physical surface-reliefs and analyse their conformity to the desired behaviour we must use a simulation method that considers the interaction of light with physical height profiles in materials. The approximations of scalar diffraction theory for surface-relief diffractive optics breaks down when the size of the surface-relief features are approximately less than 10 wavelengths [108, 194], with significant errors occurring when the features approach a wavelength in size. Off-axis gratings with even moderate deflection angles approach these limits and so a vector diffraction model for surface-relief simulation must be used.

Rigorously coupled wave analysis (RWCA), which considers the surface-relief as a stack of finite number of layers, is formulated for periodic structures and as such is difficult to apply for aperiodic diffractive optics. All diffractive optics we consider are aperiodic due to the focusing behaviour we require, and so we cannot easily use RCWA. Complex schemes exist where the diffractive optic is considered as a series of periodic structures, but we do not consider them here. For ease of implementation, we chose to use COMSOL to numerically solve Maxwell's equations using FEM. To satisfy reasonable memory requirements we do this in 2D, as we found that 3D simulations were too resource intensive. When the surface-reliefs are not radially symmetric we consider the profile in the same plane as the off-axis propagation and therefore can only simulate focusing in one dimension.

The COMSOL model was developed in close reference to a COMSOL guide on simulating Fresnel lenses [201]. A 2D COMSOL model with the *Electromagnetic Waves, Frequency Domain* physics package is used with the model geometry shown in Figure 5.7. The diffractive surface-relief is generated in MATLAB using scalar diffraction theory and then imported into COMSOL as a closed polygon in the $z = 0$ plane. A fine, adaptive mesh is applied in the region close to the surface-relief, with the remaining portion of the simulation region mapped to the adaptive mesh region. A perfectly matched layer (PML) is used to absorb all electromagnetic waves exiting the simulation region, with the thickness of the PML set such that all electromagnetic radiation is absorbed. The input field is generated by a scattering boundary condition on the $z = 0$ line. The field used in all examples is a Gaussian beam with beam waist w_0, propagation distance L and wavelength $\lambda = \lambda_0/n$ where n is the refractive index of the substrate. The source beam is polarised out-of-plane (TM) in all examples given here, but the model allows for in-plane polarised (TE) source beams. The material of the surface-relief is set to be that of its design which can be different to the substrate material, for example when the surface-relief is etched into a thin film, or a lithography resist. The remaining regions are set to air. The output field is taken suitably far away from the surface-relief, which for all simulations presented in this section is 10 μm, or ~$25\lambda_0$. The electric field is sampled at this boundary and exported to MATLAB where it is propagated using the 1D Fresnel diffraction integral

$$E(x', z') = \sqrt{\frac{z'}{i\lambda_0}} \int_{-r}^{r} E(x, z = 0) \frac{\exp\left(-i2\pi/\lambda_0 \sqrt{z'^2 + (x - x')^2}\right)}{\sqrt{z'^2 + (x - x')^2}} dx \ . \tag{5.21}$$

where r is the radius of the surface-relief. Equation 5.21 is solved very quickly using the numerical integral solver *trapz* in MATLAB, and as such it yields much faster results than fully solving the Helmholtz wave equation in COMSOL up to the desired z position. It was found in [201] that the

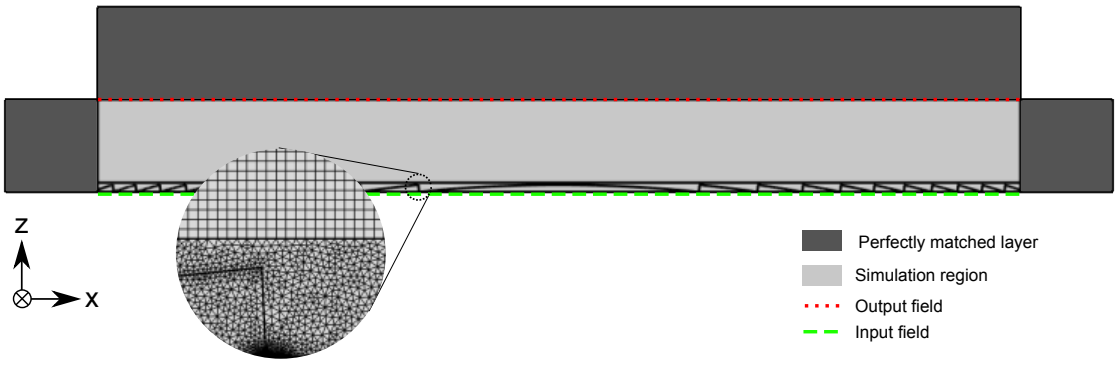

Figure 5.7: A diagram of the COMSOL model used for vector simulations of diffractive surface-reliefs. The simulation region (light grey) is divided into two regions. The first region, from $z = 0$ to 1 μm is adaptively meshed; the second region has a regular mesh mapped to the adaptive mesh at the boundary (shown on the inset). A perfectly matched layer surrounds the simulation region to absorb electromagnetic waves. The input field is injected in the $z = 0$ μm plane, and the output field is taken from the end of the simulation region.

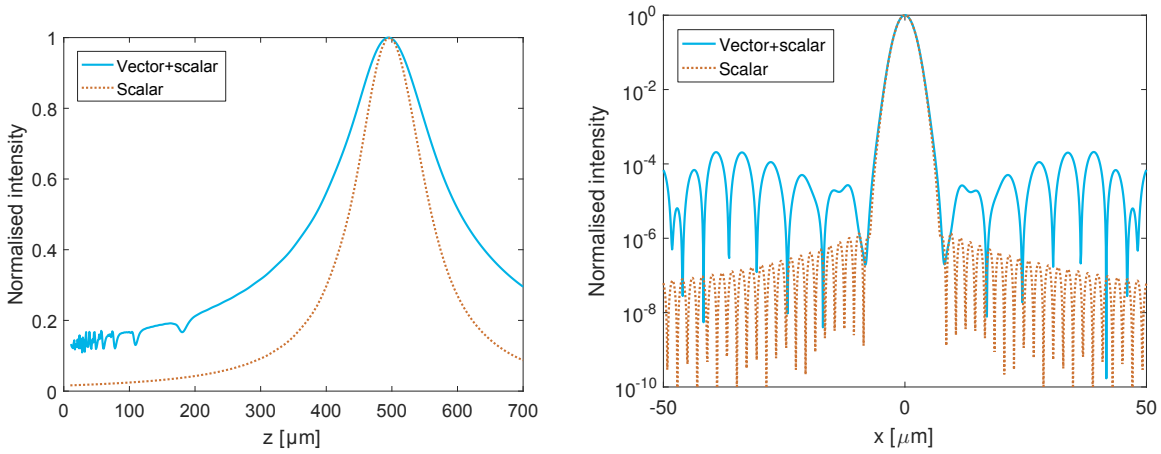

(a) Optical axis, $N = 7$

(b) Focal plane, $N = 7$

Figure 5.8: Scalar propagation of an outputted electric field from the COMSOL model with mesh parameters $N = 7$. (a) The simulated intensity along the $x = 0$ axis, (b) The simulated intensity in the $z = 500$ μm (focal) plane.

results of the Fresnel diffraction integral were in close agreement to the full Helmholtz solution, even when the output field was taken immediately after the surface-relief.

The adaptive fine mesh near the lens has a maximum element size of

$$d_{\max} = \frac{\lambda_0}{2N} \tag{5.22}$$

where $N \in \mathbb{Z}^+$. If the model converges appropriately, the accuracy of the model should increase with increasing N. As a convergence test we use a surface-relief defined in NBK7 glass, designed to take a beam of $w_0 = 3.75$ μm and $\lambda_0 = 0.405$ μm located at $z = -1000$ μm and focus it to a minimum beam radius at $z = 500$ μm. We simulate the output field for $N = 1$ to 7, in each instance propagating the field along the optical axis and in the focal plane. We define the root-mean-square-error (RMSE) as

$$\mathcal{E}_N = \sqrt{\frac{\sum_{i=1}^{m}(E_N(i) - E_{N-1}(i))^2}{m}} \tag{5.23}$$

where $E_N(i)$ is the ith element of an electric field vector simulated with the mesh parameter N. The electric field can be the one in the output plane, the focal plane, or along the optical axis and we find convergence with N in all cases. As seen in Figure 5.8 we find consistency in the location of the lens focus, and the width of the focused beam with scalar simulation, however there is a difference in the magnitude of the background intensity away from the focus. The higher relative background intensities will turn out to be more physical as shown in Chapter 6. As a way of testing the model further, we now consider three example cases of interest.

Confirming that advanced surface-relief design increases diffraction efficiency To confirm that the generalised surface-relief profile expression in Equation 5.18 improves diffraction efficiency, we simulate gratings generated using both the simple and generalised expression. In all tested cases we

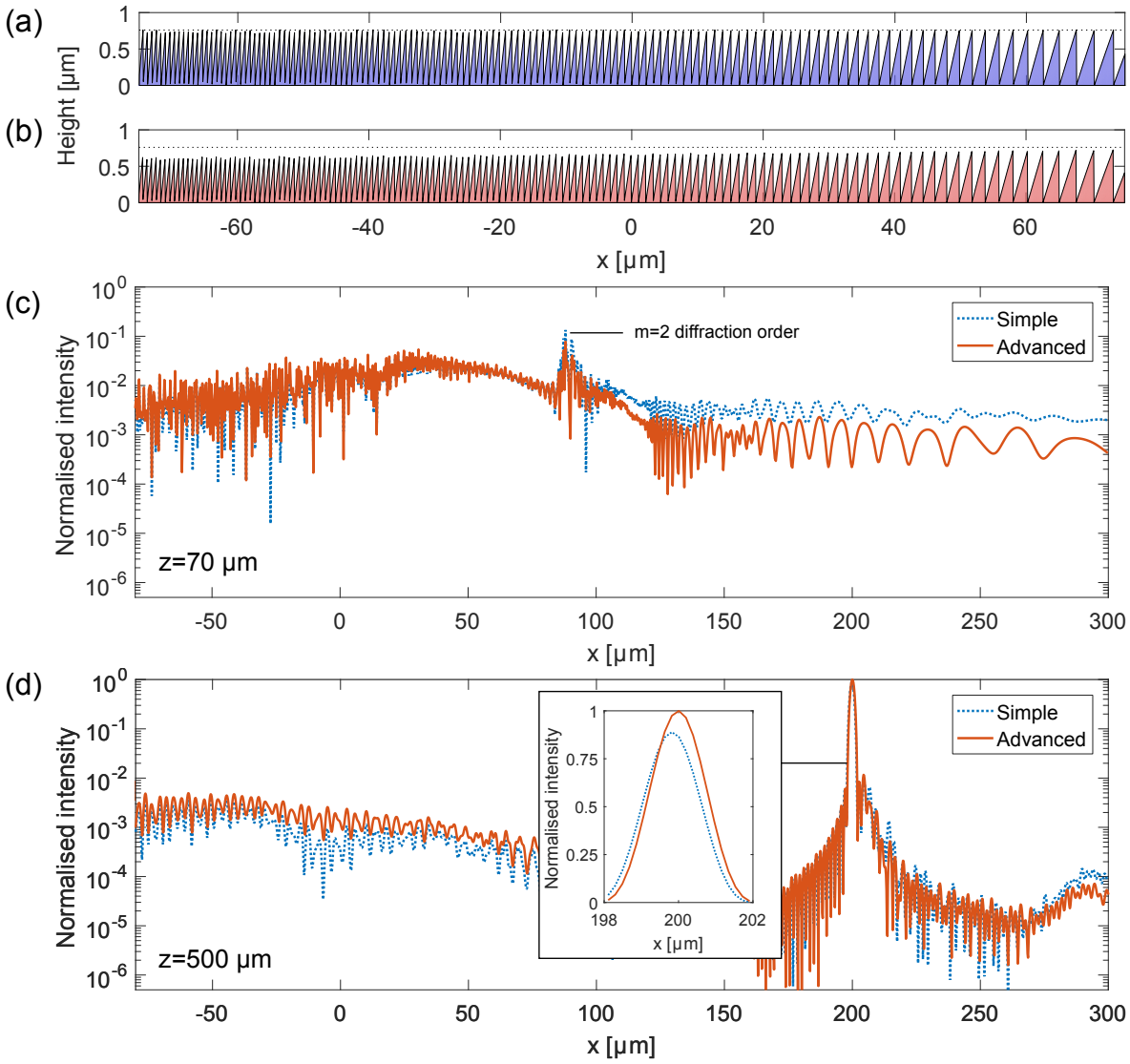

Figure 5.9: (a) Simple and (b) advanced height profiles of an off-axis DML, with a horizontal guide line to illustrate the reduction in height with pitch in the advanced profile; (c) Combined vector and scalar simulation of the x-axis at z = 70 µm demonstrating reduced power in higher order modes for the advanced surface-relief profile;(d) the simulated electric field intensity in the focal plane, with the inset demonstrating 11% more intensity for the advanced surface-relief profile.

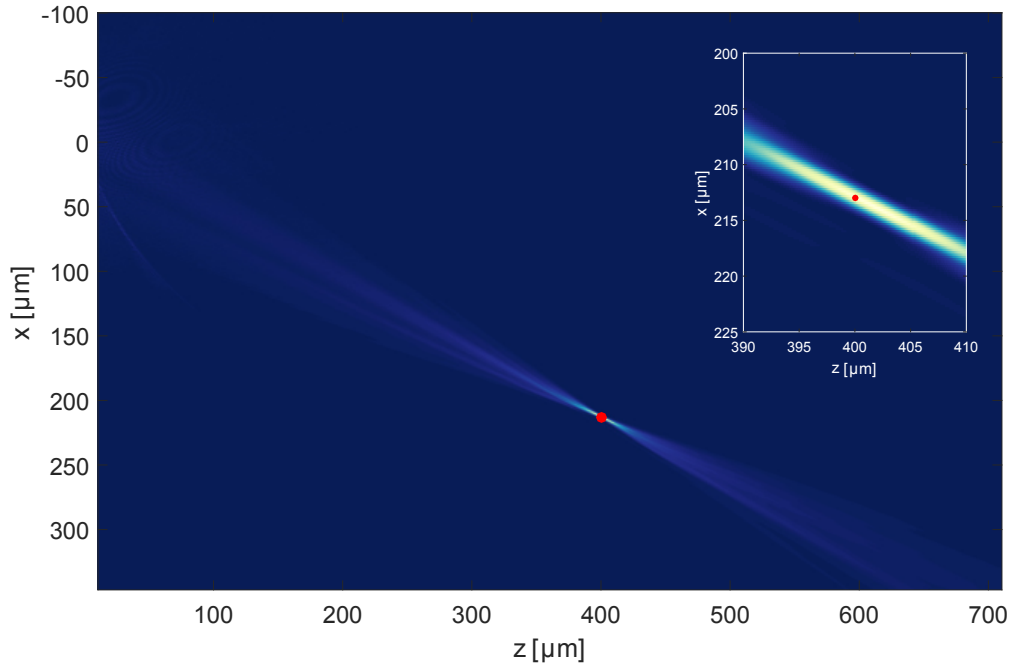

Figure 5.10: Scalar propagation of an output vector electric field from an off-axis DML designed to focus at $(213, 400)$ μm (red dot), demonstrating accurate beam focusing. The inset is a magnified view of the focus to emphasize the location of the beam focus with respect to the design focus point.

find the generalised expression reduces anomalous power into higher diffraction orders, increasing power into the desired diffraction order. However, the generalised expression does not extinguish the higher orders, and so some deviation from unit diffraction efficiency remains for off-axis surface-reliefs. An example off-axis surface-relief simulation is shown in Figure 5.9, demonstrating slight reduction in power into the higher orders. The maximum intensity at the focus is 11% higher for the generalised surface-relief, corresponding to 5% more power in the desired diffraction order.

Accurate beam focusing The capability to accurately position beam waists at a designed point in space is crucial to the realisation of a lens array for interfacing with trapped ions, where multiple beams must be overlapped at a defined ion position. To demonstrate accurate beam focusing we simulated an off-axis focusing surface-relief designed in PMMA (an electron-beam lithography resist), to focus 488 nm radiation at $(213, 400)$ μm, which corresponds to a DML design we fabricate in Chapter 6. The resulting propagation of the vector simulation is shown in Figure 5.10, demonstrating the DML focusing precisely at the design image point. The off-axis DML has a minimum grating pitch of $1.3\lambda_0$, with the pitch at the centre of the lens of $2.1\lambda_0$, in the regime where scalar diffraction theory approximations do not hold. However, we have demonstrated with a vector simulation of the physical surface-relief profile that SDT produces designs with accurate beam focusing as required for trapped ion applications.

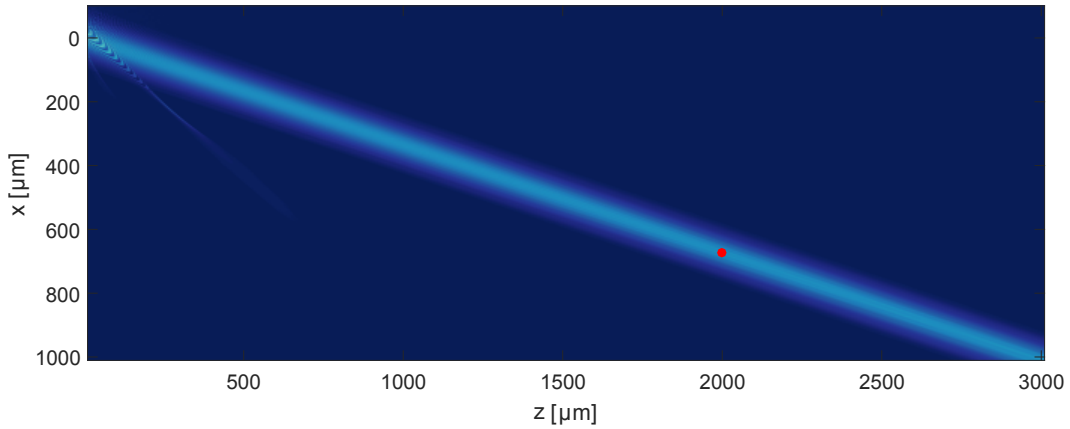

Figure 5.11: Scalar propagation of an output vector electric field from an off-axis DML designed to collimate a divergent Gaussian beam and deflect through the point $(674.4, 2000.0)$ μm (red dot), demonstrating accurate beam pointing and beam profile control.

Beam collimation and deflection We now consider a diffractive optic of interest to trapped ion addressing and design a grating for both collimating and deflecting 422 nm light through the point $(673.4, 2000.0)$ μm where $(0, 0)$ μm is the centre of the optic. A simulation of the required surface-relief in TiO_2 is shown in Figure 5.11, and demonstrates accurate pointing and a consistency with design. Despite using the generalised height profile expression, a higher diffraction order is present, but is weak (~10% intensity) compared to the desired diffraction order. Integrating the intensity profiles of the electric field in the COMSOL output plane and in the desired diffraction order we find a theoretical diffraction efficiency of 94%. A similar exercise calculates that 3.4% of power is projected into the second diffraction order. At least 1% of power is scattered into the zeroth order, however this is hard to measure due to its highly divergent nature as it does not see the lens.

5.2.3 Transmission of surface-reliefs

Surface-relief diffractive optics necessarily sit on the interface between two media of different refractive indices. The transmission, and reflection, of light at such interfaces is governed by the Fresnel equations and as we will be measuring the power focused by diffractive optics it is important to understand how power is transmitted through the optic. There are two different material systems we consider. The first is surface-reliefs patterned in bulk dielectric material, the second are surface-reliefs fabricated in thin-films.

Surface-reliefs in bulk dielectrics

The reflection and transmission of light at interfaces between two media of refractive indices n_1 and n_2 can be calculated using the Fresnel equations. The Fresnel equations for the reflection of s- and

p-polarised light are given by [202]

$$R_p = \left| \frac{n_1 \cos\theta_i - n_2 \sqrt{1 - \left(\frac{n_1}{n_2}\sin\theta_i\right)^2}}{n_1 \cos\theta_i + n_2 \sqrt{1 - \left(\frac{n_1}{n_2}\sin\theta_i\right)^2}} \right|^2 \tag{5.24}$$

$$R_s = \left| \frac{n_1 \sqrt{1 - \left(\frac{n_1}{n_2}\sin\theta_i\right)^2} - n_2 \cos\theta_i}{n_1 \sqrt{1 - \left(\frac{n_1}{n_2}\sin\theta_i\right)^2} + n_2 \cos\theta_i} \right|^2 \tag{5.25}$$

where θ_i is the angle of incidence with respect to the normal to the interface. As surface-relief diffractive optics are composed of concentric slopes, the incident light has an effective angle of incidence. The effective angle can be found from the gradient of the height profile

$$\theta_{i,\text{eff}} = \tan^{-1}\left(\frac{dh(r)}{dr}\right) \tag{5.26}$$

where we are only considering radially symmetric (on-axis) diffractive optics. The reflection coefficients for an example diffractive optic in glass is shown in Figure 5.12. As the lens is radially symmetric, the effective polarisation is uniformly orientated, and the reflection coefficient is given by $R = 1/2(R_s + R_p)$. The change in R is <0.15% over the radius of the optic. Therefore for radially symmetric diffractive surface-reliefs, the effect of the surface-relief shape on the reflection at the interface can be neglected. For off-axis optics, the effect is expected to be significant, with an asymmetric effect for s and p polarisations. However, as we do not fabricate off-axis optics in bulk material we do not study this case further.

Surface-reliefs in thin films

For light traversing several optical interfaces, where the distance between the interfaces is less than the coherence length of the light, the cumulative reflection and transmission of all interfaces must be considered concurrently. This is the case for surface-relief optics defined in thin-films on a bulk dielectric. The thickness of the thin-film alters the transmission of the material stack and as surface-reliefs are regions of varying material thickness they will have a spatially dependent transmission. The average transmission of the surface-relief will in general be different to the surrounding flat film. It is important to characterise this difference in transmission for accurate diffraction efficiency measurements.

To calculate the reflectance of thin-film stacks we use the transfer-matrix method, as typically employed for designing anti-reflection coatings [203]. The relation between the forward and backward propagating electric fields, E^+ and E^- at the ith interface can be modelled as a linear transformation

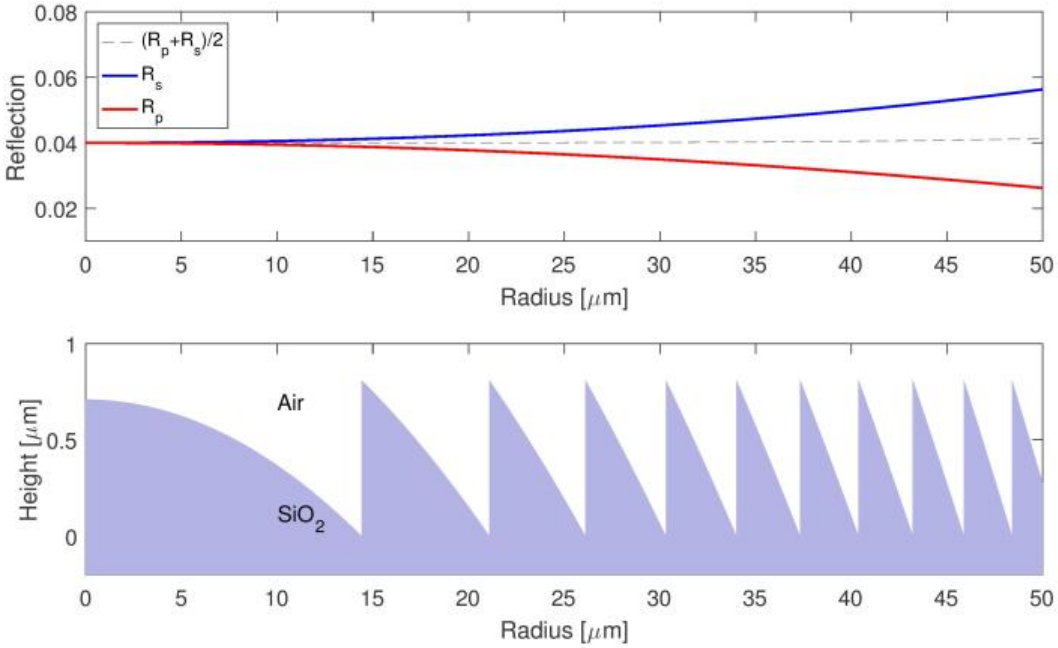

Figure 5.12: (Top) Calculated reflection of a diffractive surface-relief in glass, shown (bottom). The change in reflection over the DML radius is due to the increasing gradient of the annuli.

of the initial electric fields at the first interface ($i = 1$)

$$\begin{pmatrix} E_1^+ \\ E_1^- \end{pmatrix} = M \begin{pmatrix} E_i^+ \\ E_i^- \end{pmatrix} = \begin{pmatrix} M_{11} & M_{12} \\ M_{21} & M_{22} \end{pmatrix} \begin{pmatrix} E_i^+ \\ E_i^- \end{pmatrix} \tag{5.27}$$

where M is a matrix containing information about the layers from 1 to i. The transformation matrix takes the form

$$M = \prod_{m=2}^{i} D_{m-1}^{-1} D_m P_m \tag{5.28}$$

with

$$D_m = \begin{cases} \begin{pmatrix} 1 & 1 \\ \frac{n_m}{Z_0}\cos(\theta_m) & -\frac{n_m}{Z_0}\cos(\theta_m) \end{pmatrix} & \text{for s-polarisation} \\ \begin{pmatrix} \cos(\theta_m) & \cos(\theta_m) \\ \frac{n_m}{Z_0}) & -\frac{n_m}{Z_0} \end{pmatrix} & \text{for p-polarisation} \end{cases}$$

and

$$P_m = \begin{pmatrix} e^{-i\phi_m} & 0 \\ 0 & e^{i\phi_m} \end{pmatrix}, \quad \phi_i = \frac{2\pi}{\lambda_0} d_m n_m \cos(\theta_m) \tag{5.29}$$

where n_m, d_m, θ_m are the refractive index, thickness and angle of incidence of layer m respectively, and Z_0 is the intrinsic vacuum impedance. The reflection and transmittance coefficients can then be calculated as

$$r = \frac{M_{21}}{M_{11}}, \quad t = \frac{1}{M_{11}} \tag{5.30}$$

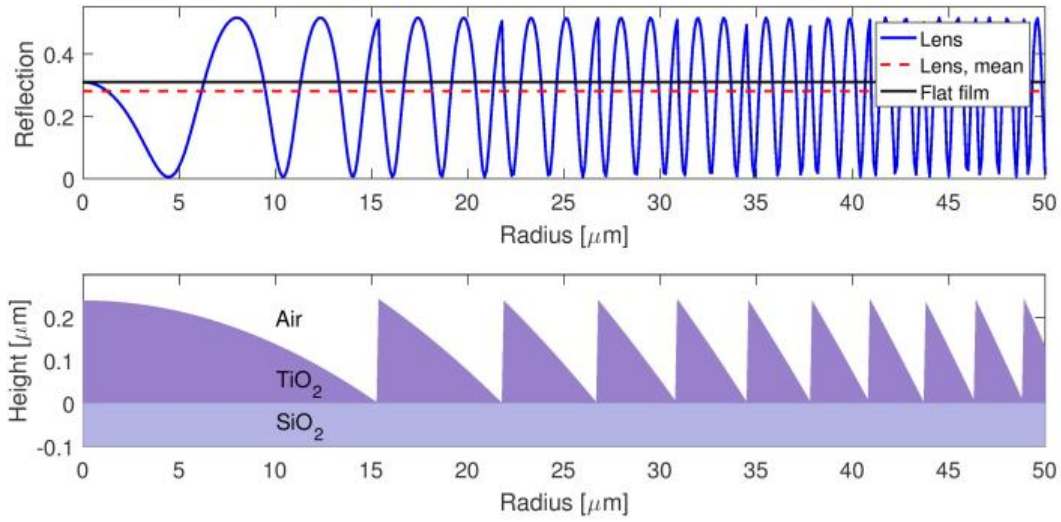

Figure 5.13: (Top) Calculated reflection of a diffractive surface-relief in titania thin film, shown (bottom). The extreme variations in reflection are due to interference effects in the thin-film which strongly depend on the film thickness.

such that for lossless media, the reflectance and transmittance are given by $|r|^2$ and $|t|^2$ respectively.

An example reflectance calculation at $\lambda_0 = 405$ nm is shown in Figure 5.13 for a surface-relief defined in a 1 μm thick titania film ($n = 2.66$) on a 1 mm thick fused silica substrate ($n = 1.47$). The average reflectance is less than for a flat thin-film, demonstrating that surface-reliefs in thin films can have a different transmission to an patterned film. The average reflectance over the full lens corresponds to the reflection of a plane wave, for a Gaussian beam the reflectance modifies the amplitude of the beam profile and the change in transmitted power can be found by integrating over the profile. The exact shape modulation of the Gaussian beam is distinctive and can be used for confirming the use of the transfer matrix method. However, the model is very dependent on the exact thickness of both the thin-film and the substrate. If sufficient control can be obtained over these thicknesses then it may be possible to design surface-relief optics that act as an anti-reflection coating.

5.3 Dielectric metasurfaces

The implementation of spatial phase fronts as surface-reliefs in optical materials both requires a grayscale (or multi-level) fabrication process, and provides no control over the polarisation state of the incident light. In this section we outline a brief exercise in the design of dielectric metasurfaces for the phase and polarisation control of 405 nm wavelength light. The majority of results previously presented for dielectric metasurfaces use amorphous silicon nanorods for manipulation of 1550 nm wavelength radiation. Phase control of blue wavelengths has been previously reported, using titanium dioxide [204], however, the functionality of the metasurface relies on the incident light being circularly polarised. We aim to develop metasurfaces based on the scheme first demonstrated by Arbabi

et al. [110], where the polarisation of the light can be arbitrarily manipulated. Such a scheme has recently been proposed in TiO_2 [205]; our modelling here uses silicon nitride however it is easily adapted for designing TiO_2 metasurfaces.

5.3.1 Theory

The application of dielectric nanorods as the unit cell in optical metasurfaces comes from the extension of Mie theory for the scattering of dielectric spheres [206]. The Mie resonances of the dielectric spheres to optical electric fields leads to the multi-pole emission of the sphere of which the electric and magnetic dipole emission are dominant. The sphere then acts as an artificial atom, with its own effective permittivity and permeability, and tuning of the Mie resonances, by changing the geometry of the scatterer, allows for control over the optical response. While close-form analytical expressions are available for dielectric spheres, they are hard to fabricate in practice and so cuboids or cylindirical nanorods are typically considered. The more complex resonant response of these structures requires the use of finite-difference-time-domain (FDTD) methods to simulate their optical properties. While many exotic optical responses are possible with such a scheme such as the creation of negative refractive indicies [181] we are interested in the simple modulation of the phase fronts of an input electric field, however we note the scope of advanced possibilities with such a scheme.

We consider a hexagonal lattice of nanorods of lattice constant $a<n_s\sqrt{3}/(2\lambda_0)$ where n_s is the substrate refractive index which we take to be fused silica (see Figure 5.14) [110]. Varying of the major and minor ellipse diameters allows for control of the resonant response, while the height, h, of the pillar can be tuned such that the nanorod has high transmission to the design wavelength. The angle, θ, of the y axis to vertical controls the polarisation axis, however for all simulations we set $\theta = 0$.

As we now have full control over independent phase control for both x and y polarisation the transmittance function becomes the matrix quantity

$$\begin{pmatrix} E_{2,x} \\ E_{2,y} \end{pmatrix} = T \begin{pmatrix} E_{1,x} \\ E_{1,y} \end{pmatrix} = \begin{pmatrix} T_{xx} & T_{xy} \\ T_{yx} & T_{yy} \end{pmatrix} \begin{pmatrix} E_{1,x} \\ E_{1,y} \end{pmatrix} . \tag{5.31}$$

For transmittance matrices with $T_{xy} = T_{yx} = 0$ (that is, there is no polarisation mixing) the values of T_{xx} and T_{yy} can be independently designed using SDT. We leave more advanced designs with polarisation mixing for further study. Our main interest is in the development of dielectric metasurfaces for the generation of circularly polarised light for optically pumping $^{88}Sr^+$ ions. A $\lambda/4$-waveplate for converting light equally polarised in the x and y axis can be realised using the transmittance function

$$T = \begin{pmatrix} T_{xx} & 0 \\ 0 & T_{xx} + \frac{\pi}{2} \end{pmatrix}, \tag{5.32}$$

where T_{xx} can be any transmittance function generated by Equation 5.4.

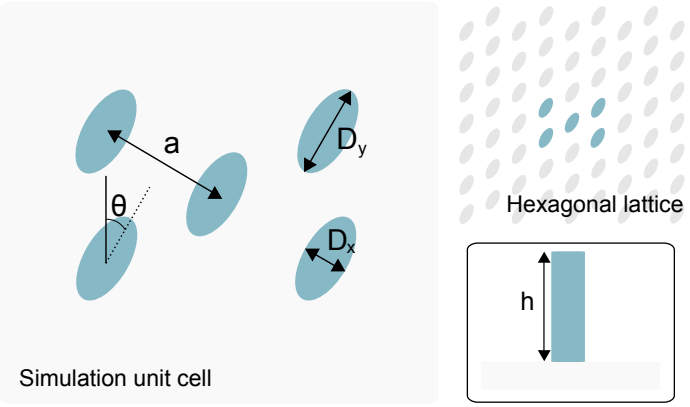

Figure 5.14: Concept of metasurface composed of dielectric nanorods. Simulations of nanorod behaviour are considered as infinitely repeating unit cells of 5 nanorods with lattice spacing a, diameters $D_{x,y}$ and angle with the polarisation axis, θ. The height, h, of the nanorod is tuned to have high transmission over the full phase shift range.

5.3.2 Design

We considered the unit cell of a hexagonal lattice as shown in Figure 5.14. The unit cell was simulated in *Lumerical FDTD* with periodic boundary conditions on a fused silica substrate. The pillar material used here is silicon nitride, however other materials transparent at blue wavelengths (such as titanium dioxide) can also be considered. Plane waves of $\lambda_0 = 405$ nm and either x or y polarisation were injected from within the substrate and the output electric field was collected at $\lambda/2$ from the top of the pillars. A lattice constant of $a = 300$ nm was used such that the pillars were subwavelength, and pillar diameters were varied in both the x and y directions from $50-300$ nm. The lower bound on the pillar diameter was due to a practical consideration of fabrication constraints, and the upper bound is the lattice constant. The electric field phase value for $D_x = D_y = 50$ nm was used as a reference, and all phase shifts were calculated with respect to its value.

An example parameter scan for a pillar height of $h = 500$ nm is shown in Figure 5.15. We found a full 2π phase coverage with average transmission of 90 and 91% for x and y polarisations respectively. Due to restrictions on computational resources it was not possible to fine tune the pillar height to maximise transmission (that is, minimising resonances), and we therefore expect maximum transmissions to be increased with further study. The measured phase shift matrices are inverted to create look up tables for x and y diameters for a desired phase shift, with any degeneracies broken by prioritising diameters with higher transmission. The presence of many pillar diameter combinations with the same phase shift led to many degeneracies which produces non-intuitive phase-shift lookup tables for maximising transmission as shown in Figure 5.15(e-h).

Metasurface lens design is achieved first by generating a desired phase profile for both x and y polarisations. For the case of no off-diagonal transformation matrix elements, this can be done separately using scalar diffraction theory. Each phase profile is mapped onto a hexagonal lattice using the

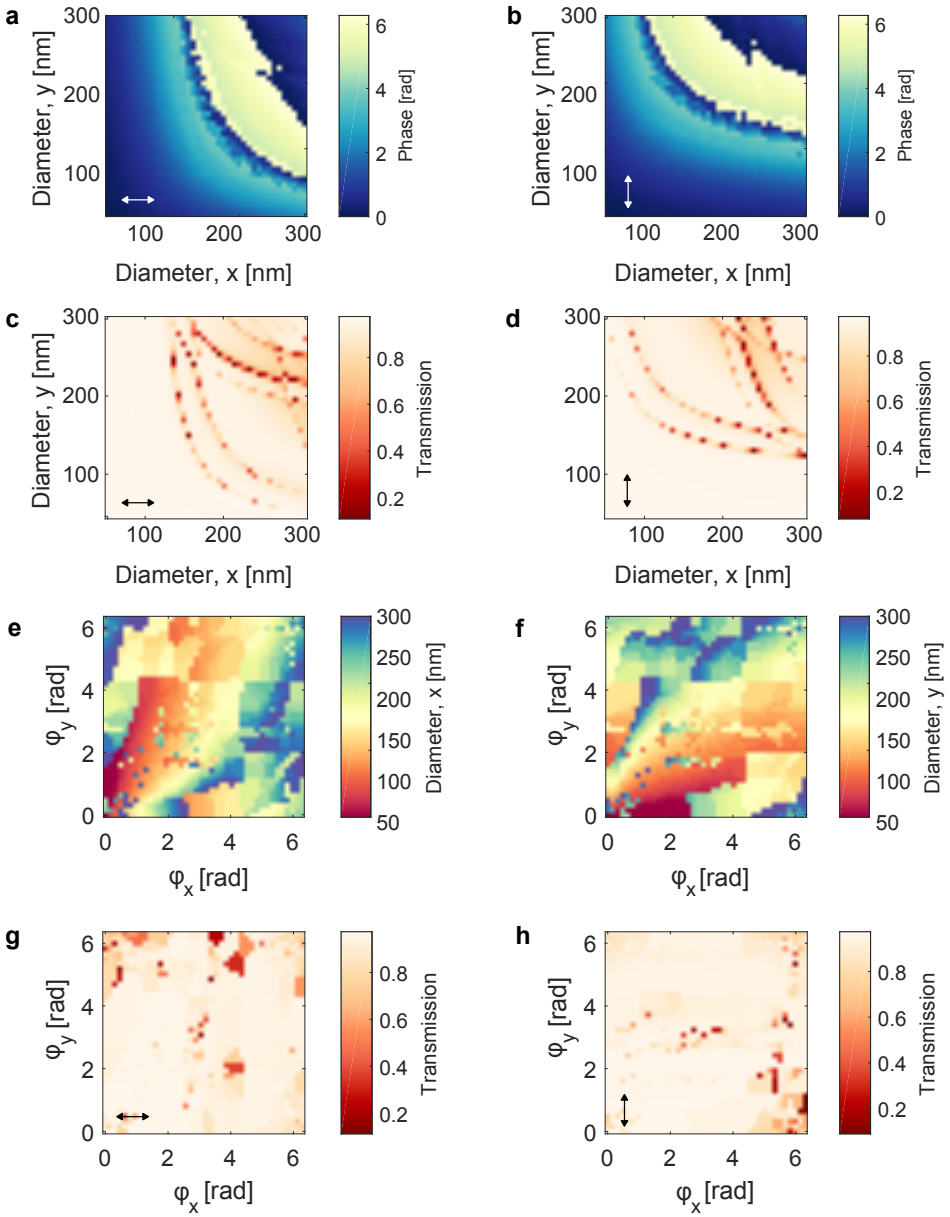

Figure 5.15: Simulation results of silicon nitride nanorods of varying diameters and h = 500 nm. The polarisation state is indicated by horizontal (x) and vertical (y) arrows. (a-b) Phase shift with pillar diameter for x and y polarisations; (c-d) respective trasnmssion for each pillar diameter; (e-f) Inverted matrices of (a) and (b) displaying required diameter with required phase shift; (g-h) respective transmission at each phase shift in (e) and (f).

nearest pixel phase value and then pillar diameters are found using the lookup matrix. For trapped ion addressing it would be useful to both rotate linear polarisations and generate circular polarisation which can be achieved using a $\lambda/2$ and $\lambda/4$-waveplate respectively. The k-vector generation is performed using off-axis DML design process as with surface-reliefs.

To demonstrate the flexibility, ease of design and applicability to trapped ion addressing, we generate three example metasurfaces shown in Figure 5.16a. The first design is polarisation insensitive, with parameters $z_1 = -1000$ μm and $z_2 = 500$ μm. As seen in Figure 5.16a(a), the majority of pillars are circular as one would expect for polarisation degeneracy. The lens has an average transmission of 90% for both polarisations. For more advanced control we also design a $\lambda/4$ waveplate, as outlined in the theory section above. Equal magnitude x and y polarisations incident on the metasurface would be converted into circularly polarised light and then focused to a point. This is achieved by setting the y-polarisation phase profile to be $+\pi/2$ to the x-polarisation profile. For the focusing $\lambda/4$ waveplate we find an average transmission of 90%. A $\lambda/2$ waveplate is also designed, with a $+\pi$ phase shift between polarisations and has an average transmission of 91%.

5.3.3 Proposed fabrication

Previously reported dielectric metasurfaces have been fabricated using a variety of process flows, but due to their small features sizes they are typically fabricated using electron beam lithography. We propose a fabrication process for silicon nitride metasurfaces similar to Arbabi et al [110], shown in Figure 5.17, and influenced by the fabrication process developed in the next Chapter 6. First, a silicon nitride film is deposited using PECVD on a fused silica substrate. The PECVD recipe would be optimised for low loss and high refractive index at blue wavelengths. A layer of poly(methyl)-methacrylate (PMMA) resist would be spun onto the silicon nitride surface, with a thickness of 100–500 nm. The elliptical cross-sections of the pillars would be exposed using electron beam lithography. For an electron acceleration voltage of 50 keV preliminary simulations of electron exposure of the PMMA resist indicate that no proximity compensation would have to be performed, however due to the small feature sizes in closely packed arrays it may be required. After exposure the PMMA would be developed in a 7 : 3 ratio of isopropyl alcohol and deionised water, with exact development time optimised for side-wall steepness and clearing of the PMMA resist to the Si_3N_4 layer. The developed sample would then be coated in a thick (~50–100 nm) aluminium film using thermal evaporation such that both the PMMA and exposed Si_3N_4 would be covered. Ideally, the sidewalls would not be coated, with a clear disconnect between the PMMA and Si_3N_4 metal films. Immersion of the sample in acetone would selectively dissolve the PMMA, *lifting off* the metal on the PMMA layer and leaving behind the Al on the Si_3N_4 layer. The metal ellipses can then be used as a hard mask for the selective etching of Si_3N_4. Reactive ion etching would be performed using a gas mixture that etches Si_3N_4 at a

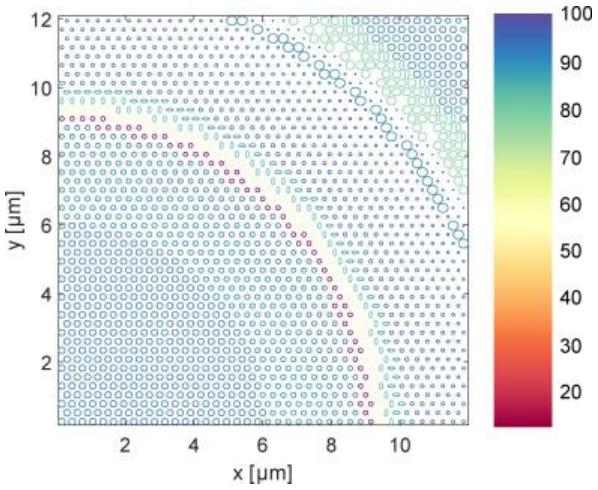

(a)

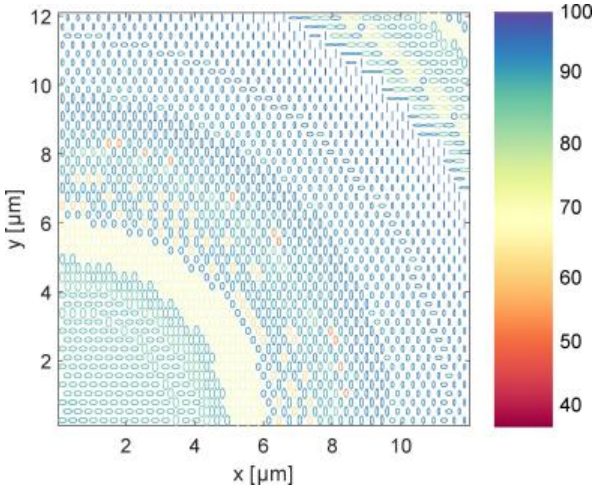

(b)

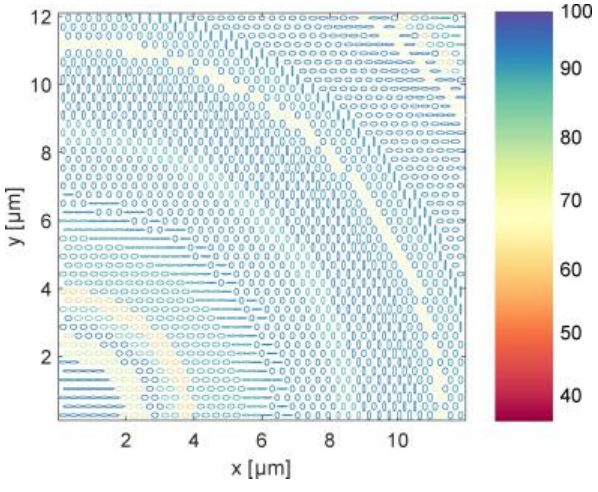

(c)

Figure 5.16: Subsections of metasurface designs for (a) a polarisation insensitive lens; (b) a focusing $\lambda/4$-waveplate; (c) a focusing $\lambda/2$-waveplate. The colour map indicates averaged x and y polarisation transmission of the silicon nitride nanorods.

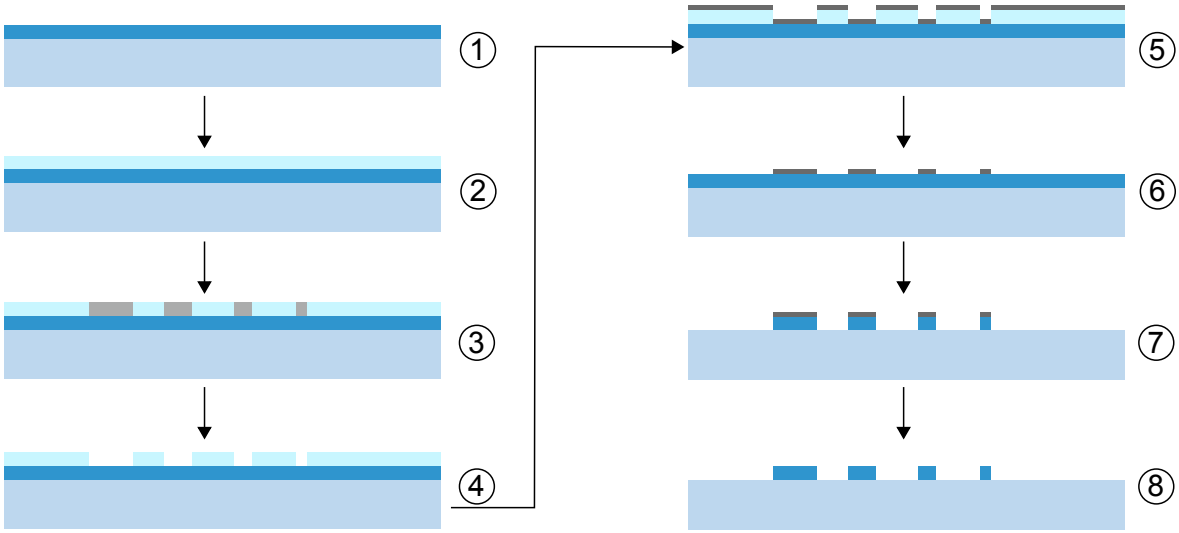

Figure 5.17: The proposed fabriction process for fabrication of silicon nitride metasurfaces. (1) PECVD growth of silicon nitride (dark blue) on fused silica (light blue); (2) Spinning of PMMA resist (lighter blue) onto silicon nitride surface; (3) Exposure of PMMA resist to electrons in the required elliptical patterns; (4) Development of the PMMA; (5) Thermal evaporation of Al; (6) Dissolving of the PMMA resist in acetone to lift off unwanted metal; (7) Reactive ion etching of sample using the Al as a hard mask; (8) Removal of the Al mask.

much faster rate than Al. An example gas mixture is $CHF_3/SF_6/Ar$, where the ratio of CHF_3:SF_6 would control sidewall polymer formation and the flow rate of Ar would control the physical etch rate. After etching the Al disks could be removed in diluted tetramethyl ammonium hydroxide.

The proposed fabrication technique could be completely performed in-house at the University of Bristol, with all apparatus required available. Optimisation of the gas mixture would be the greatest determinant in the performance of the final device, with vertical pillars with low surface roughness being essential. The metal lift-off process would also have to be optimised such that the Al had good adherence to the Si_3N_4 and the ellipses remain on the surface in their design dimensions. The motivation to undertake such an optimisation project is high, with the reward being flexible, advanced optics for the manipulation of phase and polarisation in optical electric fields at wavelengths suitable for addressing of $^{88}Sr^+$ ions.

5.4 Discussion and conclusion

The interfacing of trapped ions with diffractive optics requires an accurate, computationally efficient and flexible model for optic design. We introduced the model of scalar diffraction theory and protocols for how to design and simulate phase profiles in the SDT framework using a variety of techniques. The point-to-point model is a simple extension of the Fresnel lens model that allows for beam steering off-axis, which is a requirement for trapped ion addressing. The physical realisation of phase profiles as varying height profiles in optical materials was then discussed, and vector finite element method simu-

lations showed that SDT could design diffractive surface-reliefs with accurate, high efficiency focusing and beam steering. The transmission of surface-reliefs is a key metric for diffractive microlenses, both for power efficiency and in optical testing when determining the amount of power focused in a desired diffraction order. We outlined the reflection processes when surface-relief microlenses are defined in either a bulk material or a thin film, with the thin film experiencing large variations in transmission over the full lens profile.

The numerical demonstration of accurate and efficient surface-reliefs provides a clear path forward for the development of diffractive optics for trapped ion addressing and fluorescence collection. However, the more advanced platform of dielectric metasurfaces was also shown to be applicable, with silicon nitride metasurfaces designed for phase and polarisation control of λ = 405 nm light using FDTD simulation of dielectric nanorods. Focusing quarter and half waveplates with transmission efficiencies of ~90% were generated, which could be used for conversion of linear to circular polarisation and for linear polarisation rotation respectively. The main challenge with dielectric metasurfaces is in the sensitivity of a given wavelength to the height of the dielectric nanorods. As shown in the proposed fabrication process, the silicon nitride layer is a set thickness for all lenses and therefore a height must be found that can produce full 2π phase shifts with high transmission over the wavelength range of 405–1092 nm to be useful to interfacing with $^{88}Sr^{+}$ions. As the simulation of the phase shift of each pillar diameter is computationally intensive, the further study of wavelength independent pillar heights is best conducted for varying pillar radii before expanding candidate heights to the full x and y diameter variations.

Given the further study required for a full implementation of dielectric metasurfaces to trapped ion applications, we choose to pursue the fabrication of high efficiency and accurately focused DMLs as surface-reliefs in dielectric materials. The development of a fabrication process for realising such DMLs is presented in the next chapter.

6

Diffractive optics: fabrication and testing

Part of the work presented in this chapter appears in ***Day, Matthew, et al. "Continuous-relief diffractive microlenses for laser beam focusing." Optics express 25.22 (2017): 26987-26999.***

In the previous chapter we outlined the theory of using surface-reliefs in optical materials to impart spatial phase modulations on beam fronts for the purpose of trapped ion fluorescence collection and laser beam deflection and focusing. We now turn to the process of physically realising such structures. The fabrication of surface-relief diffractive optics can be realised using a variety of different techniques [106, 207] including electron beam lithography (EBL) [208], reactive ion etching (RIE) [208], optical lithography (masked illumination [209], or laser writing [210]), focused ion beam (FIB) milling [211] and compression moulding [212]. The choice of fabrication process is determined by the required feature sizes of the diffractive optics under consideration, which is dependent on the wavelength of the light to be manipulated and the required deflection angles of the incoming and outgoing beams. Compression moulded optics require the fabrication of a master mould which are created using diamond turning tools with a realtive low resolution of ~2 μm [212]. Optical lithography is limited by the wavelength of the light used for mask illumination, and if laser lithography is used then the diffraction limit of the focused laser beam limits the resolution of the process such that single pixel resolutions are approximately ~1 μm [106]. Photosensitive resists are used for lithography and therefore the choice of diffractive material is limited unless the resist profile is transferred into the desired optical substrate. FIB milling directly removes material through the chemical and physical interaction of focused ions with the desired substrate, allowing for single-step fabrication of diffractive surface-reliefs with resolutions of ~100 nm. EBL has the highest resolution, with typical beam diameters of ~5 nm, however structures must be written in an electron-sensitive resist. RIE is a common and mature process for transferring EBL resist patterns into semiconductor and dielectric materials, and as such can be used to fabricate surface-reliefs from an EBL resist mask. Therefore

Fabrication technique	Number of levels	Maximum diffraction efficiency [%]	Source
EBL and RIE	16	94	[208]
Laser lithography	Continuous	65	[210]
FIB milling	Continuous	91	[211]
Compression moulded	Continuous	91	[212]

Table 6.1: State-of-the-art diffraction efficiencies for several fabrication techniques of surface-relief diffractive optics.

the combination of EBL and RIE allows for the highest resolution fabrication process at the expense of optimisation of multiple fabrication steps. A summary of state-of-the-art diffraction efficiencies for a selection of fabrication techniques is shown in Table 6.1, demonstrating the gain in diffraction efficiency from using EBL and RIE over laser lithography.

The development of fabrication processes for diffractive microlenses (DMLs) for interfacing with trapped ions requires defining surface-reliefs in a vacuum compatible material with a range of designs, from on-axis collection optics to off-axis addressing optics. The DMLs must be accurately patterned such that they are high in diffraction efficiency to both reduce light scatter and increase ion fluorescence collection, as well as being accurate in beam steering such that a trapped ion can be addressed from many DMLs simultaneously. The required accuracy for overlapping two or more beams can be highlighted by considering the deflection of two Doppler cooling beams (λ = 422 nm) by 20° to the same point in space, 2 mm away from the lens plane. The beam radius of a Gaussian beam approximately corresponds to an order of magnitude drop in intensity and therefore to maintain appreciable coupling of the two beams to a trapped ion placed at the design focus point of the two DMLs then their actual focus point should not deviate by more than 1 beam radius. Considering a realistic beam radius of 10 μm, this corresponds to an approximate 1% error in beam pointing accuracy. A 1% angle error is manifested as a 1% pitch error for a 20° deflected beam, which at blue wavelengths equates to a pitch tolerance of ~10 nm. At smaller deflection angles, longer wavelengths or larger beam radii these tolerances are relaxed, whereas at greater deflection angles, shorter wavelengths and smaller beam radii the fabrication tolerances could become prohibitive. For example, at 45° beam deflections, pitch tolerances approach 1 nm. In light of these strict tolerances we concentrate on the two highest resolution fabrication techniques. In this chapter we explore FIB milling, EBL and RIE processes for fabricating surface-relief diffractive optics. We first use FIB milling for model testing and prototyping of on-axis DMLs before moving onto rapid prototyping using EBL of both on and off-axis DMLs. The transfer of EBL resist structures using RIE into a high-κ dielectric material suitable for vacuum operation will complete our study of fabrication of DMLs for ion trap applications.

6.1 Methods

The microfabrication of any device requires a combination of methods and techniques for both realising the required device, as well as for providing feedback on how to improve the fabrication recipe. In this section we outline the numerous methods used during our study.

6.1.1 Techniques for characterisation of fabricated profiles

We begin by detailing the techniques which were used to provide recipe feedback, including those to characterise fabricated lenses and test structures used to verify and calibrate fabrication processes.

Surface-profile shape analysis

The shape of diffractive surface-reliefs places some challenging constraints on the measurement techniques that can be used to characterise them. The combination of feature sizes down to 1 μm and steep vertical steps makes accurate shape analysis of fabricated profiles difficult. Optical profiling techniques are limited by coarse lateral resolution, and fail when the feature size approaches the wavelength of the light used. Physical profiling techniques, such as atomic force microscopy, are limited by the physical extent of the probe being used, meaning that sharp discontinues cannot be accurately resolved. We therefore use a combination of optical and physical profiling techniques for the characterisation of surface-reliefs.

Laser-scanning confocal microscopy An *Olympus LEXT OLS4000* laser-scanning confocal microscope was used as a non-invasive profiling technique, with ~1 μm lateral resolution. The machine is based at NPL and was used to characterise lenses fabricated using FIB milling.

Stylus profiler A *Bruker DektaXT* stylus profiler with a 2 μm tip was used to characterise step heights and other large fabricated features. The large size of the tip excluded its use for characterising small pitched features with sharp discontinuities such as gratings and surface-reliefs.

Optical profiler A *Filmetrics Profilm3D* optical profiler was used to characterise the shape of shallow surface-reliefs. It was found that the system could not resolve grating pitches of < 5 μm or diffractive surface-reliefs of depth > 500 nm. Therefore the optical profiler was typically used to characterise the central dome and neighbouring annuli of on-axis surface-reliefs of shallow depth.

Atomic force microscopy An *Agilent Technologies 5420* atomic force microscope (AFM) was used for surface roughness and surface profile analysis. A *NuNano Scount Beta* tip was used, with a tip length of 7 μm and end diameter of < 10 nm. The tip was a cone of ~25° and therefore discontinuities

in surface profiles appear as a convolution of the tip and vertical step height. For this reason the AFM was an insufficient tool for accurate profile determination of near vertical discontinuities. However, it gave accurate slope shapes, could resolve 1 μm pitch grating elements, and could measure surface roughness.

Optical testing

The optical testing of fabricated DMLs was used to characterise their performance and conformity to design, including the accuracy of beams propagating from the DMLs and their diffraction efficiency. We use a bulk testing set-up for rapid testing of fabricated structures with a well defined source beam for comparison of DML structures to both each other and to design.

Bulk optical test rig The bulk optical setup for testing diffractive optics at ~405 nm wavelengths is shown in Figure 6.1. A 404 nm laser diode (*Toptica iBeam Smart*) was first passed through an optical isolator, before being polarisation purified with a Glan-Taylor polariser. A $\lambda/2$-waveplate in a rotational mount and second polariser allows for laser power control without changing the current of the laser which would cause frequency shifts in the laser output light. The laser spectrum was spectrally filtered with a 1.5 nm bandpass filter (*Semrock LL01-407-12.5*) before the light was coupled into single-mode fibre for blue light (*Thorlabs FC/APC S405-XP*) using two silver mirrors in stable mounts (*Polaris*) and an aspheric lens. The laser preparation was designed to minimise power fluctuations, both by minimising effects inside the laser (isolating feedback, not changing the laser current) and by stabilising the coupling into fibre (stable mounts, in a z-shaped configuration).

The fibre acted as a spatial filter of the elliptical and distorted laser mode, and was out-coupled using a triplet collimator (*Thorlabs TC06APC-405*) into an approximately Gaussian profile. The beam was then focused to a beam waist of 3.75 μm (in glass) using a 10×, 0.3 NA objective (*Olympus MPLFLN10x*). The beam waist was chosen such that we could test DMLs of radius ~100 μm which reduced fabrications times. The mode-field diameter of the single-mode waveguides for blue light are smaller than the test beam waist and therefore will require larger lenses. The large test beam waist is sufficient for DML fabrication development and model testing. The collimator and objective used to generate the beam waist can be moved in 3-axes using a 3-axis micrometer stage such that the source beam waist can be freely positioned in space.

The sample under test was mounted on a rotational mount (*Thorlabs RSP1/M*), which was mounted on a 3-axis flexure stage (*Elliot Gold*) with 2 mm of travel such that the lens plane can be moved around in the $x-y$ plane with respect to the source beam. The ability to translate the lens plane independent to the source beam was useful for rapidly testing multiple lenses on the same substrate. The source beam waist was placed inside the sample such that it was the design distance from the lens plane,

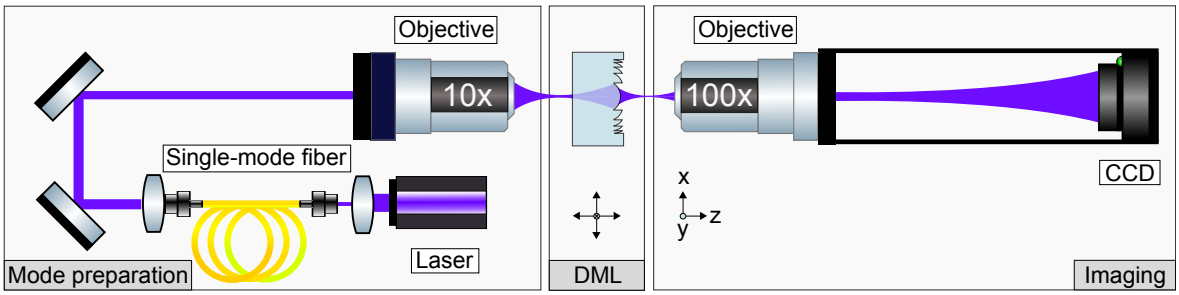

Figure 6.1: Diffractive optic characterization set up. Mode preparation consisted of coupling a 404 nm laser diode into single mode fibre before collimating and centring on a 10× objective to focus light to beam radius $w_0 = 3.75$ μm at $z = -1000$ μm from the optic surface. The source beam then expands to a radius of $w(z = 0) = 22.8$ μm at the surface of the DML. Note that 99.9% of the incident beam overlapped with a central area of the DML of radius 22.8 μm. The focused spot created by the DML was imaged onto a CCD sensor via a 100× or 50× imaging objective.

which was confirmed by measuring the beam radius in the lens plane.

The output of the diffractive optic was collected using a long working distance microscope objective (*Olympus MPLFLN100×, Olympus MPLFLN50×*) to expand the beam profile onto a beam profiling CCD (*WinCamD UCD-12*). The objective and beam profiler were mounted in a cage system, with ~16 cm between the objective and the CCD plane such that for a 100× (50×) objective, the resulting magnification of the beam was 87.64× (45.12×), calibrated with a calibration graticule (*Graticules Ltd.* 10 μ*m rules*) imaged in the same manner as the diffractive optics. The cage system was mounted on a 3-axis stage, with motion along the optical axis computer controlled (*Newport LTA-HL*) at 1 μm resolution.

Off-axis beam profiles were imaged using a 50× objective with a numerical aperture of 0.8, corresponding to a maximum acceptance angle of 53°. For characterisation of off-axis angles an exposed board camera CCD (*Raspberry Pi Camera Module V2 NoIR*) replaces the microscope objective. The 1.12 μm pixel pitch of the CCD allows beam positions to be characterised with high resolution.

Beam radius The beam profile was recorded on the CCD, typically averaging over 20 frames. The background was recorded with the same number of averages, at the same exposure time, but with the laser beam blocked. The image was imported into MATLAB, background subtracted and a 2D Gaussian function was fitted (as previously introduced in Section 4.2.5).

Diffraction efficiency measurements (bulk material) We define the diffraction efficiency, η_D, as the ratio of the input power to the outputted power in the desired diffraction order. To the best of our knowledge there is no agreed technique present in the literature for measuring diffraction efficiencies. One fairly consistent technique is to measure the input and output beams on a power meter, using a physical pinhole to reject background power. The limitation with this technique is the fixed size of the pinhole, invariably leading to an inaccurate measurement of power at a diffractive optic focus, either

taking in too much background, or clipping the beam. Often no technique is cited or no pinhole is used. If no pinhole is used, the output power is overstated as the light scattered into higher orders is collected.

To measure diffraction efficiency with a robust approach to meaningful accuracy and reproducibility, we calculate it from beam profile images taken with a beam profiling CCD fully calibrated for linearity. The signal of each pixel is directly proportional to an intensity (see Appendix A), and so numerically integrating over the beam profile (i.e. summing all the pixels) provides a power measurement. We can implement a numerical pinhole by calculating the radius of the beam and set all values of the image to zero a distance $2w_0$ from the beam centre, corresponding to 99.97% of the power of an ideal Gaussian beam. The measurement of the diffraction efficiency is performed by first taking a beam profile in the desired output mode (e.g. for an on-axis lens, this is at the focus of the lens), then measuring a beam profile of the source beam through a clear portion of the substrate, to account for Fresnel losses. The two beam profiles are background corrected, and their beam radii calculated. A numerical pinhole is implemented and the power is calculated by summing all the pixels in the resulting array. The ratio of the focussed and source beam powers is then the diffraction efficiency of the lens.

The error in our diffraction efficiency measurement was quantified by measuring the combined Allan variance of the noise of the CCD and the laser. The measurement was performed by taking 3600 beam profile measurements of a focused beam at ~0.5 Hz. The power of the beam profile was calculated in the same way as the diffraction efficiency measurements, and then the overlapping Allan variance was calculated. The square root of the Allan variance, the Allan deviation, is in the same units as the power measurement and so is equivalent to a root-mean-square error on the power measurement. For a laser power of 20 mW we find a minimum error of 0.1% on the time scale of minutes, the timescale that we take our diffraction efficiency measurements. Despite this, we use the instantaneous error (after 1 image) of 0.5%. As we are comparing two power measurements, we add the error in quadrature such that the error in the diffraction efficiency measurement is 0.7%. To reduce the error estimate, more advanced schemes could be implemented where the laser power noise is monitored during the image capture. However, we consider the error estimate to be suitably small for our required measurements.

Diffraction efficiency measurements (thin film) For surface-reliefs defined in a thin film material, we must account for the transmission modifications due to the height variations of the lens as shown in Section 5.2.3. First, we aligned the source beam to the lenses such that the source was the correct size in the lens plane and focused and centred the beam profiler on the lens. We replaced the CCD used for imaging the beam with a power meter (*Thorlabs S120C*). The power transmitted through

the lens under consideration was measured as the average value of 10^4 power meter measurements. The power through the unmodified film was measured in the same way. We define the ratio of the power through the lens to the power through the unmodified film as the transmission efficiency, η_T, of the lens. The transmission efficiency is then used as a corrective factor for the diffraction efficiency measurement. If η_T>1 (η_T<1) then this correction reduces (increases) the diffraction efficiency value. The transmission efficiency correction is necessary as we are quantifying the amount of power that propagates through the lens and is concentrated in the correct diffraction order, without compensating for the different transmission of the source beam through the flat film then the measurement does not achieve this measurement.

Propagation measurements Recording of the beam's evolution along the optical axis was performed using the computer-controlled stage the beam profiler was mounted to. First, the lens plane was imaged to define the z = 0 μm plane. Due to uncertainty in when the lens plane is in exact focus, determination of z = 0 μm has a 5 μm error associated with it. From this position two different measurements could be performed. The first was to move the beam profiler a set distance from the lens plane and image the beam profile at a single location. The location is typically the designed focus position of the lens. The second measurement was to image beam profiles over a range of z values in 1 μm increments. Larger increments did not fully resolve higher diffraction orders for on-axis microlenses.

High dynamic range beam profiling As previously discussed, it is important to determine the background light intensities away from a beam focused by a diffractive optic as any stray light away from the focus can interact with other unaddressed trapped ions, or scatter from trap electrodes into detection optics. The beam profiler used to measure the output intensity of the diffractive optics under test had a quoted maximum signal-to-noise ratio of 10^{-3}. In practice, when using the CCD within its limits of linearity we found signal-to-noise ratios of 10^{-2}. For high diffraction efficiency optics, vector diffraction simulations predicts background intensities on the order of 10^{-5}. We therefore utilised the process of high dynamic range beam profiling (HDRBP) to overcome the noise floor of the CCD [213].

The process of HDRBP is to first image the beam profile at close to the shortest exposure time allowed by the CCD. At this exposure time, the power incident on the CCD is set such that the peak intensity of the profile is 80–90% of the maximum pixel value. An image of the unsaturated beam profile is recorded. The exposure time is then increased by an order of magnitude. The centre of the beam profile then oversaturates the CCD, but any background features are increased by an order of magnitude in intensity. By repeating this process over 4 orders of magnitude, features down to relative intensities of 10^{-5} can be resolved. Recording beam profile intensities over 5 orders of magnitude is only possible if the CCD is linear over this full range. In Appendix A we perform the required CCD

characterisation and calibration, confirming linearity at each exposure time with incident power and calculate signal-to-power calibration values. The calibration allows each image taken at a different exposure time to be related to a power value and the, typically, 4 images can be stitched together. Stitching is performed in MATLAB by cropping out over-saturated, or noisy sections of each image and combining them into one image. An example HDRBP stitching is shown in Appendix A.

6.1.2 Fabrication with focused ion beam milling

Focused ion beam milling is the process of selectively removing material from a substrate by the physical bombardment of accelerated ions. The dwell time of the focused ion beam at each location on the substrate determines the total etch depth, and as such depth profiles can be machined directly. Diffractive surface-reliefs were fabricated at the University of Surrey by David Cox using an *FEI Nova NanoLab 600*. A focused beam of Ga^+ ions with a beam current of 3 nA and accelerating voltage of 30 kV, corresponding to a spot size of ~90 nm (FWHM), was raster scanned over a target area to etch the substrate to the desired profile. The profile designs were quantised into 100 nm pixel sizes, and the height profile was discretised into 1150 levels, with each level differing in height by ~0.65 nm. The finite size of the ion beam, approximately equal to the profile pixel size, leads to a continuous profile.

The FIB process was initially developed and calibrated using an silicon substrate, which could be concurrently imaged using an in-situ scanning electron microscope (SEM) during milling. An SEM image of an example test structure in silicon is shown in Figure 6.2(a). After calibration, surface-reliefs were fabricated in BK7 glass using the same recipe, with minor corrections applied for the slight difference in etch rates between silicon and glass. Before milling, the glass substrate is coated with a ~50 nm film of aluminium, and the metal in the desired lens area is selectively removed before profile milling. We find the Al film is sufficient to prevent charge build-up on the insulating glass surface over the full lens area.

Fabricated surface-reliefs were characterised using a scanning laser confocal microscope, which provided feedback to improve the etch recipe until the desired profile was obtained. A SEM image of several BK7 diffractive surface-reliefs is shown in Figure 6.2(b), as well as alignment and blank test structures. Each 125 μm diameter lens takes ~3 hours to fabricate, and therefore the process does not lend itself to future, large-scale manufacturability of lens arrays for ion trap applications. However, as the process is single-step it is useful for prototyping diffractive optics and testing our models of scalar diffraction theory.

6.1.3 Fabrication with electron beam lithography

Electron beam lithography (EBL) is the process of exposing an electron sensitive thin film (the resist) to a focused electron beam. The resulting exposure to electrons changes the solubility of the resist in

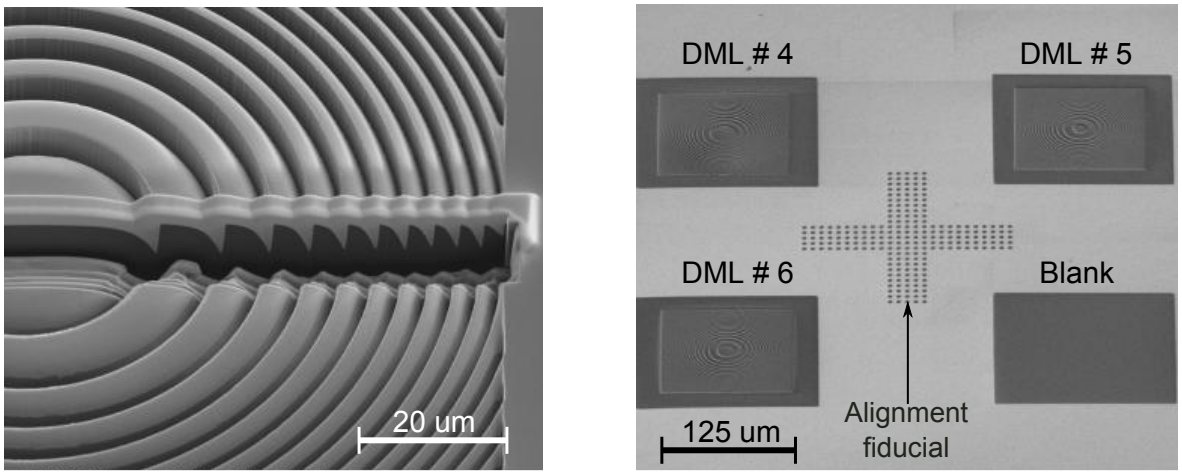

Figure 6.2: a) SEM image of a silicon sample used to test the FIB milling pattern geometry. The sample was prepared by milling a complete lens, then a narrow (~5 μm) strip of Pt was deposited across the lens using FIB-induced deposition, and finally a trench was milled through a section of Pt on Si to reveal the profile of the lens. (b) SEM of a BK7 glass substrate carrying 3 DML designs presented in Section 6.2.1 as well as a blank opening. Light areas indicate metal-coated and dark areas are BK7 glass.

a developer. If the action of the electron exposure is to increase (decrease) solubility, then the resist is called positive (negative). In the following we will discuss positive resists as we used the positive resist poly(methyl methacrylate) (PMMA) to fabricate surface-reliefs. The electron beam breaks the long polymer chains in PMMA and as such increases its solubility to a solvent developer.

Due to the very small diameter of the electron beam, nanometre patterning resolution is possible. By carefully optimising the development process, the material can be precisely removed, leaving a desired shape in the material. The most common use of EBL is to fabricate binary structures and the process development is then to find the electron dose and development time that clears the resist to the substrate, referred to as the *clearing dose*. To fabricate greyscale surface-reliefs, our aim is to fabricate a continuous change in resist height. The process development is then an exercise in determining and controlling the change in resist height with varying electron dose for a set development time.

As PMMA has a similar refractive index to glass and is transparent over the visible and near-IR spectrum, patterned surface-reliefs in the resist can be used as diffractive optics. The drawback is that PMMA films will flow at >100°C and will out-gas in UHV, so the lenses must be transferred into a dielectric material for trapped ion applications. The transfer is performed using reactive ion etching, which will be introduced and discussed in Section 6.1.4. To aide the transfer process, we opt to transfer the resist patterns into a thin film of titanium dioxide (TiO_2) due to its higher refractive index over fused silica. As motivated by Equation 5.17 the high refractive index allows the maximum depth of the surface-reliefs to be greatly reduced, decreasing aspect ratios while also allowing for the fact that the dielectric will etch slower than the polymer resist.

Process

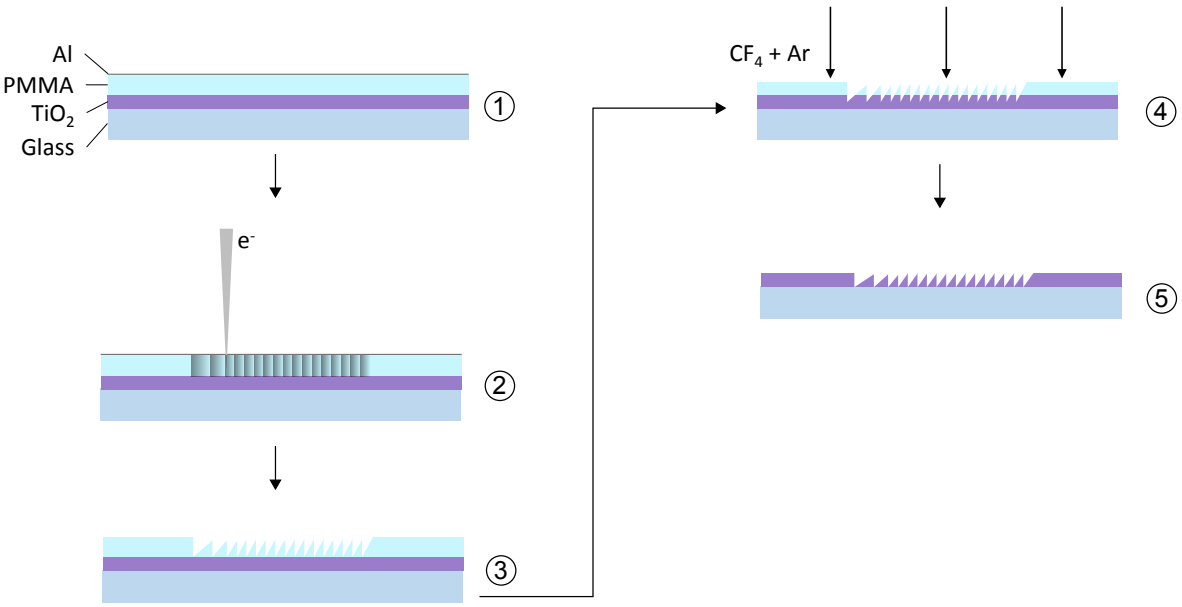

Figure 6.3: The main steps in the EBL and RIE process of fabricating DMLs in PMMA and titania. (1) Preparation of the full stack; (2) Exposure of PMMA resist to a greyscale dose pattern of electrons using a focused electron beam; (3) Removal of Al film and development of PMMA resist, leaving a continuous profile in the resist; (4) RIE of PMMA resist for transfer into the titania sub-layer (5) The final profile defined in titania. Layer thicknesses and feature sizes are not to scale for the sake of clarity.

The full material stack for the development of an EBL process for fabrication of diffractive surface-reliefs is shown in Figure 6.3. A fused silica wafer of 1 mm thickness (*Edmund Optics*) is coated with ~1 μm of amorphous titanium dioxide (provided by *PlasmaQuest*). The wafer is diced (*Loadpoint*) into 1×1 cm^2 squares. The substrates are solvent cleaned, first in methanol, then acetone, and finally isopropyl alcohol (IPA), where for each solvent, the substrates are placed in an ultrasonic bath for 5 minutes. The substrates are then rinsed in deionised water and dried with dry nitrogen. The substrates are placed on a hot plate at 100°C for 10 minutes to further dry. Resist coating is performed by depositing ~40 μL of PMMA950 A11 (*Microchem*) on each 1 cm^2 square using a pipette, leaving for 10 seconds to spread and then spinning at 2500 rpm for 45 seconds (3000 rpm/s^2 acceleration) to create a ~2.5 μm film of PMMA on the substrate surface. The samples are then baked for 4 minutes at 200°C on a hotplate to fully evaporate any remaining solvent. The increased temperature and bake time over that recommended on the PMMA datasheet was required as it was found that under-baking the samples resulted in cracks forming in the resist after development. As none of the materials in the stack are conductive, a conducting layer is required to remove electrons from the resist surface during electron exposure and we use a ~13 nm aluminium film, deposited using thermal evaporation. We found that for doses >1400 μC/cm^2 the aluminium film is damaged, however the typical doses used were far below this threshold and the 13 nm of Al was sufficient. After preparation, the samples are

placed in a vacuum storage jar to prevent degradation of the PMMA resist as it was found that PMMA stored in ambient conditions changed its electron dose response over time, most likely to to reactions of the stack (either the Al or the PMMA) to oxygen. We typically prepared 4 to 8 samples at a time (which we refer to as a *sample batch*) and therefore to maintain a consistent dose response required for precise control over surface-relief shapes for all samples the vacuum storage jar was required.

Electron beam exposure was performed using a industry-grade electron beam lithography system (*Raith VOYAGER*) with a 50 kV acceleration voltage. Structures were written on low current mode (~480 pA) with a 60 μm column aperture. Higher currents would allow for quicker write times, however it was found that desired structures were written in several minutes or less which we deemed suitable for our application. DMLs were written using greyscale dose maps with 25 nm pixel sizes. We assumed a linear relation between the dose value and the bitmap pixel value, with the maximum dose value controlling the maximum depth of the resulting DML. We used the native bitmap job preparation software of the system to quickly fracture and pattern bitmaps with millions of pixels. The square EBL write-field has a side length of 500 μm, and therefore any structures less than this dimension will not suffer from any stitching errors.

The sample is developed less than 1 hour after the end of electron exposure, as we found that leaving the sample for longer changes the developed shape in the PMMA for the same dose curve. First, the substrate was submerged in diluted tetramethyl ammonium hydroxide (*Shipley MF CD-26 developer*) for ~1.5 minutes to remove the Al film. PMMA resist is typically developed in a solution of mehtly isobutyl ketone (MIBK) and IPA in a 3:1 ratio. However it has previously been shown [214] that a solution of IPA and water offers improvements over MIBK:IPA in sensitivity, contrast, exposure latitude and surface roughness. Along with the easy and cheap availability of high purity grade IPA, the improvement in surface roughness was a major consideration in selecting IPA:water as the developer. We selected the ratio of 7:3 IPA:water as recommended by Yasin et al. [214], offering both high sensitivity (reducing write times) and high contrast (allowing for higher resolution and steeper step-heights). In practice, the samples were developed in a mixture of 21 ml and 9 ml of IPA and DI water respectively with no agitation (often called dip development) for 30 seconds, and then rinsed in DI water for a further 30 seconds to halt development and wash debris from the surface. A detailed characterisation of the dose response of the resist is performed in the next section.

Dose calibration of PMMA

The precise determination to the response of PMMA to electron doses was vital to the realisation of high-efficiency DMLs. As the dose response changes with substrate, sample preparation, conductive film thickness, developer composition and other factors, it must be calibrated for the specific process being used. In this section we perform this calibration as well as methods to faithfully realise designed

profiles in PMMA. In practice, we find that the dose response depends on the feature size of the resist pattern with smaller features developing slower than larger ones. The reason for the reduced sensitivity is most likely due to the lower mobility of fresh developer into thinner exposed regions. As DMLs are composed of thin grating-like structures, the feature size dependence of the electron dose response must be compensated for to faithfully fabricate surface-reliefs of the designed depth to maximise diffraction efficiency. We begin by quantifying the dose response of large areas of PMMA before measuring the difference in dose response for smaller feature sizes.

Dose curve determination The datasheet for PMMA 950 A11 specifies using 350 μC/cm^2 as the base electron dose and we use the convention where we specify the dose as a multiple of this base dose, called the *dose factor*. The dose response of PMMA with a ~13 nm Al film is found by exposing 5 μm wide steps at dose factors from 0 to 3, in 0.1 increments. An initial step of dose factor 1 is included before the dose factor 0 step, to mark where the dose steps start. The steps are 100 μm long such that a stylus probe can be easily traced over the step pattern. The stylus trace is translated into a dose curve by finding the centre of the first step (2.5 μm from the start) and extracting the step height every 5 μm. It was found that the exact clearing dose varied from sample batch to sample batch, most likely due to variation in the Al film thickness during evaporation. The clearing dose was consistent among sample batches, allowing calibration of a sample batch using the first sample. The clearing dose factor of the dose steps is typically ~1.1. An example dose curve is shown in Figure 6.4. The PMMA exhibited an exponential dose curve of the form

$$D(d) = \alpha_1 \exp(\alpha_2 d) + \alpha_3 \tag{6.1}$$

where D is the depth, taking negative values, d is the dose factor. α_1, α_2 and α_3 typically have values of −0.01899, ~4.3 and 0.02174 respectively, with the value of α_2 varying between sample batches.

Effect of small features on dose curve During the fabrication of test surface-relief diffractive optics, it was found that the clearing dose factor was ~1.4, greater than for the dose steps. The increased clearing dose is most likely due to a reduced penetration of the developer into the smaller feature sizes of the DML. Agitation during development may reduce the feature size dependence by increasing turn-over of fresh developer in the exposed regions. However, to increase repeatability we opted to instead characterise the modified clearing dose for agitation-free development. Ultrasonic agitation could be used in the future to improve the fabrication of small-pitched features, as previously shown by Rooks et al. [215]. The clearing dose was initially found visually on an optical microscope before using the diffraction efficiency of DMLs for a more precise determination of the clearing dose. Using the known refractive index of PMMA 950, we calculated the optimal surface-relief depth for 404 nm wavelength light as 790 nm. Fabricating surface-reliefs with different maximum dose factors, we found the dose

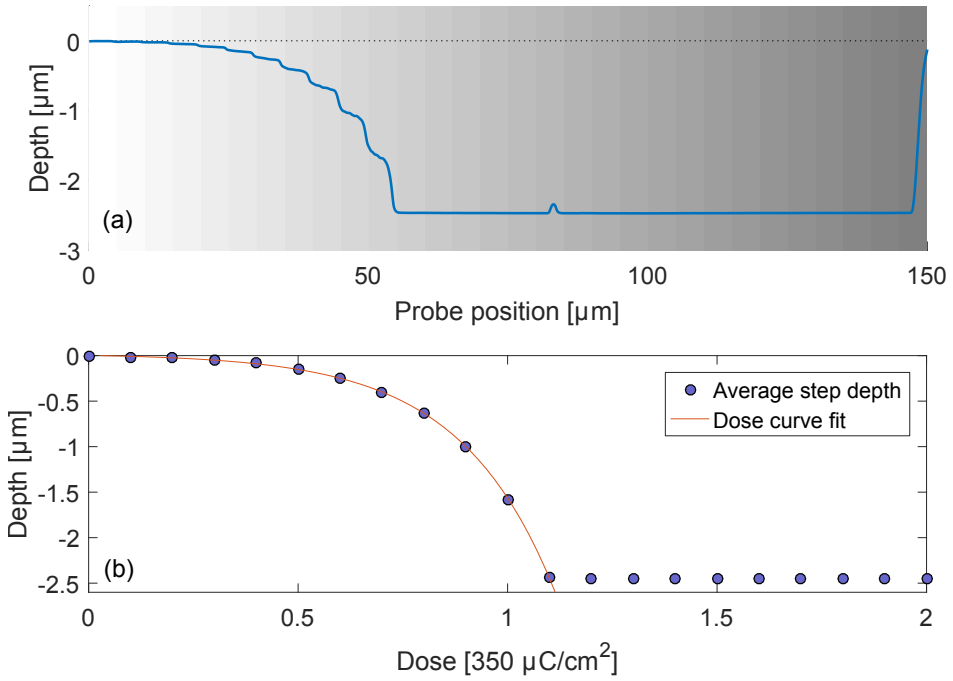

Figure 6.4: (a) An example dose step structure in PMMA with 10 µm wide steps of increasing dose factors from 0 to 3 (shown as greyscale map from white to grey) measured on a stylus profiler. (b) Extracted dose curve from three fabricated sets of dose steps, the fit to the averaged data points uses the parameters α_1, α_2 and α_3 of −0.01899, ~4.425 and 0.02174 respectively.

factor that corresponds to a maximum depth of 790 nm by measuring the diffraction efficiency of each lens. To calculate the new dose curve, the value of α_2 in Equation 6.1 was found such that the dose curve intersects the found dose value at a depth of 790 nm. We found $\alpha_2 \approx 3.4$, corresponding to a clearing dose of ~1.4, consistent with the earlier observations with an optical microscope. An example diffraction efficiency measurement with maximum dose can be seen in Fig. 6.5.

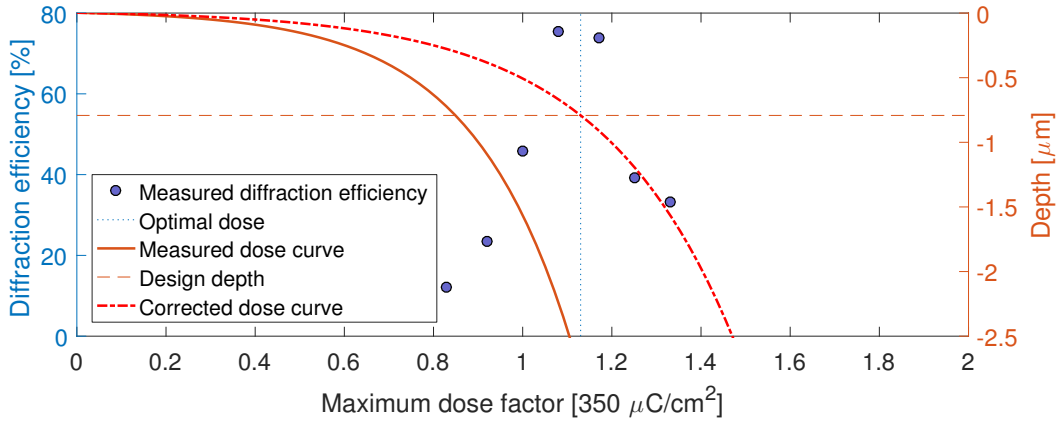

Figure 6.5: A measurement of diffraction efficiency for a set of DMLs with different maximum dose factors, controlling the surface-relief maximum depth. The maximum diffraction efficiency does not correspond to the design depth expected by the dose curve extracted from the dose steps. The dose of maximum diffraction efficiency is used to correct the dose curve for surface-reliefs by modifying α_2 to 3.325.

Dose curve correction When fabricating greyscale dose maps, we assumed a linear relation between dose and pixel depth. To fabricate faithful shapes in PMMA it was necessary to correct for the exponential electron dose response of the resist as found in the previous section. As we have a functional model for the dose response of PMMA, we used the principle of inverse functions where

$$f(f^{-1}(x)) = x \,, \tag{6.2}$$

such that by applying the inverse function of the dose response curve to the dose map the desired profile will be recovered. In practice, to correct for the dose response, we applied the inverse of the dose curve to our desired depth profile. The inverse of Equation 6.1 is

$$D^{-1}(D) = \frac{1}{\alpha_2} \ln\left(\frac{D - \alpha_3}{\alpha_1}\right) \tag{6.3}$$

Applying Equation 6.3 to a desired depth profile $D(x, y) = h(x, y) - \max[h(x, y)]$ provided a dose map that when fabricated should faithfully recover $D(x, y)$. Given the pitch dependence on the dose response of PMMA where open areas develop faster than gratings there will be higher order corrections to the dose correction model, where the dose correction would vary with pitch. We did not need to apply theses higher order correction given the relatively high diffraction efficiencies presented in the results below. However, we expect that improvement to the fabrication of fine pitched gratings is possible through careful characterisation of measuring and applying higher order corrections to the dose curve correction function.

6.1.4 Pattern transfer using reactive ion etching

Reactive ion etching is the process of using electrically accelerated plasmas to remove material from a target substrate [216]. The substrate is placed on an platter connected to an RF source, but otherwise electrically isolated from the rest of the chamber. The chamber is evacuated and a gas mixture is pumped into the chamber. Application of the RF field at powers on the order of 10^2 W accelerates electrons which then collide with the gas constituents, ionising them. The free electron ejected from the ionisation process can cause further ionisations leading to avalanche ionisation of the gas to form a plasma of free electrons and ionised atoms and molecules. The free electrons, being lighter than the positive plasma constituents, are then accelerated by the RF field and collide with the substrate platter. The removal of electrons from the gas both creates a positively charged plasma and a negative DC bias at the substrate. The positive ions are then accelerated towards the substrate with enough energy to initiate both chemical and physical reactions with the substrate material. Control of the RF power allows for control of the resulting DC bias and therefore ion acceleration energy. For low acceleration energies the process is dominated by chemical reactions, leading to isotropic etch profiles. For high acceleration energies the process becomes physically dominant with the ions removing material

from the substrate surface by bombardment. As the ions are accelerated towards the substrate, the physically dominant regime leads to anisotropic etching.

The choice of gas mixture is selected dependent on the material to be etched and the desired etch geometry. Often, some chemical etching is desired to both increase etch rates in general and control the relative etch rates of two different materials. Controlling relative etch rates is particularly important when using a thin mask material to etch deep trenches in a bulk substrate. Inert gasses such as argon are used for physical etching and chemically active gasses such as fluorides allow for chemical etching; a mixture of these two components allows for control of the relative etch rate and etch geometry. Another consideration of the gas choice is that it is often desired to allow for some fluorocarbon polymer deposition on the sidewalls of etched structures. The polymer layer retards etching of the sidewalls and can enhance the anisotropy of the etch, however excess polymer deposition can stop etching all-together and so the etch recipe must be carefully optimised.

Recipe development

We sought to faithfully transfer the fabricated shape in the PMMA resist into TiO_2. As we have steep discontinuities that we wish to preserve, the etch must be anisotropic such that the vertical steps do not become slanted. As a general guide, to maximise anisotropy we should maximise the self-bias voltage, minimise the process pressure and include a physical etch component.

Initial trial: $CHF_3/Ar/O_2$ An initial recipe used a gas mix of CHF_3/O_2 using a JLS PlasmaPod Etch System, with gas mix motivated by previous reports of RIE processes optmised for etching fused silica [217]. It was found that surface roughness occurred, as indicated by a visible clouding of the resist. As we wished to transfer the resist pattern into the TiO_2 layer, any surface roughness would translate into the final design and so was unacceptable. In an attempt to reduce the surface roughness the proportion of O_2 in the gas mix was decreased and Ar was introduced [218]. However, the reduction of the O_2 fraction led to excess polymer formation, with the net result being polymer deposition rather than etching of the substrate.

Reducing polymer formation: CF_4/Ar The key parameter that determines whether a process is predominantly polymer forming rather than etch dominant is the ratio of F/C ions present in the plasma [219, 220]. A higher fluorine content suppresses the build up of organic deposition by carbon ions. Oxygen can be used to tune the F/C ratio as it bonds with excess carbon ions. However, because we found O_2 to roughen the PMMA resist we used a new chemistry of CF_4/Ar, which had a natural F/C ratio in the etch dominant regime. Over 6 runs we optimised the recipe in a Plasmatherm RIE system. We found a selectivity of the PMMA over TiO_2 of 3.2, and therefore to use the full latitude of the TiO_2 film the final process must use >3.2 μm of PMMA resist. Despite fabricating surface-relief

Aim	RF Power (W)	Pressure (mT)	Gas flow rate (sccm)			
			CHF_3	CF_4	O_2	Ar
Initial recipe	100	20	30	0	10	0
Reduce polymer roughness	100	20	50	0	3	8
Reduce polymer formation	100/200	21	0	25	0	25
Reduce titania roughness	300	15.5	0	12.5	0	25

Table 6.2: Used recipes in the development of an RIE etch recipe for the formation of high efficiency TiO_2 diffractive surface-reliefs. The table entries are in chronological order of recipes used.

profiles in close agreement to design, maximum diffraction efficiencies of TiO_2 surface-reliefs were limited to 75%. AFM measurements indicated that excess surface roughness was present in the TiO_2 film, which could lead to scattering of light, reducing the power in the focus.

Reducing surface roughness: Ar/CF_4 It has been previously reported that when TiO_2 is etched in a CF_4 process, chemically inert TiF is redeposited onto the surface [221]. To reduce this redeposited material, it was suggested that an increase in the physical etch component was required. We therefore decreased the CF_4 component such that our gas mixture was 2/3 Ar and 1/3 CF_4. The RF power was also increased, which increased the physical ion bombardment energy. The positive side effect was an increase in anisotropy, however there was risk in excess heating of the PMMA resist, leading to feature deformation. For this recipe we found a decreased selectivity of 3.0 over the equal Ar/CF_4 mixture.

Distortion correction

Transferred surface-relief profiles of dose-corrected PMMA structures were found to be distorted from their ideal shape. Linear slopes in PMMA became concave when transferred into TiO_2 which limited the diffraction efficiency of the structures. Distortion correction was performed in a similar manner to PMMA dose correction, by modelling the distortion as a function and applying the inverse of this function to the designed height profile.

The distortion correction function was measured by fabricating a linear slope in PMMA and transferring it into TiO_2. The function that best models the measured, distorted slope was

$$T(u) = u \exp(\beta_2(u^{\beta_1} - 1)) \,, \tag{6.4}$$

where $u = D/\max(D)$ is the normalised depth of the slope, taking values between 0 and 1. The value of β_2 determines the magnitude of the concavity, and β_1 controls the location of the minimum of the curve. The function is chosen such that for $0<u<1$ then $0<T<1$. The inverse of Equation 6.4 is

$$T^{-1}(u) = \sqrt[\beta_1]{\frac{W(\beta_1\beta_2 u^{\beta_1} \exp(\beta_1\beta_2))}{\beta_1\beta_2}} \,, \tag{6.5}$$

where W is the product logarithm function (or, Lambert W function). The application of T^{-1} to the designed height profile (before dose correction) compensates the distortion that occurs during etching

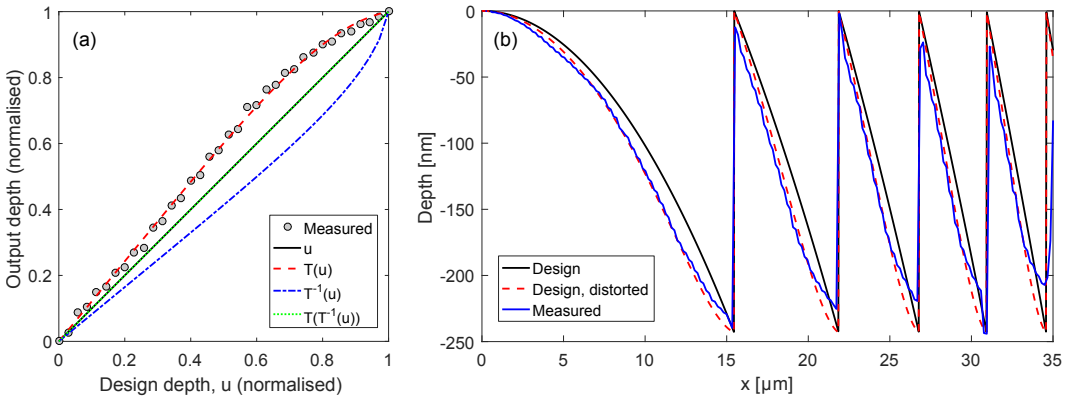

Figure 6.6: (a) Measurement of the depth profile in titania resulting from the transfer of a linear slope fabricated in PMMA using RIE. The distortion function $T(u)$ is fitted to the profile with parameters $\beta_1 = 4.163$ and $\beta_2 = -0.1947$. It is shown that if the profile $T^{-1}(u)$ is fabricated instead of u then etching will recover the profile u by the effective application of T on $T^{-1}(u)$. (b) A DML in titania resulting from the transfer of a dose corrected DML fabricated in PMMA, measured using an optical profiler. By applying the distortion function T with parameters $\beta_1 = 4.163$ and $\beta_2 = -0.1947$ to the design profile we approximately recover the fabricated profile.

(i.e. an application of the function T), and the desired height profile, u, is recovered by the laws of inverse functions. An illustration of the distortion effect is shown in Figure 6.6. By fabricating a linear slope in PMMA and then transferring into titania using RIE we fitted $T(u)$ to the measured slope, finding distortion parameters of $\beta_1 = 4.163$ and $\beta_2 = -0.1947$. A DML fabricated in the same sample as the linear test slope also demonstrated shape distortion, as shown in Figure 6.6(b). By applying the measured $T(u)$ to the DML design profile, we find a good agreement with the fabricated profile indicating the $T(u)$ serves as a good model for surface-relief distortion during RIE.

6.2 Results

The results presented in the following are the optimal lenses fabricated during several trial rounds of optimisation; FIB milling results were optimised over 8 separate fabrication runs, while EBL and RIE results were optimised over 23 samples.

6.2.1 Focused ion beam milling results

We demonstrated the performance of the FIB milling process by fabricating 6 lenses over two samples [197]. The first sample contained 3 lenses of identical design, referred to as design A. The lenses were designed with an object of a beam waist of a Gaussian beam with $w_0 = 3.75$ μm, located 1 mm before the lens plane within a substrate of NBK7 glass. The image point of design A was designed to be $z_D = 500$ μm from the lens plane in air using the finite-source optimisation procedure. The second sample contains lenses of design A, B and C, where designs B, C have the same object point as design A, but with $z_D = 450$ and 400 μm respectively. We refer to the lenses in the first sample

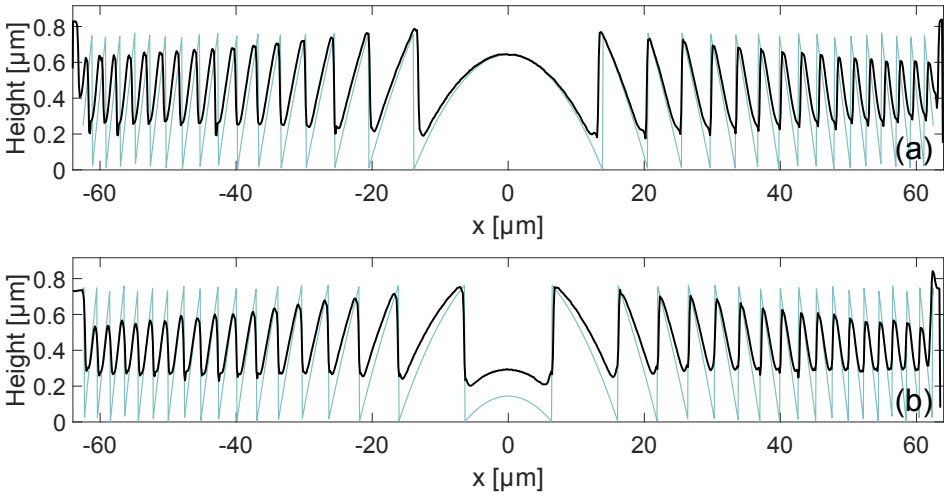

Figure 6.7: Measured profiles (dark) of typical DMLs fabricated using FIB milling and design profiles (light) for comparison; (a) DML 2, and (b) DML 5.

as DMLs 1–3 and lenses in the second sample as DMLs 4–6. We found through scalar simulations of the design phase profiles that the finite-source optimisation procedure produced image points slightly offset from the designed values of z_D. The offset is most likely due to the finite step size required for the computationally intensive optimisation routine.

Measurements of the surface-profiles using laser-confocal microscopy determined that all DMLs were under-etched from their design depth. Two example DML designs are shown in Figure 6.7. We found during optimisation that under-etching was preferable in terms of diffraction efficiency measurements. Due to limitations of reliable determination of the etch rate of NBK7 glass, we opted for a cautious approach and under-etched the lenses. We also found that annulus height decreased with decreasing annulus pitch. We attribute this to clipping of the neighbouring annulus tip when milling deep trenches.

DML	**Waist distance from lens, z_D (µm)**		**η_D (%)**	**Relative intensity**	
	Design	Measured		$x = 2w_0$	$x = 4w_0$
1	500	505	80.9	1×10^{-2}	2×10^{-4}
2	500	503	84.0	7×10^{-3}	3×10^{-4}
3	500	498	82.4	2×10^{-2}	5×10^{-4}
4	500	507	77.2	1×10^{-2}	3×10^{-4}
5	450	445	53.6	5×10^{-3}	7×10^{-4}
6	400	390	50.7	8×10^{-3}	2×10^{-4}

Table 6.3: Summary of measured optical performance of fabricated DMLs. All fabricated lenses focus within 10 µm of their design length, while only DML 1 – 4, of design A, achieve high diffraction efficiencies of > 75 %

The fabricated lenses were characterised optically and their performance is summarised in Table 6.3. The first substrate demonstrates the repeatability of the process, with all three lenses focusing to within ~1 % of their designed value, achieving $\eta_D > 80$ % and relative side-lobe intensities of 10^{-4}

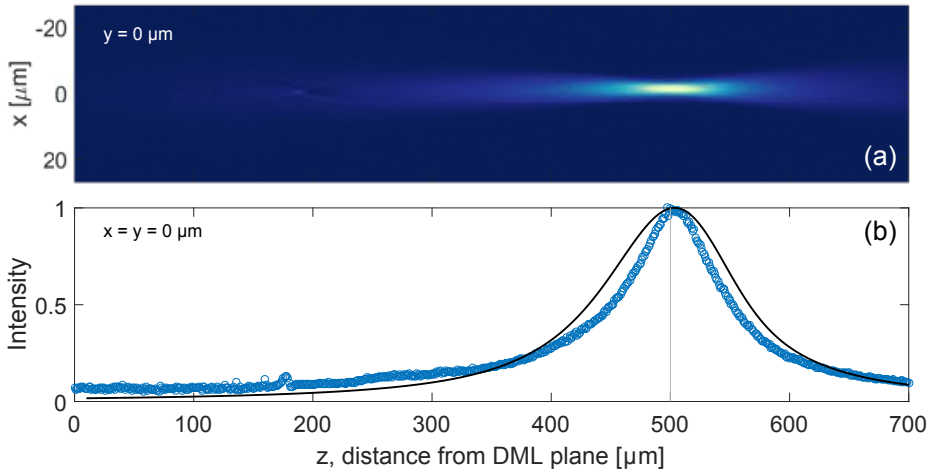

Figure 6.8: Measured propagation of DML 2, designed to focus at 500μm. (a) Colour map of the measured beam profile after the DML plane. Dark represents an intensity of 0, and bright represents a normalized intensity of 1. (b) The measured intensity (open circles) along the optical axis, z, with equivalent scalar simulation of the design profile for comparison (solid line).

at $x = \pm 4w_0$. Beam propagation along the z-axis for DML 2 is illustrated in Fig. 6.8. The optical intensity variation in the $x - z$ plane for DML 2 is shown, as well as the measured beam intensity on the optical axis ($x = y = 0$) compared with a scalar simulation. The measured beams exhibit a shorter depth of focus and a very weak local maximum at $z \approx 185$ μm due to the second diffraction order (the focal length f for the second diffraction order is $f/2$ corresponding to an image point of ~186 μm, which is close to the observed peak position). The deviations are attributed to the imperfect profile of the fabricated lens. At the image plane, the beam quality was examined in more detail through high dynamic range images. Both the 1D and 2D HDR beam profile of DML 2 is shown in Fig. 6.9. In the 1D profile we include scalar simulations of the ideal and fabricated lenses. The deviation in the measured beam waist ($w_0 = 3$ μm) from the design is ~5 % while the relative optical intensities away from the beam center are $\sim 10^{-4}$, corresponding to that expected from a simulation using the as-fabricated lens profile. DMLs 1 and 3 exhibit similar beam profiles.

Propagation measurements of the second substrate for lenses 4–6 are shown in Fig. 6.10, where the measured beam intensity along the $z-$axis is compared to scalar simulations of the ideal lenses, along with a composite image of the beam at focus. The measured distances of the beam waist for each lens, summarised in Table 6.3, agree with designed values to within 2.5 %. The diffraction efficiency η_D of DML 4 is comparable to DML 1–3 which is expected as they are of the same design, while DML 5 and 6 were significantly lower. The reduction in diffraction efficiency of DML 5 and 6 is due both to their altered design and to an under-etched central dome (see Fig. 6.7(b)). As the central dome overlaps with $\approx$ 25 % of the incident beam power it has a large influence in the realisation of the correct transmittance function. HDR beam profiles at the focus position of DML 5 and 6 are shown in Fig. 6.9(c, d). The majority of the power is concentrated at the focal plane and we measured

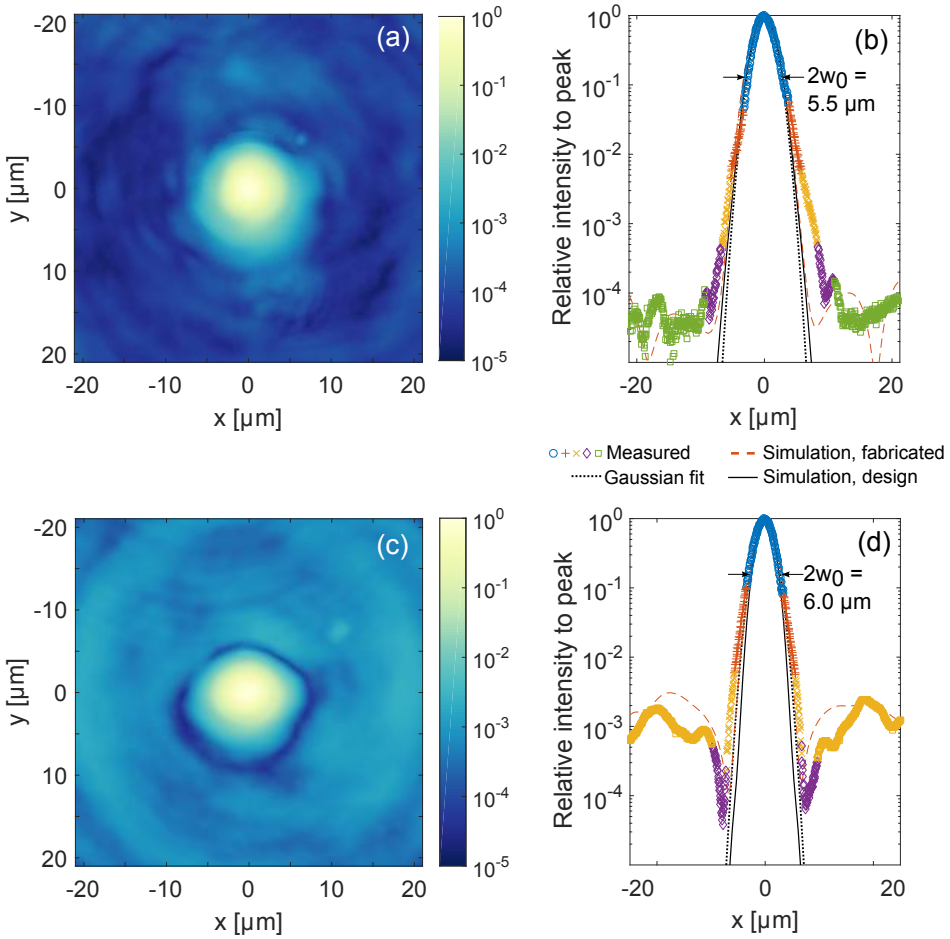

Figure 6.9: Beam profile at 500 μm from the plane of DML 2 (design A): (a) 2D profile normalized to the peak intensity, (b) 1D log plot along the x-axis of the beam profile at $y = 0$ demonstrating the background intensity away from the peak and deviation from simulations of the designed and fabricated lens. (c) and (d) are corresponding plots for DML 5 (design B). In (b) and (d), the data acquired with different exposure times are represented by different colors and symbols. In (b) these are 0.2 ms (blue), 0.8 ms (orange), 6.8 ms (yellow), 64.9 ms (purple) and 118.4 ms (green). In (d) these are 0.2 ms (blue), 1.1 ms (orange), 10.3 ms (yellow), and 101.3 ms (purple).

background intensities of $\sim 10^{-3}$ relative to the peak which is expected due to the decreased diffraction efficiencies.

6.2.2 Electron beam lithography results

The realisation of accurate surface-relief profiles in PMMA is required before such structures can be used as greyscale masks for RIE etching. We therefore began by demonstrating control in shaping accurate surface-reliefs in PMMA before transitioning to transferring structures into the vacuum compatible titania thin film below the PMMA resist.

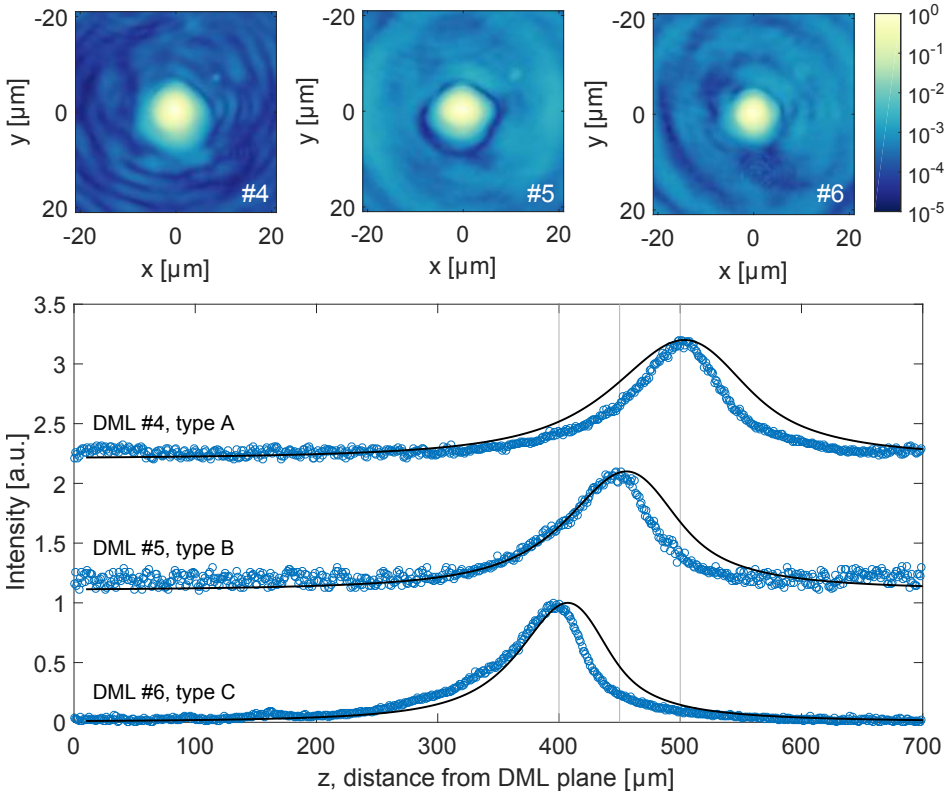

Figure 6.10: Intensity propagation of lenses 4, 5 and 6 along the optical axis. The measured optical intensity (open circles) at $x = y = 0$ is shown along with the equivalent simulated profile from the design (solid line). The data for different lenses has been vertically offset for clarity. The HDR beam profiles at the beam waist are shown above for all three lenses.

Surface-reliefs in PMMA

As previously mentioned, the similarity of the optical properties of PMMA to glass makes it an ideal material to prototype diffractive optics directly using EBL. We found write times of ~1 min per 100 µm^2, with exact write time depending on the DML design, and therefore allowed for the writing of many lenses in one write session. We typically write ~100 lenses on each substrate containing design variations, dose variations, correction tests, and duplicates, allowing for rapid refinement of the EBL process. As highlighted in Section 6.1.1, the main constraint is in accurately measuring the DML profiles and therefore we typically use the diffraction efficiency and conformity of optical response to design as our figure of merits. In most cases, after optical testing, the PMMA samples are used in the development of the RIE process, with specific etch-testing structures included in the EBL write process. The PMMA resist is etched to study surface-relief formation in titania, allowing for rapid development of the RIE etch recipe at the expense of PMMA sample destruction. In this section we present PMMA DMLs with both high diffraction efficiency and accurate beam steering demonstrating that DMLs designed using scalar diffraction theory are suitable for trapped ion addressing.

Dose curve correction Before fabricating any high-efficiency DMLs we first confirmed that the dose curve correction procedure produced linear responses in the PMMA resist. We fabricated greyscale slopes in PMMA of dimensions 100×100 μm^2 such that they can be profiled by a stylus probe. The slopes were designed to be linear, and therefore the applied dose profile took the form of Equation 6.3. Due to the large size of the slopes we used the dose curve parameters measured using the dose steps, which take the values of $\alpha_1 = -0.01899$, $\alpha_2 = 4.3313$ and $\alpha_3 = 0.02174$ for this sample batch. An example fabricated slope in PMMA is shown in Figure 6.11 along with the non-linear dose profile used. A linear fit to the slope is performed, with a root-mean-square-error of 10 nm.

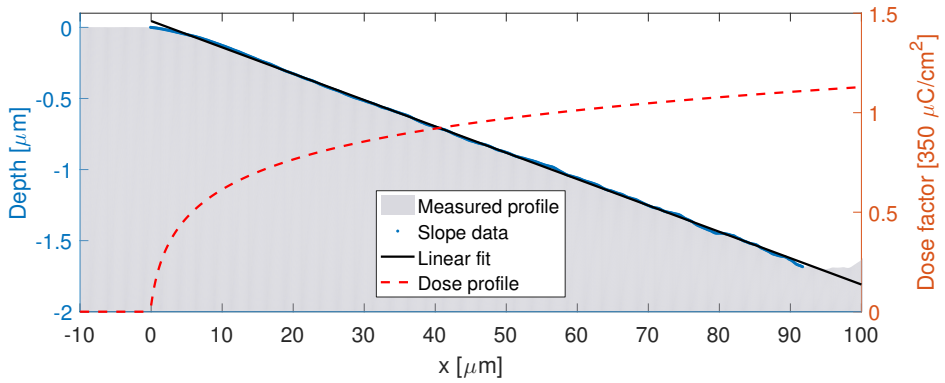

Figure 6.11: A linear slope in PMMA (grey area) fabricated by applying a non-linear dose profile (red dashed line) defined as the inverse of the dose response function (Equation 6.3) with $\alpha_1 = -0.01899$, $\alpha_2 = 4.3313$ and $\alpha_3 = 0.02174$. A linear fit to the highlighted section of the slope (blue) is shown, demonstrating successful dose response correction. The slope is measured using a stylus probe.

Hologram of University of Bristol logo To both test our implementation of the Gerchberg-Saxton algorithm and the capabilities of the developed EBL process, we fabricated a hologram in PMMA. The optic was designed to shape an input beam ($z_1 = -1000$ μm, $\lambda_0 = 405$ nm and $w_0 = 3.75$ μm) into a 50 μm diameter University of Bristol logo at $z_2 = 500$ μm, using the design previously shown in Figure 5.5. Dose curve calibration and correction was performed on the designed dose maps, with one hologram fabricated at the design maximum dose value. For confirmation of process control, we fabricated 4 holograms with maximum dose values less than design, and 4 with dose values greater than design. We measured that the hologram with the greatest power in the shaped beam is the one at the design dose value, with the intensity profile in the image plane shown in Figure 6.12. The diffraction efficiency was measured to be $82.5 \pm 0.7\%$ using a square, numerical aperture around the image. However, the transmission efficiency was not measured and so a calibrated diffraction efficiency cannot be stated. We note that the University of Bristol logo is accurately recovered, indicating both correctness of the GS algorithm and accuracy of the fabrication process.

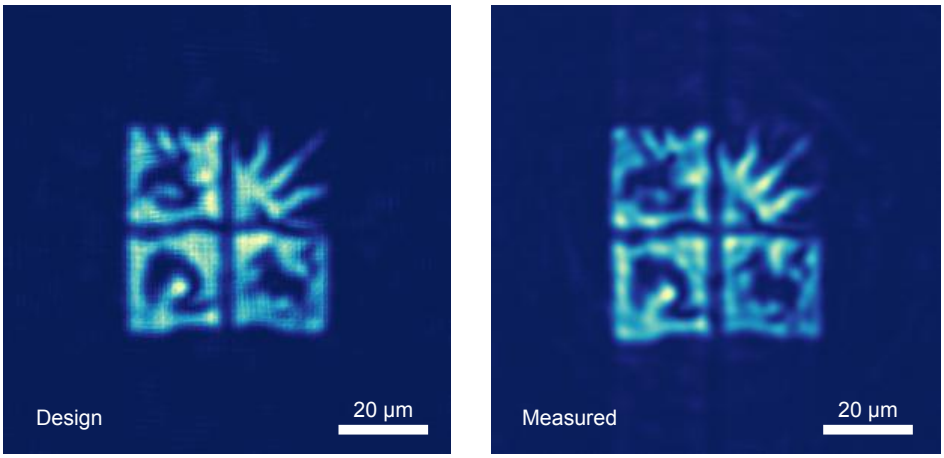

Figure 6.12: Comparison of the image plane of a fabricated diffractive optic in PMMA to design, where the intensity in the image plane has been shaped into the University of Bristol logo using the GS algorithm. The (uncorrected) diffraction efficiency of the measured optic is 82.5 ± 0.5%.

High diffraction efficiency of on-axis lenses To demonstrate the accuracy of dose curve correction we fabricated 16 lenses in PMMA of design A (see Section 6.2.1). The dose response on the sample batch used was first calibrated in a separate substrate. The fabricated lenses had different maximum dose factors, centred around the optimal dose factor found during calibration of 1.131. Measurements of the a subset of the DMLs are shown in Figure 6.13, with a maximum, uncorrected diffraction efficiency of 107% [1] for a dose factor of 1.145. Correcting for the increased transmission through the PMMA lenses over the surrounding film we find a corrected diffraction efficiency of 93.8(0.7)%. The transmission efficiency shows oscillatory behaviour with dose factor confirming that the maximum lens depth is changing with maximum dose, as shown in Figure 6.13(b). An HDR beam profile measurement in the image plane of the optimal lens is shown in Figure 6.13(c) and (d) demonstrating clear interference fringes as predicted by simulation and good agreement with the measured beam diameter. While the optimal dose factor (1.145) is different to design (1.131), the diffraction efficiency for a dose factor of 1.126 is measured to be 91.2% and therefore the design dose factor is contained in the range of doses that produce high diffraction efficiencies (>90%). Deterministically achieving maximum diffraction efficiencies requires further process control within each sample batch.

Off-axis angle testing Due to our inability to realise off-axis DMLs using FIB milling, we used the rapid prototyping capability of the EBL process to test off-axis DMLs in PMMA. Similar to the fabricated hologram in the previous section, the testing of off-axis DMLs was both to confirm that our design model is accurate and that the EBL process faithfully realised these designs. A strict requirement of the proposed optical assembly concept is the overlapping of multiple, focused beams at the same point in space. We have simulated that our DML designs focus beams at design positions, however now we

[1] The measurement of >100% diffraction efficiencies is not a cause for concern, as it is due to increased transmission through the DML than the surround unpatterned film.

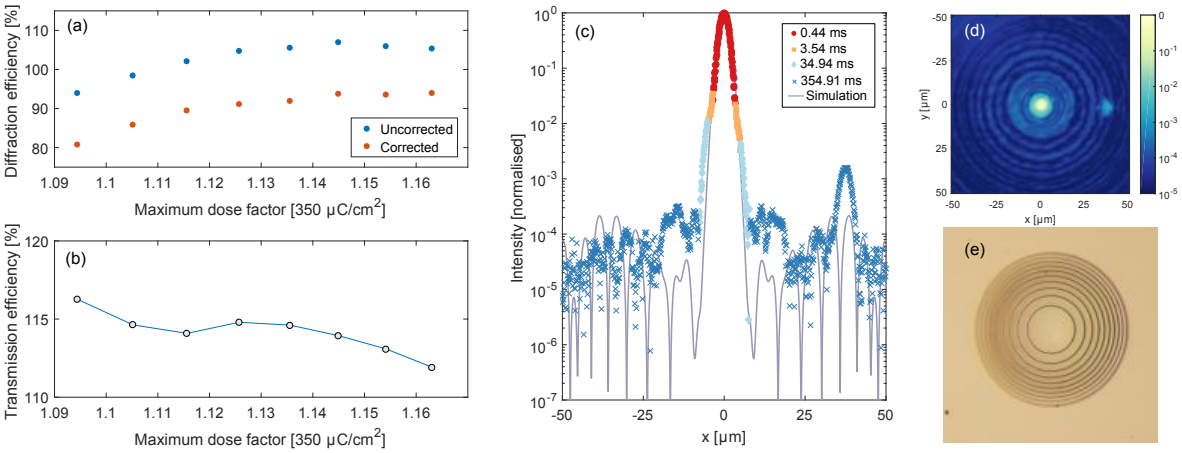

Figure 6.13: Measurements of a set of on-axis DML lenses with design A. (a) Change in diffraction efficiency with varying maximum dose factor, including both the raw, measured power ratios (uncorrected) and the inferred diffraction efficiencies from the measured transmission efficiencies shown in (b), we note that the transmission efficiency is >100%; (c) HDR beam profile in the design image plane of the DML with dose factor of 1.145 (diffraction efficiency of 93.8(0.7)%), the simulation is a combination of vector and scalar propagations of the electric field; (d) 2D HDR beam profile on a logarithmic scale, the colormap has been limited to 10^{-5}, the brighter spot at $x \approx 37$ μm is most likely a ghost reflection from the microscope objective; (e) Optical microscope image of the DML with a maximimum dose factor of 1.145, the DML diameter is 100 μm.

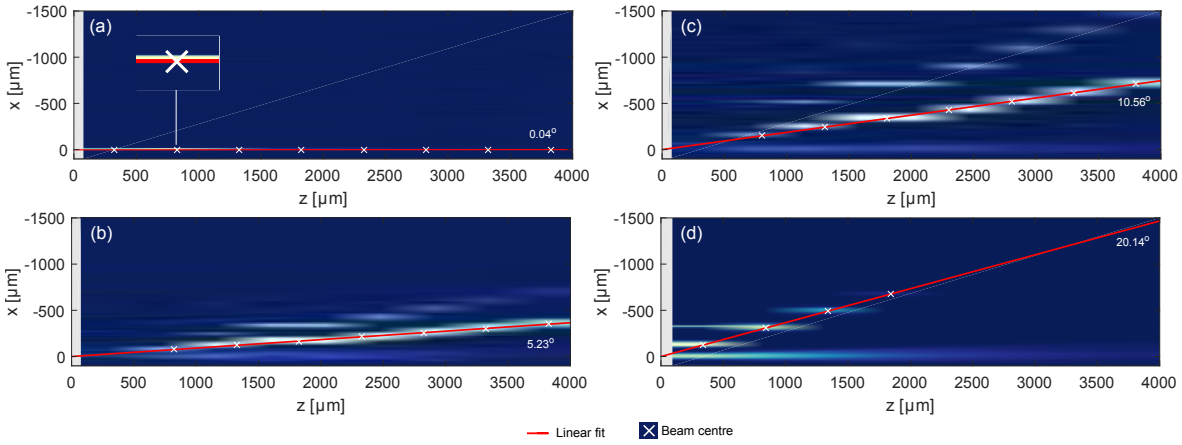

Figure 6.14: Measurements of 4 off-axis DMLs fabricated in PMMA using an exposed board CCD. Intensity profiles are shown for z values over 4 mm in the $y = 0$ plane. Beam centres of the $m = 1$ diffraction order are shown as blue crosses, with a linear fit through the beam centres shown as a solid red line. The corresponding angle of propagation inferred from the linear fit is shown. The DMLs are designed to deflect 405 nm radiation (a) 0°, (b) 5° (c) 10°, (d) 20°. Higher diffraction orders can be seen due to non-optimal lens depths. The on-axis lens inset highlights that the focused beam is mostly obscured by the fit line. The grey region is unmeasured due to restrictions of bringing the CCD close to the lens plane.

corroborate those simulations with results from fabricated DMLs.

The first test performed of off-axis DMLs was the fabrication of off-axis DMLs with angles from 0° (on-axis) to 20° off-axis. We made no attempt to dose-correct the profiles, making note that the pitch rather than the exact profile shape of the grating is fundamental to the beam steering. After fabrication, each grating was tested using the design source beam and the output propagation was

imaged using an exposed board CCD from $z \approx 300$–4000 μm. By extracting the beam centre positions at each z position and performing a linear fit the angle of propagation could be determined. As shown in Figure 6.14, we found all angles were as designed within 0.6°. The angle error of the 20° deflection DML was within our specified angle tolerance of 1% indicating that the strict fabrication tolerances may be achievable with EBL. Due to the experimental set up, the angle error source could not be determined and could equally be due to a misalignment of the CCD to the lens plane as it could be due to incorrect beam steering of the DMLs. It is therefore not possible to draw firm conclusions without further study. We therefore move onto referencing two DMLs to one another by focusing their outputs at the same point in space to remove this ambiguity.

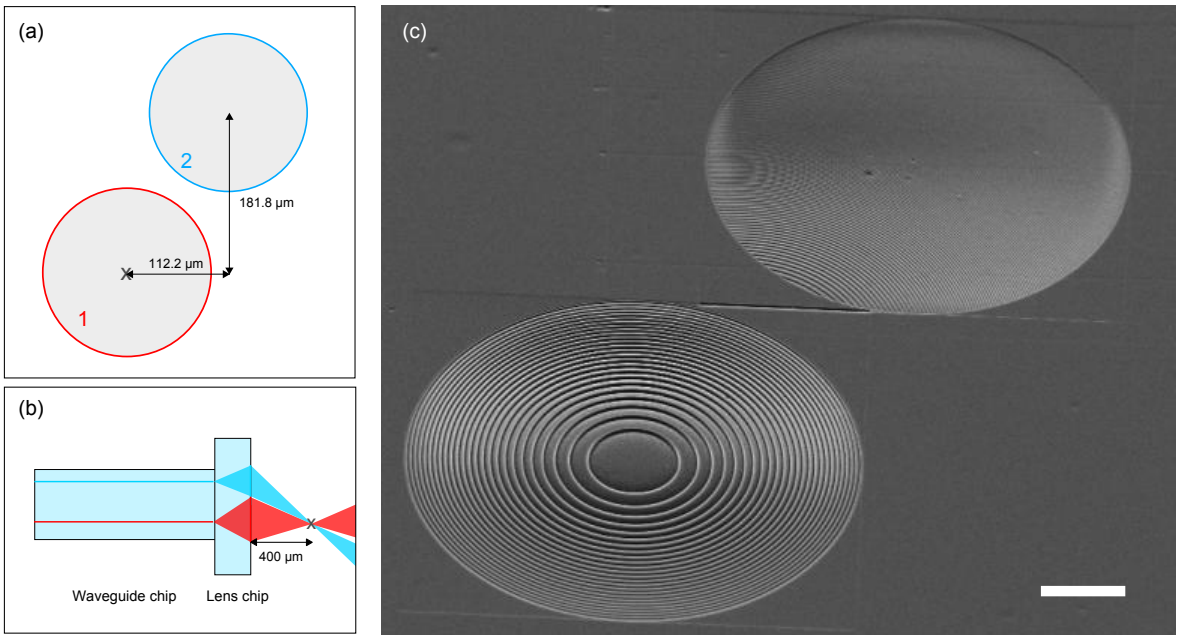

Figure 6.15: Lens layout and fabrication for testing off-axis focusing accuracy. (a) Two lenses are designed 112.2 and 181.8 μm apart in the x and y directions respectively, DML 1 is designed to focus λ_0 = 680 nm radiation at the labelled cross, DML 2 is designed to focus λ_0 = 488 nm radiation at the same labelled cross; (b) side-view of the optical setup, with two waveguides coupled to the two lenses, focusing at the image point at z = 400 μm; (c) SEM image of a fabricated lens pair, imaged at 45°. The scale bar is 20 μm.

Two beams crossing in space To further test the accuracy of off-axis DMLs we attempted to overlap the output of two fabricated lenses. To coupled input light simultaneously to two DMLS we utilised a LW waveguide chip fabricated during waveguide development in Chapter 4 that contains two waveguides with (x, y) relative positions of $(112.2, 181.8)$ μm. One waveguide supported a single-mode of red wavelength radiation, the other supported a single-mode of blue wavelength radiation. We designed two DMLs to simultaneously reimage the waveguide outputs to a congruent point in space, 400 μm from the lens plane. The lens for the red waveguide was designed to be on-axis (DML 1), and

the lens for the blue waveguide was designed to be off-axis (DML 2)[2]. The optical layout is shown in Figure 6.15(a-b). The design wavelengths were chosen by the availability of lasers, such that the on-axis DML was designed for λ_0 = 680 nm and the off-axis DML was designed for λ_0 = 488 nm. We fabricated an array of the lens pairs for different maximum dose factors in PMMA, with a SEM image of an example pair of lenses shown in Figure 6.15. The lenses were tested at the designed wavelengths by aligning the waveguide chip (using a 6-axis stage) to the lens chip (mounted on a 3-axis stage). The lens propagation was measured using using an exposed board CCD, with an example propagation shown in Figure 6.16. We found that the two beams cross in the $x-y$ plane at $\Delta z = -10$ μm from the focus of DML 1. We are unable to determine whether the discrepancy in the z position is due to a focusing error, or an angle error. However, we note that the k-vector of the off-axis beam intersects the on-axis beam at $(x = 1, y = 0)$ μm,corresponding to a 1 μm positioning error from design in the x–y plane. Further tests of the off-axis positioning errors will be performed in Chapter 7.

Off-axis diffraction efficiencies The diffraction efficiencies of off-axis DMLs were tested by fabricating DMLs designed with image points z_2 = 2 mm and 5°, 10°, 15° and 20° off-axis. For each DML design we fabricated 5 optics with varying maximum dose factors. Output beam profiles were imaged 2 mm from the lens plane using a 50× objective and a beam profiling CCD. Corrected diffraction efficiencies were measured for every fabricated optic and are shown in Figure 6.17(a). We found optimal maximum dose factor of 1.17 for 5° and 10° and 1.2 for 15° and 20°. The higher dose requirement for larger off-axis deflection indicates the previously discussed pitch dependence on the dose response of PMMA. These optimal dose factors can be directly compared to the on-axis optimal dose (1.145) as they are fabricated in the same substrate. For angles 5°–15° we found high maximum diffraction efficiencies of ~88%, however for 20° diffraction efficiency is reduced to 77%. HDR beam profiles of the 5° and 20° DMLs are shown in Figure 6.17(b-e), demonstrating an increase in background intensities away from the focus at higher deflection angles. We do not optimise for the found pitch dependence of the dose factor and therefore there is scope for improvement in diffraction efficiencies for off-axis DMLs due to this opportunity for optimisation.

Surface-reliefs in titania

The precise forming of surface-reliefs in PMMA now allows the study of the transfer of the structures into the titania sub-layer. We begin by confirming our proposed technique of correcting for distortions during the etch process, before moving on to the fabrication of high efficiency DMLs in titania.

[2]Choosing the blue wavelength radiation to be deflected off-axis, rather than the red wavelength, is the harder challenge due to the decreased pitch of the off-axis DML at blue wavelengths.

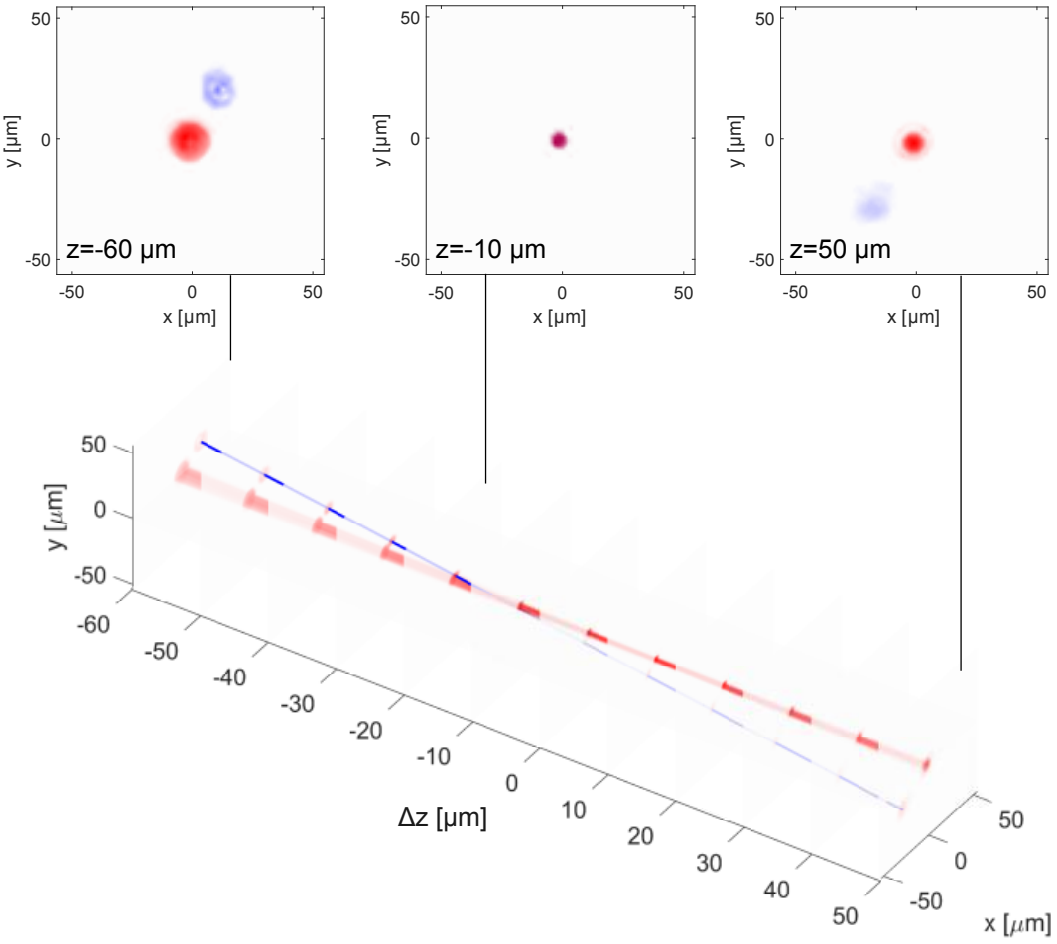

Figure 6.16: Measured beam propagation of two lenses designed to overlap their output at the same point in space, excited simultaneously, at different z values. Δz is defined relative to the position of the beam waist of DML 1. The solid blue line is a guide to the eye of the measured k-vector of DML 2. The start, intersection, and end x-y planes are also shown for clarity. The colours represent the red and blue wavelengths accordingly.

Distortion correction Distortion correction model testing was performed by attempting to fabricate a linear grating in titania. The grating design varied monotonically in pitch from 10 µm to 1 µm over 30 grating periods and had a design depth of 500 nm. The EBL dose map was generated first by applying distortion correction, multiplying the TiO_2 design depth by the selectivity of titania over PMMA and then dose curve corrected. An AFM trace of a portion of the fabricated linear grating with and without distortion correction is shown in Figure 6.18. The grating with distortion correction had a much closer conformity to design, with the previously shown distortion curve present on the uncorrected grating. Applying a linear fit to the grating segment highlighted in Figure 6.18 we found a RMSD of 2 nm for the corrected slope and 44 nm for the uncorrected slope. We therefore conclude that the deviation of the corrected slope from design is from slight overetching. It can be seen that the AFM tip does not resolve the grating trenches before being deflected by the next grating peak and therefore the full profile could not be obtained. We conclude the distortion correction can fabricate

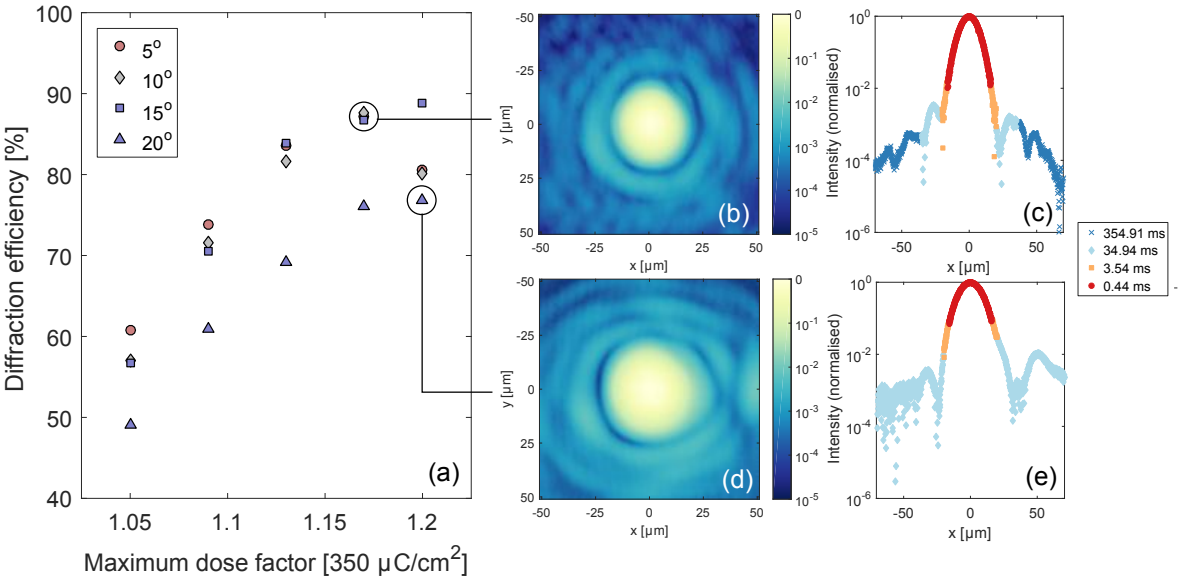

Figure 6.17: Measurements of a set of off-axis DMLs fabricated in PMMA, with design image points 2 mm from the lens plane. (a) Diffraction efficiences, corrected for transmission efficiencies. (b-c) HDR beam profiles (2D and 1D) of the optimal 5° DML; (d-e) HDR beam profile (2D and 1D) of the optimal 20° DML.

linear slopes in titania within ±2 nm of linearity, with exact angle of the slope controlled by the selectivity of PMMA over titania.

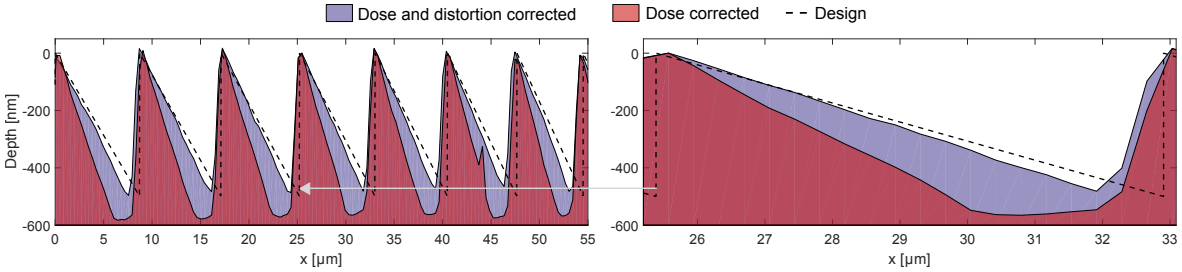

Figure 6.18: Fabrication of a linear grating in titania by transfer of a greyscale PMMA mask using RIE. Two separate gratings are shown, one that has not been corrected for distortion during the RIE process and was initially a grating of linear slopes in PMMA, and a second that has been distortion compensated. The increase in linearity of the distortion corrected slope can be seen to have good conformity to design. The gratings are measured using AFM.

Near-unit diffraction efficiency over a range of focal lengths The successful implementation of distortion correction allows for the forming of DML designs in titania. To demonstrate the flexibility in the process we fabricated an array of 10, on-axis DMLs. Each DML was designed to reimage a Gaussian beam waist with parameters $z_1 = -1000$ μm, $\lambda_0 = 404$ nm and $w_0 = 3.75$ μm at a different z_D. We chose the range of design z_D values to span over 1 order of magnitude, from 200 μm to 2000 μm. These z_D values correspond to z_2 values from 201.91 μm to 3206.1 μm to take into account the finite size of the source beam as outlined in Section 5.1.3, which corresponds to lenses ranging in focal length over ~300 μm.

EBL dose maps were prepared using both distortion correction and dose curve correction. We used a selectivity of 3.98 as we found that selectivity of PMMA over titania was increased for DMLs compared to open areas. The increased selectivity was measured by optimising etching parameters for maximum diffraction efficiency. The measured refractive index of the titania thin film at λ_0 = 404 nm was 2.66 and therefore the required DML depth was 243 nm. The PMMA surface-reliefs were designed to be 967.5 nm deep accounting for the selectivity during RIE etching. SEM images of the fabricated lens set in titania is shown in Figure 6.19. DML 1 corresponds to z_D = 200 μm and DML 10 to z_D = 2000 μm.

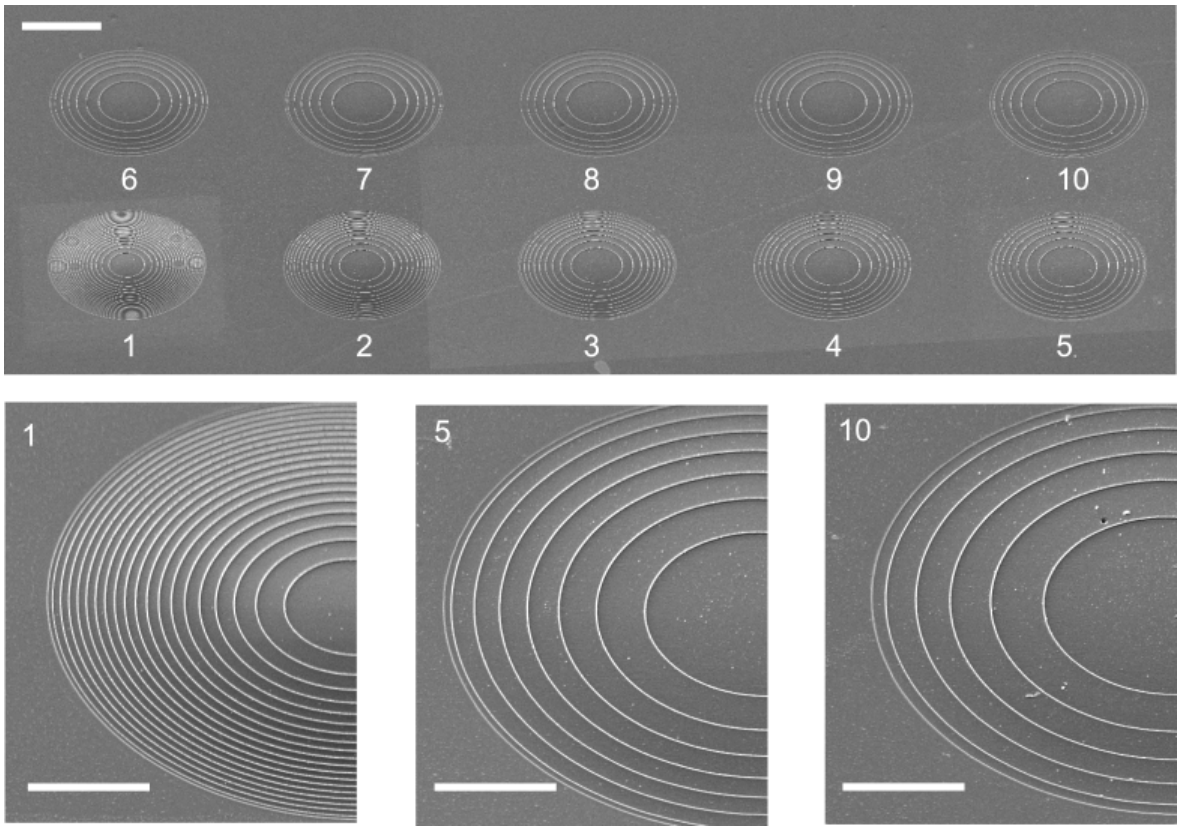

Figure 6.19: SEM images at 45° inclination of an on-axis lens array in titania with design z_D from 200 μm (DML 1) to 2000 μm (DML 10). The scale bar for the top image is 50 um, and 20 um for the bottom images. The lighter areas are a result of extended exposure to the imaging beam. The contamination on the surface is likely due to the lenses being imaged after optical testing outside of a cleanroom environment.

The DML array was tested for a fixed source beam position, with the lens under test being laterally translated into the beam path. For this lens set we measured transmission efficiencies of ~85 – 95% with the variation attributed to changes of the etch depth for each lens design. Further optimisation of the lenses would require accounting for both dose response and etch distortion dependence with DML feature sizes. For the full lens set we measured an average corrected diffracted efficiency of 93(5)%, with the quoted error of 1σ, as shown in Figure 6.20. The maximum measured diffraction efficiency was 98(1.5)% for z_D = 1000 μm, and the minimum was 84(1.2)% for z_D = 200 μm, with 8 of the 10

lenses having diffraction efficiencies >90%. HDR beam profiles at z_D were taken for DMLs 1, 5 and 10. For DML 1 we found elevated background intensities <20 μm from the beam centre compared to simulations of the lens profile, however for x>20 μm the background intensities fall to the simulated intensities of $<10^{-4}$. For DML 5 and 10, restrictions on the size of the imaged beam area did not allow for confirmation of the same behaviour.

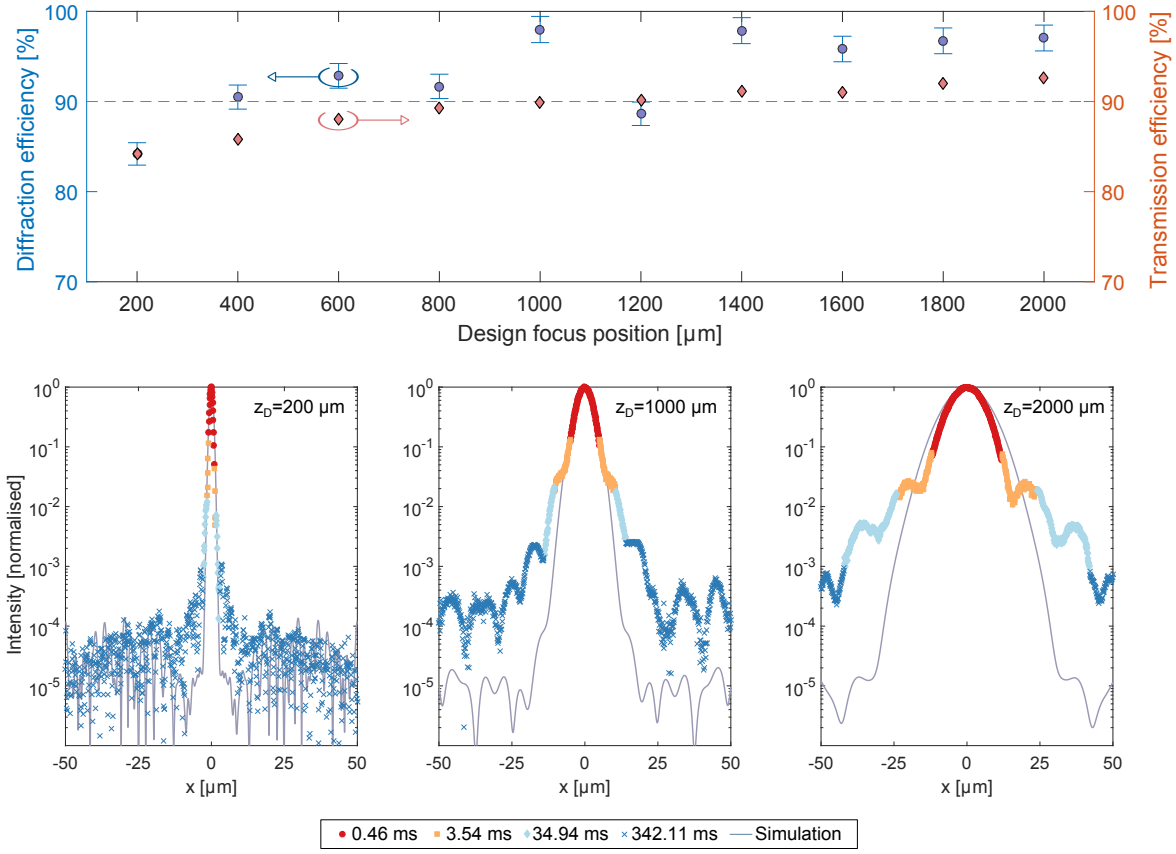

Figure 6.20: Characterisation of diffractive microlenses in titania designed to reimage a Gaussian beam waist at different positions from the lens plane. The source beam parameters are λ_0 = 404 nm, w_0 = 3.75 μm and z_1 = −1000 μm. The transmission efficiency (diamonds) is the ratio of the power transmitted by the lens to the power transmitted by the unstructured thin film and is used to calibrate the diffraction efficiency (circles) measurement. HDR beam profiles at the design focus position are shown for three of the lenses along with vector-scalar simulations of the designed surface-reliefs.

Off-axis diffraction efficiency Having demonstrated near-unit diffraction efficiency with on-axis DMLs, we now demonstrate the maximum diffraction efficiency found for off-axis DMLs in titania. We fabricated off-axis DMLs in titania with identical design to the off-axis DMLs fabricated in PMMA (z_1 = −1000 μm, z_D = 2000 μm, 5–20° deflection angles) with the fabrication parameters modified for accurate transfer into titania. We used identical fabrication parameters to the on-axis lenses presented previously and in the same substrate for direct comparison. No attempts were made to account for the smaller feature sizes of the off-axis grating, nor was advanced surface-relief profile generation performed. Therefore the results presented here do not represent the maximum possible diffraction

efficiency for off-axis DMLs in titania.

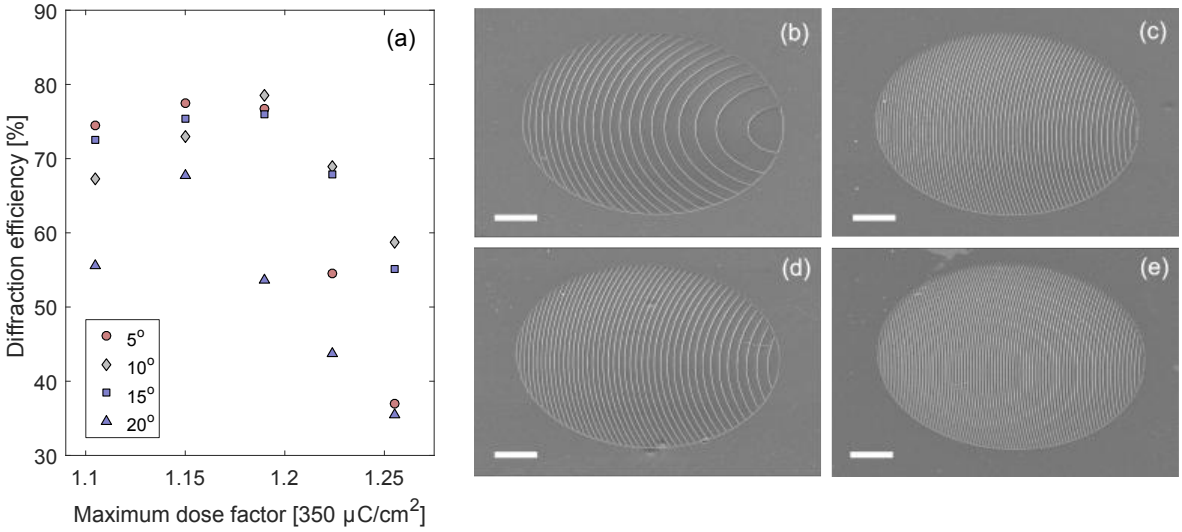

Figure 6.21: Measurements of a set of off-axis DMLs fabricated in titania, with design image points 2 mm from the lens plane. The titania DMLs are formed from PMMA surface-reliefs designed to be 3.97× deeper than the final titania DMLs. (a) Diffraction efficiences, corrected for transmission efficiencies; (b-e) SEM images at 45° inclination of the optimal 5, 10, 15 and 20 degree DMLs. The scale bar is 20 μm.

Corrected diffraction efficiency measurements of the fabricated off-axis DMLs are shown in Figure 6.21 and we find that the 5° and 20° lenses have a maximum efficiency for a maximum dose factor of 1.15, while the 10° and 15° are maximum at the design maximum dose factor of 1.19. The reason for this discrepancy is unknown. In all cases the diffraction efficiency decreases rapidly with increasing lens depth after the maximum value is obtained, demonstrating a tight requirement on calibration of fabrication parameters. Maximum diffraction efficiencies are approximately 10% lower for all angles when compared to the PMMA DMLs, indicating profile distortion not fully accounted for by the distortion correction model for small grating pitches. The reason for this is most likely a similar effect that causes the pitch dependence in PMMA resist, with reduced transport of the etching plasma in narrow trenches. Further study of both the PMMA resist pitch dependence during development, and the titania pitch dependence during etching is therefore the foremost route to improving diffraction efficiencies in off-axis DMLs.

6.3 Discussion and conclusion

We have introduced and demonstrated several processes for forming diffractive surface-reliefs in optical materials. The initial development of a FIB milling technique for forming DMLs in glass allowed for testing of our scalar diffraction theory models and confirmation that accurate and high-efficiency beam focusing was possible. The technique shows some limitations. One of the biggest drawbacks were long write times (~3 hours per lens), limiting the prototyping time and ultimately the number

of designs that could be included on the same substrate, which was typically limited to 4. We also found that fabrication parameters optimised for one DML design did not readily transfer to other DML designs, as shown by the reduced diffraction efficiency of designs B and C over the optimised design A. The greatest limitation to the technique was the restriction in the maximum aspect ratio that could be fabricated and attempts to fabricate off-axis DMLs in glass using FIB milling were unsuccessful.

The capability to form surface-reliefs directly in PMMA using EBL was enabled by the delivery of an industry-grade EBL machine during the course of the project. The ability to write 100s of optics and calibration markers in a single write session (~2 hours) allowed for truly rapid prototyping. It was possible to generate new optic designs in the morning and have a finished PMMA sample ready for testing by the afternoon. We did not attempt to find the limits of the maximum aspect ratio structures that could be written in PMMA, however aspect ratios of 10:1 have been previously reported using the same developer combination of IPA and water used here [215]. The increased resolution over FIB milling allowed us to fabricate high-efficiency on-axis, off-axis and beam-shaping diffractive optics. DMLs with deflection angles from 0–15° were successfully demonstrated with diffraction efficiencies greater than the maximum diffraction efficiency measured for any DML formed by FIB milling. This allowed us to test the beam pointing accuracy of the DMLs by showing that an off-axis beam crossed an on-axis beam to 1 μm accuracy in the x–y plane and −10 μm away from the on-axis beam waist.

While the formation of DMLs in PMMA allowed for rapid prototyping, the transfer of surface-reliefs into a vacuum compatible material is pivotal to achieving the proposed optical assembly. The process for surface-relief formation in titania was optimised such that fabrication maps that were corrected for non-linear dependence of PMMA to electron exposure and titania to etching were able to fabricate linear slopes in titania with 2 nm deviation from linearity. The optimised RIE recipe added a further 180 minutes onto fabrication time (120 minute RIE chamber evacuation, 60 minute etch time), however it is a completely parallel process and could accommodate many samples simultaneously. With an EBL time of ~1 min per 100 μm^2 plus the additional parallel etch we claim to have developed a semi-scalable technique for DML formation in a dielectric material, where the fabrication of an additional optic carries only a small time penalty. With the optimised RIE process we demonstrate high diffraction efficiencies (84–98%) for lenses with z_D values spanning an order of magnitude showing flexibility in the fabrication process. The variation in the diffraction efficiency with design indicates further optimisation of the fabrication process is possible, this is especially shown by the lower efficiencies of off-axis DMLs and is due to no attempt being made to compensate for any negative effects from small pitch sizes. Having demonstrated and optimised the fabrication of DMLs for accurate and high diffraction efficiency performance, we continue in the next chapter to explore their suitability for trapped ion addressing by interfacing them with laser-written waveguide circuits.

7

Demonstration of a micro-optical assembly at operational wavelengths

The realisation of the micro-optical assembly for interfacing with trapped ions has so far led us to develop fabrication processes in Chapters 4 and 6 for laser-written waveguides and diffractive microlenses respectively. We now attempt to combine the developed optical sub-components and demonstrate the micro-optical assembly concept outlined in Chapter 2. The transition from fabricating and testing individual components to arrays of components that must operate simultaneously contains its own set of challenges. In this chapter we perform the process of designing, fabricating, testing and assembling an optical assembly suitable for addressing two neighbouring microtrap segments of a linear microtrap array. As a starting point, we do not consider integrating the probe (λ=674 nm) and optical pump (λ = 422 nm) as they require deflection angles of ~45° and the optical pump requires circular polarisation. However, we include both blue (λ=422 nm) and near-IR beams (λ=1033, 1092 nm) to demonstrate integrating disparate wavelengths into the same micro-optical system. We first begin with the demonstrator assembly design, before moving onto the fabrication and testing of individual components. The testing of the full assembly at operational wavelengths is then performed and its performance will be outlined.

7.1 Demonstrator optical assembly design

During our investigations in Chapters 3 to 6, we identified some limitations to realising the micro-optical assembly concept. Firstly, it was found that a grounded, conductive layer was required surrounding the diffractive microlenses to reduce perturbations to the microtrap pseudopotential. Secondly, laser-written waveguide mode expansion tapers could not be reliably fabricated. For a proof-of-principle demonstration, we concluded that the best compromise of the system requirements was met by an optical assembly with a lens-to-ion distance of 2 mm. At this distance, the microlenses

Beam name	Wavelength (nm)	Unit k-vector
Doppler Cooling 1	422	$-0.5946\hat{x} - 0.6995\hat{y} - 0.3964\hat{z}$
Doppler Cooling 2	422	$-0.6701\hat{x} - 0.6701\hat{y} + 0.3191\hat{z}$
Doppler Cooling 3	422	$-0.7044\hat{x} - 0.5870\hat{y} - 0.3991\hat{z}$
Repumper 1	1092	$-0.6738\hat{x} - 0.6738\hat{y} - 0.3032\hat{z}$
Quencher 2	1033	$-0.6891\hat{x} - 0.6891\hat{y} - 0.2240\hat{z}$

Table 7.1: The included addressing beams included in the demonstrator optical assembly for one segment of the microtrap with their wavelength and chosen k-vectors. The unit vectors are in the coordinate system of the principal trap axes such that $B = 0.5\hat{x} + 0.5\hat{y} - 1/\sqrt{2}\hat{z}$.

for deflecting and focusing addressing beams are spaced far enough apart that microlens diameters can be used that fully collect the waveguide outputs, minimising scattered light. The microlenses are also far enough away from the microtrap to minimise perturbations to the trapping field without a conductive coating on the lens array. However, a collection lens diameter of ~800 μm is required to satisfy the 1% collection efficiency requirement. Such a large collection optic would cover the locations of the required addressing beams and therefore a choice between collection and addressing optics must be performed. We therefore choose to only use addressing optics to demonstrate a complex optical system delivering multiple wavelengths to multiple trapping segments. When interfaced with the microtrap, the ion fluorescence could be collected through the front face of the microtrap as there is still optical access from that side. Such an assembly would offer a significant advance over the previous state-of-the-art interfacing of trapped ions with microfabricated optics. Collection optics could be incorporated after the completed development of waveguide mode-expansion tapers and a fabrication process for selectively coating the microlens array in gold. These future research avenues are discussed further in Section 8.1 where we consider optical arrangements for closer optic-to-ion positions that would realise the full optical assembly concept presented in Section 2.3. Although the demonstrator assembly presented here is an intermediary to the final device in some respects there are more stringent fabrication requirements, such as larger diameters of the addressing microlenses. As the design of the optical assembly is constrained by the large lens sizes and the required k-vectors for the atom-light interactions the design process begins with the micro-lens array.

Micro-lens array design Micro-lens placements were calculated as the intersection point of an addressing beam's k-vector with the lens plane. During optical assembly design, the optic placements were tuned such that they were sufficiently spaced to accommodate the required lens radii. The radius of the optics are chosen such that they approximately match the numerical aperture of single mode fibre (~0.13, see Table 7.3), which corresponds to a radius of 85 μm for a substrate thickness of 1 mm.

The addressing beams chosen for a proof of principle demonstration were: Doppler cooling beams for minimising micromotion in all three directions, a single repumper and a single quencher beam. The k-vectors for the Doppler cooling beams were chosen such that each one preferentially Doppler

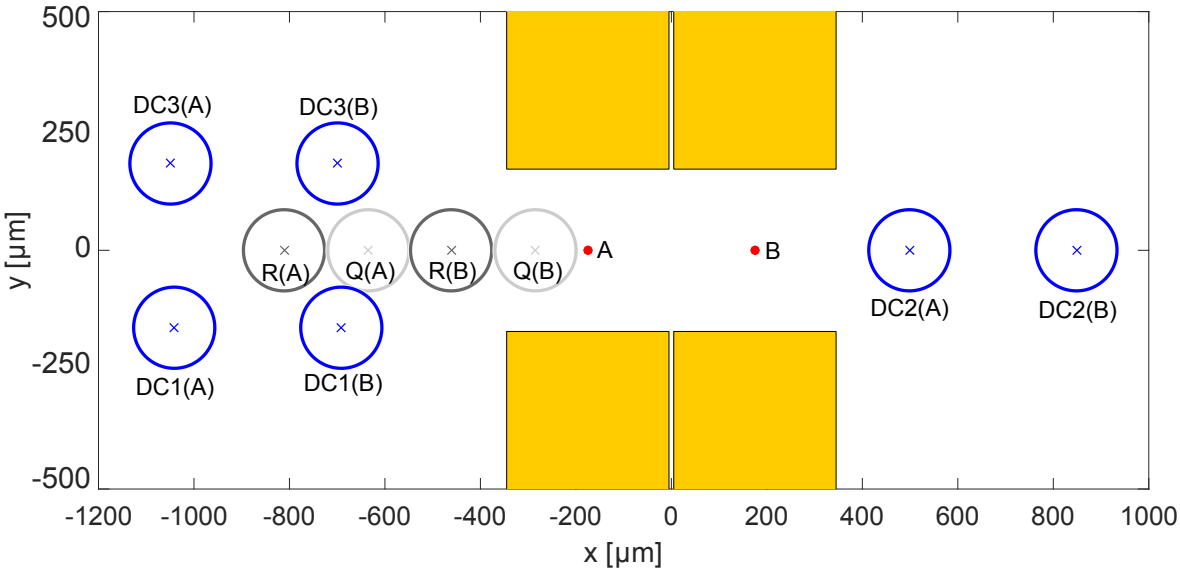

Figure 7.1: The designed DML array for realising the k-vectors shown in Table 7.1 at points A and B, located 2 mm from the lens plane in the z-axis (shown here projected onto the lens plane). The lens labels are the abbreviated beam name along with their associated electrode centre in parentheses. The gold microtrap electrodes are superposed on the lens plane and shown in yellow.

cools motion on each of the principal trap axes, while not being perpendicular to any other axis of motion. The repumper and the quencher beams were situated such that they were in the plane of the trap aperture (minimising their design complexity) and so that their lens centres were spaced >170 µm apart so they do not overlap. A summary of the k-vectors used for a set of addressing beams is presented in Table 7.1.

To further demonstrate scalability of the chosen micro-optical platform we chose to include two sets of addressing beams, with each set focusing at separate points in space, 350 µm apart, corresponding to the centre of two neighbouring microtrap segments. The full lens array is therefore composed of 10 optics. Further scaling of the lens array is possible, however there will be a limit where lenses begin to overlap and optic layouts will be need to be optimised for these cases; we do not expect the increase in optic layout complexity to be a fundamental limit of the approach. The optical layouts become more compact for closer lens-to-ion distances such that fully interlocking and scalable optical layouts can be designed as is shown later in Figure 8.2 of Section 8.1.

The micro-lens placements for the chosen k-vectors are shown in Figure 7.1 along with the corresponding microtrap segment centres to be addressed. Optics are referenced by their abbreviated name and their related microtrap segment. The surface-relief diffractive optics can then be generated using the point-to-point model as outlined in Section 5.1.2, using an on-axis object point 1 mm from the lens (the waveguide source) and an off-axis image point (the microtrap segment centre).

LW waveguide array design The LW waveguide array is included in the optical assembly to remap fibre optic positions in a fibre array to the positions of the microlenses in the DML array. The first

consideration in designing a waveguide circuit for remapping the microlens array positions to the fibre array positions is the trajectory of the waveguides. The waveguide must undergo an s-bend transition from one position to another, with the exact curve size and shape influencing bend losses. Several trajectories have been previously considered [222], such as Bezier curves, raised-sine and cosine curves. We opt for cosine curves due to their regular use at Macquarie university, with legacy code already existing for proven fabrication and understanding of their bend losses [103]. The cosine s-bend takes the functional form in 3-dimensions

$$x(z) = x_{\text{start}} + \frac{\Delta x}{2}\left(1 - \cos\left(\frac{\pi(z - z_{\text{start}})}{\Delta z}\right)\right), \tag{7.1}$$

$$y(z) = y_{\text{start}} + \frac{\Delta y}{2}\left(1 - \cos\left(\frac{\pi(z - z_{\text{start}})}{\Delta z}\right)\right), \tag{7.2}$$

where $\Delta x = x_{\text{end}} - x_{\text{start}}$, $\Delta y = y_{\text{end}} - y_{\text{start}}$. The radius of curvature is defined as

$$R_x(z) = \frac{(1 + x'(z))^{3/2}}{|x''(z)|}, \tag{7.3}$$

$$R_y(z) = \frac{(1 + y'(z))^{3/2}}{|x''(z)|}, \tag{7.4}$$

$$R(z) = \sqrt{R_x(z)^2 + R_y(z)^2} \tag{7.5}$$

such that the minimum bend radius is given by

$$\min[R(z)] = \sqrt{\frac{1}{\frac{\Delta x}{2}\left(\frac{\pi}{\Delta z}\right)^2} + \frac{1}{\frac{\Delta y}{2}\left(\frac{\pi}{\Delta z}\right)^2}}. \tag{7.6}$$

To minimise bend losses we wish to maximise the minimum bend radius for each waveguide curve, which as Equation 7.6 demonstrates, is equivalent to minimising the values Δx and Δy and maximising Δz.

The constructed figure of merit of maximising the minimum bend radius of each waveguide curve can be used to design the LW waveguide array. We opt to design waveguides for coupling to fibre arrays supplied by *OzOptics* due to the ability to easily order arbitrarily populated fixed pitch arrays of the required fibres. For our 10-waveguide chip, the closest available fibre array has 16 possible slots with each slot spaced 127 μm apart. The fibre array therefore defines a set of 16 positions that each lens could potentially be coupled to, with an x–y displacement associated with each fibre port. To maximise the minimum radius of curvature for each waveguide independently of z we choose to use the quantity $r = \sqrt{\Delta x^2 + \Delta y^2}$ as our figure of merit. For all lenses in the array, a cost vector is generated of the values of r for each fibre port, which is then constructed into a cost matrix. In order to efficienctly, globally minimise the cost matrix we use the Hungarian algorithm [223, 224] which is polynomial in run-time and therefore scalable to large waveguide circuits. The resulting waveguide-fibre assignment is shown in Table 7.2 for remapping a 16-port fibre array, populated with 10 fibres, to the designed microlens array in Figure 7.1. The corresponding waveguide circuit is shown in

Waveguide number	Fibre port	Beam name	Wavelength (nm)
1	1	Doppler Cooling 1 (A)	422
2	2	Doppler Cooling 3 (A)	422
3	3	Repumper (A)	1092
4	4	Quencher (A)	1033
5	5	Repumper (B)	1092
6	6	Doppler Cooling 1 (B)	422
7	7	Quencher (B)	1033
8	8	Doppler Cooling 3 (B)	422
9	12	Doppler Cooling 2 (A)	422
10	15	Doppler Cooling 2 (B)	422

Table 7.2: The assignment of each beam to a fibre port and waveguide, where fibres/waveguides are labelled from left to right in the x-axis. The beams with a wavelength of 422 nm use the fibre S405-XP and the beams with wavelengths 1033 nm or 1092 nm use the fibre 1060XP.

Figure 7.2, which for a 12 mm long remapping section has minimum bend radii of >44 mm. Previous reports at λ = 1550 nm have shown that bend radii >22.5 mm show no increased loss over straight waveguides and therefore it may be possible to use shorter remapping sections, however a detailed study of bend losses in blue wavelength LW waveguides would be required.

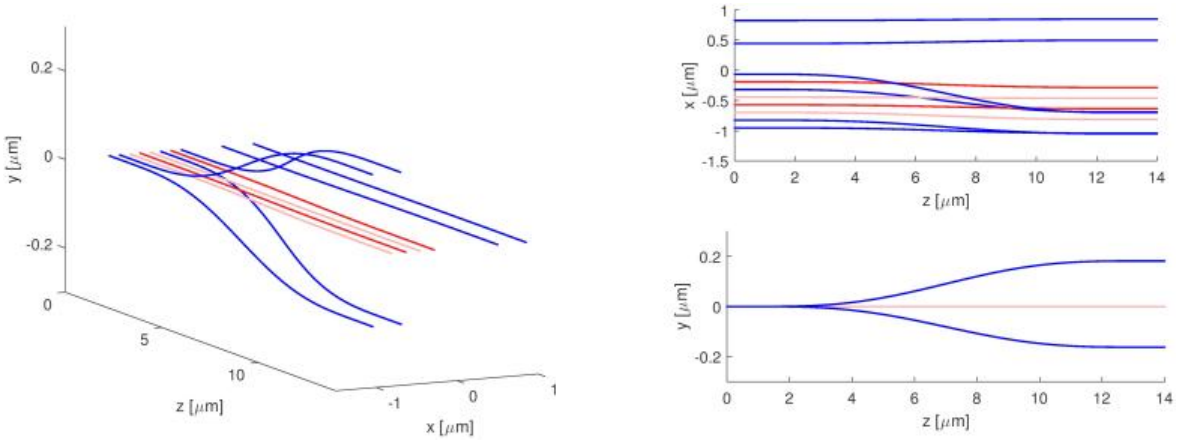

Figure 7.2: The designed waveguide chip, from 3 different perspectives, for demonstrating the optical assembly concept and interfacing with the DML array shown in Figure 7.1. Waveguide design wavelengths are indicated by the colours blue (422 nm), dark red (1033 nm) and light red (1092 nm). The x and y axis scales have been exaggerated for clarity.

Full assembly design The full demonstrator assembly as designed in the previous two sections is presented in Figure 7.3 to scale providing an overview of all beam propagations. We emphasise that the assembly has been algorithmically generated and therefore the scaling to larger number of beams (e.g. for addressing more segments) is trivial from a design perspective. We now proceed to fabricate the designed demonstrator assembly, facing the difficulties of practically realising the design.

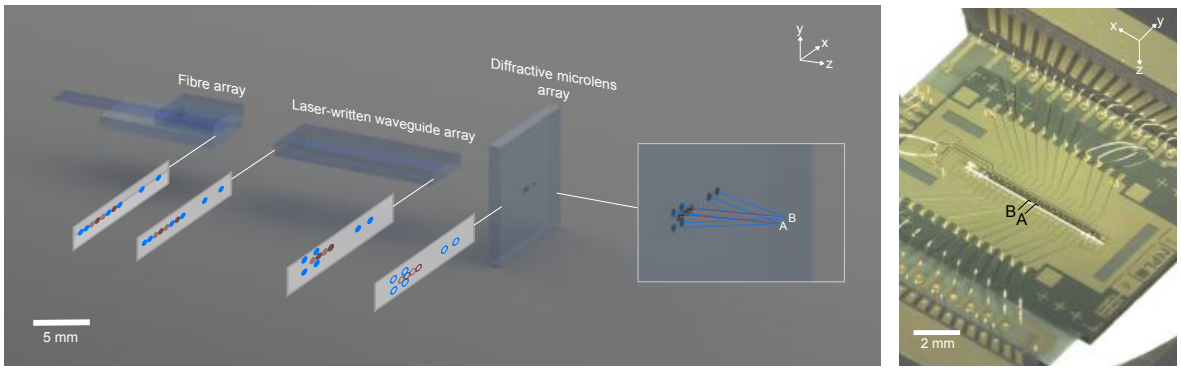

Figure 7.3: (Left) A render of all components of the optical assembly to scale. Shown are the relative beam positions at each interface, showing their propagation through the full system. Inset is a zoomed in render of the intersection points of the lens array. Beam wavelengths are indicated by the colours blue (422 nm), dark red (1033 nm) and light red (1092 nm). (Right) The microtrap to be addressed, with the two segment centres, A and B, labelled.

7.2 Fabrication

The fabrication of the designed optical assembly is enabled by the developed processes for fabrication of individual optical components as outlined in Chapters 4 and 6. During the development of those processes, multiple waveguides or lenses were fabricated at the same time and therefore the transition to waveguide and microlens arrays has been shown to be feasible. However, when all these optical components must work in tandem there are additional considerations in order for the system to work as designed. In this section we outline these additional considerations and the fabrication of the demonstrator assembled tested later in the chapter.

7.2.1 Diffractive microlens array

We fabricated the designed DML array using the same technique as outlined in Sections 6.1.3 and 6.1.4. In fact, the DML array we present here was fabricated on the same substrate and in the same process as the near-unit efficiency titania DMLs and the off-axis DMLS presented in Figures 6.19 and 6.21. The lens chip substrate was measured to be 1030 μm thick and therefore the DMLs were designed with an object position of z_1 = 1050 μm to provide some alignment flexibility. The image positions were those determined in the design of the DML array considered above. Effective off-axis angles of the designed DMLS for λ = 422 nm ranged from 19° to 24° and therefore we expect diffraction efficiencies similar to the 20° off-axis titania DML already presented at λ = 405 nm, which for the dose factor used is ~50%.

The included off-axis DMLs for near-IR wavelengths required special consideration as we have not previously fabricated DMLs for these wavelengths. Due to the thickness of the PMMA resist being 2.5 μm, there wasn't enough latitude to fabricate DMLs of the required depth (~1 μm) in titania due to the found selectivity of ~3.9. We therefore calibrated the dose curve for 2.5 μm deep surface-reliefs

in a previous fabrication run using λ = 1064 nm light, and found a slight adjustment was required compared to DMLs for blue wavelengths. We used the updated dose curve to fabricate dose curve corrected and distortion corrected PMMA DMLs of 2.5 μm depth, which we then transferred into the titania film using reactive-ion etching. The titania DMLs were shallower than that required for a full 2π phase shift of near-IR wavelengths, however as high efficiency operation of these beams are not critical to ion trap operation we choose to test their beam pointing performance with the reduced diffraction efficiencies that result from the under-etching.

The fabricated DML lens array designed for operational wavelengths is shown in Figure 7.4. Optical and SEM images confirm the similarity of the resulting surface-reliefs to design, with the near-IR DMLs deeper than the blue DMLs. Due to the fine-pitch of all the DMLs, surface profiling of the structures is not performed, and so we assess their conformity to design by measuring their beam pointing accuracy and diffraction efficiency.

7.2.2 Laser-written waveguide chip

The 10 LW waveguides included in the demonstrator optical assembly must interface with a VGA such that all waveguides are excited simultaneously. The tolerances on both the waveguide and the fibre array positions must be considered during the fabrication process and the ability to match the position of all fibres with all waveguides simultaneously is critical for low losses. In the following we outline the fabrication of a waveguide chip that takes into account these requirements, as well as additional considerations of the 3D nature of the required waveguide circuits.

V-groove array characterisation

The position of a core in a single-mode fibre, the *core-cladding concentricity*, is typically defined to within ±1 μm with respect to the centre of the fibre end facet. Therefore, when commissioning a fibre array populated with the required fibres, the fibre core positions will not necessarily be at their design positions (that is, aligned on the y = 0 line, spaced exactly 127 μm apart). Compounding the fibre core variations, the relative position of each fibre with respect to their design position in the V-groove array (VGA) is specified to a tolerance of ±0.5 μm (*OzOptics*). Therefore, in the worst case scenario fibre core positions may differ from their design locations in the fibre array by displacements of up to 1.5 μm. When considering the start positions of the LW waveguide array designed to couple to a given fibre array, if these fibre core position variations are not compensated for then a decrease in coupling efficiency is likely due to mode misalignment between fibre modes and waveguide modes. The effect is particularly pronounced for waveguides and fibres supporting a blue wavelength single-mode. As shown in Figure 7.5, for an MFD of 3 μm, a misalignment of 1.5 μm corresponds to a reduction in the mode overlap to only 13.5%. To minimise losses from mode misalignment we requested a measure-

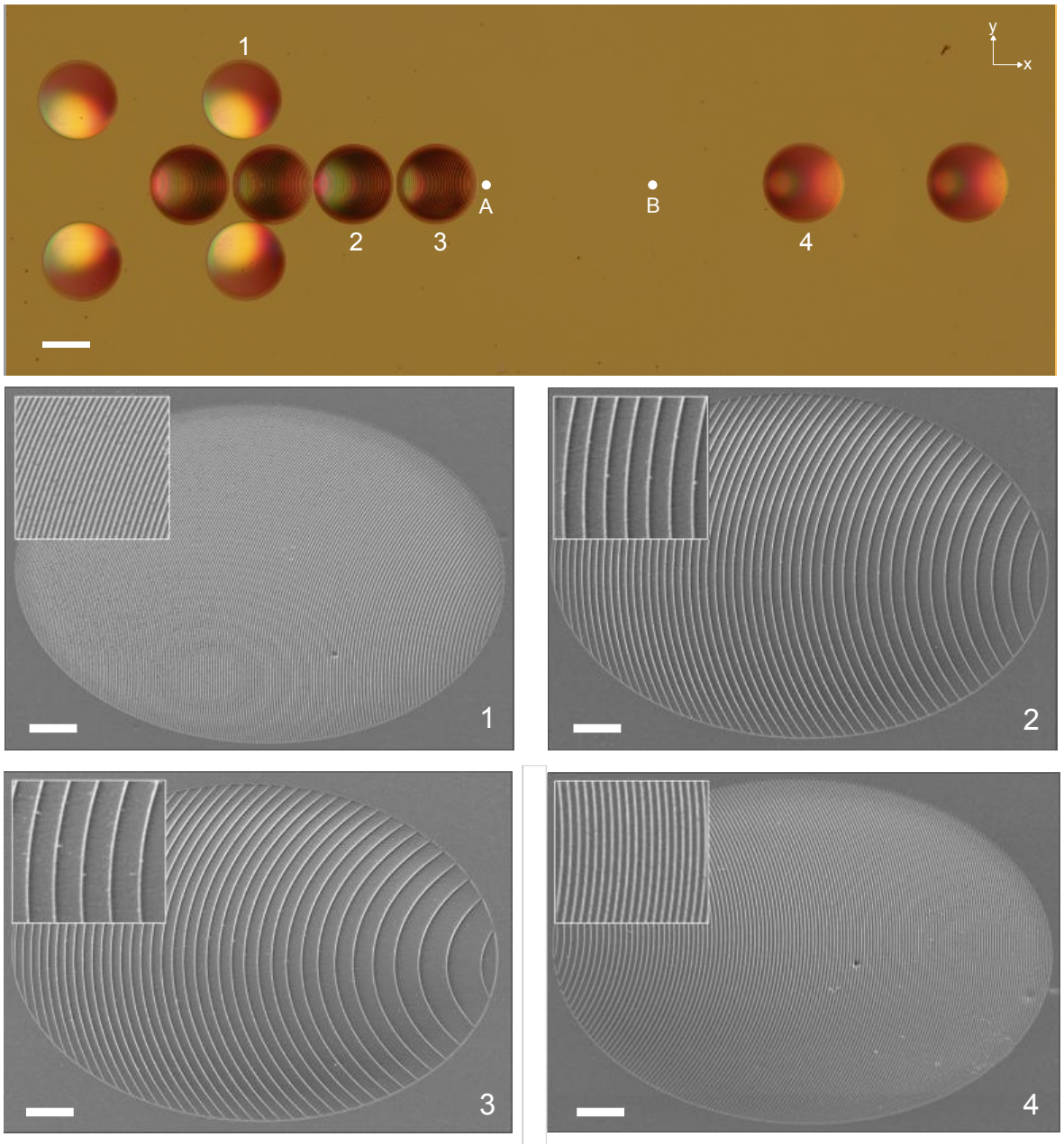

Figure 7.4: Optical and SEM images of a fabricated DML array in titania corresponding to the design shown in Figure 7.1. The scale bar on the optical image is 100 μm, and the SEM images are 20 μm. The x–y positions of the design ion locations are projected onto the optical image. The SEM images correspond to the numbered DMLs on the optical image, with the insets showing the central ~30 μm of the DML.

ment report of absolute fibre core positions from *OzOptics* upon VGA delivery. For two separate fibre arrays it was found that fibre core position variations were conservatively specified, with maximum $x(y)$ deviations of 0.7 μm(0.5 μm). To maximise coupling efficiencies between fibre and waveguide modes we used the measured fibre core positions as the start positions of the waveguide array. The success of this correction is contingent on the accuracy of the LW waveguide fabrication in relative waveguide positioning, which we will discuss when aligning fabricated waveguide chips to VGAs.

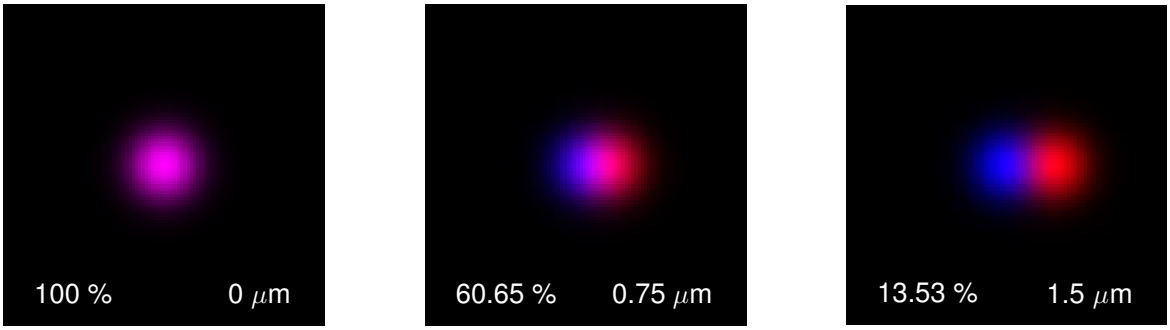

Figure 7.5: Simulations of the overlap of two Gaussian beams with MFDs of 3 μm for varying displacement of one Gaussian profile from 0 μm to 1.5 μm. The annotated text is (left) calculated mode overlaps of the two profiles, (right) the relative displacement.

Fibre	Core diameter (μm)	NA	Wavelength range (nm)	MFD (μm)
S405-XP	3.0	0.12	400–680	3.3 ± 0.5 at λ = 405 nm
1060XP	5.8	0.14	980–1600	6.2 ± 0.5 at λ = 1060 nm

Table 7.3: The specifications of the fibres used in the fibre array for interfacing with LW waveguides. NA and MFD are short for numerical aperture and mode-field diameter respectively. The numbers are from the respective *Thorlabs*' specification sheets [225, 226].

Depth correction

In all the development work of LW waveguides for blue and near-IR wavelengths we fabricated waveguides at a depth of 245 μm, however as previously explained in Section 4.2.1 the pulse energy required to fabricate a fixed diameter waveguide will change with depth. We characterised this change by fabricating waveguides of a constant pulse energy of 46 nJ at various depths from 63 μm to 407 μm in Corning Eagle2000 and measuring the resulting waveguide diameter using TDIC microscopy. The diameters, D, followed a third-order polynomial trend with depth, d, as shown in Figure 7.6, with fitted parameters

$$D = 141.9d^3 - 109.4d^2 + 22.8d + 10.6\ . \tag{7.7}$$

During fabrication, we control the pulse energy of the HPO to change the resulting the diameter of the fabricated waveguides. Therefore, we model the change in the waveguide diameter as an effective change in the pulse energy with depth, thereby mapping the problem to a parameter we are able to control. We associate the diameters found from Equation 7.7 with an effective pulse energy, using a typical calibration set associating waveguide diameter with pulse energy, and then apply an opposite change in pulse energy when writing waveguides to make the effective pulse energy constant at all depths. We performed depth correction on the demonstrator waveguide chip presented in the Section 7.4.2 where we will comment on its effectiveness.

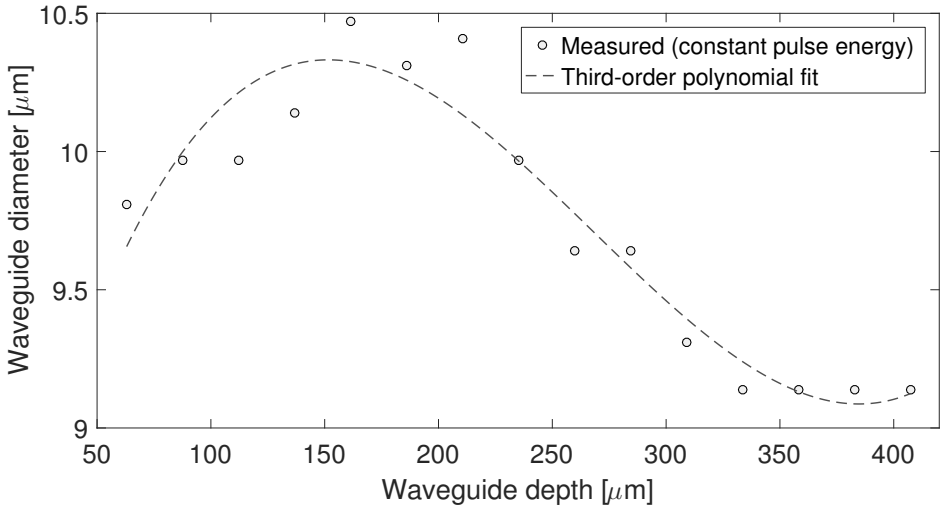

Figure 7.6: Measurements of waveguide diameters fabricated at different depths for a constant pulse energy of 46 nJ. The fitted third-order polynomial is used for depth correction by providing an effective pulse energy at each depth.

Laser-writing of demonstrator waveguide chips

The demonstrator waveguide chip was optimised over 3 fabrication runs, with the fourth fabrication run yielding the devices tested in the remainder of the chapter. The final set of waveguide devices were written by Simon Gross at Macquarie University using the HPO using identical techniques to those outlined in Chapter 4. Six separate waveguide devices were fabricated in a 30 mm ×14 mm sample of Corning Eagle2000. Three devices had waveguide start positions that are uncorrected for the VGA fibre core positions, and three devices were position corrected. Each device was 5 mm wide and were separated by a scribe mark demarcating the dicing line for eventual device separation; device label text was also included so that after dicing each device can be uniquely identified. For redundancy, a second sample was prepared identically but with the position corrected waveguides designed for a different VGA. Our aim was to demonstrate a manufacturable process for fabricating waveguide chips where multiple devices are written in the same substrate and then later separated after all post-processing is completed.

There were some challenges encountered during the initial write attempts of the multi-device sample and it was found that the waveguides for blue light started several millimetres from the start chip face - after the waveguide circuit had entered the remapping section. It was found that the immersion oil was not being properly transported during fabrication and the solution was to place an additional piece of glass before the input face of the waveguide chip. After implementation of this solution waveguide samples were written without any defects in any waveguide, with a device yield of 100%.

Lap and polish One benefit of fabricating all waveguide devices in the same glass substrate is that the time consuming process of the lap and polish can be easily parallelised. One waveguide sample was ground back and polished at the University of Bristol in the same way as outlined in Section 4.2.4.

Dicing After brief initial optical testing to confirm the waveguide devices were close to design, the waveguide sample was diced along the dicing lines. While the dicing machine has an automatic stepping function, we manually confirmed that each dicing line was spaced 5 mm apart, which we expect due to the precision of the fabrication stages. In the future, large numbers of waveguide devices fabricated in the same substrate could be automatically diced after initial alignment of the dicing machine to one edge of the sample.

7.3 Assembling

Critical to the realisation of the optical assembly is the assembly process itself. In this section we align and bond the VGA to the waveguide chip in a way that does not depend on the number of waveguides present. The bonding of the waveguide chip to the lens array chip is *not* performed so as to enable continued development of better optimised or more advanced lens arrays in the future, however we note that its bonding could be performed in a very similar way.

7.3.1 Alignment

Alignment of the VGA to the demonstrator chip was performed using the first and last fibres of the VGA. The VGA was mounted on a 6-axis flexure stage (*Thorlabs Nanomax*) with piezo actuators. The horizontal, vertical and roll piezo actuators were connected to a 3-channel voltage controller that could be addressed using RS232 serial commands. The yaw was first visually aligned using an overhead vision system, angling the VGA edge such that it was parallel with the waveguide chip edge, before optimising both the pitch and yaw using the coupling efficiency into a single waveguide. A laser source and a fibre beamsplitter was used to excite both the first and last fibres of the VGA with λ = 642 nm light and the horizontal, vertical and roll degrees of freedom were then roughly optimised by eye using a near-field projection of the output facet of the waveguide chip. To optimise the coupled power with alignment, the output of waveguide 1 was focused using a 10x objective onto a power meter with a pinhole to suppress background power. The output of waveguide 10 was picked off using a 45 degree prism mirror and directed to an apertured power meter on a separate 2-axis stage such that the waveguide output could be aligned through the centre of the pinhole onto the power meter. Raster scans of horizontal and vertical piezo voltages were performed for various roll voltages, with the coupled power in each waveguide measured for each voltage to construct a map of the overlaps between the fibre and waveguide modes. The roll was optimised by minimising the root-mean-square

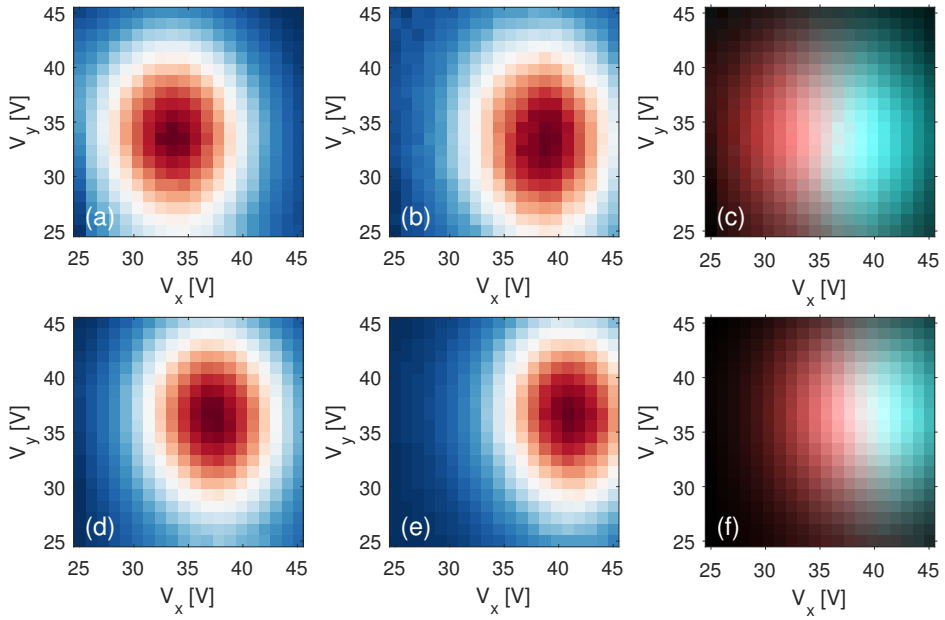

Figure 7.7: Output power of the first and last waveguide of (a-c) a waveguide set uncorrected for fibre position and (d-f) a waveguide set corrected for fibre positions. (a-b) and (d-e) show measured output power in the two waveguides for different combinations of the x and y piezo voltages. (c) and (f) shows the data on the same plot to emphasis the displacement between the maxima of the two datasets. Assuming linear displacement with voltage, 1 V corresponds to 0.4 μm change in the x or y position. The y-axis is not necessary for alignment purposes as the roll optimisation is designed to correct for any y-displacements. We show y data here to demonstrate that the roll has indeed been optimised.

distance between the horizontal and vertical piezo voltages of maximum overlap for each waveguide. After roll optimisation, the horizontal and vertical piezo voltages were raster scanned and the mean position between the two optimal found piezo voltages is found. The waveguide chip position is then set to this mean position as the position of best alignment. We note that the vertical raster scan is not strictly necessary as the roll optimisation has negated any vertical displacement between the best coupling positions. However, we include the vertical scan to confirm that no alignment drift has occurred between roll optimisation and horizontal axis alignment. After horizontal alignment, the remaining 8 waveguides were checked for similar coupling powers to the first and last waveguides to confirm that the alignment procedure had been successful.

The alignment procedure was tested on two waveguide chips of the fabricated set of devices, one was fibre core position corrected and the other had no correction applied. Overlap maps for the two chips after roll optimisation are shown in Figure 7.7 demonstrating that the position-corrected waveguides had a smaller distance between optimal overlaps in the two extreme waveguides when compared to the uncorrected set. Assuming a linear displacement with voltage, the 3.16 V (5.26 V) between the optimal couplings of the extrema waveguides for the corrected (uncorrected) set corresponds to position errors of 1.3 μm (2.1 μm). For the corrected set, the first and last waveguides were separated by 1905 μm and therefore the measured position error between these waveguides is 0.1%,

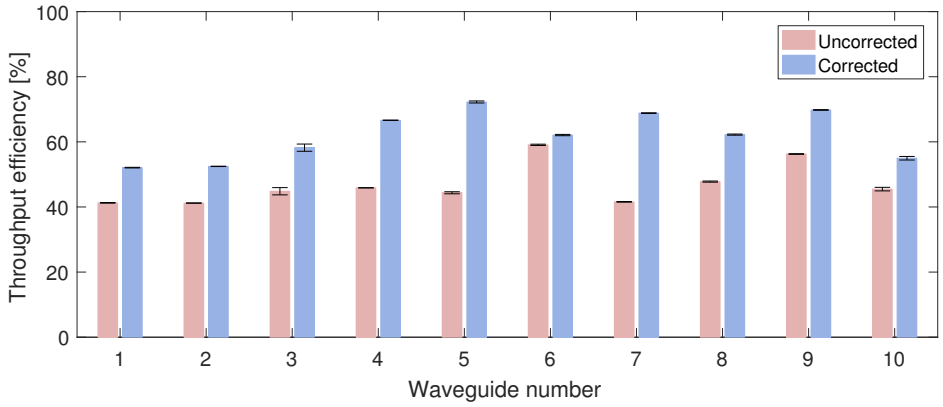

Figure 7.8: Output power measured in all waveguides after the optimal alignment is found as shown in Figure 7.7 for both the uncorrected and position-corrected sets where the first and last waveguides are 1 and 10 respectively. Increased power trasnmission is found in every waveguide in the corrected set compared to the uncorrected set, with an average increase of 15%.

highlighting combined accuracy of the precision stages used for fabrication and the VGA fibre core positions measurement. Power measurements of each waveguide after alignment in both the corrected and uncorrected sets are shown in Figure 7.8, demonstrating that the corrected waveguide set has a greater mode overlap with all fibres with an average 15% increase in power transmission. As we test the alignment at λ = 642 nm, which is far from all design wavelengths, the power measurements do not represent operational coupling efficiencies but only give an indication of the relative position of each waveguide to the fibre core. We present coupling efficiency measurements at operational wavelengths in Section 7.4.2 after bonding of the fibre array to the corrected waveguide set.

7.3.2 Bonding

The increased transmission found for the corrected waveguide set led to it being chosen as the demonstrator waveguide chip and it was subsequently prepared for bonding to preserve the alignment. The waveguide chip and fibre array end facets were cleaned with IPA and blown dry with compressed air before mounting both samples on vacuum chucks for easy removal of what will become a fragile assembly. The fibre array was aligned to the waveguide chip as before using λ = 642 nm radiation, with high power transmission confirmed in all 10 waveguides before proceeding with gluing. The use of red wavelengths for aligning and monitoring power during the bonding procedure was to avoid the curing of the adhesive as it was found during practice runs that when bonding fibres and waveguides using blue wavelength radiation for power monitoring that the adhesive begun curing at the fibre core position without any UV exposure. The tip of a syringe was used to transfer a small quantity of UV-curing optical adhesive (*Norland Optical Adhesive 86*) to the top of the waveguide-fibre array interface. The power of waveguide 1 was monitored, with the penetration of the adhesive into the gap between the interfaces confirmed by increased transmission due to the presence of an index

matching medium between the fibre and waveguide. Waveguides 1, 5 and 10 were all confirmed to have similar power transmissions before an initial, 10 second low-power cure using a directional UV lamp was performed while monitoring the power out of waveguide 1. Further short cures, interleaved with checking the power transmissions of the three waveguides was performed several times to make sure that the curing adhesive was not shrinking and displacing the alignment. The power of the UV lamp was increased to maximum with the power of waveguide 1 being monitored, and waveguide 10 occasionally checked. Coupled power increased during curing for an unknown reason, and once power stabilised in the first and last waveguide the assembly was left to cure for ~18 hours. After curing the assembly was left to age for 1 week to further strengthen the bond to minimise the chance of misalignment after moving.

After ageing, a 1 cm $\times$ 4 cm section of a microscope slide was diced as a support base for the waveguide-VGA assembly. Any torsional force on the interface risks misaligning the waveguides or, in the worst case, breaking the bond. The bottom of the fibre array extended slightly beneath the waveguide chip and so a ~100 μm thick piece of cover slip of approximate dimensions of the waveguide chip is bonded to the top surface of the glass slide. The assembly was then laid on top of the glass slide with the fibre bundle secured to the 6-axis stage. The glass slide was translated with respect to the assembly such that the assembly and slide were flush and temporary, UV-curing adhesive (*Norland Blocking Adhesive*) was placed along the long edge of the waveguide chip and fibre array on both sides. The adhesive was rapidly pulled into the gap between the assembly and the glass slide due to surface tension, as seen on an overhead vision system, and when sufficient area of the assembly and glass slide were contacted with the adhesive a directional UV lamp was used to cure the assembly in place. The risk in this procedure was in the fibre array and the waveguide chip being tensioned differently by the shrinking adhesive, hence why care was taken to place a coverslip under the waveguide chip. After curing the waveguide chip could be packaged for transport to an optical testing rig. The blocking adhesive can be later removed by heating the glass slide to ~70°C for assembly into the final optical system.

The fully glued waveguide-VGA assembly is shown in Figure 7.9 demonstrating continuous guiding of blue light from the fibre array to the waveguide array after all bonding has occurred. As will be shown in the next section, no negative affects of the bonding process or of transport of the assembly is found and the waveguide chip maintains its alignment as evident by the high transmission of blue wavelengths through the full assembly as shown in Section 7.4.2.

7.4 Testing and characterisation

Having fabricated all the required components for partially demonstrating the concept presented in Chapter 2 we now proceed to thoroughly characterise its performance for analysing the concept's

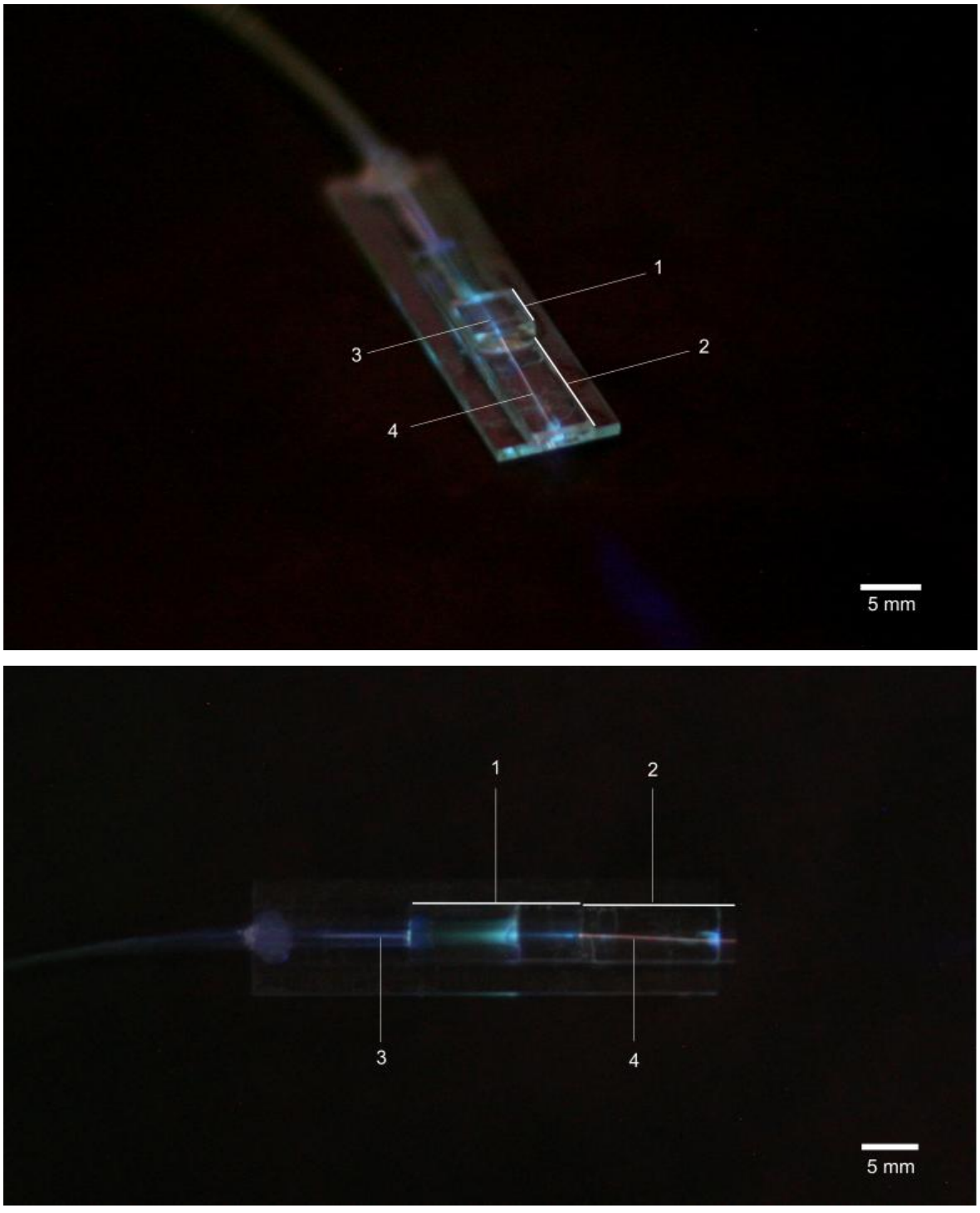

Figure 7.9: Long exposure images of fibre array bonded to the fabricated waveguide chip with a single, blue waveguide illuminated. (1) Fibre array (2) Waveguide array (3) Illuminated waveguide (4) Illuminated fibre. (Top) A perspective view of the assembly (Bottom) A plan view of the assembly demonstrating the propagation of light through a waveguide bend. The significant colour difference of light scattering from the fibre and the waveguide is visible.

feasibility. As the attaching and aligning of the assembly to the vacuum housing of the microtrap is an unsolved challenge we perform these characterisations in free space using CCDs and power meters to measure how accurately and efficiently the assembly propagates light at operational wavelengths to the design ion positions. All testing occurred at NPL due to the requirement for laser sources at the operational wavelengths, and therefore the optical assembly was transported there. The bonded waveguide-VGA assembly was packaged in the same folio box the VGA was delivered in, while the lens chip was mounted on its test mount and secured inside a small optics box. Both sub-components made the journey from Bristol to London without any measurable performance degradation.

7.4.1 Methods

The majority of the methods used to characterise the optical assembly are familiar as they are ones that have been used to characterise individual components in previous chapters. Our testing methodology involves characterising each sub-component to analyse how each one contributes to the final device performance and so there are some nuances, and extra techniques employed, that we now outline.

Lasers

We performed optical testing using lasers designed to operate with trapped $^{88}Sr^{+}$ ions, based at NPL, of which more information can be found in [9]. A *Toptica DLC DL pro HP 422* laser was used as the laser source for 422 nm light, and coupled into PM405-XP APC fibre using two mirrors. An SM400 APC-to-PC fibre was used to interface the PM405-XP APC fibre with the fibre array which contains PC terminated fibres. 1033 nm wavelength radiation, generated using an external cavity diode laser (ECDL), was coupled into PM980-XP APC before conversion to the PC fibre interface using an SM980 APC-to-PC fibre. A neodymium-doped fibre laser was used to generate 1092 nm light and was coupled into a duplicate of the fibres used for the 1033 nm wavelength. All laser powers were set to ~1 mW at the fibre outputs for safe operation due to the uncontained beams that will propagate from the DML array. The fibres were interfaced to the fibre array using a narrow-key fibre mating sleeve (*Thorlabs ADAFCPM2*). As only three fibre sources are used, all measurements of different guides at the same wavelength occur consecutively.

Optomechanics of optical assembly testing

The bonded waveguide and fibre-array were mounted on a 6-axis flexure stage (*Elliot Gold*) such that the alignment of the waveguide chip to the lens chip could be fully optimised. The lens chip was mounted on a support block such that the waveguide chip can be brought up against the back of the lens chip. The lens chip support block was mounted on a cantilever which was secured to a high-load, 3-axis stage (*Newport ULTRAlign M-461-XYZ-M*) so that it could be arbitrarily translated with respect

to the waveguide chip. Coarse alignment of the two independent sub-components was performed using an overhead vision system.

Beam profile measurements

We performed beam profile measurements for two purposes, one was for characterisation of fibre and waveguide modes, the other was to measure the propagation of beams deflected and focused by the DML array. Guided modes were studied with an objective and CCD combination, while propagating modes were studied with a bare CCD.

Objective and CCD A 100× objective mounted ~16 cm from a *Dataray WinCamD* beam profiling CCD on a cage system is used to image fibre and waveguide modes. The cage system was mounted on a 3-axis stage allowing for alignment of the modes to the CCD.

Bare CCD An exposed board camera (*Raspberry Pi Camera Module v2 NoIR*), sensitive at blue and near-IR wavelengths, was used to image propagating beams from the DML array, with a closest approach distance of ~400 μm from the lens plane. The pixel pitch of the CCD is 1.12 μm allowing for precise determination of beam positions and resolving of tightly focused Gaussian beams.

Power measurements

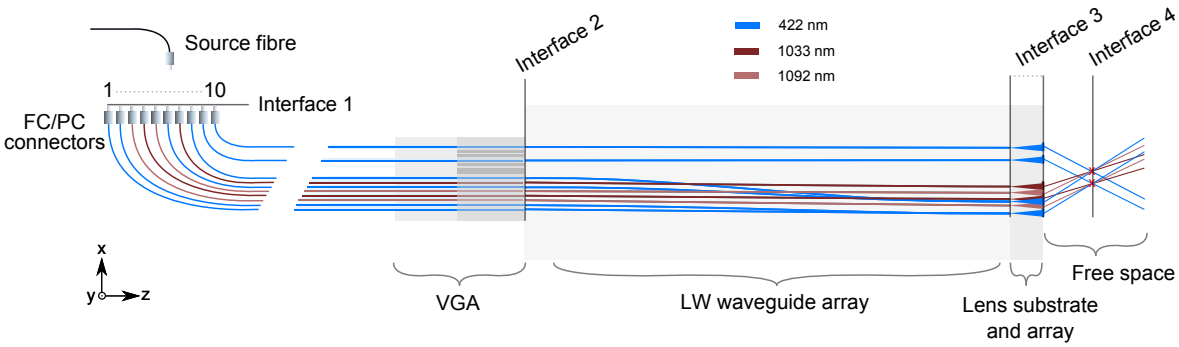

Figure 7.10: A plan view of the demonstrator assembly with the interfaces and power efficiencies defined in the text illustrated. The fibre/waveguide number is labeled 1–10 from left to right respectively.

In order to determine the component and assembly loss we measure the power at all interfaces in the assembly (see Figure 7.10): (1) Fibre-array input facets; (2) fibre-array to waveguide coupling (plus waveguide propagation loss); (3) transmission of light through the lens chip; and (4) efficiency of DML array in focusing light to the desired intersection point. We assign the transmission efficiency at each interface 1 to 4 as η_1 to η_4. Power calibration was performed for all measurements by measuring the output power from the source fibre over 10^2 samples both before and after optical component testing using a fibre power meter (*Thorlabs S151C*). The source fibres were then sequentially coupled

to the fibre-array fibres and the output power at the measured interface focused onto an apertured power meter using a 10× objective. As the power of the source fibre and the interface are measured using different techniques, the power from the source fibre will be overstated due to the Fresnel reflections and losses due to the objective used to focus light onto the power meter. As we have made no attempt to optimise the in-coupling into the optical assembly this is not an issue as this power discrepancy is separated from the intrinsic losses of the system through the measurement process.

As interface 2 (fibre array to waveguide array) was not directly accessible due to already being bonded, we performed a measurement on an identically prepared fibre array to measure the average loss at interface 1. The duplicate VGA was mounted on the 6-axis stage such that the output power could be imaged onto the power meter, and the outputted power from the VGA for all fibres was measured 3 times per fibre, with the source fibre unplugged and replugged into the fibre coupler between power measurements. An average coupled power was found for each wavelength and used to approximate the effective power at interface 2 in the demonstrator assembly so that losses at interface 2 could be quantified. Propagated standard deviations on the mean of all power measurements were used to formalise the errors in this approximation.

7.4.2 Results

In this section we outline the results of the full characterisation of the micro-optical assembly. We aimed to breakdown the contribution of the individual sub-components to assess any potential improvements and their influence on the ultimate performance if interfaced with an operational microtrap. We start with the coupling of the VGA to the waveguide chip before demonstrating operation of the full assembly.

Waveguide profiles and overlaps with single-mode fibre

A summary of the average of the measured MFDs of the fibre and waveguide modes is presented in Table 7.4 along with their average overlaps. Mode overlaps were calculated between an ideal Gaussian profile with the listed major and minor MFDs of the fibre and the actual measured waveguide mode profile, to take into account any non-Gaussian aspect of the waveguide modes (such as Lorentzian wings). We found a good overlap between S405-XP fibre and the fabricated waveguides for guiding blue wavelengths, with a 96.2(0.5)% mode overlap. The effectiveness of the depth correction procedure is supported by the fact that the quadratic mean MFDs of waveguides 1 and 2 (ending at depths of 63 μm and 407 μm respectively) are within error of each other indicating that the waveguide diameters are very similar despite their large depth separation. The waveguides for supporting a singlemode of 1033 nm and 1092 nm were found to be smaller in physical diameter than ideal as the supported mode profiles were measured to have Lorentzian profiles which we have previously

Wavelength (nm)	Fibre MFD (µm)		Waveguide MFD (µm)		Overlap (%)
	Major	Minor MFD	Major MFD	Minor MFD	
422	3.11 ± 0.01	3.08 ± 0.01	2.67 ± 0.04	2.45 ± 0.04	96.2 ± 0.5
1033	6.15 ± 0.02	6.06 ± 0.06	8.50 ± 0.06	6.50 ± 0.5	87.1 ± 0.6
1092	6.78 ± 0.03	6.54 ± 0.03	9.73 ± 0.04	7.00 ± 0.2	80.4 ± 0.2

Table 7.4: Averaged, measured MFDs of all waveguides and fibre modes. Quoted errors are standard deviations on the mean over the sampled modes.

measured to be a signature of the weakly guiding regime (Section 4.5.1). As shown in Figure 7.11, while the central portion of the waveguide mode overlaps well with the fibre mode profile, the decreased mode overlap is caused by the increase power in the mode wings. No such wings are present for λ = 422 nm indicating that the waveguides are close to design in the optimal guiding regime. As we will show, the fact that the near-IR waveguides are in the weakly guiding regime leads us to expect that they will have both reduced coupling efficiency (due to lower mode overlaps) and reduced propagation efficiency (as shown in Section 4.3.3).

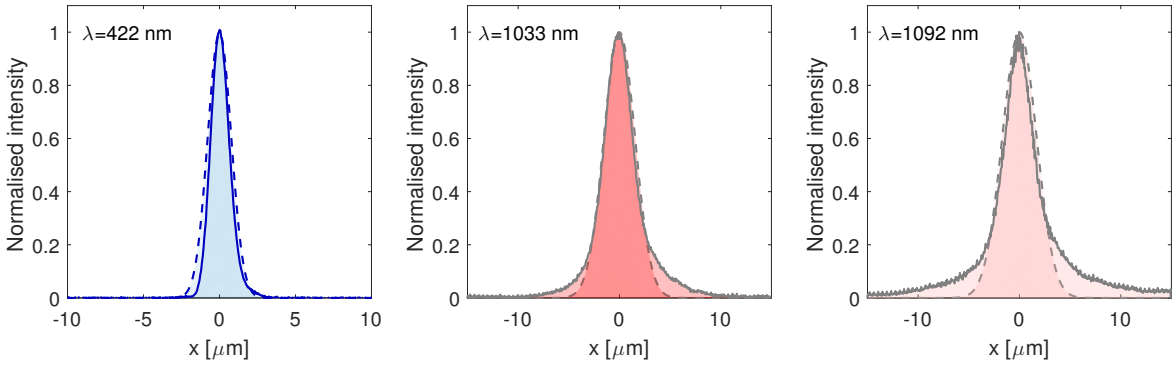

Figure 7.11: Example beam profile cross sections of waveguides (solid lines) and corresponding fibre modes (dashed) for all three wavelengths used in the optical assembly. The reduced overlaps of the near-IR beams summarised in Table 7.4 are due to the extended Lorentzian tails visible in their waveguide cross-sections.

Power losses

The mean fibre-to-fibre coupling efficiencies at interface 1 were found to be low at 29(3)%, 49.5(0.4)% and 42.4(0.7)% for wavelengths of 422 nm, 1033 nm and 1092 nm respectively. The two main reasons for these coupling efficiencies are that the source fibres were not identical to the fibres in the VGA, and fibre core position tolerances leading to fibre-fibre core misalignment. The particularly low coupling efficiency between the source fibre and VGA fibres at blue wavelengths is most likely due to the smaller MFDs of the fibre and therefore the tolerances on the exact core alignments are more critical, which is supported by the increased variance in the coupling efficiency between different fibres. We do not consider the fibre-fibre coupling at interface 1 to be an intrinsic loss of the optical assembly and could

be easily increased by improvements in the selection of optical components, such as using the same source fibres as used in the VGA, components with tighter tolerances or even splicing source fibres to the array.

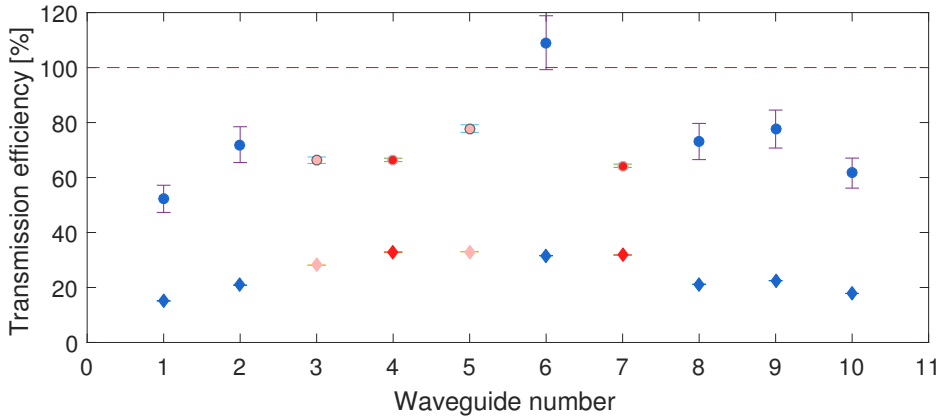

Figure 7.12: The measured transmission efficiency of the waveguide chip, (diamonds) total transmission including the fibre-fibre interface (1) and the fibre-waveguide interface (2); (circles) transmission of just interface 2, including propagation losses in the waveguides providing information on the coupling efficiencies of the fibre array to the waveguide array. Increased errors for the circle data points are due to variances in the fibre-fibre coupling efficiencies. The apparent >100% transmission for waveguide 6 is within error and likely from high fibre-fibre coupling.

Having calibrated the transmission at interface 1, we could calculate the transmission at interface 2 by measuring the power output of all the waveguides and correct for the known losses at interface 1. The potential variation in fibre-fibre coupling at interface 1 appears as increased error bars when determining the corrected power at interface 2. Measured powers for all waveguides out of the waveguide chip are presented in Figure 7.12 with both the raw, measured transmission efficiency as well as the corrected values. We found that the near-IR waveguide corrected transmission efficiencies were similar to those measured at λ = 642 nm, while the blue waveguides were all increased over the measurements at the red wavelength. The increase in transmission efficiency for blue wavelengths indicates that the fibre and waveguide cores were well aligned, as even when the mode diameter is reduced, by decreasing λ, the coupling efficiency increases due to an increased overlap with the waveguide mode, which can only happen if the waveguide mode is not significantly displaced from that of the fibre core. Waveguide 6 demonstrated a transmission efficiency of 109(10)%, most likely caused by a high coupling from the source fibre into the VGA fibre as is supported by a transmission efficiency of <100% being within error. However the high transmission indicates that the waveguide has a high propagation efficiency despite it having a finite bend radius. The transmission of the near-IR wavelengths is much lower than expected given the decreased absorption of the material at these wavelengths as well as the more relaxed alignment tolerances. The reason for the higher losses is due to the waveguides operating in the weakly guiding regime, which we have previously shown to increases losses in blue waveguides, as well as the 10–20% mismatch in the mode overlaps

between the fibre and waveguide mode. With increased waveguide diameters we expect a significant improvement to >90% transmission at near-IR wavelengths.

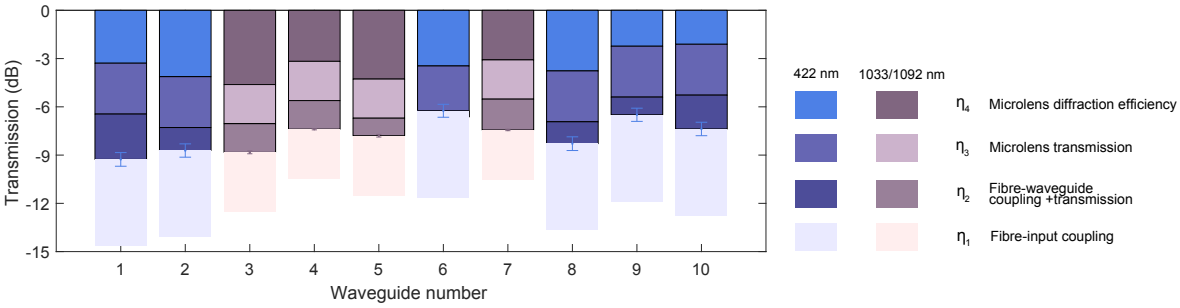

Figure 7.13: A full breakdown of transmission efficiencies at each interface of the optical assembly. The loss at interface 1 is not considered instrinsic to the system and is included for reference.

A summary of the measured transmissions at each interface is shown in Figure 7.13 where the powers at interfaces 3 and 4 are backed out using the same method as for interface 2. The averaged transmissions for each wavelength are summarised in Table 7.5, where we quote the transmissions in decibels as they are additive and can be calculated from percentages using the formula

$$\mathrm{dB} = -10 \log_{10}\left(\frac{\mathrm{percent}}{100}\right) . \tag{7.8}$$

The power lost by reflection at the lens chip and the decreased diffraction efficiency of the DMLs are the dominant loss mechanisms in the assembly. The loss at the lens chip interface will be improved when the waveguide chip is bonded to the lens chip, providing an index matching layer which will reduce the current ~8% Fresnel reflection from the waveguide-air and air-lens chip interfaces. Reflection at the glass-titania-air interface is likely to be the main contribution to loss at interface 3, however as discussed in Section 5.2.3 this transmission can be tuned with suitable control over the fabrication process such that precise film thicknesses can be optimised for maximum transmission - an exercise we have not performed. The diffraction efficiencies of the DMLs are as expected, with those for λ = 422 nm having a mean diffraction efficiency of −3.1 dB (49%), and for the near-IR DMLs where the depth is not optimised but the features sizes are larger we found mean diffraction efficiencies of −3.1 dB (49%) and −4.4 dB (36.1%) for wavelengths of 1033 nm and 1092 nm respectively. Diffraction efficiencies of the blue wavelength DMLs can be increased to ~70% by optimising the maximum electron dose factor, and perhaps increased further by employing more advanced dose and distortion correction protocols to accommodate pitch-dependent effects. The near-IR wavelengths DMLs can be improved by increasing the thickness of the PMMA resist during fabrication such that DMLs of the correct depth can be fabricated in the titania. Process re-optimisation would be required to account for the thicker PMMA resist such that it does not negatively affect the fabrication of DMLs for blue wavelengths.

Interface	Average transmission (dB)		
	λ = 422 nm	λ = 1033 nm	λ = 1092 nm
1	−5.4	−3.1	−3.7
2	−1.3	−1.8	−1.4
3	−3.2	−2.5	−2.5
4	−3.1	−3.1	−4.4
1–4	−13.0	−10.5	−12.0
2–4	−7.6	−7.4	−8.3

Table 7.5: A breakdown of the averaged, measured power transmission of all beams at their operational wavelengths at each interface in the optical assembly, where the interfaces are defined in Figure 7.10. The transmission of interfaces 1–4 includes the fibre-fibre input loss, which is not an intrinsic loss of the system. The internal losses of the optical assembly are represented by the interfaces 2–4.

The average total transmission of the optical assembly are −7.6, −7.4, and −8.3 dB for wavelengths 422 nm, 1033 nm and 1092 nm respectively. Despite the scope for improvement of the transmission of the optical assembly, the demonstrated transmissions are already favourable for large scale addressing of ion microtrap arrays, which we will discuss further in Section 7.5.

Overlap of beams at design intersection point

To test the overlap of the beams at the design intersection points we first carefully aligned the waveguide chip to the lens chip. Alignment was begun by illuminating waveguide 1 and observing the shadow of the DML array on the exposed board CCD while translating the lens chip along the z-axis towards the waveguide chip. The approach of the waveguide chip to the lens chip was monitored using the overhead vision system, with the final approach using the exposed board CCD. When the waveguide chip comes in contact with the back of the lens chip, further translation of the lens chip does not cause any changes on the image observed on the CCD. Once contact was found, the lens chip was translated back again by 20 μm to approximately achieve the designed waveguide-lens distance. Coarse roll alignment of the waveguide chip to the lens chip was performed by observing the shadow of the DML array when waveguide 10 was illuminated with λ = 422 nm light and waveguide 7 was illuminated with λ = 1033 nm light. The roll was adjusted such that the expanded waveguide outputs were simultaneously aligned with both their corresponding DMLs, which required adjustment of the lens array x and y translations as the roll was optimised. Finer roll alignment was performed using the same pair of waveguides but instead observing the propagation of the DML outputs. As these two beams were in the $y = 0$ plane they should intersect at some z position of the CCD and knowledge of this fact allowed for the roll to be fine tuned such that the beams satisfied this behaviour. Final alignment was performed using waveguides 1, 2 and 9 which corresponded to the three Doppler cooling beams designed to overlap at position A. Waveguides 1 and 2 were sequentially illuminated and the CCD was placed at the z position where the beams overlapped, using a marked position on the

computer monitor. The roll was then adjusted to overlap the output of waveguide 9 on the position of the other two Doppler cooling beams. After roll optimisation, the z-position of the CCD was tuned for maximum overlap of all 3 Doppler cooling beams. CCD images are then sequentially recorded of all waveguides illuminated at their design wavelength at the found intersection point, with fixed alignment between images. The processed images are shown in Figure 7.14, with intersection point

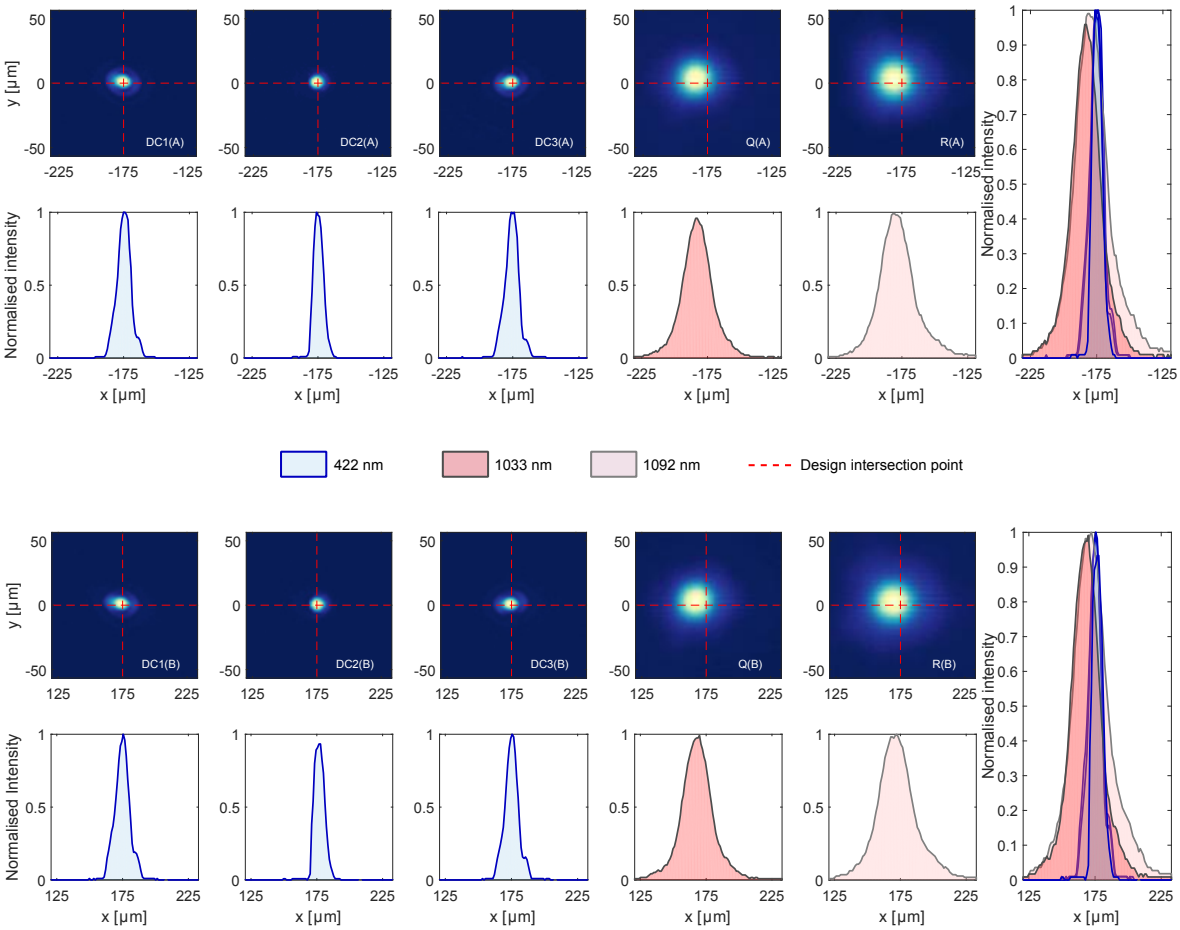

Figure 7.14: The position of all beams (labelled as inset text) in the same x–y plane after alignment of the waveguide chip to the DML array. Both 2D beam profiles and 1D cross-sections are shown with red dashed lines to indicate the design intersection points of A ($x = -175$ µm) and B ($y = -175$ µm). The overlap of all beams at each position are shown in 1D cross-sections to illustrate how well they intersect.

B found to be the designed 350 µm from intersection point A (which we aligned to). The maximum intensity peak of all Doppler cooling beams are congruent to the resolution of the CCD (1.12 µm) with the exception of DC2(B) which is displaced by one pixel. The accuracy, and precision, of the overlapped Doppler cooling beams demonstrates the capability of the developed EBL process, and that the 25 nm pixel size of the fabrication map is sufficient for the demonstrated design. The near-IR beams are not perfectly overlapped with the Doppler cooling beams, with slightly reduced intensities of the quencher beam of 69% and 78% at positions A and B respectively, and of the repumper beam of 90% and 93%. The error in the repumper beam pointing is 0.8% and within tolerance, however

the quencher beam pointing error is 2.2%. The quencher beams have the smallest deflection angle and therefore should have the most relaxed tolerance on fabrication imperfections. The consistency between the displacements in the repumper and quencher beams between sets suggests a systematic design error rather than a fabrication issue. The accuracy of the Doppler cooling beam overlaps supports this assumption as they have much stricter fabrication tolerances. The misalignments of the NIR wavelength beams is therefore most likely due to development of diffractive microlenses design models and processes at ~405 nm wavelengths. We expect beam pointing accuracy of these beams to be improved in later iterations with better understanding of DMLs for near-IR operation, however it is worth noting that these demonstrated intersections would be sufficient for driving atomic transitions in $^{88}Sr^{+}$ ions. The Lorentzian wings of the waveguide modes had been preserved by the DML and therefore it is of great interest to remove these wings to reduce cross-talk with neighbouring microtrap segments, which can be performed by increasing waveguide diameters.

To illustrate the free-space propagation of the Doppler cooling beams to intersection point A we imaged the three beams along the z-axis at 50 μm increments around the point of intersection. The converging modes were sequentially imaged at each point, and a composite set of image slices were constructed in MATLAB. A graphical representation of the sliced beam propagation is shown in Figure 7.15.

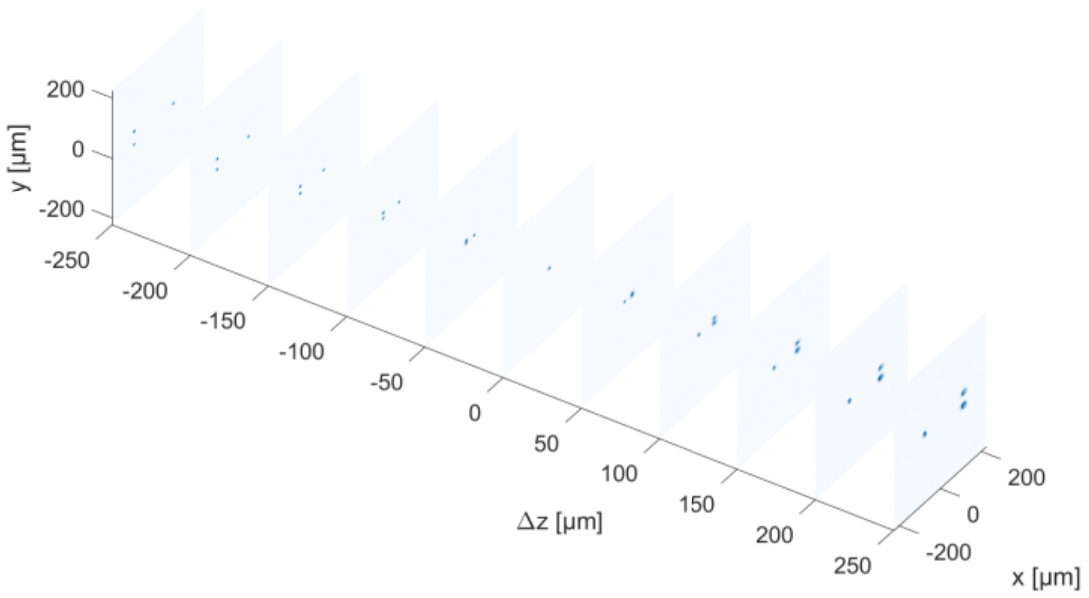

Figure 7.15: The propagation of the three Doppler cooling beams designed to intersect at position A in 50 μm increments along the z axis, where we have defined $z = 0$ to be the intersection plane for this plot.

Having characterised the x–y positions of the intersection points we then measured the z-axis position with respect to the lens plane. To do so we imaged the intersection point with a 50× objective

projecting the beam locations onto a beam profiling CCD. The beam profiler was then translated ~2 mm towards the lens plane and the DC3(B) DML is brought into the image. Determination of the lens plane is performed by sharply focusing the grating lines of the DML on the CCD which could be done to ±10 μm accuracy due to uncertainty on the exact location that the lens image was best focused. The lens plane is determined to be 1990(10) μm from the intersection point corresponding to a discrepancy of ~10 μm with the design image point which is consistent with the previous error found for two PMMA lenses demonstrated in Section 6.2.2. Further testing is required to find the origin of this discrepancy as it is inconsistent with our simulations that predict exact imaging at the design image point.

Crosstalk intensities

By providing the capability of individually addressing two microtrap segments independently, it is crucial that background light caused by illuminating beams for addressing one segment is of sufficiently low intensity such that it does not excite ions in the other segment. To quantify this effect, referred to as *crosstalk*, we image the intersection points at intensities over 4 orders of magnitude using an exposed board CCD for all 6 of the Doppler cooling beams. Practically the procedure is to sequentially excite each beam with $\lambda = 422$ nm light and record images at exposure times of 20, 200, 2000 and 20,000 ms. Calibration of the CCD, perfomed in Appendix B, allows an association of the measured signals with a relative intensity and HDR beam profile stitching as described in Section 6.1.1 is performed. The relative intensity at the unaddressed intersection point is possible due to the large field-of-view of the CCD which allows for both points to be imaged simultaneously. The resulting beam profiles are shown in Figure 7.16 and the crosstalk intensities are summarised in Table 7.6. All crosstalk intensities are $<2.4 \times 10^{-4}$ relative to the peak intensity, however the noise-floor of the measurement procedure, $\sim 1.7 \times 10^{-4}$, was reached for some measurements due to the limited sensitivity of the CCD used. We are not aware of previous reports of studies on the effects of scattered dipole-allowed light at unaddressed ion positions, most likely because it is not usually an issue. Previous reports of crosstalk have all been on the qubit transition due to it importance on single and multi-qubit gates [60, 227]. The influence of scattered light that drives dipole-allowed transitions is more subtle, as it can couple to qubits in the $|0\rangle$ state and thereby measure the state and decohere any prepared superpositions. However, this unwanted measurement could potentially be modelled as a gate error in error correction models. The error threshold per operation is on the order of 10^{-5} for Steane codes [228], and 10^{-2} for surface codes at the expense of higher qubit overheads [229]. It is expected that further improvement on the diffraction efficiency of the DML array would reduce the background scattered light, and improvements in the measurement technique used here would allow for study of lens arrays with potential crosstalks of $<10^{-4}$. We therefore expect the measured

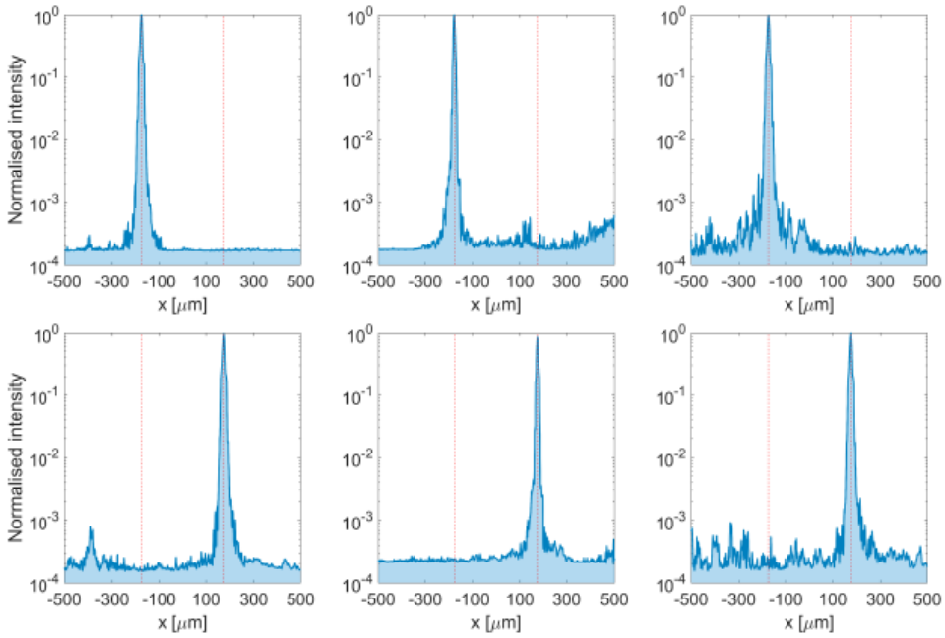

Figure 7.16: HDR beam profile cross-sections of each of the Doppler cooling beams 1, 2 and 3 (left to right) at positions A ($x = -175$ μm) and B ($x = 175$ μm). Red dashed lines indicate the intersection points and correspond to positions of the quoted intensity values in Table 7.6

Beam	Relative intensity	
	$x = -175$ μm	$x = +175$ μm
DC1(A)	1	1.7×10^{-4}
DC2(A)	1	1.9×10^{-4}
DC3(A)	1	1.9×10^{-4}
DC1(B)	1.7×10^{-4}	1
DC2(B)	2.4×10^{-4}	1
DC3(B)	2.1×10^{-4}	1

Table 7.6: Cross-talk intensities as measured by a HDR beam profile measurement of the beams in the intersection plane using an exposed board CCD calibrated for its power response over 4 orders of magnitude. The relative intensity 1.7×10^{-4} is the noise floor of the measurement procedure.

cross-talk efficiencies to be sufficient for most trapped ion applications, including the implementation of fault-tolerant digital quantum computation with surface codes. Experimental study of scattered 422 nm light on $^{88}Sr^{+}$ ions is required to make any further conclusions.

7.5 Discussion and conclusion

We have designed, fabricated and tested an optical assembly for addressing two segments in an ion microtrap array. To the best of our knowledge, this is the first demonstration of a multi-beam, multi-wavelength micro-optical system for trapped ion addressing, with the previous demonstration being at a single wavelength and with a single beam [60]. The fabricated assembly successfully overlapped two sets of 5 beams spanning wavelengths from $\lambda = 422$ nm to $\lambda = 1092$ nm at two points in space

laterally separated by 350 μm. The LW waveguide chip used in the assembly is shown to have simultaneously high total transmission efficiencies over all 10 waveguides when bonded to a fibre array of −1.5 dB. The DML array is the dominant loss mechanism of the full system, contributing an average loss of 6.3 dB which can be readily improved by optimising the DML fabrication recipe, bonding the waveguide chip to the lens chip, and optimising the titania thin film thickness for maximum transmission. The average transmission through the full assembly, from the fibre array input to the ion position is −7.8dB and offers a significant improvement over the previous state of the art of −33dB [60]. The average, demonstrated transmissions are favourable for large scale addressing of ion microtrap arrays. Assuming a −3 dB coupling overhead from the laser source to each fibre, the average transmission of −7.63 dB at λ = 422 nm would allow for ~3000 Doppler cooling beams to be driven simultaneously. These calculations are based on the maximum power output of the laser source of 70 mW, and the Doppler cooling beam saturation power at the ion position of 2 μW [9]. Further to this, the average beam radii of the demonstrated Doppler cooling beams at the intersection point were ~9 μm which are smaller than the 35 μm beam waists used in the current bulk optical apparatus [9]. The smaller beam sizes at the ion position reduces the required power to produce the same intensity at the ion by ~15×, increasing the number of possible simultaneous Doppler cooling beams to ~45, 000. Therefore, the demonstrated transmissions of the micro-optical assembly are sufficient for interfacing with thousands of operational microtrap segments, such that the limit is in delivering this number of beams to the optical assembly. Despite the powers propagating to the ion being sufficient for operation, the concern is where the lost light is propagating to, and whether this will have a negative effect on ion trap operation. The potential for scattered light from poor coupling and diffraction efficiencies was the greatest concern when the assembly was designed, however we measured background intensities away from focused beams on the order of $\sim 2 \times 10^{-4}$ with scope for improvement. These crosstalk intensities could potentially be modelled as measurement or gate errors in error correction models, and would be below the fault tolerant threshold in surface code error correction models for digital quantum information processing. Therefore we expect them to be suitable for most trapped ion applications, with further scope for reducing scattered light by improving DML diffraction efficiencies. We therefore conclude that the proposed concept in Chapter 2 has significant promise, with demonstrated high (and improvable) transmission efficiencies and low background scattering rates such that individual addressing of ion microtrap segments is possible using a scalable microfabrication technique. We will further discuss the potential and future of the platform in the next chapter.

8

Summary and outlook

The versatility of trapped ions as a resource for applications such as atomic clocks, quantum-enhanced sensing and quantum computing motivates the development of robust and scalable control systems for interfacing with large numbers of ions. The accomplishment of segmented microtraps for flexible and scalable storage of trapped ion goes part way in the development of scalable control systems, however the required optical laser beam delivery and fluorescence collection has not undergone the same treatment. Motivated by this technological shortfall, we introduced the concept of an optical assembly based on fibre arrays, laser-written waveguides and diffractive optics for the addressing and fluorescence collection of multiple ions. Realisation of the the proposed optical assembly required the resolution of many identified challenges which spanned all sub-components of the assembly as well as its final interfacing in proximity to the microtrap.

The requirements of efficient fluorescence collection and trap geometry necessitates the proposed optical assembly to be brought in close proximity to the ion microtrap, and it was unknown how the presence of the dielectric materials in the assembly would perturb the microtrap operation. We studied these proximity effects numerically using finite-element methods to find the distances from the ion at which the microtrap parameters are perturbed from their baseline values. We found that for a realistically charged glass substrate, this threshold was 2.6 mm. By covering the glass surface apart from an optical aperture in a grounded, conductive layer the threshold is reduced to 1 mm. Further, it was demonstrated that for a coated glass substrate placed 400 μm from the microtrap centre, the resulting displacement of the trapping potential minimum could be corrected using modest voltages (<4 V) on the DC compensation electrodes already present in the microtrap structure. The numerical study shows that if precautions and compensations are taken to account for perturbations to the trapping potential by a micro-optical assembly then normal operation of the microtrap should be possible.

The operational wavelengths for $^{88}Sr^{+}$ ions span from 422 nm to 1092 nm, with additional wave-

lengths of 405 nm and 461 nm currently used at NPL for photoionisation of neutral strontium. While waveguides directly written into glass substrates using femtosecond lasers had routinely demonstrated single-moded guidance of near-IR wavelengths, the guiding of blue wavelengths was far less established. We explored the fabrication parameter space of femtosecond laser writing and found a recipe in *Corning Eagle2000* glass suitable for coupling to S405-XP singlemode fibre with 99.9% mode overlap at a wavelength of 406 nm. A slightly modified recipe with a reduced mode overlap of 98.3% demonstrated a total transmission efficiency of -1.4 dB in a 8 mm length of waveguide allowing us to upper bound the propagation losses at 1.55 dB/cm. Brief spectral analysis of laser-written waveguides under excitation at wavelengths of 404 nm found no measurable increase of the photoluminescence over and above that normally present from the fibre-optic cables routinely used for trapped ion addressing, and we therefore conclude that the waveguides will have negligible influence on trapped ion addressing over currently used systems. Laser-written waveguides for guiding a single-mode of 976 nm wavelength light were also developed to facilitate the writing of a waveguide array for trapped ion addressing at operational wavelengths. We found a recipe suitable for maximum overlap of 1060XP fibre at a wavelength of 976 nm of 99.6%. The found recipes show versatility in the laser-writing fabrication process for the defining of single-mode waveguides in glass over the full range of $^{88}Sr^{+}$ ion wavelengths.

The development of single-mode waveguides at operational wavelengths allowed for the study of waveguide tapers that would expand the output waveguide mode field diameter. The mode field diameter increase is required to reduce the expansion of light from the waveguide aperture in the lens array substrate and decrease mode diameters at the lens plane. Initial investigations used simple tapering of the waveguide diameter over the waveguide length, starting from the diameter optimised for high fibre mode overlaps. Tapering the diameter down produced modes with large Lorentzian wings, and no Gaussian mode expansion was observed. Increasing the diameter of the waveguide over the taper found that mode-expansion increased too slowly with waveguide diameter such that the required end diameters for 2× mode-field diameter expansion were beyond the limits of fabrication for a single waveguide. To overcome the maximum diameter limit of femtosecond laser writing we investigated building large-mode area structures out of many waveguides and coupling to them adiabatically from a single-mode waveguide. The single-to-multi core tapers were demonstrated for both strong and weakly guiding component waveguides and in the weakly guiding regime we found that when the sub-waveguide diameter equalled the lattice spacing of the waveguide array then a single, Gaussian mode at a wavelength of 406 nm was supported. The expanded mode had a ~13× expansion compared to the single-mode waveguide due to the step-index nature of the large-mode area structure. Single-to-multi core tapers with only 7 constituent waveguides in the multi-core region would allow for >2× mode expansion and satisfy our requirements while providing the smallest

increase in fabrication complexity.

The coupling of laser-written waveguides to trapped ions required the development of a flexible and accurate model for the design of diffractive optics. Scalar diffraction theory was shown to be suitable for our application and allowed for the design of on-axis diffractive microlenses for fluorescence collection, and off-axis DMLs for deflecting and focusing laser light onto ions. The DMLs were designed as surface-relief profiles in dielectric materials, with their performance characterised by a vector simulation model. Dielectric metasurfaces were also briefly simulated and designs generated for a polarisation insensitive DML, and for quarter and half waveplates. The design simplicity of surface-relief DMLs motivated proof-of-principle demonstrations of surface-reliefs for coupling to trapped ions instead of dielectric metasurfaces, with the latter being an advanced goal of interfacing microfabricated optics with trapped ions.

Surface-relief diffractive microlenses were fabricated using three separate techniques: focused ion beam milling; electron beam lithography in resists; and reactive ion etching of electron beam lithography resist masks. Focused ion beam milling demonstrated on-axis lenses with accurate (1%) focusing of Gaussian beams of λ = 405 nm and high diffraction efficiencies of >80% for beams focused 500 μm from the lens plane. The procedure was not readily flexible to other DML designs, and was limited to on-axis lenses due to the finite size of the milling beam (~100 nm) restricting the minimum grating pitch. The fabricated lenses took approximately 3 hours per 100 μm^2 and therefore focused ion beam milling does not constitute a scalable fabrication process for large lens arrays. In contrast, electron beam lithography was found to be capable of defining both on and off-axis DMLs in a polymer resist with fabrication speeds of ~1 min per 100 μm^2. The defining of surface-reliefs in polymer required correcting for its non-linear response to electron dose, which we demonstrated was possible such that linear slopes in the polymer were written with root-mean-square error of 10 nm from linearity. Dose-corrected polymer surface-reliefs allowed for rapid prototyping of designed phase profiles and we demonstrated accurate on and off-axis DMLs as well as a hologram of the University of Bristol logo. Maximum diffraction efficiencies of on-axis DMLs were shown to be 91%, $5° - 15°$ off-axis DMLs to be ~88% and 20° off-axis DML to be 77%. The reduction for a 20° off-axis DML is most likely due to scope for improvement of the fabrication process of small pitched DMLs. To confirm accurate beam focusing we demonstrate the crossing of the output of two DMLs, with their minimum beam waists separated by 10 μm along the perpendicular axis to the lens plane and 1μm displacement in the transverse plane. The polymer surface-reliefs were useful for testing conformity of physical profiles to design, however for applications in a vacuum chamber the profiles must be patterned in a dielectric material which does not out-gas contaminants into the chamber. We developed a reactive-ion etching process that transferred polymer surface-reliefs into a titanium dioxide thin-film, which was selected for its vacuum compatibility and high refractive index to allow for shallow etch

depths. The etch process was found to distort the polymer profiles when transferred into titania, and a distortion correction was applied to the electron dose maps during polymer profile fabrication to compensate for the effect. Linear slopes in titania were fabricated with a root-mean square deviation of 2 nm from linearity. The distortion compensation procedure allowed for the fabrication of near-unit diffraction efficiency on-axis DMLs in titania for focusing beams at positions from the lens plane over two orders of magnitude, from 200 – 2000 μm. The on-axis DMLs had an average diffraction efficiency of 93 ± 5%, with a maximum of 98 ± 1.5% for a focused beam position of 1000 μm from the lens plane. Off-axis DMLs were also demonstrated with a ~10% reduction in diffraction efficiency over the equivalent polymer surface-reliefs suggesting that further study of the etch dependence on DML pitch is required.

After independently developing fabrication processes for laser-written waveguides and diffractive surface-relief microlenses, we designed an optical system for combining arrays of waveguides and lenses as a demonstration of the optical assembly concept for trapped ion addressing. A diffractive microlens array was designed for addressing to neighbouring ion microtrap segments with five beams each. Three beams were for λ = 422 nm and were orientated such that they dominantly coupled to different axes of $^{88}Sr^{+}$ ion motion for Doppler cooling and micromotion minimisation. The other two beams were a λ = 1033 nm quencher beam and λ = 1092 nm repumper beam, both for dark state repumping of $^{88}Sr^{+}$ ions. The position of the 10 lenses was determined by their required k-vectors and relative position to their associated microtrap segment. The lens positions defined the termination positions of a 10-waveguide array which remapped a 10-fibre array populated with blue and near-IR single-mode fibre for λ = 422 nm and λ = 1033/1092 nm light respectively. Compensations for variations in the fibre core positions from design and changes in waveguide diameter with depth were both performed in the fabricated waveguide arrays. The fibre array was bonded to the waveguide array with UV curing epoxy after aligning the two components with only the first and last waveguide in the array. The lens array was fabricated using electron beam lithography of polymer profiles which were then transferred into a titania thin film on a 1.03 mm thick fused silica substrate. The full optical assembly was tested in free space at operational wavelengths, including the power transmission at each interface, accuracy of beam overlaps, and the intensity cross-talk at the neighbouring microtrap segment. We measured average transmission efficiencies of $-7.63,\ -7.4,\ -8.3$ dB through the full assembly for λ = 422, 1033, 1092 nm respectively. The majority of the power loss occurs in the lens array through reflection of the titania thin film and propagation of light into undesired diffraction orders. We found that all beams were overlapped at their design intersections points, with the near-IR beams slightly displaced from the Doppler cooling beam intersection point but still with sufficient (>69%) intensity. Despite the loss from low diffraction efficiencies, which could scatter light into undesired locations, we measured relative intensities at the unaddressed intersection point

of $<2.4 \times 10^{-4}$ for all Doppler cooling beams. The physical implication of the cross-talk intensities requires further study of trapped ion quantum dynamics in the presence of such background scatter, however we expect the measured values to be suitable for implementation of surface code quantum computation below the error threshold. The diffraction efficiency of all lenses can be improved, with 20% higher diffraction efficiencies already demonstrated at blue wavelengths for equivalent off-axis angles. Our analysis suggests that the near-IR DMLs are underetched and therefore do no experience the required full 2π phase shift, limiting their diffraction efficiency. The solution would be to use thicker polymer films to achieve deeper titania profiles. To the best of the author's knowledge, we have demonstrated the first microfabricated optical assembly for guiding and focusing multiple beams of multiple wavelengths, spanning from blue to near-IR, to multiple microtrap segments. The efficiency of light delivery surpasses the previous state of the art of −33 dB transmission for a single beam of λ = 674 nm light focused on $^{88}Sr^{+}$ ions from a planar waveguide grating coupler. While we have not interfaced the fabricated optical assembly with an operational microtrap we have fully characterised its performance to be convinced it will deliver operational wavelengths for $^{88}Sr^{+}$ control with the correct k-vectors to two microtrap segments simultaneously. The interfacing of the assembly with an operational microtrap is a challenge in itself which must be solved in future study. The reward would be the coupling of a scalable optical interface to $^{88}Sr^{+}$ions for the control of many ion trap segments simultaneously with applications to quantum information processing, optical atomic clocks and quantum-enhanced sensing with large numbers of ions.

8.1 Future work

The developed microfabricated optical components for interfacing with ion microtrap arrays go part way to fully realising a scalable and manufacturable assembly. There are many possible research avenues going forward, some necessary to achieve the stated goal of coupling to trapped ions, and some to advance the platform in functionality. We briefly outline these research directions to provide a sense of the remaining challenges going forward as well as the opportunities present in the proposed optical assembly concept.

Interfacing with an operational microtrap The current NPL ion microtrap is mounted in a vacuum chamber by indium sealing of a leadless chip carrier (LCC) on one side to a vacuum flat, as shown in Figure 8.1(a). The other side of the chip carrier has an optical window sealed to it with a steel spacer to increase the glass-to-ion distance to minimise distortions to the trapping field. We propose exchanging the optical window and steel spacer for the front face of the optical assembly as first shown in Figure 2.3. The milling of a trench into the LCC would allow for space for an indium seal to be located while the lens array chip sits flush with the LCC, as shown in Figure 8.1(f). The manufacturing tolerances on

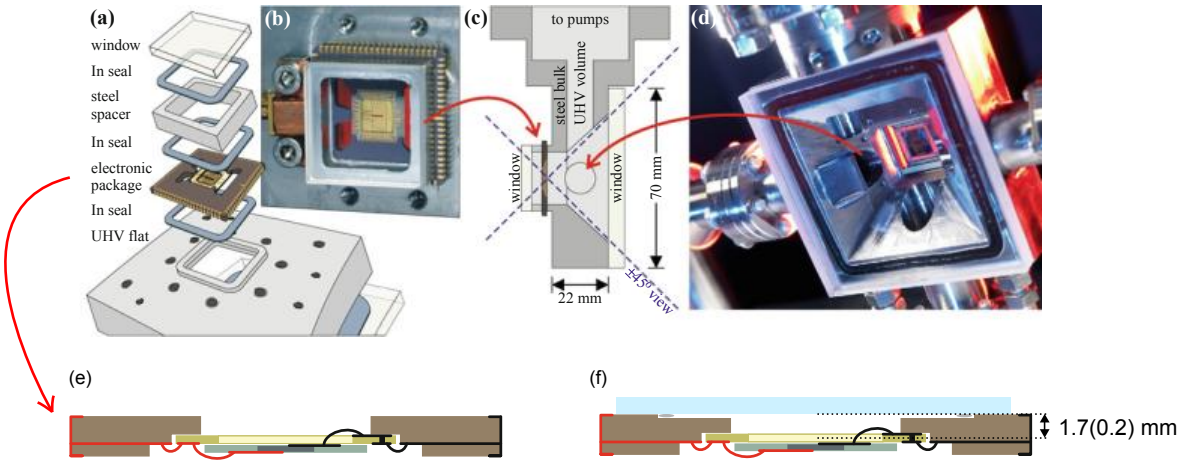

Figure 8.1: Proposed vacuum interface for optical assembly with ion microtrap array, all images reprinted or adapated with permission from [73]. (a) Exploded view of vacuum assembly of the ion microtrap mounted in a leadless chip carrier; (b) mounted microtrap housed in the vacuum chamber; (c) Side view of the vacuum chamber showing the asymmetry in the chamber layout with a much larger vacuum volume on the right side; (d) the front side of the microtrap showing large optical access despite being recessed from the chamber window by ~2 cm; (e) Side view of the leadless chip carrier with the mounted microtrap, the orientation is the same as in (a); (f) modified leadless chip carrier with the microlens array mounted on the top face with a recess milled in for an indium seal to sit in.

the LCC and the intermediate substrate the microtrap is mounted to mean that the distance from the LCC top face, that the lens array would rest on, and the microtrap centre is 1.7 ± 0.2mm. This 200 μm tolerance is much larger than the intersection volume of the beam overlaps of the focused beams from the lens array (~10 μm) and the error margin must be reduced to be on the order of <10 μm to ensure the microtrap and the beam intersection point are at the same point in space. The microtrap could be mounted on a translational stage to provide alignment flexibility, however this would require modifying the existing LCC and further experimental complexity. Alternatively, after a microtrap is mounted in an LCC the distance from the top face of the LCC (which defines the lens plane) to the microtrap top face could be measured before fabrication of the microlens array. While calibration of each microtrap mounting is undesirable from a manufacturing point of view, it would certainly be suitable for a first proof of concept experiment to demonstrate operation of a microtrap interfaced with an array of microfabricated optical components. Later, more precise production of the microtrap mountings could be performed to attempt to bring alignment tolerances within the focal volume of the beam overlaps. The transverse alignment of the optical assembly to the microtrap array could be achieved using dedicated alignment waveguides. The alignment light could either be focused through apertures lithographically defined in the microtrap electrodes, or reflected off diffractive structures on the microtrap surface and recoupled back into the same, or a secondary, waveguide with optimal alignment determined by maximal return signal. Once the alignment was fixed and the vacuum chamber was evacuated it is expected that the alignment would be extremely robust given that is held

in place by 1 atmosphere of pressure.

Advanced optical assemblies The demonstrator optical assembly presented in Chapter 7 does not have the maximum optical density and optic numbers that can be envisioned for the technology. The waveguide pitch was limited by the 127 μm fibre array pitch, and the lens array was limited by the small numerical aperture of the waveguide outputs which leads to rapid expansion of the modes in the free propagation region. A simple way to increase the waveguide density is to use a 2D fibre array, which are commercially available with custom fibre layouts. For example, *Fibreguide Industries* provides 2D fibre arrays with 150 μm pitch with <0.5 μm tolerance on the fibre core positions which can be measured and supplied to the customer [230]. Such a 2D array would allow for a density of nine fibres per microtrap segment assuming a maximum waveguide depth range of 300 μm, which is smaller than the range used for the demonstrator waveguide chip. Nine fibres are the maximum required number of fibres for full control and fluorescence collection of $^{88}Sr^{+}$ ions. Increasing the density of the microlens array would require further study of single-to-multi core tapers, which show promise for doubling the output mode-field diameter of blue light using an adiabatic taper from a single-mode waveguide to a seven sub-waveguide array. Mode-field diameters of 6 μm at λ = 422 nm would allow for lens diameters for addressing beams of <100 μm, increasing lens number densities while still allowing for flexibility in lens placements.

Increasing the optical density of the micro-assembly is one way of advancing the platform, using diffractive optics with increased functionality is another. We have numerically shown that dielectric metasurfaces composed of arrays of nanorods would allow for full phase and polarisation control of blue wavelengths. The fabrication of nanorod arrays with minimum feature sizes of 50 nm would be challenging, however it is within the capability of the *Raith VOYAGER* electron beam lithography system at the University of Bristol. The development of metasurfaces designed for disparate wavelengths in the same dielectric film thickness is an open challenge which would be instrumental in their use for trapped ion addressing and requires further study. The benefit to realising metasurfaces for full polarisation and phase control of blue, red and near-IR light would be and advanced optical platform that could prepare and control polarisation states directly before ion interaction. The main application of such a scheme is the preparation of circularly polarised blue wavelength light for optically pumping $^{88}Sr^{+}$ ions.

Reducing the optic-ion distance Increasing the optical density of the micro-assembly would allow for smaller lens diameters and therefore lenses that are spaced smaller distances apart. As many of the lens positions are fixed by a specific k-vector, when the distance between the lens plane and the ion position is reduced the lens layout becomes more compact. Therefore, increasing the optical density is necessary for smaller optic-ion distances. Further, decreasing the diameters of the lenses used for the

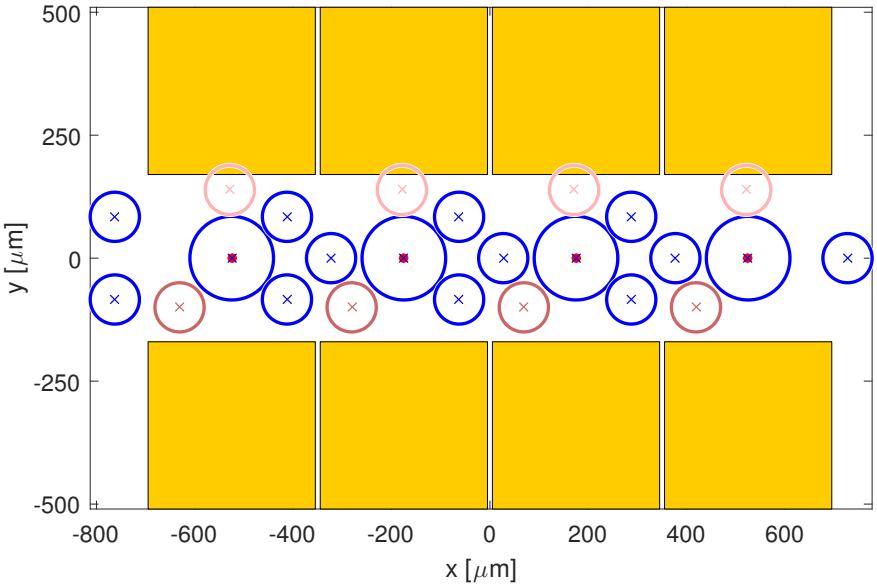

Figure 8.2: An advanced microlens layout designed to be located 400 μm from the microtrap centre. All beams that were in the demonstrator have been included: three Doppler coolings beams (blue), one repumper beam (light pink), and one quencher beam (dark pink) per segment. A collection lens has also been included for each segment with a radius of 85 μm. Four electrodes, shown as yellow rectangles projected onto the lens plane, are shown but there is no fundamental limit to the number of segments that can be addressed with this layout. The used lens diameters requires waveguide mode-expansion tapers for doubling the mode-field diameter of the currently used waveguide modes for optimal coupling to single-mode fibre.

addressing increases the available space for a collection optic and therefore increases its maximum numerical aperture, and collection efficiency. An example lens layout for an optic-to-ion distance of 400 μm with addressing optic diameters of 100 μm and collection optic diameters of 170 μm is shown in Figure 8.2, demonstrating the smaller addressing lens diameters to achieve the required lens layout. A circular collection optic diameter of 170 μm corresponds to a collection efficiency of 1.1% for a optic-to-ion distance of 400 μm and therefore satisfies the 1% collection efficiency requirement imposed in Chapter 2. We have shown the optical layout for four segments, however with the chosen addressing beams it can be scaled to an arbitrary number of segments as the optics for neighbouring segments interlock with no position conflicts. The further addition of the probe and optical pumping beams would require careful consideration due to their large (45 °) deflection angles however it is expected that all lenses would be able to be placed due to flexibility in the majority of the beam k-vectors.

Bringing the optical assembly to within 400 μm of the microtrap centre also requires careful characterisation and study of the perturbations of the microtrap pseudopotential. In Chapter 3 we numerically demonstrated that the displacement of the pseudopotential minimum from the microtrap centre could be corrected for by applying <4 V on the compensation electrodes. Further study is required to confirm the numerical predictions, ideally using a glass substrate on a translation stage to

measure ion trap operation for varying glass-to-ion distances. The coating of the glass surface with a conductive film will most likely be required for a distance of 400 μm, and this could be achieved as an additional step in the fabrication process. The microlens array could be coated in a negative electron beam lithography resist, the microlens areas exposed to electrons and the resist developed to leave the microlenses covered while revealing the open areas. Thermal evaporation of gold on the microlens array and subsequent removal of the resist covering the microlenses would provide an electrically conductive coating surrounding the exposed microlenses. Connecting the gold film to ground would be an additional challenge to solve during the development of the vacuum mounting.

An optical interface on both microtrap sides Up to this point the interfacing of trapped ions with microfabricated optics has only been explored from one side of the microtrap. The unique benefit of the NPL microtrap over microfabricated surface traps is that optical access is possible from both sides. While the k-vectors of all addressing beams can be satisfied from one side, by interfacing from the second side further collection optics could be added, increasing collection efficiency. In a more advanced implementation, a cavity between optics fabricated on both sides of the microtrap could enhance collection efficiency further [116]. The introduction of a second optical assembly would require a full reworking of the vacuum chamber, as is made evident in Figure 8.1(c-d) as the optical window on the front microtrap side is >2 cm from the microtrap. Current restrictions on reducing the vacuum chamber size are the atomic oven and the vacuum pump. Both of these restrictions have been overcome in a previously demonstrated miniature vacuum chamber for trapped ions by Schwindt et al. [231]. A micro-hotplate, made using standard MEMS fabrication techniques, was used to evaporate neutral atomic vapour. The hotplate has a footprint of approximately 2×3 mm with a thickness of 400 μm [231, 232] and therefore further work is required in further miniaturising the hotplate for our application. The miniaturisation is in principle possible at the expense of a reduction in the mass, and therefore lifetime, of the atomic source. Schwindt et al. use a 3 mm inner diameter copper tube to connect the ~0.1 L volume of the vacuum chamber to a vacuum pump which is later pinched off. Due to the expected small optic-to-ion distance, the volume of the eventual vacuum chamber will be on the order of 10^{-4} L with any increase in vacuum volume to be caused by the interfacing of the vacuum tubing to the leadless-chip-carrier and optical assemblies. We therefore expect that a bespoke vacuum chamber can be designed with micro-optical interfacing of the ion trap from both sides and an integrated atomic oven. The resulting optical stability, as well as the possiblity of addressing many microtrap segments would represent an important advance in applying trapped ions for uses in portable atomic clocks or quantum information processing modules. One expected challenge to the realisation of such a physics package is the minimisation of scattered light from addressing beams from one optical interface on the opposing lens array. It may therefore be desirable to use a transparent

conductive film, such as indium-tin oxide, instead of gold such that the addressing beams can freely propagate to the vacuum support block where beam dumps could be milled and coated with a highly absorbing material such as carbon nanotubes [233].

8.2 Conclusion

We have demonstrated an optical assembly based on fibre arrays, laser-written waveguide and diffractive surface-relief microlenses which is designed for trapped ion control. The micro-optical assembly delivers both blue and near-IR wavelengths to two different points in space which correspond to the centre of neighbouring ion microtrap segments. The demonstration was enabled by the developmental work in laser-written waveguides and diffractive surface-reliefs, especially at blue wavelengths which are crucial for control of trapped $^{88}Sr^{+}$ ions. The fabricated micro-optical assembly supports the viability of the proposed concept for future operation with trapped ions, for which further study of vacuum chamber engineering is required. The proposed platform offers many eventual improvements and advancements over the demonstrated assembly, with advanced diffractive optics, waveguide tapers and 2D fibre arrays promising greater optical densities and optical functionalities. If the further study is performed, then it is expected that the resulting optical assemblies would be relevant for advancing the capabilities of all applications of trapped ions, including ultra-precise portable atomic clocks, quantum-enhanced sensors, and quantum-information processing.

Research outputs

The work described in this thesis has resulted in the following publications and presentations.
Journal articles:

- Matthew Day, Kaushal Choonee, David Cox, Mark Thompson, Graham Marshall, and Alastair G. Sinclair, *Continuous-relief diffractive microlenses for laser beam focusing*, Optics Express 25, 26987-26999 (2017); **Peer-reviewed publication**
- Matthew Day, Kaushal Choonee, Alastair G. Sinclair, Graham D. Marshall, *Near-unit diffraction efficiency microlenses in titanium dioxide thin film*; **In preparation**
- Matthew Day, Kaushal Choonee, Zachary Chaboyer, Simon Gross, Alastair G. Sinclair, Graham D. Marshall, *A microfabricated optical assembly for scalable addressing of ion microtrap arrays*; **In preparation**

Conference presentations:

- *Continuous-relief diffractive optical elements for atomic quantum technologies*, Photon 16, September 2016; **Poster**
- *A micro-optical assembly for ion microtrap arrays*, Bristol Quantum Information Technology Workshop, April 2018; **Poster**
- *A micro-optical assembly for portable quantum clocks*, DSTL PhD Showcase, April 2018, **Poster**
- *Microfabricated optical elements towards a photonic interface for ion microtrap array*, 26th International Conference on Atomic Physics, July 2018; **Poster**
- *A microfabricated optical assembly for scalable addressing of ion microtrap arrays*, Photon 18, September 2018; **Oral**

Bibliography

[1] J. Mizrahi, B. Neyenhuis, K. Johnson, W. Campbell, C. Senko, D. Hayes, and C. Monroe, "Quantum control of qubits and atomic motion using ultrafast laser pulses," *Applied Physics B*, vol. 114, no. 1-2, pp. 45–61, 2014.

[2] J. Wong-Campos, S. Moses, K. Johnson, and C. Monroe, "Demonstration of two-atom entanglement with ultrafast optical pulses," *Physical Review Letters*, vol. 119, no. 23, p. 230501, 2017.

[3] V. Schäfer, C. Ballance, K. Thirumalai, L. Stephenson, T. Ballance, A. Steane, and D. Lucas, "Fast quantum logic gates with trapped-ion qubits," *Nature*, vol. 555, no. 7694, p. 75, 2018.

[4] J. Zhang, G. Pagano, P. W. Hess, A. Kyprianidis, P. Becker, H. Kaplan, A. V. Gorshkov, Z.-X. Gong, and C. Monroe, "Observation of a many-body dynamical phase transition with a 53-qubit quantum simulator," *Nature*, vol. 551, no. 7682, p. 601, 2017.

[5] D. Leibfried, M. D. Barrett, T. Schaetz, J. Britton, J. Chiaverini, W. M. Itano, J. D. Jost, C. Langer, and D. J. Wineland, "Toward Heisenberg-limited spectroscopy with multiparticle entangled states," *Science*, vol. 304, no. 5676, pp. 1476–1478, 2004.

[6] D. A. Dalvit, R. de Matos Filho, and F. Toscano, "Quantum metrology at the Heisenberg limit with ion trap motional compass states," *New Journal of Physics*, vol. 8, no. 11, p. 276, 2006.

[7] D. J. Wineland and D. Leibfried, "Quantum information processing and metrology with trapped ions," *Laser Physics Letters*, vol. 8, no. 3, pp. 175–188, 2011.

[8] F. Schmidt-Kaler, S. Gulde, M. Riebe, T. Deuschle, A. Kreuter, G. Lancaster, C. Becher, J. Eschner, H. Häffner, and R. Blatt, "The coherence of qubits based on single Ca^+ ions," *Journal of Physics B: Atomic, Molecular and Optical Physics*, vol. 36, no. 3, p. 623, 2003.

[9] J. A. Thom, *An agile and stable optical system for high-fidelity coherent control of a single $^{88}Sr^+$ ion*. PhD thesis, University of Strathclyde, 2015.

[10] D. Yum, D. De Munshi, T. Dutta, and M. Mukherjee, "Optical barium ion qubit," *JOSA B*, vol. 34, no. 8, pp. 1632–1636, 2017.

[11] B. B. Blinov, D. Leibfried, C. Monroe, and D. J. Wineland, "Quantum computing with trapped ion hyperfine qubits," *Quantum Information Processing*, vol. 3, no. 1-5, pp. 45–59, 2004.

[12] T. Ruster, C. T. Schmiegelow, H. Kaufmann, C. Warschburger, F. Schmidt-Kaler, and U. G. Poschinger, "A long-lived zeeman trapped-ion qubit," *Applied Physics B*, vol. 122, no. 10, p. 254, 2016.

[13] D. Leibfried, R. Blatt, C. Monroe, and D. Wineland, "Quantum dynamics of single trapped ions," *Reviews of Modern Physics*, vol. 75, no. 1, p. 281, 2003.

[14] J. Eschner, G. Morigi, F. Schmidt-Kaler, and R. Blatt, "Laser cooling of trapped ions," *JOSA B*, vol. 20, no. 5, pp. 1003–1015, 2003.

[15] K. Mølmer and A. Sørensen, "Multiparticle entanglement of hot trapped ions," *Physical Review Letters*, vol. 82, no. 9, p. 1835, 1999.

[16] M. Brownnutt, V. Letchumanan, G. Wilpers, R. Thompson, P. Gill, and A. Sinclair, "Controlled photoionization loading of $^{88}Sr^{+}$ for precision ion-trap experiments," *Applied Physics B*, vol. 87, no. 3, pp. 411–415, 2007.

[17] C. Adams and E. Riis, "Laser cooling and trapping of neutral atoms," *Progress in Quantum Electronics*, vol. 21, no. 1, p. 1, 1997.

[18] J. Höffges, H. Baldauf, W. Lange, and H. Walther, "Heterodyne measurement of the resonance fluorescence of a single ion," *Journal of Modern Optics*, vol. 44, no. 10, pp. 1999–2010, 1997.

[19] D. Berkeland, J. Miller, J. C. Bergquist, W. M. Itano, and D. J. Wineland, "Minimization of ion micromotion in a Paul trap," *Journal of Applied Physics*, vol. 83, no. 10, pp. 5025–5033, 1998.

[20] M. Brownnutt, G. Wilpers, P. Gill, R. Thompson, and A. Sinclair, "Monolithic microfabricated ion trap chip design for scaleable quantum processors," *New Journal of Physics*, vol. 8, no. 10, p. 232, 2006.

[21] P. See, G. Wilpers, P. Gill, and A. G. Sinclair, "Fabrication of a monolithic array of three dimensional Si-based ion traps," *Journal of Microelectromechanical Systems*, vol. 22, no. 5, pp. 1180–1189, 2013.

[22] G. Wilpers, P. See, P. Gill, and A. G. Sinclair, "A monolithic array of three-dimensional ion traps fabricated with conventional semiconductor technology," *Nature Nanotechnology*, vol. 7, no. 9, pp. 572–576, 2012.

[23] M. Brownnutt, *$^{88}Sr^{+}$ Ion Trapping Techniques and Technologies for Quantum Information Processing*. PhD thesis, Imperial College London, 2007.

[24] K. Choonee, G. Wilpers, and A. G. Sinclair, "Silicon microfabricated linear segmented ion traps for quantum technologies," in *Solid-State Sensors, Actuators and Microsystems (TRANSDUCERS), 2017 19th International Conference on*, pp. 615–618, IEEE, 2017.

[25] Y.-Y. Jau, H. Partner, P. Schwindt, J. Prestage, J. Kellogg, and N. Yu, "Low-power, miniature $^{171}Yb^{+}$ ion clock using an ultra-small vacuum package," *Applied Physics Letters*, vol. 101, no. 25, p. 253518, 2012.

[26] G. P. Barwood, P. Gill, G. Huang, and H. A. Klein, "Observation of a sub-10-hz linewidth $^{88}Sr^{+}$ $S_{1/2} \rightarrow D_{5/2}$ clock transition at 674 nm," *IEEE Transactions on Instrumentation and Measurement*, vol. 56, no. 2, pp. 226–229, 2007.

[27] H. Margolis, "Optical frequency standards and clocks," *Contemporary Physics*, vol. 51, no. 1, pp. 37–58, 2010.

[28] A. D. Ludlow, M. M. Boyd, J. Ye, E. Peik, and P. O. Schmidt, "Optical atomic clocks," *Reviews of Modern Physics*, vol. 87, no. 2, p. 637, 2015.

[29] S. T. Cundiff and J. Ye, "Colloquium: Femtosecond optical frequency combs," *Reviews of Modern Physics*, vol. 75, no. 1, p. 325, 2003.

[30] N. Huntemann, C. Sanner, B. Lipphardt, C. Tamm, and E. Peik, "Single-ion atomic clock with 3×10^{-18} systematic uncertainty," *Physical Review Letters*, vol. 116, no. 6, p. 063001, 2016.

[31] J.-S. Chen, S. M. Brewer, C. Chou, D. Wineland, D. Leibrandt, and D. Hume, "Sympathetic ground state cooling and time-dilation shifts in an $^{27}Al^{+}$ optical clock," *Physical Review Letters*, vol. 118, no. 5, p. 053002, 2017.

[32] J. Cao, P. Zhang, J. Shang, K. Cui, J. Yuan, S. Chao, S. Wang, H. Shu, and X. Huang, "A compact, transportable single-ion optical clock with 7.8×10^{-17} systematic uncertainty," *Applied Physics B*, vol. 123, no. 4, p. 112, 2017.

[33] P. Gill, H. Margolis, A. Curtis, H. Klein, S. Lea, S. Webster, and P. Whibberley, "Optical atomic clocks for space," *National Physical Laboratory*, 2008.

[34] S. Narayanan, N. Daniilidis, S. Möller, R. Clark, F. Ziesel, K. Singer, F. Schmidt-Kaler, and H. Häffner, "Electric field compensation and sensing with a single ion in a planar trap," *Journal of Applied Physics*, vol. 110, no. 11, p. 114909, 2011.

[35] J. B. Brask, R. Chaves, and J. Kołodyński, "Improved quantum magnetometry beyond the standard quantum limit," *Physical Review X*, vol. 5, no. 3, p. 031010, 2015.

[36] P. A. Ivanov, N. V. Vitanov, and K. Singer, "High-precision force sensing using a single trapped ion," *Scientific Reports*, vol. 6, p. 28078, 2016.

[37] C.-W. Chou, D. Hume, T. Rosenband, and D. Wineland, "Optical clocks and relativity," *Science*, vol. 329, no. 5999, pp. 1630–1633, 2010.

[38] C. L. Degen, F. Reinhard, and P. Cappellaro, "Quantum sensing," *Reviews of Modern Physics*, vol. 89, no. 3, p. 035002, 2017.

[39] R. Blatt and C. F. Roos, "Quantum simulations with trapped ions," *Nature Physics*, vol. 8, no. 4, p. 277, 2012.

[40] D. Porras and J. I. Cirac, "Effective quantum spin systems with trapped ions," *Physical Review Letters*, vol. 92, no. 20, p. 207901, 2004.

[41] A. Montanaro, "Quantum algorithms: an overview," *npj Quantum Information*, vol. 2, p. 15023, 2016.

[42] J. Adcock, E. Allen, M. Day, S. Frick, J. Hinchliff, M. Johnson, S. Morley-Short, S. Pallister, A. Price, and S. Stanisic, "Advances in quantum machine learning," *arXiv:1512.02900*, 2015.

[43] J. Biamonte, P. Wittek, N. Pancotti, P. Rebentrost, N. Wiebe, and S. Lloyd, "Quantum machine learning," *Nature*, vol. 549, no. 7671, p. 195, 2017.

[44] L. K. Grover, "Quantum mechanics helps in searching for a needle in a haystack," *Physical Review Letters*, vol. 79, no. 2, p. 325, 1997.

[45] A. Montanaro and S. Pallister, "Quantum algorithms and the finite element method," *Physical Review A*, vol. 93, no. 3, p. 032324, 2016.

[46] M. Reagor, C. B. Osborn, N. Tezak, A. Staley, G. Prawiroatmodjo, M. Scheer, N. Alidoust, E. A. Sete, N. Didier, M. P. da Silva, *et al.*, "Demonstration of universal parametric entangling gates on a multi-qubit lattice," *Science Advances*, vol. 4, no. 2, p. eaao3603, 2018.

[47] J. W. Silverstone, D. Bonneau, K. Ohira, N. Suzuki, H. Yoshida, N. Iizuka, M. Ezaki, C. M. Natarajan, M. G. Tanner, R. H. Hadfield, *et al.*, "On-chip quantum interference between silicon photon-pair sources," *Nature Photonics*, vol. 8, no. 2, p. 104, 2014.

[48] C. D. Hill, E. Peretz, S. J. Hile, M. G. House, M. Fuechsle, S. Rogge, M. Y. Simmons, and L. C. Hollenberg, "A surface code quantum computer in silicon," *Science Advances*, vol. 1, no. 9, p. e1500707, 2015.

[49] N. Friis, O. Marty, C. Maier, C. Hempel, M. Holzäpfel, P. Jurcevic, M. B. Plenio, M. Huber, C. Roos, R. Blatt, *et al.*, "Observation of entangled states of a fully controlled 20-qubit system," *Physical Review X*, vol. 8, no. 2, p. 021012, 2018.

[50] E. T. Campbell, B. M. Terhal, and C. Vuillot, "Roads towards fault-tolerant universal quantum computation," *Nature*, vol. 549, no. 7671, p. 172, 2017.

[51] E. Shimshoni, G. Morigi, and S. Fishman, "Quantum zigzag transition in ion chains," *Physical Review Letters*, vol. 106, no. 1, p. 010401, 2011.

[52] C. Monroe and J. Kim, "Scaling the ion trap quantum processor," *Science*, vol. 339, no. 6124, pp. 1164–1169, 2013.

[53] K. R. Brown, J. Kim, and C. Monroe, "Co-designing a scalable quantum computer with trapped atomic ions," *npj Quantum Information*, vol. 2, p. 16034, 2016.

[54] B. Lekitsch, S. Weidt, A. G. Fowler, K. Mølmer, S. J. Devitt, C. Wunderlich, and W. K. Hensinger, "Blueprint for a microwave trapped ion quantum computer," *Science Advances*, vol. 3, no. 2, p. e1601540, 2017.

[55] D. Kielpinski, C. Monroe, and D. J. Wineland, "Architecture for a large-scale ion-trap quantum computer," *Nature*, vol. 417, no. 6890, p. 709, 2002.

[56] C. Monroe, R. Raussendorf, A. Ruthven, K. Brown, P. Maunz, L.-M. Duan, and J. Kim, "Large-scale modular quantum-computer architecture with atomic memory and photonic interconnects," *Physical Review A*, vol. 89, no. 2, p. 022317, 2014.

[57] S. Crain, E. Mount, S. Baek, and J. Kim, "Individual addressing of trapped $^{171}Yb^{+}$ ion qubits using a microelectromechanical systems-based beam steering system," *Applied Physics Letters*, vol. 105, no. 18, p. 181115, 2014.

[58] S. Debnath, N. M. Linke, C. Figgatt, K. A. Landsman, K. Wright, and C. Monroe, "Demonstration of a small programmable quantum computer with atomic qubits," *Nature*, vol. 536, no. 7614, p. 63, 2016.

[59] D. Kielpinski, C. Volin, E. W. Streed, F. Lenzini, and M. Lobino, "Integrated optics architecture for trapped-ion quantum information processing," *Quantum Information Processing*, vol. 15, no. 12, pp. 5315–5338, 2016.

[60] K. K. Mehta, C. D. Bruzewicz, R. McConnell, R. J. Ram, J. M. Sage, and J. Chiaverini, "Integrated optical addressing of an ion qubit," *Nature Nanotechnology*, vol. 11, no. 12, p. 1066, 2016.

[61] R. Nigmatullin, C. J. Ballance, N. De Beaudrap, and S. C. Benjamin, "Minimally complex ion traps as modules for quantum communication and computing," *New Journal of Physics*, vol. 18, no. 10, p. 103028, 2016.

[62] A. VanDevender, Y. Colombe, J. Amini, D. Leibfried, and D. J. Wineland, "Efficient fiber optic detection of trapped ion fluorescence," *Physical Review Letters*, vol. 105, no. 2, p. 023001, 2010.

[63] T. H. Kim, P. F. Herskind, and I. L. Chuang, "Surface-electrode ion trap with integrated light source," *Applied Physics Letters*, vol. 98, no. 21, p. 214103, 2011.

[64] M. Ghadimi, V. Blūms, B. G. Norton, P. M. Fisher, S. C. Connell, J. M. Amini, C. Volin, H. Hayden, C.-S. Pai, D. Kielpinski, *et al.*, "Scalable ion–photon quantum interface based on integrated diffractive mirrors," *npj Quantum Information*, vol. 3, no. 1, p. 4, 2017.

[65] G. R. Brady, A. R. Ellis, D. L. Moehring, D. Stick, C. Highstrete, K. M. Fortier, M. G. Blain, R. A. Haltli, A. A. Cruz-Cabrera, R. D. Briggs, *et al.*, "Integration of fluorescence collection optics with a microfabricated surface electrode ion trap," *Applied Physics B*, vol. 103, no. 4, pp. 801–808, 2011.

[66] E. W. Streed, B. G. Norton, A. Jechow, T. J. Weinhold, and D. Kielpinski, "Imaging of trapped ions with a microfabricated optic for quantum information processing," *Physical Review Letters*, vol. 106, no. 1, p. 010502, 2011.

[67] J. T. Merrill, C. Volin, D. Landgren, J. M. Amini, K. Wright, S. C. Doret, C. Pai, H. Hayden, T. Killian, D. Faircloth, *et al.*, "Demonstration of integrated microscale optics in surface-electrode ion traps," *New Journal of Physics*, vol. 13, no. 10, p. 103005, 2011.

[68] P. F. Herskind, S. X. Wang, M. Shi, Y. Ge, M. Cetina, and I. L. Chuang, "Microfabricated surface ion trap on a high-finesse optical mirror," *Optics Letters*, vol. 36, no. 16, pp. 3045–3047, 2011.

[69] A. Jechow, E. Streed, B. Norton, M. Petrasiunas, and D. Kielpinski, "Wavelength-scale imaging of trapped ions using a phase Fresnel lens," *Optics Letters*, vol. 36, no. 8, pp. 1371–1373, 2011.

[70] C. R. Clark, C. Chou, A. Ellis, J. Hunker, S. A. Kemme, P. Maunz, B. Tabakov, C. Tigges, and D. L. Stick, "Characterization of fluorescence collection optics integrated with a microfabricated surface electrode ion trap," *Physical Review Applied*, vol. 1, no. 2, p. 024004, 2014.

[71] D. H. Slichter, V. B. Verma, D. Leibfried, R. P. Mirin, S. W. Nam, and D. J. Wineland, "UV-sensitive superconducting nanowire single photon detectors for integration in an ion trap," *Optics Express*, vol. 25, no. 8, pp. 8705–8720, 2017.

[72] A. Sinclair, M. Wilson, and P. Gill, "Improved three-dimensional control of a single strontium ion in an endcap trap," *Optics Communications*, vol. 190, no. 1-6, pp. 193–203, 2001.

[73] G. Wilpers, P. See, P. Gill, and A. G. Sinclair, "A compact UHV package for microfabricated ion-trap arrays with direct electronic air-side access," *Applied Physics B*, vol. 111, no. 1, pp. 21–28, 2013.

[74] J. Wang, S. Paesani, Y. Ding, R. Santagati, P. Skrzypczyk, A. Salavrakos, J. Tura, R. Augusiak, L. Mančinska, D. Bacco, *et al.*, "Multidimensional quantum entanglement with large-scale integrated optics," *Science*, p. eaar7053, 2018.

[75] R. Santagati, J. Silverstone, M. Strain, M. Sorel, S. Miki, T. Yamashita, M. Fujiwara, M. Sasaki, H. Terai, M. Tanner, *et al.*, "Silicon photonic processor of two-qubit entangling quantum logic," *Journal of Optics*, vol. 19, no. 11, p. 114006, 2017.

[76] M. J. Paniccia, "A perfect marriage: optics and silicon," *Optik & Photonik*, vol. 6, no. 2, pp. 34–38, 2011.

[77] M. Asghari and A. V. Krishnamoorthy, "Silicon photonics: Energy-efficient communication," *Nature Photonics*, vol. 5, no. 5, p. 268, 2011.

[78] C. Batten, A. Joshi, J. Orcutt, A. Khilo, B. Moss, C. W. Holzwarth, M. A. Popovic, H. Li, H. I. Smith, J. L. Hoyt, *et al.*, "Building many-core processor-to-DRAM networks with monolithic CMOS silicon photonics," *IEEE Micro*, vol. 29, no. 4, 2009.

[79] G. Roelkens, L. Liu, D. Liang, R. Jones, A. Fang, B. Koch, and J. Bowers, "III-V/silicon photonics for on-chip and intra-chip optical interconnects," *Laser & Photonics Reviews*, vol. 4, no. 6, pp. 751–779, 2010.

[80] Y. Jiang, P. T. DeVore, and B. Jalali, "Analog optical computing primitives in silicon photonics," *Optics Letters*, vol. 41, no. 6, pp. 1273–1276, 2016.

[81] A. Leinse, S. Zhang, and R. Heideman, "Triplex: The versatile silicon nitride waveguide platform," in *Progress in Electromagnetic Research Symposium (PIERS)*, pp. 67–67, IEEE, 2016.

[82] K. Wörhoff, R. G. Heideman, A. Leinse, and M. Hoekman, "Triplex: a versatile dielectric photonic platform," *Advanced Optical Technologies*, vol. 4, no. 2, pp. 189–207, 2015.

[83] G. N. West, W. Loh, D. Kharas, C. Sorace-Agaskar, K. K. Mehta, J. Sage, J. Chiaverini, and R. J. Ram, "Low loss optical waveguides in the blue and ultraviolet spectrum," *arXiv:1808.00429*, 2018.

[84] M. Stegmaier, J. Ebert, J. Meckbach, K. Ilin, M. Siegel, and W. Pernice, "Aluminum nitride nanophotonic circuits operating at ultraviolet wavelengths," *Applied Physics Letters*, vol. 104, no. 9, p. 091108, 2014.

[85] T.-J. Lu, M. Fanto, H. Choi, P. Thomas, J. Steidle, S. Mouradian, W. Kong, D. Zhu, H. Moon, K. Berggren, *et al.*, "Aluminum nitride integrated photonics platform for the ultraviolet to visible spectrum," *Optics Express*, vol. 26, no. 9, pp. 11147–11160, 2018.

[86] G. N. West, K. K. Mehta, and R. J. Ram, "Alumina waveguides for full-spectrum integrated photonics," in *Photonics Society Summer Topical Meeting Series (SUM), 2017 IEEE*, pp. 133–134, IEEE, 2017.

[87] M. Soltani, R. Soref, T. Palacios, and D. Englund, "AlGaN/AlN integrated photonics platform for the ultraviolet and visible spectral range," *Optics Express*, vol. 24, no. 22, pp. 25415–25423, 2016.

[88] C. C. Evans, C. Liu, and J. Suntivich, "Low-loss titanium dioxide waveguides and resonators using a dielectric lift-off fabrication process," *Optics Express*, vol. 23, no. 9, pp. 11160–11169, 2015.

[89] A. Glass, I. P. Kaminow, A. A. Ballman, and D. Olson, "Absorption loss and photorefractive-index changes in Ti:LiNbO(3) crystals and waveguides," *Applied Optics*, vol. 19, no. 2, pp. 276–281, 1980.

[90] L. Tsonev, I. Savatinova, and P. Simova, "Ti:LiNbO(3) optical waveguides," *Applied Physics*, vol. 24, no. 3, pp. 205–209, 1981.

[91] F. Naccarato, F. Ricci, J. Suntivich, G. Hautier, L. Wirtz, and G.-M. Rignanese1, "Designing materials with high refractive index and wide band gap: A first-principles high-throughput study," *arXiv:1809.01132*, 2018.

[92] D. Kharas, C. Sorace-Agaskar, S. Bramhavar, W. Loh, J. M. Sage, P. W. Juodawlkis, and J. Chiaverini, "Multi-level photonics for trapped-ion quantum computing," in *Photonics Society Summer Topical Meeting Series (SUM), 2017 IEEE*, pp. 105–106, IEEE, 2017.

[93] C. Sorace-Agaskar, S. Bramhavar, D. Kharas, W. Loh, P. W. Juodawlkis, J. Chiaverini, and J. M. Sage, "Multi-layer integrated photonics from the ultraviolet to the infrared," in *Frontiers in Biological Detection: From Nanosensors to Systems X*, vol. 10510, p. 105100D, International Society for Optics and Photonics, 2018.

[94] Q. Fang, T.-Y. Liow, J. F. Song, C. W. Tan, M. B. Yu, G. Q. Lo, and D.-L. Kwong, "Suspended optical fiber-to-waveguide mode size converter for silicon photonics," *Optics Express*, vol. 18, no. 8, pp. 7763–7769, 2010.

[95] D. Dai, Y. Tang, and J. E. Bowers, "Mode conversion in tapered submicron silicon ridge optical waveguides," *Optics Express*, vol. 20, no. 12, pp. 13425–13439, 2012.

[96] F. Van Laere, T. Claes, J. Schrauwen, S. Scheerlinck, W. Bogaerts, D. Taillaert, L. O'Faolain, D. Van Thourhout, and R. Baets, "Compact focusing grating couplers for silicon-on-insulator integrated circuits," *IEEE Photonics Technology Letters*, vol. 19, no. 23, pp. 1919–1921, 2007.

[97] D. Taillaert, F. Van Laere, M. Ayre, W. Bogaerts, D. Van Thourhout, P. Bienstman, and R. Baets, "Grating couplers for coupling between optical fibers and nanophotonic waveguides," *Japanese Journal of Applied Physics*, vol. 45, no. 8R, p. 6071, 2006.

[98] S. Ura, Y. Furukawa, T. Suhara, and H. Nishihara, "Linearly focusing grating coupler for integrated-optic parallel pickup," *JOSA A*, vol. 7, no. 9, pp. 1759–1763, 1990.

[99] I. Kawakubo, J. Funazaki, K. Shirane, and A. Yoshizawa, "Integrated optical-disk pickup that uses a focusing grating coupler with a high numerical aperture," *Applied Optics*, vol. 33, no. 29, pp. 6855–6859, 1994.

[100] H.-S. Kim, T.-Y. Kim, E.-H. Cho, J.-S. Sohn, M.-S. Jung, M.-B. Lee, N.-Y. Park, G.-P. Han, M.-C. Paek, and G.-Y. Sung, "Diffraction limit of the focusing waveguide grating coupler for optical probe information storage," *Nanotechnology*, vol. 14, no. 6, p. 684, 2003.

[101] J. Wang, D. Bonneau, M. Villa, J. W. Silverstone, R. Santagati, S. Miki, T. Yamashita, M. Fujiwara, M. Sasaki, H. Terai, *et al.*, "Chip-to-chip quantum photonic interconnect by path-polarization interconversion," *Optica*, vol. 3, no. 4, pp. 407–413, 2016.

[102] G.-i. Hatakoshi, H. Fujima, and K. Goto, "Waveguide grating lenses for optical couplers," *Applied Optics*, vol. 23, no. 11, pp. 1749–1753, 1984.

[103] A. Arriola, S. Gross, N. Jovanovic, N. Charles, P. G. Tuthill, S. M. Olaizola, A. Fuerbach, and M. J. Withford, "Low bend loss waveguides enable compact, efficient 3D photonic chips," *Optics Express*, vol. 21, no. 3, pp. 2978–2986, 2013.

[104] T. Meany, S. Gross, N. Jovanovic, A. Arriola, M. Steel, and M. J. Withford, "Towards low-loss lightwave circuits for non-classical optics at 800 and 1,550 nm," *Applied Physics A*, vol. 114, no. 1, pp. 113–118, 2014.

[105] L. Tong, R. R. Gattass, I. Maxwell, J. B. Ashcom, and E. Mazur, "Optical loss measurements in femtosecond laser written waveguides in glass," *Optics Communications*, vol. 259, no. 2, pp. 626–630, 2006.

[106] H. P. Herzig, *Micro-optics: elements, systems and applications*. CRC Press, 2014.

[107] D. Gil, R. Menon, and H. I. Smith, "The promise of diffractive optics in maskless lithography," *Microelectronic Engineering*, vol. 73, pp. 35–41, 2004.

[108] T. Shiono, T. Hamamoto, and K. Takahara, "High-efficiency blazed diffractive optical elements for the violet wavelength fabricated by electron-beam lithography," *Applied Optics*, vol. 41, no. 13, pp. 2390–2393, 2002.

[109] M. A. Golub, "Generalized conversion from the phase function to the blazed surface-relief profile of diffractive optical elements," *JOSA A*, vol. 16, no. 5, pp. 1194–1201, 1999.

[110] A. Arbabi, Y. Horie, M. Bagheri, and A. Faraon, "Dielectric metasurfaces for complete control of phase and polarization with subwavelength spatial resolution and high transmission," *Nature Nanotechnology*, vol. 10, no. 11, p. 937, 2015.

[111] A. Milton and W. Burns, "Mode coupling in optical waveguide horns," *IEEE Journal of Quantum Electronics*, vol. 13, no. 10, pp. 828–835, 1977.

[112] Y. Fu, T. Ye, W. Tang, and T. Chu, "Efficient adiabatic silicon-on-insulator waveguide taper," *Photonics Research*, vol. 2, no. 3, pp. A41–A44, 2014.

[113] J. Zou, Y. Yu, M. Ye, L. Liu, S. Deng, X. Xu, and X. Zhang, "Short and efficient mode-size converter designed by segmented-stepwise method," *Optics Letters*, vol. 39, no. 21, pp. 6273–6276, 2014.

[114] P. Sethi, A. Haldar, and S. K. Selvaraja, "Ultra-compact low-loss broadband waveguide taper in silicon-on-insulator," *Optics Express*, vol. 25, no. 9, pp. 10196–10203, 2017.

[115] B. L. Chuah, N. C. Lewty, R. Cazan, and M. D. Barrett, "Detection of ion micromotion in a linear Paul trap with a high finesse cavity," *Optics Express*, vol. 21, no. 9, pp. 10632–10641, 2013.

[116] N. Podoliak, H. Takahashi, M. Keller, and P. Horak, "Comparative numerical studies of ion traps with integrated optical cavities," *Physical Review Applied*, vol. 6, no. 4, p. 044008, 2016.

[117] M. Harlander, M. Brownnutt, W. Hänsel, and R. Blatt, "Trapped-ion probing of light-induced charging effects on dielectrics," *New Journal of Physics*, vol. 12, no. 9, p. 093035, 2010.

[118] M. Steiner, H. M. Meyer, C. Deutsch, J. Reichel, and M. Köhl, "Single ion coupled to an optical fiber cavity," *Physical Review Letters*, vol. 110, no. 4, p. 043003, 2013.

[119] M. Madsen, W. Hensinger, D. Stick, J. Rabchuk, and C. Monroe, "Planar ion trap geometry for microfabrication," *Applied Physics B: Lasers and Optics*, vol. 78, no. 5, pp. 639–651, 2004.

[120] K. Johnson, J. Wong-Campos, A. Restelli, K. Landsman, B. Neyenhuis, J. Mizrahi, and C. Monroe, "Active stabilization of ion trap radiofrequency potentials," *Review of Scientific Instruments*, vol. 87, no. 5, p. 053110, 2016.

[121] J. Home, D. Hanneke, J. D. Jost, D. Leibfried, and D. J. Wineland, "Normal modes of trapped ions in the presence of anharmonic trap potentials," *New Journal of Physics*, vol. 13, no. 7, p. 073026, 2011.

[122] K. M. Davis, K. Miura, N. Sugimoto, and K. Hirao, "Writing waveguides in glass with a femtosecond laser," *Optics Letters*, vol. 21, no. 21, pp. 1729–1731, 1996.

[123] J. B. Spring, P. S. Salter, B. J. Metcalf, P. C. Humphreys, M. Moore, N. Thomas-Peter, M. Barbieri, X.-M. Jin, N. K. Langford, W. S. Kolthammer, *et al.*, "On-chip low loss heralded source of pure single photons," *Optics Express*, vol. 21, no. 11, pp. 13522–13532, 2013.

[124] T. Meany, M. Gräfe, R. Heilmann, A. Perez-Leija, S. Gross, M. J. Steel, M. J. Withford, and A. Szameit, "Laser written circuits for quantum photonics," *Laser & Photonics Reviews*, vol. 9, no. 4, pp. 363–384, 2015.

[125] R. Osellame, V. Maselli, R. M. Vazquez, R. Ramponi, and G. Cerullo, "Integration of optical waveguides and microfluidic channels both fabricated by femtosecond laser irradiation," *Applied physics letters*, vol. 90, no. 23, p. 231118, 2007.

[126] Y. Liao, J. Song, E. Li, Y. Luo, Y. Shen, D. Chen, Y. Cheng, Z. Xu, K. Sugioka, and K. Midorikawa, "Rapid prototyping of three-dimensional microfluidic mixers in glass by femtosecond laser direct writing," *Lab on a Chip*, vol. 12, no. 4, pp. 746–749, 2012.

[127] R. R. Gattass and E. Mazur, "Femtosecond laser micromachining in transparent materials," *Nature Photonics*, vol. 2, no. 4, p. 219, 2008.

[128] D. Lancaster, S. Gross, H. Ebendorff-Heidepriem, K. Kuan, T. Monro, M. Ams, A. Fuerbach, and M. Withford, "Fifty percent internal slope efficiency femtosecond direct-written Tm^{3+}:ZBLAN waveguide laser," *Optics Letters*, vol. 36, no. 9, pp. 1587–1589, 2011.

[129] Y.-C. Chen, P. S. Salter, S. Knauer, L. Weng, A. C. Frangeskou, C. J. Stephen, S. N. Ishmael, P. R. Dolan, S. Johnson, B. L. Green, *et al.*, "Laser writing of coherent colour centres in diamond," *Nature Photonics*, vol. 11, no. 2, p. 77, 2017.

[130] J.-P. Bérubé and R. Vallée, "Femtosecond laser direct inscription of surface skimming waveguides in bulk glass," *Optics Letters*, vol. 41, no. 13, pp. 3074–3077, 2016.

[131] Y. Hanada, K. Sugioka, and K. Midorikawa, "UV waveguides light fabricated in fluoropolymer CYTOP by femtosecond laser direct writing," *Optics Express*, vol. 18, no. 2, pp. 446–450, 2010.

[132] G. Douglass, A. Arriola, I. Heras, G. Martin, E. Le Coarer, S. Gross, and M. Withford, "Novel concept for visible and near infrared spectro-interferometry: laser-written layered arrayed waveguide gratings," *Optics Express*, vol. 26, no. 14, pp. 18470–18479, 2018.

[133] M. Ams, G. Marshall, D. Spence, and M. Withford, "Slit beam shaping method for femtosecond laser direct-write fabrication of symmetric waveguides in bulk glasses," *Optics Express*, vol. 13, no. 15, pp. 5676–5681, 2005.

[134] N. Jovanovic, N. Cvetojevic, B. Norris, C. Betters, C. Schwab, J. Lozi, O. Guyon, S. Gross, F. Martinache, P. Tuthill, *et al.*, "Demonstration of an efficient, photonic-based astronomical spectrograph on an 8-m telescope," *Optics Express*, vol. 25, no. 15, pp. 17753–17766, 2017.

[135] N. Riesen, S. Gross, J. D. Love, Y. Sasaki, and M. J. Withford, "Monolithic mode-selective few-mode multicore fiber multiplexers," *Scientific Reports*, vol. 7, no. 1, p. 6971, 2017.

[136] S. Gross, N. Riesen, J. D. Love, and M. J. Withford, "Three-dimensional ultra-broadband integrated tapered mode multiplexers," *Laser & Photonics Reviews*, vol. 8, no. 5, 2014.

[137] M. Ams, G. D. Marshall, P. Dekker, M. Dubov, V. K. Mezentsev, I. Bennion, and M. J. Withford, "Investigation of ultrafast laser–photonic material interactions: Challenges for directly written glass photonics," *IEEE Journal of Selected Topics in Quantum Electronics*, vol. 14, no. 5, pp. 1370–1381, 2008.

[138] K. Miura, J. Qiu, H. Inouye, T. Mitsuyu, and K. Hirao, "Photowritten optical waveguides in various glasses with ultrashort pulse laser," *Applied Physics Letters*, vol. 71, no. 23, pp. 3329–3331, 1997.

[139] A. M. Streltsov and N. F. Borrelli, "Study of femtosecond-laser-written waveguides in glasses," *JOSA B*, vol. 19, no. 10, pp. 2496–2504, 2002.

[140] A. Zoubir, M. Richardson, C. Rivero, A. Schulte, C. Lopez, K. Richardson, N. Hô, and R. Vallée, "Direct femtosecond laser writing of waveguides in As_2S_3 thin films," *Optics Letters*, vol. 29, no. 7, pp. 748–750, 2004.

[141] P. Nandi, G. Jose, C. Jayakrishnan, S. Debbarma, K. Chalapathi, K. Alti, A. Dharmadhikari, J. Dharmadhikari, and D. Mathur, "Femtosecond laser written channel waveguides in tellurite glass," *Optics Express*, vol. 14, no. 25, pp. 12145–12150, 2006.

[142] G. D. Marshall, M. Ams, and M. J. Withford, "Direct laser written waveguide-bragg gratings in bulk fused silica," *Optics Letters*, vol. 31, no. 18, pp. 2690–2691, 2006.

[143] M. Hughes, W. Yang, and D. Hewak, "Fabrication and characterization of femtosecond laser written waveguides in chalcogenide glass," *Applied Physics Letters*, vol. 90, no. 13, p. 131113, 2007.

[144] J. Thomas, M. Heinrich, J. Burghoff, S. Nolte, A. Ancona, and A. Tünnermann, "Femtosecond laser-written quasi-phase-matched waveguides in lithium niobate," *Applied Physics Letters*, vol. 91, no. 15, p. 151108, 2007.

[145] Y. Tan, A. Rodenas, F. Chen, R. R. Thomson, A. K. Kar, D. Jaque, and Q. Lu, "70% slope efficiency from an ultrafast laser-written Nd:$GdVO_4$ channel waveguide laser," *Optics Express*, vol. 18, no. 24, pp. 24994–24999, 2010.

[146] T. T. Fernandez, S. Eaton, G. Della Valle, R. M. Vazquez, M. Irannejad, G. Jose, A. Jha, G. Cerullo, R. Osellame, and P. Laporta, "Femtosecond laser written optical waveguide amplifier in phospho-tellurite glass," *Optics Express*, vol. 18, no. 19, pp. 20289–20297, 2010.

[147] J. Siebenmorgen, T. Calmano, K. Petermann, and G. Huber, "Highly efficient Yb:YAG channel waveguide laser written with a femtosecond-laser," *Optics Express*, vol. 18, no. 15, pp. 16035–16041, 2010.

[148] S. Vukelic, B. Gao, S. Ryu, and Y. Yao, "Structural modification of amorphous fused silica under femtosecond laser irradiation," in *ASME 2008 International Manufacturing Science and Engineering Conference collocated with the 3rd JSME/ASME International Conference on Materials and Processing*, pp. 227–236, American Society of Mechanical Engineers, 2008.

[149] D. J. Little, M. Ams, S. Gross, P. Dekker, C. T. Miese, A. Fuerbach, and M. J. Withford, "Structural changes in BK7 glass upon exposure to femtosecond laser pulses," *Journal of Raman Spectroscopy*, vol. 42, no. 4, pp. 715–718, 2011.

[150] W. J. Reichman, D. M. Krol, L. Shah, F. Yoshino, A. Arai, S. M. Eaton, and P. R. Herman, "A spectroscopic comparison of femtosecond-laser-modified fused silica using kilohertz and megahertz laser systems," *Journal of Applied Physics*, vol. 99, no. 12, p. 123112, 2006.

[151] C. B. Schaffer, J. F. García, and E. Mazur, "Bulk heating of transparent materials using a high-repetition-rate femtosecond laser," *Applied Physics A*, vol. 76, no. 3, pp. 351–354, 2003.

[152] S. M. Eaton, H. Zhang, P. R. Herman, F. Yoshino, L. Shah, J. Bovatsek, and A. Y. Arai, "Heat accumulation effects in femtosecond laser-written waveguides with variable repetition rate," *Optics Express*, vol. 13, no. 12, pp. 4708–4716, 2005.

[153] S. M. Eaton, H. Zhang, M. L. Ng, J. Li, W.-J. Chen, S. Ho, and P. R. Herman, "Transition from thermal diffusion to heat accumulation in high repetition rate femtosecond laser writing of buried optical waveguides," *Optics Express*, vol. 16, no. 13, pp. 9443–9458, 2008.

[154] A. W. Snyder and J. Love, *Optical waveguide theory*. Springer Science & Business Media, 2012.

[155] D. Marcuse, "Loss analysis of single-mode fiber splices," *Bell System Technical Journal*, vol. 56, no. 5, pp. 703–718, 1977.

[156] D. Marcuse, "Gaussian approximation of the fundamental modes of graded-index fibers," *JOSA*, vol. 68, no. 1, pp. 103–109, 1978.

[157] M. W. Lee, M. C. Jarratt, C. Marciniak, and M. J. Biercuk, "Frequency stabilization of a 369 nm diode laser by nonlinear spectroscopy of ytterbium ions in a discharge," *Optics Express*, vol. 22, no. 6, pp. 7210–7221, 2014.

[158] PGO, "Eagle2000, alkali free boro-aluminosilicate glass," *url: https://www.pgo-online.com/intl/eagle2000.html*, 2018.

[159] F. Dreisow, M. Heinrich, A. Szameit, S. Döring, S. Nolte, A. Tünnermann, S. Fahr, and F. Lederer, "Spectral resolved dynamic localization in curved fs laser written waveguide arrays," *Optics Express*, vol. 16, no. 5, pp. 3474–3483, 2008.

[160] D. J. Little, M. Ams, P. Dekker, G. D. Marshall, J. M. Dawes, and M. J. Withford, "Femtosecond laser modification of fused silica: the effect of writing polarization on Si-O ring structure," *Optics Express*, vol. 16, no. 24, pp. 20029–20037, 2008.

[161] K. Mishchik, C. D'Amico, P. K. Velpula, C. Mauclair, A. Boukenter, Y. Ouerdane, and R. Stoian, "Ultrafast laser induced electronic and structural modifications in bulk fused silica," *Journal of Applied Physics*, vol. 114, no. 13, p. 133502, 2013.

[162] D. Krol, "Femtosecond laser modification of glass," *Journal of Non-Crystalline Solids*, vol. 354, no. 2-9, pp. 416–424, 2008.

[163] W. Burns, A. Milton, and A. Lee, "Optical waveguide parabolic coupling horns," *Applied Physics Letters*, vol. 30, no. 1, pp. 28–30, 1977.

[164] C. D'Amico, G. Cheng, C. Mauclair, J. Troles, L. Calvez, V. Nazabal, C. Caillaud, G. Martin, B. Arezki, E. Lecoarer, *et al.*, "Large-mode-area infrared guiding in ultrafast laser written waveguides in sulfur-based chalcogenide glasses," *Optics Express*, vol. 22, no. 11, pp. 13091–13101, 2014.

[165] R. Stoian, C. D'Amico, M. Bhuyan, and G. Cheng, "Ultrafast laser photoinscription of large-mode-area waveguiding structures in bulk dielectrics," *Optics & Laser Technology*, vol. 80, pp. 98–103, 2016.

[166] G. Cheng, C. D'Amico, X. Liu, and R. Stoian, "Large mode area waveguides with polarization functions by volume ultrafast laser photoinscription of fused silica," *Optics Letters*, vol. 38, no. 11, pp. 1924–1926, 2013.

[167] A. Szameit, D. Blömer, J. Burghoff, T. Pertsch, S. Nolte, and A. Tünnermann, "Hexagonal waveguide arrays written with fs-laser pulses," *Applied Physics B: Lasers and Optics*, vol. 82, no. 4, pp. 507–512, 2006.

[168] H. Kikuta, Y. Ohira, and K. Iwata, "Achromatic quarter-wave plates using the dispersion of form birefringence," *Applied Optics*, vol. 36, no. 7, pp. 1566–1572, 1997.

[169] D. Faklis and G. M. Morris, "Spectral properties of multiorder diffractive lenses," *Applied Optics*, vol. 34, no. 14, pp. 2462–2468, 1995.

[170] M. K. Tey, Z. Chen, S. A. Aljunid, B. Chng, F. Huber, G. Maslennikov, and C. Kurtsiefer, "Strong interaction between light and a single trapped atom without the need for a cavity," *Nature Physics*, vol. 4, no. 12, p. 924, 2008.

[171] M. K. Tey, G. Maslennikov, T. C. Liew, S. A. Aljunid, F. Huber, B. Chng, Z. Chen, V. Scarani, and C. Kurtsiefer, "Interfacing light and single atoms with a lens," *New Journal of Physics*, vol. 11, no. 4, p. 043011, 2009.

[172] A. Nottola, A. Gerardino, M. Gentili, E. Di Fabrizio, S. Cabrini, P. Melpignano, and G. Rotaris, "Fabrication of semi-continuous profile diffractive optical elements for beam shaping by electron beam lithography," *Microelectronic Engineering*, vol. 53, no. 1-4, pp. 325–328, 2000.

[173] S. Lu, Y.-B. Yan, D.-E. Yi, G.-F. Jin, and M.-X. Wu, "Integrated diffractive optical mode converter for fiber-to-waveguide coupling," *Optics & Laser Technology*, vol. 35, no. 5, pp. 369–373, 2003.

[174] K. Rastani, A. Marrakchi, S. F. Habiby, W. M. Hubbard, H. Gilchrist, and R. E. Nahory, "Binary phase Fresnel lenses for generation of two-dimensional beam arrays," *Applied Optics*, vol. 30, no. 11, pp. 1347–1354, 1991.

[175] J. Jahns and S. J. Walker, "Two-dimensional array of diffractive microlenses fabricated by thin film deposition," *Applied Optics*, vol. 29, no. 7, pp. 931–936, 1990.

[176] Y. Li, Y. Yu, L. Guo, S. Wu, C. Chen, L. Niu, A. Li, and H. Yang, "High efficiency multilevel phase-type Fresnel zone plates produced by two-photon polymerization of SU-8," *Journal of Optics*, vol. 12, no. 3, p. 035203, 2010.

[177] A. Koshelev, G. Calafiore, C. Piña-Hernandez, F. I. Allen, S. Dhuey, S. Sassolini, E. Wong, P. Lum, K. Munechika, and S. Cabrini, "High refractive index Fresnel lens on a fiber fabricated by nanoimprint lithography for immersion applications," *Optics Letters*, vol. 41, no. 15, pp. 3423–3426, 2016.

[178] L. Huang, X. Chen, H. Mühlenbernd, H. Zhang, S. Chen, B. Bai, Q. Tan, G. Jin, K.-W. Cheah, C.-W. Qiu, *et al.*, "Three-dimensional optical holography using a plasmonic metasurface," *Nature Communications*, vol. 4, p. 2808, 2013.

[179] E. Karimi, S. A. Schulz, I. De Leon, H. Qassim, J. Upham, and R. W. Boyd, "Generating optical orbital angular momentum at visible wavelengths using a plasmonic metasurface," *Light: Science & Applications*, vol. 3, no. 5, p. e167, 2014.

[180] F. Ding, Z. Wang, S. He, V. M. Shalaev, and A. V. Kildishev, "Broadband high-efficiency half-wave plate: a supercell-based plasmonic metasurface approach," *ACS Nano*, vol. 9, no. 4, pp. 4111–4119, 2015.

[181] H.-T. Chen, A. J. Taylor, and N. Yu, "A review of metasurfaces: physics and applications," *Reports on Progress in Physics*, vol. 79, no. 7, p. 076401, 2016.

[182] F. Aieta, P. Genevet, M. A. Kats, N. Yu, R. Blanchard, Z. Gaburro, and F. Capasso, "Aberration-free ultrathin flat lenses and axicons at telecom wavelengths based on plasmonic metasurfaces," *Nano Letters*, vol. 12, no. 9, pp. 4932–4936, 2012.

[183] J. N. Mait, "Understanding diffractive optic design in the scalar domain," *JOSA A*, vol. 12, no. 10, pp. 2145–2158, 1995.

[184] D. W. Prather, M. S. Mirotznik, and J. N. Mait, "Boundary element method for vector modeling diffractive optical elements," in *Diffractive and Holographic Optics Technology II*, vol. 2404, pp. 28–40, International Society for Optics and Photonics, 1995.

[185] D. W. Prather, M. S. Mirotznik, and J. N. Mait, "Boundary integral methods applied to the analysis of diffractive optical elements," *JOSA A*, vol. 14, no. 1, pp. 34–43, 1997.

[186] M. Moharam and T. Gaylord, "Rigorous coupled-wave analysis of planar-grating diffraction," *JOSA*, vol. 71, no. 7, pp. 811–818, 1981.

[187] M. Moharam and T. K. Gaylord, "Diffraction analysis of dielectric surface-relief gratings," *JOSA*, vol. 72, no. 10, pp. 1385–1392, 1982.

[188] M. Moharam and T. Gaylord, "Three-dimensional vector coupled-wave analysis of planar-grating diffraction," *JOSA*, vol. 73, no. 9, pp. 1105–1112, 1983.

[189] N. Chateau and J.-P. Hugonin, "Algorithm for the rigorous coupled-wave analysis of grating diffraction," *JOSA A*, vol. 11, no. 4, pp. 1321–1331, 1994.

[190] M. Moharam, E. B. Grann, D. A. Pommet, and T. Gaylord, "Formulation for stable and efficient implementation of the rigorous coupled-wave analysis of binary gratings," *JOSA A*, vol. 12, no. 5, pp. 1068–1076, 1995.

[191] D. W. Prather and S. Shi, "Formulation and application of the finite-difference time-domain method for the analysis of axially symmetric diffractive optical elements," *JOSA A*, vol. 16, no. 5, pp. 1131–1142, 1999.

[192] G. Bao, Z. Chen, and H. Wu, "Adaptive finite-element method for diffraction gratings," *JOSA A*, vol. 22, no. 6, pp. 1106–1114, 2005.

[193] J. M. Bendickson, E. N. Glytsis, and T. K. Gaylord, "Scalar integral diffraction methods: unification, accuracy, and comparison with a rigorous boundary element method with application to diffractive cylindrical lenses," *JOSA A*, vol. 15, no. 7, pp. 1822–1837, 1998.

[194] D. A. Pommet, M. Moharam, and E. B. Grann, "Limits of scalar diffraction theory for diffractive phase elements," *JOSA A*, vol. 11, no. 6, pp. 1827–1834, 1994.

[195] F. Shen and A. Wang, "Fast-Fourier-transform based numerical integration method for the Rayleigh-Sommerfeld diffraction formula," *Applied Optics*, vol. 45, no. 6, pp. 1102–1110, 2006.

[196] D.-L. Liu and R. C. Waag, "Propagation and backpropagation for ultrasonic wavefront design," *IEEE Transactions on Ultrasonics, Ferroelectrics, and Frequency Control*, vol. 44, no. 1, pp. 1–13, 1997.

[197] M. Day, K. Choonee, D. Cox, M. Thompson, G. Marshall, and A. G. Sinclair, "Continuous-relief diffractive microlenses for laser beam focusing," *Optics Express*, vol. 25, no. 22, pp. 26987–26999, 2017.

[198] R. W. Gerchberg, "A practical algorithm for the determination of phase from image and diffraction plane pictures," *Optik*, vol. 35, pp. 237–246, 1972.

[199] G.-z. Yang, B.-z. Dong, B.-y. Gu, J.-y. Zhuang, and O. K. Ersoy, "Gerchberg–Saxton and Yang–Gu algorithms for phase retrieval in a nonunitary transform system: a comparison," *Applied Optics*, vol. 33, no. 2, pp. 209–218, 1994.

[200] J. R. Fienup, "Phase retrieval algorithms: a comparison," *Applied Optics*, vol. 21, no. 15, pp. 2758–2769, 1982.

[201] COMSOL, "Fresnel lens," 2017. (Online, application ID: 46571; accessed 30-November-2017).

[202] E. Hecht, "Optics, 4th," *International edition, Addison-Wesley, San Francisco*, 2002.

[203] U. Sikder and M. A. Zaman, "Optimization of multilayer antireflection coating for photovoltaic applications," *Optics & Laser Technology*, vol. 79, pp. 88–94, 2016.

[204] M. Khorasaninejad, W. T. Chen, A. Y. Zhu, J. Oh, R. C. Devlin, C. Roques-Carmes, I. Mishra, and F. Capasso, "Visible wavelength planar metalenses based on titanium dioxide," *IEEE Journal of Selected Topics in Quantum Electronics*, vol. 23, no. 3, pp. 43–58, 2017.

[205] Y. Liang, H. Liu, F. Wang, H. Meng, J. Guo, J. Li, and Z. Wei, "High-efficiency, near-diffraction limited, dielectric metasurface lenses based on crystalline titanium dioxide at visible wavelengths," *Nanomaterials*, vol. 8, no. 5, 2018.

[206] Q. Zhao, J. Zhou, F. Zhang, and D. Lippens, "Mie resonance-based dielectric metamaterials," *Materials Today*, vol. 12, no. 12, pp. 60–69, 2009.

[207] E.-B. Kley, "Continuous profile writing by electron and optical lithography," *Microelectronic Engineering*, vol. 34, no. 3-4, pp. 261–298, 1997.

[208] M. Ferstl and A.-M. Frisch, "Static and dynamic Fresnel zone lenses for optical interconnections," *Journal of Modern Optics*, vol. 43, no. 7, pp. 1451–1462, 1996.

[209] T. J. Suleski and D. C. O'Shea, "Gray-scale masks for diffractive-optics fabrication: I. Commercial slide imagers," *Applied Optics*, vol. 34, no. 32, pp. 7507–7517, 1995.

[210] M. Haruna, M. Takahashi, K. Wakahayashi, and H. Nishihara, "Laser beam lithographed micro-Fresnel lenses," *Applied Optics*, vol. 29, no. 34, pp. 5120–5126, 1990.

[211] F. Yong-Qi, N. K. A. Bryan, and O. N. Shing, "Diffractive optical elements with continuous relief fabricated by focused ion beam for monomode fiber coupling," *Optics Express*, vol. 7, no. 3, pp. 141–147, 2000.

[212] P. He, F. Wang, L. Li, K. Georgiadis, O. Dambon, F. Klocke, and A. Yi, "Development of a low cost high precision fabrication process for glass hybrid aspherical diffractive lenses," *Journal of Optics*, vol. 13, no. 8, p. 085703, 2011.

[213] K. K. Mehta and R. J. Ram, "Precise and diffraction-limited waveguide-to-free-space focusing gratings," *Scientific Reports*, vol. 7, no. 1, p. 2019, 2017.

[214] S. Yasin, D. Hasko, and H. Ahmed, "Comparison of MIBK/IPA and water/IPA as PMMA developers for electron beam nanolithography," *Microelectronic Engineering*, vol. 61, pp. 745–753, 2002.

[215] M. Rooks, E. Kratschmer, R. Viswanathan, J. Katine, R. Fontana Jr, and S. MacDonald, "Low stress development of poly (methylmethacrylate) for high aspect ratio structures," *Journal of Vacuum Science & Technology B: Microelectronics and Nanometer Structures Processing, Measurement, and Phenomena*, vol. 20, no. 6, pp. 2937–2941, 2002.

[216] S. M. Sze, *Semiconductor devices: physics and technology*. John Wiley & Sons, 2008.

[217] A. B. M. K. Alam, "Etching process development of SiO_2 etching using inductively coupled plasma," Master's thesis, University of Eastern Finland, 2015.

[218] Y.-H. Ting, C.-C. Liu, S.-M. Park, H. Jiang, P. F. Nealey, and A. E. Wendt, "Surface roughening of polystyrene and poly (methyl methacrylate) in Ar/O_2 plasma etching," *Polymers*, vol. 2, no. 4, pp. 649–663, 2010.

[219] G. Oehrlein, Y. Zhang, D. Vender, and O. Joubert, "Fluorocarbon high-density plasmas. II. silicon dioxide and silicon etching using CF_4 and CHF_3," *Journal of Vacuum Science & Technology A: Vacuum, Surfaces, and Films*, vol. 12, no. 2, pp. 333–344, 1994.

[220] R. Legtenberg, H. Jansen, M. De Boer, and M. Elwenspoek, "Anisotropic reactive ion etching of silicon using $SF_6/O_2/CHF_3$ gas mixtures," *Journal of the electrochemical society*, vol. 142, no. 6, pp. 2020–2028, 1995.

[221] A. A. Garay, S. M. Hwang, and C. W. Chung, "Inductive couple plasma reactive ion etching characteristics of TiO_2 thin films," *Thin Solid Films*, vol. 587, pp. 20–27, 2015.

[222] K. L. Kruse and C. T. Middlebrook, "Fan-out routing and optical splitting techniques for compact optical interconnects using single-mode polymer waveguides," *Journal of Modern Optics*, vol. 62, pp. S1–S10, 2015.

[223] J. Munkres, "Algorithms for the assignment and transportation problems," *Journal of the Society for Industrial and Applied Mathematics*, vol. 5, no. 1, pp. 32–38, 1957.

[224] Y. Cao, "Hungarian algorithm for linear assignment problems v2.2," *url: http://www.mathworks.com/matlabcentral/fileexchange/20652-hungarian-algorithmfor-linear-assignment-problems–v2-3-/content/munkres.m*, 2011.

[225] Thorlabs, *S405-XP spec sheet*. 24323-S01, Rev D, October 17, 2016.

[226] Thorlabs, *1060XP spec sheet*. 11338-S01, Rev F, November 29, 2017.

[227] C. Piltz, T. Sriarunothai, A. Varón, and C. Wunderlich, "A trapped-ion-based quantum byte with 10^{-5} next-neighbour cross-talk," *Nature Communications*, vol. 5, p. 4679, 2014.

[228] K. M. Svore, D. P. Divincenzo, and B. M. Terhal, "Noise threshold for a fault-tolerant two-dimensional lattice architecture," *Quantum Information & Computation*, vol. 7, no. 4, pp. 297–318, 2007.

[229] A. G. Fowler, M. Mariantoni, J. M. Martinis, and A. N. Cleland, "Surface codes: Towards practical large-scale quantum computation," *Physical Review A*, vol. 86, no. 3, p. 032324, 2012.

[230] F. Industries, *Fibre Optic 2D arrays datasheet*. REF 723 DS006, Accessed: 28 August,2018.

[231] P. D. Schwindt, Y.-Y. Jau, H. Partner, A. Casias, A. R. Wagner, M. Moorman, R. P. Manginell, J. R. Kellogg, and J. D. Prestage, "A highly miniaturized vacuum package for a trapped ion atomic clock," *Review of Scientific Instruments*, vol. 87, no. 5, p. 053112, 2016.

[232] R. P. Manginell, M. W. Moorman, J. M. Anderson, G. R. Burns, K. E. Achyuthan, D. R. Wheeler, and P. D. Schwindt, "In situ dissolution or deposition of Ytterbium (Yb) metal in microhotplate wells for a miniaturized atomic clock," *Optics Express*, vol. 20, no. 22, pp. 24650–24663, 2012.

[233] K. Mizuno, J. Ishii, H. Kishida, Y. Hayamizu, S. Yasuda, D. N. Futaba, M. Yumura, and K. Hata, "A black body absorber from vertically aligned single-walled carbon nanotubes," *Proceedings of the National Academy of Sciences*, pp. pnas–0900155106, 2009.

[234] M. A. Pagnutti, R. E. Ryan, G. J. Cazenavette, M. J. Gold, R. Harlan, E. Leggett, and J. F. Pagnutti, "Laying the foundation to use Raspberry Pi 3 V2 camera module imagery for scientific and engineering purposes," *Journal of Electronic Imaging*, vol. 26, no. 1, p. 013014, 2017.

A

CCD calibration for high-dynamic range beam profiling

During our investigations of the quality of beams focused by diffrative optics we employed the technique of high-dynamic range (HDR) beam profiling. The reason for requiring HDR profiling is due to some beam features having relative intensity of $< 10^{-3}$ to the beam peak. The signal-to-noise ratio of the Dataray WinCamD CCD is $\sim 10^{-3}$ and therefore to overcome this noise floor and image the low-intensity features we had to take exposures over multiple orders of magnitude and stitch them together to make a composite beam profile. To be sure we were accurately imaging the features and their relative intensities to the beam peak a rigorous calibration of the CCD response with beam power was required. We found that this investigation was warranted due to anomolous behaviour of the CCD at short exposure times.

Background intensity

We begun our calibration by extracting images from the CCD at varying programmed exposure times, t_p, with no incident laser beam, with the laboratory lights off and CCD shielded (but not fully-blocked) with a lens tube. This configuration was the same ambient conditions as the rest of the calibration (and final measurements) were performed in.

The background signal, $B(t_p)$, was determined as the mean background intensity of the image taken at t_p. Background signals were measured for the full range of possible programmed exposure times, from 40 μs to 500 ms. The extracted backgrounds signals are shown in Figure A.1. A deviation from linearity at 100 μs is visible.

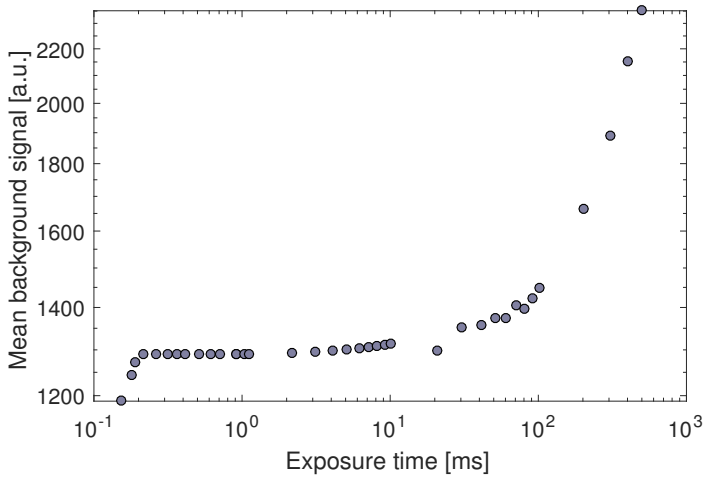

Figure A.1: The averaged background signal of the Dataray WincamD CCD for no incident laser radiation.

Determination of actual exposure time

To investigate the deviation from linearity in the background signal, we measured a signal of fixed power P incident on the CCD from a programmed exposure time of 40 μs to 640 μs. We performed linear regression on the background corrected signal $[S(t_P) - B(t_P)]$, where $S(t_P)$ is the maximum signal value measured on the CCD array. The ideal performance of the CCD would be a trend such that at $t_P = 0$ μs then the background corrected signal is zero. However, we found a non-zero $y-$intercept and therefore concluded that t_P is not equivalent to the actual exposure time, t_A. From the measured data we determine the constant offset $t_A = t_P + 112\ \mu s$ such that the $y-$intercept is set to zero. The reason for this offset is unknown, however a $\sim$ 100 μs discrepancy in the CCD electronics is reasonable. For the remainder of this appendix, we use the actual exposure time, applying the offset to the programmed exposure time.

Measurement of calibration curves

To use the CCD for high dynamic range beam profiling, we required a calibration curve that maps measured signal at an actual exposure time t_A to a relative power. For a Gaussian beam, the beam power is directly proportional to the intensity and therefore by performing the signal-power calibration we could calibrate relative intensities of Gaussian beams imaged at different exposure times. To vary the laser power incident on the CCD over the required orders of magnitude, we used both the laser current (10^2 range) and a half-waveplate and polariser (10^3 range). An ND3 filter was used to attenuate the power before the CCD to keep the signal below saturation over the power range investigated. We measured the laser power before the ND filter, as the power after the filter is outside the sensitivity of the power-meter. For each exposure time, the power is varied using the half-waveplate

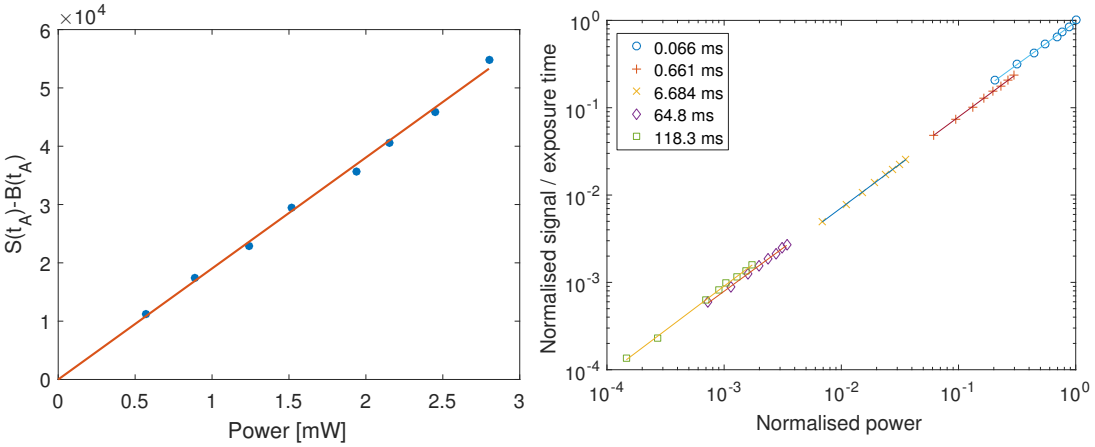

(a) **(b)**

Figure A.2: Signal response of the Dataray WinCamD beam profiling CCD, (a) Background corrected signal for an exposure time of $t_p = 0.066$ ms with a linear fit, (b) Measured data for all programmed exposure times with linear fits, the data is normalised by the exposure time and the maximum recorded signal.

and polariser such that the signal is measured from 20% to 90% of the CCD ADC (a measure of the peak current read-out on the CCD array) in steps of 10%. This is the quoted range of linearity by the manufacturer. For each data set corresponding to a fixed exposure time we performed linear regression on the quantity $[S(t_A) - B(t_A)]/(t_A \max(P))$ where $\max(P)$ was the maximum power used in the shortest exposure time data set. We fixed the $y-$intercept to zero, assuming linearity with ADC, and therefore find the gradients $m(t_A)$ to provide a mapping from normalised signal to normalised power. The linear response curves of the CCD are summarised in Figure A.2.

To perform a calibration on measured beam profiles, we first normalised all the beam profiles in a set to the maximum signal of the shortest exposure time image. The calibrated, scaled signal, $\hat{S}$ was calculated from

$$\hat{S}(t_A) = [S(t_A) - B(t_A)]/[m(t_A)t_A] \tag{A.1}$$

The profiles could then be stitched together, removing the sections of profile where the CCD was over-saturated. An example HDR beam profile calibration is shown in Figure A.3 demonstrating the overlapping of beam profiles after calibration.

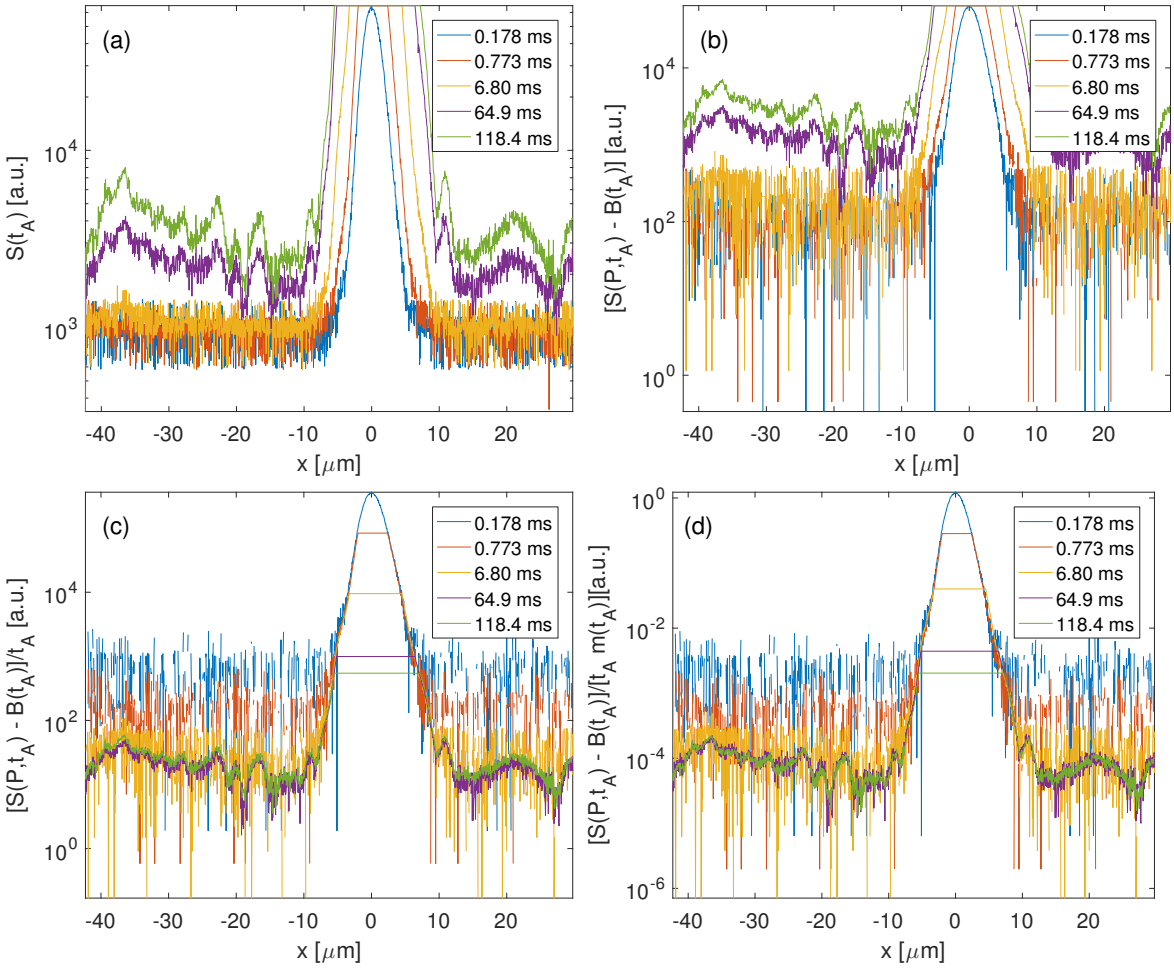

Figure A.3: Example high dynamic range beam profile calibration and stitching, (a) Raw measured data of a Gaussian beam at different actual exposure times, (b) Background corrected signals, (c) Background corrected signals normalised to their exposure time, (d) Background corrected and exposure time normalised signals corrected for the gradients of the linear response curves found from calibration.

B

Using the Raspberry Pi camera module as a beam profiler

The *Raspberry Pi Camera Module V2* has been previously suggested and characterised for scientific imaging by Pagnutti et al. [234]. It is shown that the *Sony IMX219* CMOS CCD used by the module is linear in exposure time and gain for all RGB spectral bands, an important consideration for accurate imaging. For beam profiling, it is also important that a linear reponse of the CCD with incident power can be recovered from the raw CCD signal. Here we characterise a *Raspberry Pi Camera Module V2 NoIR* which does not have an infrared filter over the CCD. The camera module comes with a lens mounted over the CCD which we carefully removed with a razor blade to leave an exposed board CCD. The CCD board is mounted to a Thorlabs cage mount (see Figure B.1) so that it can be mounted onto a cage system on a 3-axis micrometer stage. There are no obstructions protruding above the CCD and therefore it can brought arbitrarily close to a surface for optical characterisation.

To characterise the CCD for beam profiling, a λ = 404 nm laser beam is focused onto the CCD using a 10× objective with incident power controlled using a $\lambda/2$-waveplate and polariser, such that the CCD is not saturated. For each tested exposure time, an image of the Gaussian beam is recorded over a range of incident powers, as measured using a power meter placed before the 10× objective. A background image is recorded for each exposure time with the laser beam blocked and subtracted from every recorded image. As shown in Figure B.2a, it is found that a linear signal response with power only occurs above a certain power value, which is dependent on the exposure time. Below the critical power value the signal falls off as a power law, and therefore we must calibrate this non-linear signal response to use the CCD as a beam profiler.

The calibration occurs as follows. First, the linear region of the CCD signal response curve is fit with a first-order polynomial

$$(S_{\mathrm{L}}(t) - B(t)) = \alpha(t)p + \beta(t)\,, \tag{B.1}$$

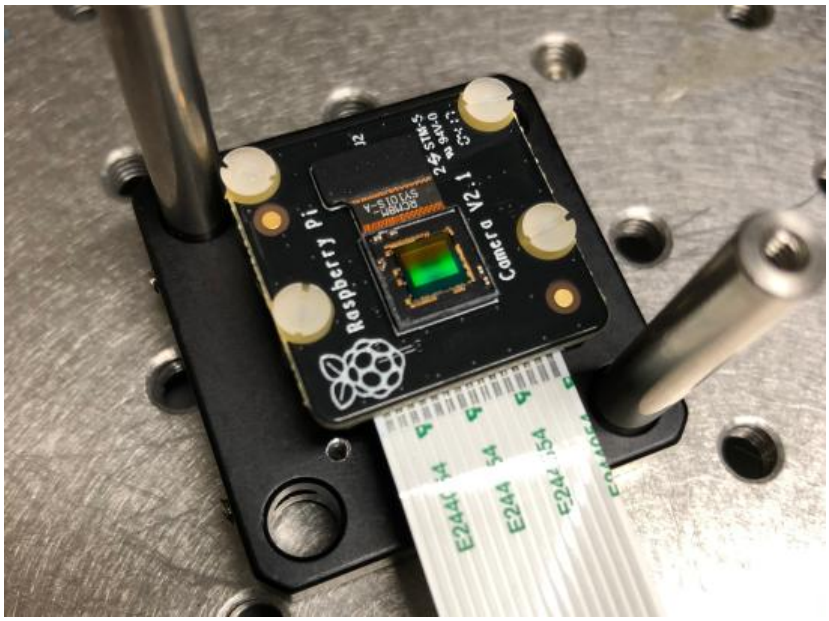

Figure B.1: Raspberry Pi Camera Module V2 NoIR mounted onto a cage mount with its lens removed. The included cage rods are not present during measurement.

where S_{L} is the peak signal of the recorded image in the linear region, B is the mean background intensity of for the corresponding exposure time, t is the exposure time and p is the incident power. We enforce the constraint that at $p = 0$ no background corrected signal should be recorded by subtracting the off-set β from $(S - B)$ to define

$$\bar{S}_{\mathrm{L}} = (S(t) - B(t)) - \beta(t) = \alpha(t)p \,, \tag{B.2}$$

where $\bar{S}_{\mathrm{L}}$ is the background corrected and off-set corrected linear signal. In the second calibration step we fit a power law to all the data points

$$\bar{S}_{\mathrm{NL}} = ((S(t) - B(t)) - \beta(t)) = \gamma(t)p^{\delta} + \epsilon(t) \,, \tag{B.3}$$

where $\bar{S}_{\mathrm{NL}}$ is the background corrected and off-set corrected non-linear signal. Rearranging Equation B.3 for power we find

$$p = \sqrt[\delta]{\frac{\bar{S}_{\mathrm{NL}} - \epsilon}{\gamma}} \tag{B.4}$$

which provides a mapping to a linear signal response by substitution into Equation B.2

$$\bar{S}_{\mathrm{L}} = \alpha(t)^{\delta}\sqrt{\frac{\bar{S}_{\mathrm{NL}} - \epsilon}{\gamma}} \,. \tag{B.5}$$

Therefore by substituting the full background corrected and offset corrected signal into Equation B.5 we recover a linearised signal. The process is shown for $t = 20$ ms in Figures B.2a-B.2c demonstrating that a linear signal response can be recovered from the measured non-linear response curve. Figure B.2d shows the results of performing the process for exposure times from 20 ms to 20000 ms where

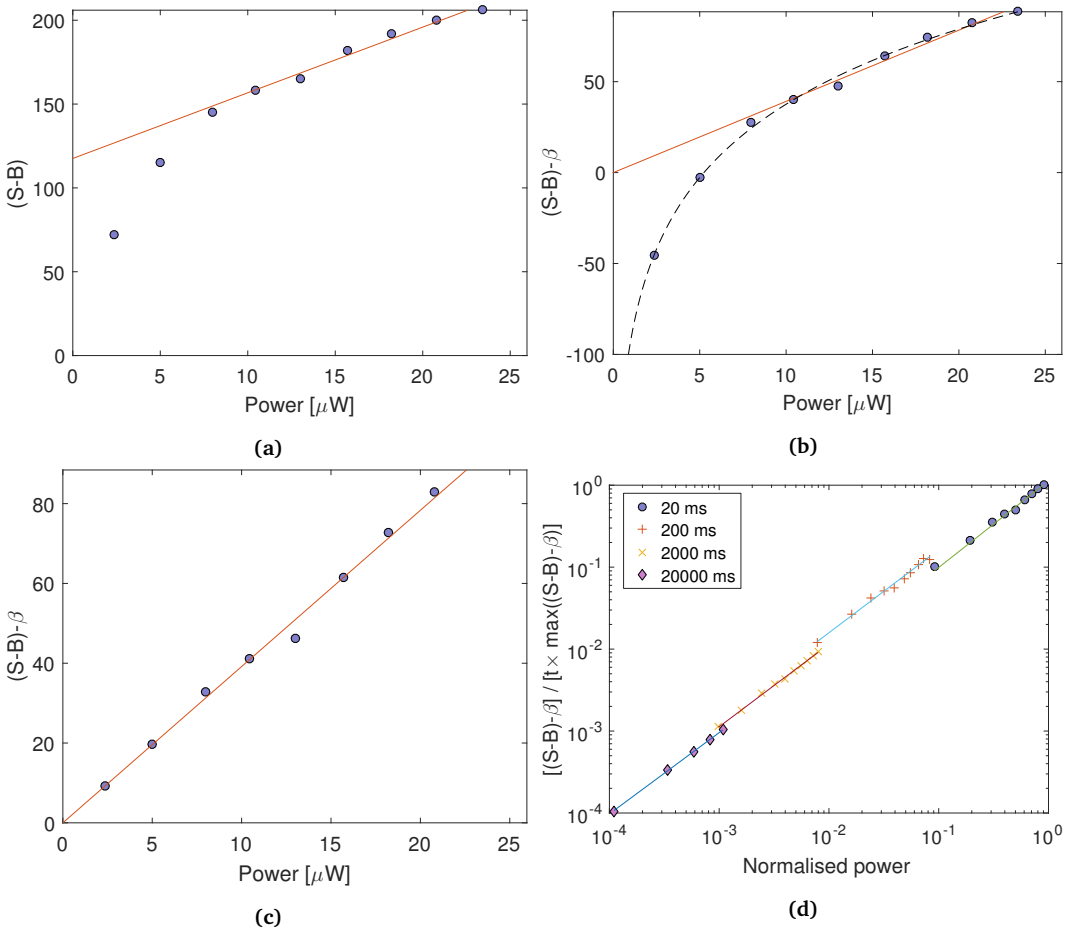

Figure B.2: The calibration process of the Raspberry Pi Camera Module V2 NoIR, (a) The measured, background corrected signal $(S - B)$ for an exposure time of $t = 20$ ms with a linear fit to the linear response region; (b) Offset corrected signal with a power law fit to all the data; (c) Linearised signal using the power law as a mapping to the linear trend line; (d) Linearised signal at various exposure times, normalised in power and signal to the data point of maximum power and divided by the exposure time. The linear fits at each exposure time provide an additional correction to deviations from a linear response with exposure time.

the signal at each exposure time has been normalised to the maximum recorded signal and divided by the corresponding exposure time. Linear fits to these calibration curves on the normalised scale provides an additional correction to deviations from linearity with exposure time. The performed calibration allows for the imaging of beam profiles over 4 orders of magnitude by applying the same correction process to full beam profile images to correct for the non-linear response with power.

C

A MATLAB package for optical assembly design, simulation, fabrication and testing

A comprehensive suite of MATLAB classes was developed to enable semi-automation of the optical assembly development process, from design right through to measurement processing. While we will not formally outline all of the properties and methods of all classes that have been written, we will give an overview of the class structure and example codes for generation of the optical assembly. An overview of the class structure is shown schematically in Figure C.1.

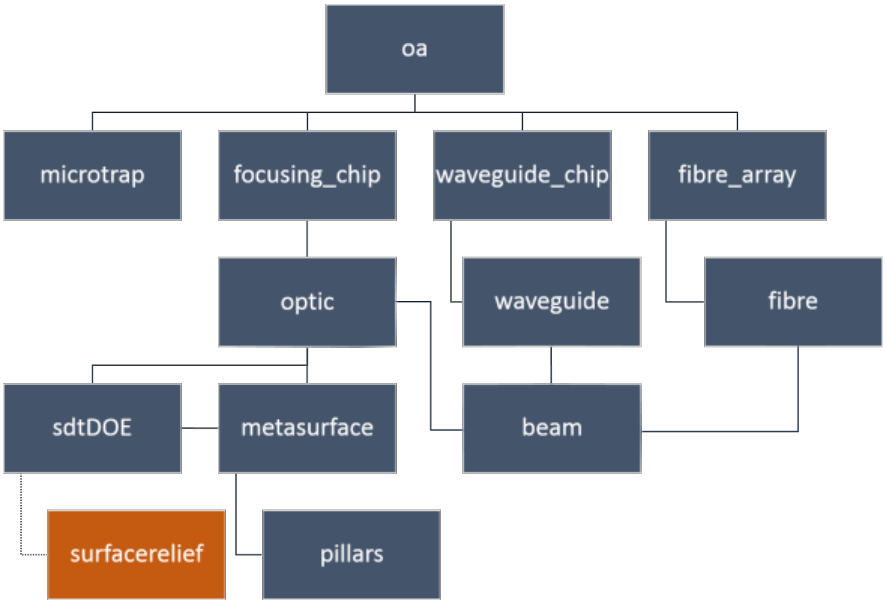

Figure C.1: Class structure for the optical assembly design code. Each block is a seperate class representing a physical object. Solid connecting lines indicate the class above acts as a container for that object. A dashed line indicates a parent-child relationship such that the class above is a superclass to the class below which has been coloured orange. The child class inherents all of its parents properties and methods. The class *oa* (optical assembly) acts as a container for all the subcomponents of the assembly

The design philosophy of the code package was to represent physical objects (lenses, waveguides,

microtraps etc.) as class objects. The main class is the *oa* class which represents the full optical assembly. *oa* serves as a container for object representations of all the system components and subcomponents. *oa* takes as input the design requirements of the system, which are user-specified, and through a series of methods the sub-component designs are generated. Importantly, the subcomponents can also be designed independently of any specific optical assembly, allowing for subcomponent development. An example of this is the comprehensive *surfacerelief* class that handles the design and fabrication of diffractive surface-reliefs.

For the full design of an optical assembly, the workflow occurs as following. First, the microtrap is fully specified with its number of electrode segments and the function of each segment. The function of a segment dictates which laser beams (e.g. Doppler cooling, photoionisation) are required for that segment. Secondly, the focusing element chip is specified by its distance from the microtrap, and which side of the microtrap it is on. Other specifications such that the focusing chip's materials are also included. The required optic positions on the focusing chip face are then calculated using stored *k*-vectors for each specified beam. The optic positions specify the end waveguide positions, and the waveguide chip is designed by mapping the optic positions to a fibre array - using the bend radius of a waveguide as a figure of merit. The optic associated with each waveguide specifies the beam, and therefore wavelength, of the light the waveguide must support. This in turn specifies the required fibre in each port of the fibre array. Once the components of the assembly have been designed (focusing chip, waveguide chip, fibre array), the subcomponents can then be designed and fabricated. The optic positions and associated *k*-vectors full specify the inputs of the diffractive optic design class (either *surfacerelief* or *metasurface*) which then outputs a fabrication map which has been prior calibrated. The start and end positions of the waveguides, as well as their wavelength, fully specify the inputs of the laser-written waveguide fabrication script. The specification of the fibre array can be sent directly to a commercial supplier who will then assemble the array.

As well as design of the optical assembly, the *sdtDOE* and *surfacerelief* classes include many methods for simulation and analysis of diffractive optics. These methods include diffraction efficiency calculations, high dynamic range beam stitching, 2D Gaussian beam fitting, and multiple different simulation techniques. These methods standardise testing procedure to enable repeatable and comparable results. To illustrate the capabilities that the class structure allows for, we outline two example scripts.

Example: Surface relief design, simulation and fabrication

```
%% DML parameters, SI units
```

```
radius=50e-6;
profile_resolution=40; % 1/40 um pixel size
degree=20;
object_coords=[0,0,1000].*1e-6;
image_coords=2000*[tan(degree*pi/180),0,1].*1e-6;
direction='f'; % light travels forwards
material_substrate='FS'; % fused silica
material_DML='PMMA950';
design_wavelength=405e-9;

%% Generate DML object to hold design information
DML=surfacerelief(radius, profile_resolution, object_coords,
    image_coords, direction, material_substrate, material_DML,
    design_wavelength);

%% Optimise the lens image point to focus Gaussian beam at desired
    position

w0=3.75e-6; % beam waist of source beam

DML=DML.optimisation_1D(w0);

%% Generate phase profile based on point-to-point model
DML=DML.gen_p2p_phase_profile;

%% Simulation of DML

Z=linspace(1500e-6,2500e-6,30);
DML=DML.simulation1D(1,w0,design_wavelength,object_coords(3),Z);

%% Generate physical surface-relief

DML=DML.gen_surface_profile(0);
DML.plot_profile('surface','');
```

```
fprintf('Maximum etch depth is %.1f nm\n',max(max(DML.surface_profile)
    ).*1e9)

%% EBL map generation

height_mult=linspace(0.75,1.25,5); % scan over a range of DML depths
    for dose optimisation

for i=1:length(height_mult)
    [DML,max_dose(i)]=DOE.gen_EBL_map_v2('PMMA950_calibration',
        height_mult(i));
    file_string=['DML_',num2str(i)];
    save_EBL_map(DML,file_string)
end
```

Example: Optical assembly design

```
OA=oa(); % initialise optical assembly

%% Trap Geometry

% Selection of trap design string changes preset geometries, user can
    also specify their own custom ones by hand.
trap_design='demonstrator2mm_2seg';

if strcmp(trap_design,'Original')
    electrode_widths=[340e-6,340e-6,340e-6];
    electrode_spacings=[10e-6,10e-6];
    electrode_functions={'ionisation','operation','operation'};
    aperture_width=340e-6;
    thickness_silicon=340e-6;
    thickness_electrode=20e-6;
    magnetic_field_vector='default';
elseif strcmp(trap_design,'Current')
    electrode_widths=340e-6 * ones(1,9);
```

```
    electrode_widths(2)=3*electrode_widths(2);
    electrode_spacings=10e-6 * ones(1,8);
    electrode_functions={'ionisation','transfer','operation','
        operation','operation','operation','operation','operation','
        operation'};
    aperture_width=340e-6;
    thickness_silicon=340e-6;
    thickness_electrode=20e-6;
    magnetic_field_vector='default';
elseif strcmp(trap_design,'demonstrator2mm_2seg')
    electrode_widths=[340e-6 340e-6];
    electrode_spacings=[10e-6];
    electrode_functions={'demonstrator2mm_addressing','
        demonstrator2mm_addressing'};
    aperture_width=340e-6;
    thickness_silicon=340e-6;
    thickness_electrode=20e-6;
    magnetic_field_vector='default';
end

% Generate microtrap
OA.microtrap=microtrap(electrode_widths,electrode_spacings,
    electrode_functions,aperture_width,thickness_silicon,
    thickness_electrode,magnetic_field_vector);

% Plot microtrap
figure
plot_microtrap(OA.microtrap)
axis equal
title('Electrode geometry')

%% Focusing chip generation

chip_thickness=1000e-6;
chip_material='FS'; % Fused silica
```

```
optic_material='TiO2_PQ' % Titania film supplied by PlasmaQuest
distance_from_trap_centre=2000e-6;
trap_side='back';

% Generate focusing chip, will auto-find optic positions from trap
    geometry
OA.focusing_chip=focusing_chip(OA.microtrap,chip_thickness,
    chip_material,optic_material,distance_from_trap_centre,trap_side);

% Plot optic layout with microtrap overlaid for reference
figure('color',[1,1,1])
plot_microtrap(OA.microtrap)
plot_optic_positions(OA.focusing_chip,1)
xlabel('x [\mum]')
ylabel('y [\mum]')
axis equal tight

%% Fibre array

number_of_horizontal_slots=16; % Standard v-groove array size,
    increases in powers of 2
number_of_vertical_slots=1;
fibre_pitch_horizontal=127e-6;
fibre_pitch_vertical=127e-6;

% Generate fibre array
OA.fibre_array=fibre_array(fibre_pitch_horizontal,fibre_pitch_vertical
    ,number_of_horizontal_slots,number_of_vertical_slots);

%Plot fibre array with optics overlaid for reference
figure('color',[1,1,1],'position',[0,0,800,600])
plot_vga(OA.fibre_array)
plot_optic_positions(OA.focusing_chip,1)
title('Fibre array (o) and optic (x) positions')
```

```
%% Match optics to fibres

OA=match_vga_to_optics_hungarian(OA);
plot_associated_optics(OA) % plots optics positions and fibre
    positions, with lines showing found pairings
OA=OA.assign_fibres_to_ports();
print_fibres(OA.fibre_array); %prints the fibres in each port for
    sending to v-groove manafacturer

%% Waveguide chip specification

waveguide_chip_length=12e-3;
curve_type='bezier';
z_step_size=1e-6; % for plotting
straight_section_length=1000e-6;

OA.waveguide_chip=waveguide_chip(waveguide_chip_length);
OA=define_waveguides(OA);
OA.waveguide_chip=generate_waveguides(OA.waveguide_chip,z_step_size,
    straight_section_length,curve_type);

figure
plot_waveguides(OA.waveguide_chip)

% Output waveguide coordinates in format accepted by waveguide
    fabrication code
XCoords(1,:)=OA.waveguide_chip.waveguide_positions_start(:,1)'.*1e3;
XCoords(2,:)=OA.waveguide_chip.waveguide_positions_end(:,1)'.*1e3;

ZCoords(1,:)=OA.waveguide_chip.waveguide_positions_start(:,2)'.*1e3;
ZCoords(2,:)=OA.waveguide_chip.waveguide_positions_end(:,2)'.*1e3;
```